

# TTF/TCNQ-based thin films and microcrystals – growth and charge transport phenomena

Dissertation  
zur Erlangung des Doktorgrades  
der Naturwissenschaften

vorgelegt beim Fachbereich Physik  
der Johann Wolfgang Goethe – Universität  
in Frankfurt am Main

von  
Vita Solovyeva  
aus St. Petersburg, Russland

Frankfurt am Main 2011

(D 30)

vom Fachbereich Physik der  
Johann Wolfgang Goethe – Universität als Dissertation angenom-  
men.

Dekan: Prof. Dr. Michael Huth

Gutachter: Prof. Dr. Michael Huth

Gutachter: Prof. Dr. Jens Müller

Datum der Disputation: 26.05.2011

for Notes



## ZUSAMMENFASSUNG

Organische Materialien haben bis zur Mitte des 20. Jahrhunderts hinsichtlich ihrer elektronischen Eigenschaften keine besondere Aufmerksamkeit auf sich gezogen. Größeres Interesse an diesen Materialien entstand erst durch die Entdeckung einer ungewöhnlich hohen elektrischen Leitfähigkeit des organischen Perylen-Bromin Ladungstransfer-Komplexes durch Inokuchi *et al.* im Jahr 1954 [1].

Diese neue Klasse von Materialien besteht typischerweise aus Donor- und Akzeptor-Molekülen, die in einer bestimmten Stöchiometrie aneinander gebunden sind. Elektrische Ladung wird zwischen den Donor- und Akzeptor-Molekülen transferiert. Um diesen Prozess zu beschreiben, entwickelte Robert Mulliken in den 60er Jahren ein theoretisches Gerüst (siehe [2]). Abhängig von der Anordnung der Moleküle und transferierten elektrischen Ladung kann der Ladungstransfer-Komplex (oder Salz) ein Isolator, ein Halbleiter, ein Metall oder sogar ein Supraleiter sein.

Noch mehr Aufmerksamkeit erhielten Ladungstransfer-Materialien mit der Entdeckung des ersten quasi-eindimensionalen organischen Metalls TTF-TCNQ (tetrathiafulvalene-tetracyanoquinodimethane) im Jahr 1973 [3,4].

Der Grund dafür ist einfach: das Studium organischer Ladungstransfer-Verbindungen kombiniert die Bedürfnisse der Elektronikindustrie in effizienten organischen Feldeffekttransistoren und organischen Solarzellen sowie der grundlegenden physikalischen Forschung. Das Forschungsgebiet liegt im Grenzbereich zwischen Chemie und Physik, was durch die Vergabe von Nobelpreisen auf diesem Sektor wiedergespiegelt wird:

- 1966, in Chemie, an Robert S. Mulliken “for his fundamental work concerning chemical bonds and the electronic structure of molecules by the molecular orbital method”.
- 1969, in Chemie, an Derek H. R. Barton und Odd Hassel “for their contributions to the development of the concept of conformation and its application in chemistry”.

- 1977, in Physik, an Philip Warren Anderson, Sir Nevill Francis Mott und John Hasbrouck van Vleck “for their fundamental theoretical investigations of the electronic structure of magnetic and disordered systems”.
- 2000, in Chemie, an Alan J. Heeger, Alan G. MacDiarmid und Hideki Shirakawa “for the discovery and development of conductive polymers”.

Diese Arbeit konzentriert sich auf das Studium dünner Schichten von organischen Ladungstransfer-Komplexen, d.h. Wachstumspfeferenzen, Ladungstransport, Phasenübergänge etc. Heute existiert eine Vielzahl möglicher Donor- und Akzeptor-Moleküle zur Herstellung von Ladungstransfer-Salzen, die an dieser Stelle nicht alle genauer betrachtet werden können. Die Untersuchung beschränkt sich auf die zwei verschiedenen Ladungstransfer-Systeme (i) TTF-TCNQ, bestehend aus dem Donor Tetrathiafulvalen (TTF) und dem Akzeptor Tetracyanoquinodimethan (TCNQ), und (ii) (BEDT-TTF)TCNQ, bestehend aus dem Donor Bis(ethylenedithio)tetrathiafulvalen (BEDT-TTF) und dem Akzeptor TCNQ. Die Wahl dieser Verbindungen wurde durch folgende Faktoren motiviert:

- Beide Systeme werden als Referenzverbindungen auf diesem Gebiet angesehen;
- Der TTF-TCNQ Ladungstransfer-Komplex existiert lediglich in einer kristallografischen Phase, während (BEDT-TTF)TCNQ in mehreren Strukturvarianten existieren kann;
- TTF-TCNQ ist das Paradebeispiel für ein quasi-eindimensionales Metall, während sein “Abkömmling” (BEDT-TTF)TCNQ je nach Phase unterschiedliches elektronisches Transportverhalten zeigt;
- Die TTF-TCNQ- und (BEDT-TTF)TCNQ-Komplexe durchlaufen eine Reihe von Phasenübergängen, wie den Peierls-Übergang oder den Mott-Metall-Isolator Übergang;
- Die Untersuchung von Unterschieden und Ähnlichkeiten zwischen den zwei Ladungstransfer-Salzen erlaubt ein tieferes Verständnis der zugrundeliegenden physikalischen Prozesse, die den Ladungstransport in leitfähigen organischen Materialien beeinflussen;

TTF-TCNQ besteht aus getrennten, parallelen Stapeln von Akzeptor (TCNQ)- und Donor (TTF)-Molekülen. Es zeigte sich, dass durch die Wechselwirkung zwischen den  $\pi$ -Orbitalen entlang der Stapelrichtung (siehe Abb. 1) die elektrische

Leitfähigkeit von TTF-TCNQ stark anisotrop ist. Bei Raumtemperatur gilt  $\sigma_b/\sigma_a > 10^2$ , wobei  $\sigma_a$  und  $\sigma_b$  die elektrischen Leitfähigkeiten entlang der  $a$ - bzw.  $b$ -Achse sind [5]. TTF-TCNQ-Einkristalle zeigen metallisches Verhalten oberhalb von etwa 60 K und durchlaufen eine Reihe von Phasenübergängen bei  $T_H = 54$  K,  $T_I = 49$  K und  $T_L = 38$  K [6–8], die sukzessive die metallische Leitfähigkeit der TTF- und TCNQ-Ketten unterdrücken und das Material in einen Isolator verwandeln. Der Phasenübergang bei 54 K wird durch eine Ladungsdichtewelle (CDW)-Peierls-Instabilität in den TCNQ-Ketten verursacht und üblicherweise als Peierls-Übergang bezeichnet [9].

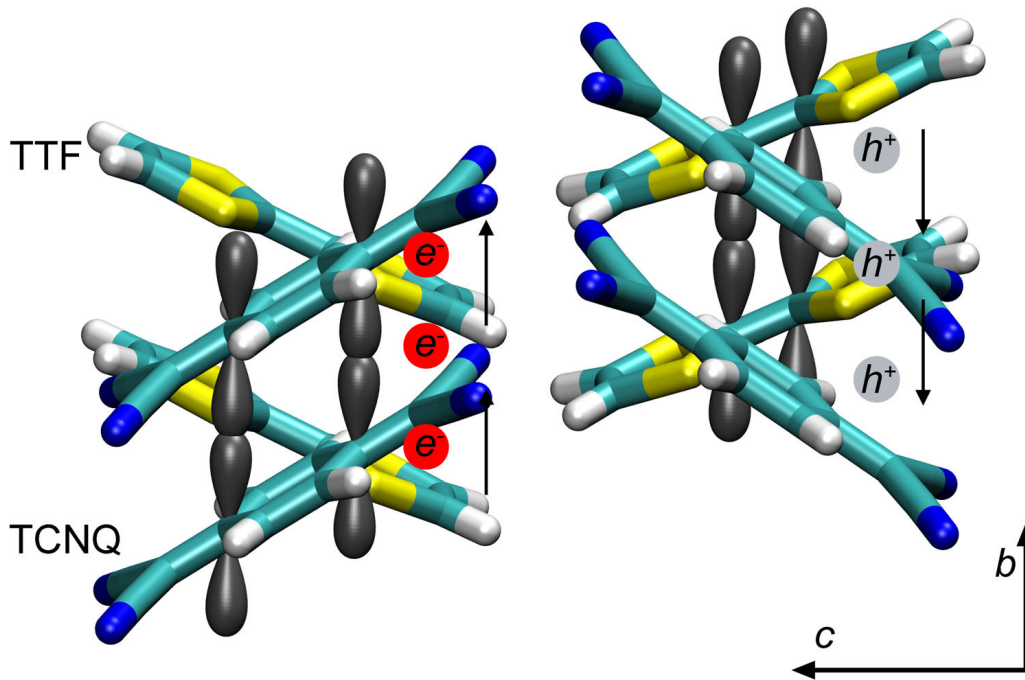


**Figure 1:** Schema des Überlapps der  $\pi$ -Orbitale der Donor (TTF) und Akzeptor (TCNQ) Stapeln entlang der Stapel Achse. Die  $a$ -Achse ist senkrecht zur  $b$ -Achse. Für diese Darstellung wurde das Programm VMD benutzt [10].

BEDT-TTF ist ein Abkömmling des TTF Molekül mit 2 zusätzlichen Ringen, die jeweils 2 zusätzliche Schwefel-Atome enthalten. Eine der bemerkenswerten Eigenschaften des BEDT-TTF-Moleküls ist die große Zahl von kristallographischen Phasen, die es mit diversen Anionen bildet. Man kennt heute die Kristallstrukturen von mehr als 200 BEDT-TTF-Salzen [11–13]. Die verschiedenen Kristallstrukturen werden als  $\alpha$ -,  $\alpha''$ -,  $\beta$ -,  $\beta'$ -,  $\beta''$ -,  $\theta$ -,  $\kappa$ - und  $\lambda$ -Phase bezeichnet. Die strukturellen Besonderheiten der vorhandenen Phase beeinflussen die kristallinen

Eigenschaften des (BEDT-TTF)TCNQ-Komplexes. In den letzten drei Jahrzehnten wurden drei strukturelle Varianten von (BEDT-TTF)TCNQ entdeckt: eine isolierende, monokline Phase [14], eine halbleitende, trikline Phase ( $\beta'$ ) [15] und eine metallische, trikline Phase ( $\beta''$ ) [16]. Eine der kristallographischen Phasen zeigt ein Mott-Metall-Isolator Übergang bei ungefähr Raumtemperatur. Eine andere zeigt eine hohe elektrische Leitfähigkeit im Vergleich zu anderen organischen Ladungstransfer-Komplexen und besitzt zudem eine sehr exotische Fermi-Oberfläche unter Raumtemperatur: zwei quasi-eindimensionale Fermi-Oberflächen kreuzen aneinander bei einem Winkel von  $90^\circ$ . Widerstandsmessungen der  $\beta''$ -Phase von (BEDT-TTF)TCNQ zeigen drei Anomalien bei 170 K, 80 K und 20 K.

TTF-TCNQ und (BEDT-TTF)TCNQ Ladungstransfer-Salze wurden bereits zuvor untersucht [3, 4, 6, 8, 9, 14–16], jedoch sind noch viele Fragen offen und interessant für ein weiteres Studium. In dünnen Schichten kann eine Reihe von Aspekten untersucht werden, die in Einkristallen nicht zugänglich sind. Beispiele sind grenzflächen- und oberflächen-induzierte Zustände, substrat-induzierte Spannungseffekte und die Rolle von substrat-induzierten Defekten im Hinblick auf die elektronischen Eigenschaften der Materialien. Diese Arbeit setzt sich mit verschiedenen Problemen bezüglich des Wachstums und der Ladungstransport-Phänomene in dünnen Schichten von TTF-TCNQ und (BEDT-TTF)TCNQ auseinander.

Zur Herstellung der untersuchten Dünnschichten wurde die Methode der physikalischen Gasphasenabscheidung verwendet. Der Wachstumsprozess fand in einer Ultrahochvakuum-Kammer mit einem Basisdruck von weniger als  $3 \times 10^{-7}$  mbar statt. Die präparierten Dünnschichten wurden in einem Rasterelektronenmikroskop sorgfältig untersucht. Die Morphologie wurde mit einem Rasterkraftmikroskop analysiert. Die chemischen Bestandteile der Mikrokristalle und Dünnschichten wurden mithilfe der energiedispersiven Röntgenspektroskopie analysiert. Durch Röntgen-diffraktometrie wurde die kristallographische Phase der erhaltenen Dünnschichten bestimmt. Durch fokussierte Elektronen- und Ionenstrahldeposition konnten Kontakte an die TTF-TCNQ Mikrokristalle angebracht werden.

Die folgenden Hauptprobleme werden ins Auge gefasst:

- Der Einfluss dünnschichtspezifischer Faktoren, wie das Substratmaterial und wachstumsinduzierte Defekte, auf die Temperatur des Peierls-Übergangs in TTF-TCNQ-Dünnschichten [17];
- Finite-Size Effekte in TTF-TCNQ wurden durch Messung der Transporteigenschaften von TTF-TCNQ-Mikrokristallen untersucht, wobei sich die Wichtigkeit der Kristallgröße für die Temperatur des Peierls-Übergangs zeigte. Zur



Verbesserung dieser Messungen wurde eine neue Methode zur Herstellung von Mikrokontakten angewendet [18];

- Separat davon wurde eine Analyse der strahlungsinduzierten Defekte in TTF-TCNQ-Dünnschichten und Mikrokristallen durchgeführt. Es zeigte sich, dass ein Elektronenstrahl eine gravierende Schädigung der Probe verursachen kann, sodass die elektronischen Eigenschaften der Probe stark verändert werden;
- Die elektrische Leitfähigkeit von TTF-TCNQ Mikrokristallen folgt einem “Variable Range Hopping”-Verhalten aufgrund von Defekten, die durch den Elektronenstrahl induziert wurden;
- Die Methode des Doppelschicht-Wachstums wurde zur Herstellung von (BEDT-TTF)TCNQ aus der Gasphase etabliert. Diese neu entwickelte Methode stellte sich als nützlich für das Erproben der Ladungstransfer-Salz-Bildung heraus [19];
- Die Struktur des gebildeten (BEDT-TTF)TCNQ wurde sorgfältig mit einem breiten Spektrum experimenteller Techniken untersucht;

Es wurde eine Reihe unterschiedlicher Substratmaterialien, wie zum Beispiel MgO(100), NaCl(100),  $\alpha$ -Al<sub>2</sub>O<sub>3</sub>(11 $\bar{2}$ 0), Si(100)/SiO<sub>2</sub>(285 nm), MgF<sub>2</sub>(001) etc. eingesetzt und der Einfluss des Substrats auf den Peierls-Übergang in TTF-TCNQ-Dünnschichten analysiert. Mit Ausnahme von NaCl(100) zeigte keines der Substratmaterialien einen signifikanten Einfluss auf die Temperatur des Peierls-Übergangs. Im Falle des NaCl(100)-Substrats ließ sich eine Abhängigkeit der Temperatur des Peierls-Übergangs von der Schichtdicke ausmachen. In diesem Fall lässt sich der Einfluss des Substrats durch das epitaktische Wachstum des TTF-TCNQ erklären [20], welches in den anderen Fällen nicht stattfand. In jedem Fall können die Defekte, die in TTF-TCNQ-Mikrokristallen durch den Nicht-Gleichgewichtsprozess entstehen, die Fernordnung stören. Sie sind teilweise für die beobachtete Verschiebung der Phasenübergangstemperatur verantwortlich.

Durch die endliche Größe der Proben beginnen in individuellen TTF-TCNQ-Mikrokristallen im Vergleich zu Dünnschichten und Einkristallen neue physikalische Aspekte eine Rolle zu spielen. Der Peierls-Übergang lässt sich durch die Änderung des Transportverhaltens identifizieren und liegt bei etwa 50 K. In dieser Arbeit wurden zwei konkurrierende Faktoren untersucht, die den Peierls-Übergang beeinflussen: (i) durch Elektronenstrahlung induzierte Defekte und (ii) substrat-induzierte Zugspannung. Dabei erwies sich der erste Faktor als der dominante.

Die monokline Phase von (BEDT-TTF)TCNQ wurde über die Gasphase erfolgreich hergestellt. Die hier entwickelten Techniken zum Test der Formierung einer

Ladungstransfer-Phase (bei der Gasphasenabscheidung) konnten mit Erfolg auch in anderen Laboren zur Untersuchung ähnlicher organischer Ladungstransfer-Salze eingeführt werden [21].

Diese Arbeit stellt ein ausführliches Studium von TTF-TCNQ- und (BEDT-TTF)TCNQ-Ladungstransfer-Komplexen in der Form dünner Schichten dar. Die in dieser Arbeit vorgestellten Methoden sind allgemein anwendbar und können auf ähnliche Untersuchungen an verschiedenen Materialien mit speziellen Ladungstransfer-Eigenschaften übertragen werden. Die Anwendung der fokussierten Elektron- und Ionenstrahlinduzierte-Deposition zum Studium der Transporteigenschaften von Mikrokristallen organischer Ladungstransfer-Komplexe erwies sich als erfolgreich und kann auch in zukünftigen Experimenten verwendet werden.

## CONTENTS

<b>1</b>	<b>Introduction</b>	<b>1</b>
1.1	Aims of the thesis . . . . .	2
<b>2</b>	<b>Organic charge transfer compounds</b>	<b>5</b>
2.1	Principal mechanism of charge transfer in organic donor – acceptor complexes . . . . .	6
2.2	The variety of organic charge transfer salts . . . . .	9
2.3	Application of organic charge transfer thin films in modern electronics	13
<b>3</b>	<b>Techniques for fabrication and characterization of thin films and microcrystals of organic charge transfer compounds</b>	<b>19</b>
3.1	Thin film growth methods . . . . .	19
3.1.1	Principal methods for thin film preparation . . . . .	20
3.1.2	Organic molecular beam deposition . . . . .	21
3.1.3	Ultra high vacuum chambers and effusion cells . . . . .	27
3.1.4	Bilayer growth method . . . . .	28
3.2	Methods for structure and morphology investigation . . . . .	29
3.2.1	X-ray diffraction . . . . .	30
3.2.2	Scanning electron microscopy and energy-dispersive X-ray spectrometry . . . . .	31
3.2.3	Atomic force microscopy . . . . .	32
3.2.4	Focused particle beam processing . . . . .	33
3.3	Electrical conductivity measurements . . . . .	34
3.3.1	Electrical transport measurement technique . . . . .	34
3.3.2	Conductivity measurements at low temperatures . . . . .	36
<b>4</b>	<b>Organic materials and substrates used for thin film fabrication</b>	<b>39</b>

4.1	TTF-TCNQ . . . . .	40
4.2	(BEDT-TTF)TCNQ . . . . .	45
4.3	Merging of organic charge transfer compounds in the solution growth method . . . . .	50
4.4	Substrates used for thin film growth . . . . .	52
<b>5</b>	<b>Defect-induced shift of the Peierls transition in TTF-TCNQ thin films</b>	<b>55</b>
5.1	Factors influencing the Peierls transition in TTF-TCNQ single crystals	56
5.2	TTF-TCNQ thin film growth and characterization . . . . .	59
5.3	Angle-resolved photoelectron spectroscopy of TTF-TCNQ thin films	77
5.4	Strain in TTF-TCNQ thin films . . . . .	79
5.5	Influence of substrate material and film thickness on electrical conductivity of TTF-TCNQ thin films . . . . .	84
5.6	Dependence of the Peierls transition temperature on the defects in TTF-TCNQ thin films . . . . .	86
5.7	Summary . . . . .	92
<b>6</b>	<b>Influence of the substrate-induced strain and irradiation disorder on the Peierls transition in TTF-TCNQ microdomains</b>	<b>93</b>
6.1	Experimental studies of TTF-TCNQ microcrystals . . . . .	94
6.2	Fabrication of TTF-TCNQ microcrystals and contacts . . . . .	96
6.3	Radiation-induced defects in TTF-TCNQ microcrystals . . . . .	102
6.4	Temperature dependence of electrical conductivity of TTF-TCNQ microdomains . . . . .	105
6.5	Substrate-induced shift of the Peierls transition in TTF-TCNQ microcrystals . . . . .	111
6.6	Summary . . . . .	114
<b>7</b>	<b>Organic charge-transfer phase formation in thin films of the BEDT-TTF/TCNQ donor-acceptor system</b>	<b>117</b>
7.1	Evaporation parameters of the BEDT-TTF donor and TCNQ acceptor molecules . . . . .	118
7.2	BEDT-TTF/TCNQ bilayer growth . . . . .	121
7.3	BEDT-TTF/TCNQ bilayer characterization . . . . .	122
7.3.1	Optical microscopy . . . . .	123

---

7.3.2	SEM and EDX investigations of BEDT-TTF/TCNQ bilayers	124
7.3.3	Hard X-ray photoelectron spectroscopy . . . . .	127
7.3.4	Focused ion beam cross-sectioning and X-ray diffraction . . .	128
7.3.5	Conductivity measurements . . . . .	131
7.4	Preparation of (BEDT-TTF)TCNQ thin films by the co-evaporation method . . . . .	132
7.5	Summary . . . . .	137
<b>8</b>	<b>Conclusion</b>	<b>139</b>
<b>A</b>	<b>Photolithography and lift-off processes</b>	<b>141</b>
<b>B</b>	<b>EDX measurements of TTF-TCNQ thin films</b>	<b>145</b>
<b>C</b>	<b>FEBID and FIBID parameters</b>	<b>147</b>
<b>D</b>	<b>Fitting of temperature-dependent electrical conductivity of TTF- TCNQ thin films and domains</b>	<b>149</b>
	<b>Acknowledgments</b>	<b>151</b>
	<b>Bibliography</b>	<b>153</b>
	<b>List of Figures</b>	<b>171</b>
	<b>List of Tables</b>	<b>181</b>
	<b>Biography (Lebenslauf)</b>	<b>183</b>



## INTRODUCTION

Organic conductors did not attract significant attention until the middle of the 20<sup>th</sup> century. The interest to this topic was brought by Inokuchi *et al.* in 1954 when organic material perylene-bromine complex with unusually high electrical conductivity was fabricated [1]. Since then, the research on organic materials has gained increasing interest, which has led, among others, to the establishing of a new class of organic materials called organic charge transfer compounds. An organic charge transfer compound (complex) typically consists of donor and acceptor molecules in stoichiometric proportions and with electric charge transferred between donor and acceptor. In the 60s, Robert Mulliken developed a theoretical framework for describing the charge transfer process in the donor-acceptor complexes (see e.g. [2]). Depending on the molecules arrangement and charge transfer degree, the charge transfer complex can be an insulator, semiconductor or even molecular metal and superconductor.

After 1973, i.e., when the first quasi-one-dimensional organic charge transfer metal TTF-TCNQ (tetrathiafulvalene-tetracyanoquinodimethane) was discovered, the field of organic charge transfer (CT) materials gained even more attention. The reason for that is simple: the study of organic charge transfer compounds serves the needs of electrical industry and fundamental physics at the same time. The problem of organic CT compounds lies on the borderline of chemistry and physics, as reflected in the Nobel prizes awarded in the area:

- 1966, in chemistry, to Robert S. Mulliken “for his fundamental work concerning chemical bonds and the electronic structure of molecules by the molecular orbital method”.

- 1969, in chemistry, to Derek H. R. Barton and Odd Hassel “for their contributions to the development of the concept of conformation and its application in chemistry”.
- 1977, in physics, to Philip Warren Anderson, Sir Nevill Francis Mott and John Hasbrouck van Vleck “for their fundamental theoretical investigations of the electronic structure of magnetic and disordered systems”.
- 2000, in chemistry, to Alan J. Heeger, Alan G. MacDiarmid and Hideki Shirakawa “for the discovery and development of conductive polymers”.

## 1.1 Aims of the thesis

This thesis is focused on the study of thin films of organic charge transfer compounds. Nowadays, the variety of possible donor and acceptor molecules used to fabricate charge transfer compounds is enormous [22–25], and one cannot review all of them. The present thesis studies two charge transfer compound systems grown from the donors tetrathiafulvalene (TTF) (see Fig. 1.1a) and bis(ethylenedithio)tetrathiafulvalene (BEDT-TTF) (see Fig. 1.2) with tetracyanoquinodimethane (TCNQ) as acceptor shown in Fig. 1.1b. The choice of the studied compounds was motivated by the following main factors:

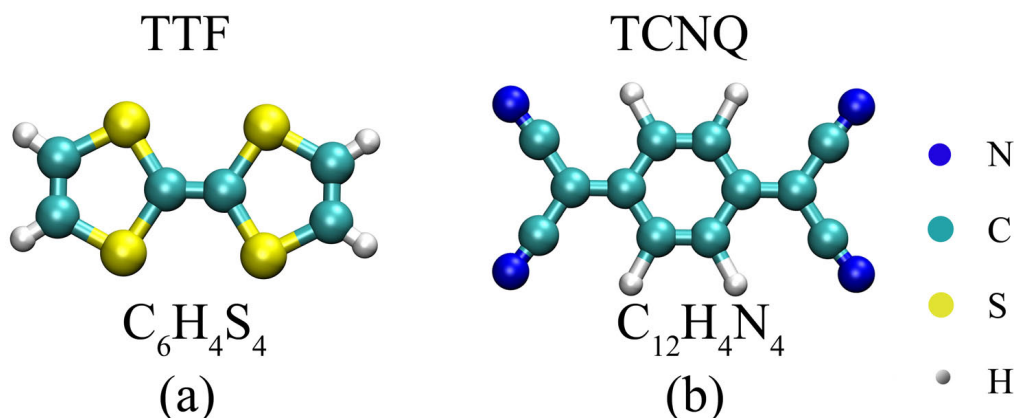


**Figure 1.1:** The schematic representation of (a) the donor molecule TTF and (b) the acceptor molecule TCNQ. The VMD program was used for molecules representation [10].

- Both compounds are considered as model systems among the organic charge transfer compounds;



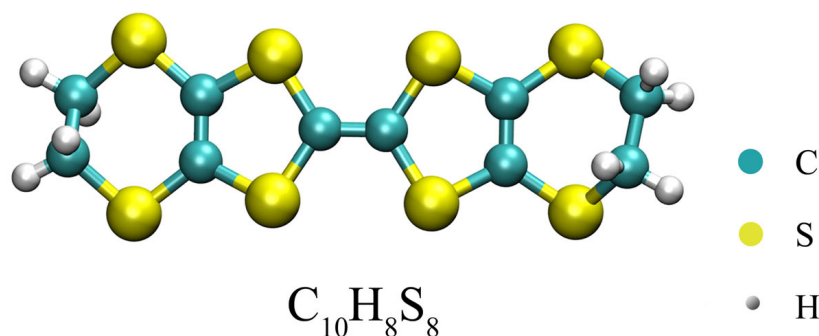


**Figure 1.2:** Donor molecule bis(ethylenedithio)tetrathiafulvalene (BEDT-TTF) favoring the formation of two dimensional CT complexes.

- TTF-TCNQ has one crystallographic motif, while the compound (BEDT-TTF)TCNQ exists in three crystallographic modifications;
- TTF-TCNQ provides an example of a quasi-one-dimensional metal, while its derivative (BEDT-TTF)TCNQ exhibits several crystallographic phases showing transport behavior from insulator to metal;
- TTF-TCNQ and semiconductor phase of (BEDT-TTF)TCNQ exhibit a series of phase transitions of the Peierls- and Mott-type;
- The study of the differences and similarities in the two charge transfer compounds helps to obtain an in-depth understanding of the underlying physical processes which govern the transport properties in organic conducting materials;

TTF-TCNQ and (BEDT-TTF)TCNQ are well studied CT compounds [3, 4, 6, 8, 9, 14–16], however, many questions are still open and interesting for further investigation. In particular, the study of thin films of these charge transfer compounds allows one to probe various physical properties of the compounds which are hardly accessible in single crystals. The thesis addresses several problems related to growth and charge transport phenomena in thin films of TTF-TCNQ and (BEDT-TTF)TCNQ. The following main new problems are addressed:

- The influence of thin films-specific factors, such as the substrate material and growth-induced defects, on the Peierls transition temperature in TTF-TCNQ thin films was studied;

- Finite size effects in TTF-TCNQ were investigated by considering transport properties in TTF-TCNQ microcrystals. The influence of the size of the crystal on the Peierls transition temperature was studied. In this context, a new method of microcontact fabrication was employed to favor the measurements;
- An analysis of radiation-induced defects in TTF-TCNQ thin films and microcrystals was performed. It was demonstrated that an electron beam can induce appreciable damage to the sample such that its electronic properties are strongly modified;
- A bilayer growth method was established to fabricate (BEDT-TTF)TCNQ from the gas phase. This newly developed bilayer growth method was showed to be suitable for testing (BEDT-TTF)TCNQ charge transfer phase formation;
- The structure of the formed (BEDT-TTF)TCNQ charge transfer compounds was analyzed by using a wide range of experimental techniques;

The structure of this thesis is divided into several chapters. An overview and the description of the basic physical principles underlying charge transfer compounds is given in chapter 2. Experimental techniques used for the growth and characterization of thin films and microcrystals are presented in chapter 3. Chapter 4 gives an overview of the physical properties of the studied organic materials. The study comprises the two different organic charge transfer complexes introduced above. Chapter 5 discusses the experimental study of TTF-TCNQ thin films. The Peierls transition in TTF-TCNQ is a consequence of the quasi-one-dimensional structure of the material and depends on different factors, studied in chapters 5 and 6. In contrast to TTF-TCNQ, the (BEDT-TTF)TCNQ charge transfer compound crystallizes in several different modifications with different physical properties. This difference is due to the respective peculiarities of the crystallographic structures. Chapter 7 presents the formation process of (BEDT-TTF)TCNQ charge transfer complex via the bilayer growth method. The thesis is concluded in chapter 8 by giving a summary and an outlook for future investigations. Some of the methods used in this work are quite general and can be applied to similar studies on other organic CT materials with interesting charge transfer properties.

## ORGANIC CHARGE TRANSFER COMPOUNDS

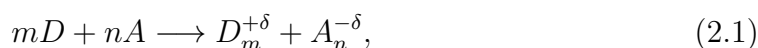
Organic materials have attracted significant attention for many years because of their interesting physical properties rendering them promising for applications [26–28] and for basic research on electronic correlation phenomena [22]. The interest in electronic properties of organic materials arose shortly after the pioneering paper by Inokuchi *et al.* [1], who discovered unusually high electrical conductivity in the organic charge transfer perylene-bromine complex in 1954. Before this discovery, the organic materials were considered to be insulators. Within the class of organic materials, charge transfer compounds are attractive since they hold the promise to significantly extend the presently developing organic electronics. Organic charge transfer systems represent a material class for interdisciplinary research on the borderline of correlation physics, material science and chemistry [22]. They also form the basis for extending the rapidly growing field of organic electronics towards binary donor-acceptor systems. In this regard, thin film growth studies, as well as surface- and interface-oriented research on the electronic properties of these materials have become more and more important [19–21, 29, 30]. Besides, there are several aspects which can be studied only in thin films and that are not accessible in single crystals, such as interface- and surface-induced states, substrate-induced strain effects and the role of substrate-induced defects with regard to the electronic properties of these materials.

In this chapter, basic definitions and examples of organic charge transfer compounds are outlined. The principal charge transfer reaction, which takes place when the organic charge transfer complex forms, is discussed in section 2.1 together with a short glimpse into theoretical approaches used for the study of the band structure

of organic CT compounds. Section 2.2 gives a historical review of the primary studies on CT compounds. The basic properties and examples of organic CT salts are also discussed in this section. Section 2.3 introduces several possible applications of thin films of organic charge transfer materials in electronics, reflecting the industrial interest in the area.

## 2.1 Principal mechanism of charge transfer in organic donor – acceptor complexes

An appealing class of organic materials is the donor-acceptor complex or the organic charge-transfer complex, where two individual molecules form a new compound, consisting of two partner molecules in a certain stoichiometric ratio, thereby partially transferring the charge density from one molecule (donor) to another (acceptor) [31]. The formed compounds have new physical properties, which differ from the ones of the initial donor and acceptor molecules. These properties stem from the crystallographic structure and band filling of the newly formed complex. The generic charge transfer reaction can be written as



where  $D$  represents a donor molecule,  $A$  represents an acceptor molecule,  $m$  and  $n$  are integer numbers and  $\delta$  is the charge transfer ratio [22]. This reaction takes place under favorable energy condition:

$$E_{CT} = I_D - E_A - E_e < 0. \quad (2.2)$$

Here  $I_D$  is the ionization energy of the donor molecule.  $E_A$  is the electron affinity of the acceptor molecule.  $E_e$  describes the Madelung energy, polarization and exchange energy [2, 32]. Equation (2.2) gives a necessary condition for the formation of a CT complex, which combines the requirement of a low ionization energy of the donor molecule and a high electron affinity of the acceptor molecule. The process of the charge transfer is schematically shown in Fig. 2.1. HOMO denotes the highest occupied molecular orbital and LUMO stands for the lowest unoccupied molecular orbital.  $I_D$  is the ionization energy gained by the originally neutral donor molecule after ejecting an electron from HOMO of this molecule. The affinity energy  $E_A$  characterizes the energy gained by the originally neutral acceptor molecule when an electron is added to its LUMO.

In order to quantify the energies of the HOMO and the LUMO for the molecules participating in the charge transfer process, the energy-band structure of the CT

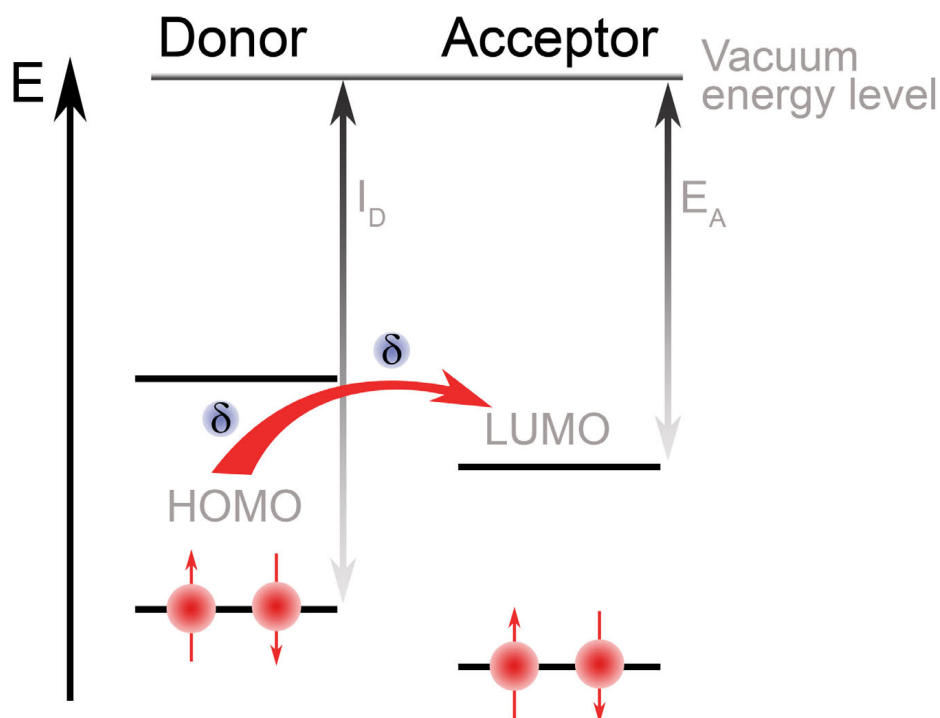


**Figure 2.1:** Energy diagram for the donor and the acceptor energy levels. The process of charge transfer is schematically illustrated with the curved arrow.

compounds is needed to be taken into account. To do so, the individual molecular orbitals for the donor and the acceptor molecules should be determined [23]. This can be achieved within the framework of the molecular orbital method, where the valence electrons are considered to be delocalized over the entire volume of the molecule and only those electrons (holes), residing in the vicinity of the Fermi surface, are taken into account [22]. The molecular orbitals  $\sigma$  and  $\pi$  are calculated as a linear combination of atomic  $s$ - and  $p$ -orbitals. Due to the periodic structure of the molecular organic crystal, the Bloch condition is applied to the wave-functions. In its simplest form, this approach is known as a tight-binding model [33].

There are several theoretical approaches used to describe the interaction of the electrons in the organic CT complex. In order to describe the strength of the electron correlation in organic CT complex, the interplay between the intra- and interatomic electron interaction in the material is of importance. An important parameter here

is the ratio between the Coulomb energy describing the on-site electron interaction  $U$  and the kinetic (electron hopping) term calculated as the interchain transfer integral  $t = W/4$ .  $W$  is the bandwidth [22]. When  $U/W \ll 1$  the electrons in CT compound are delocalized resulting in a weak electron correlation, while for  $U/W > 1$  the electronic correlations dominate leading to the formation of localized states in the material and, at half-filling, to an insulating state. Materials with a high degree of electron correlations are Mott-insulators, exhibiting charge-order states etc. [22].

The intrasite and intersite electron interaction in the correlated systems can be accounted for with the use of the Hubbard model. This model captures the main characteristics of the interaction processes taking place in a CT complex. The Hubbard model makes it possible to construct a Hamiltonian, which includes terms responsible for the inter- and intraatomic interactions describing correlation effects in the material. In its simplest form, the Hubbard model assumes a single band and considers the electron interaction to be local [34]:

$$H = -t \sum_{\langle i,j \rangle, \sigma} c_{i,\sigma}^\dagger c_{j,\sigma} + U \sum_j \hat{n}_{j\uparrow} \hat{n}_{j\downarrow}, \quad (2.3)$$

where  $c_{j,\sigma}^\dagger$  and  $c_{j,\sigma}$  are the creation and the annihilation operators for an electron at site  $j$  with spin  $\sigma$ , which is either  $\uparrow$  or  $\downarrow$ , respectively.  $t$  is the hopping integral between the nearest neighbors  $i$  and  $j$ ,  $\hat{n}_{j\uparrow}$  is a partial number operator equals to  $c_{j,\sigma}^\dagger c_{j,\sigma}$ . The summation in Eq. (2.3) is performed over nearest neighbors. The hopping integral can be determined within the framework of the density functional theory [35–37], while the determination of interaction parameter  $U$  is more complicated. In the limiting case  $U = 0$ , the Hubbard Hamiltonian simplifies to the tight-binding Hamiltonian. In the case of strong intersite interactions, a nearest neighbor interaction term is added to the Hamiltonian which is then written as:

$$H = -t \sum_{\langle i,j \rangle, \sigma} c_{i,\sigma}^\dagger c_{j,\sigma} + U \sum_j \hat{n}_{j\uparrow} \hat{n}_{j\downarrow} + \frac{1}{2} V \sum_{\langle i,j \rangle} \hat{n}_i \hat{n}_j. \quad (2.4)$$

In this case, the Hamiltonian is called the extended Hubbard Hamiltonian [22]. Here  $\hat{n}_i$  is equal to  $\hat{n}_{i\uparrow} + \hat{n}_{i\downarrow}$  and  $V$  is a next neighbor Coulomb interaction term. Despite its simple structure, the Hubbard model defines the basis for many powerful theoretical approaches towards gaining insight into the consequence of electronic correlations, in particular at reduced dimensions. The strong electron correlations in one-dimensional metal cannot be satisfactorily described within the framework of the Fermi liquid theory, which should in this case be substituted by the Tomonaga-Luttinger liquid model. The latter is characterized by the vanishing of the sharp edge at energy Fermi ( $E_F$ ). Knowledge of the principles of CT reaction and the

models describing the interaction of the electrons in the material enables one to understand the physical processes in CT materials in great details.

## 2.2 The variety of organic charge transfer salts

As follows from section 2.1, the properties of organic charge transfer complexes strongly depend on the crystallographic structure of the material. By combining different donor and acceptor molecules, a variety of geometry arrangements can be obtained, thereby allowing one to tune the physical properties of the CT compounds. An example of such combination is the TTF-TCNQ complex of which the crystal structure is presented in Fig. 2.2 [3, 4]. Starting at elevated temperature it shows a highly anisotropic conductivity until 60 K with a series of phase transitions at 54 K, 49 K and 38 K. The phase transition at 54 K is referred to as Peierls transition. The electrical conductivity of TTF-TCNQ is strongly anisotropic with  $\sigma_b/\sigma_a > 10^2$  at room temperature, where  $\sigma_a$  and  $\sigma_b$  are the electrical conductivities along the  $a$ - and  $b$ - directions, respectively [5]. The room temperature electrical conductivity along  $b$ -axis is about  $500 \text{ } \Omega\text{cm}^{-1}$ . A detailed description of the properties of the TTF-TCNQ CT complex is given in chapters 4-6, where the transport properties and phase transitions in TTF-TCNQ thin films and microcrystals are studied.

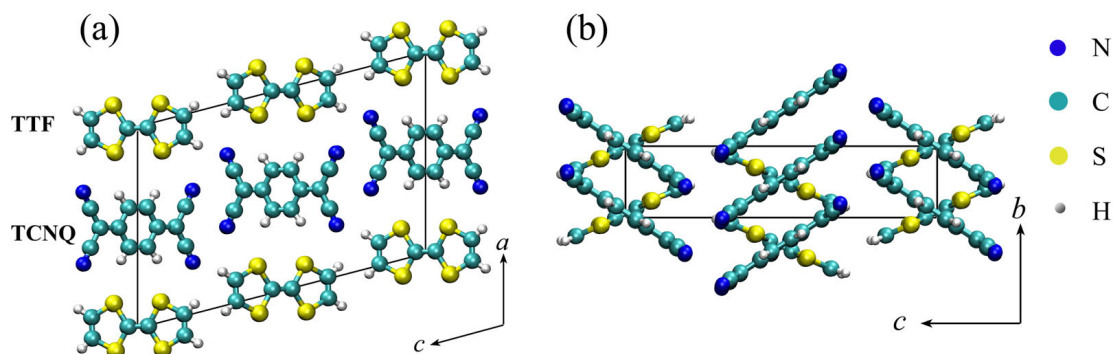


**Figure 2.2:** *Crystalline structure of TTF-TCNQ in the monoclinic crystal system with the space group  $P2_1/c$  [38]. (a) Orthogonal view along the stacking  $b$ -axis. (b) Orthogonal view along the direction perpendicular to the  $(bc)$ -plane of TTF-TCNQ. The VMD program was used for molecules representation [10].*

A selenium modification of TTF, the TSF (tetraselenafulvalene), results in the TSF-TCNQ complex, first described in 1974, one year after the discovery of TTF-TCNQ [39]. This complex also undergoes a Peierls transition at about 29 K.

The electrical properties of the newly-found metallic organic CT complexes inspired scientists in the 70s-80s to search for novel organic superconductor materials. In 1980, a first superconducting organic charge transfer compound, later named after Bechgaard, the Bechgaard salt  $(\text{TMTSF})_2\text{PF}_6$ , was found, having a superconducting phase transition at  $T_C=0.9$  K at the pressure of 12 kbar [40]. TMTSF stands for tetramethyltetraselenafulvalen. TMTSF is a derivative of TSF, synthesized by Klaus Bechgaard in 1974 [41]. This discovery started a boom which led to the discovery of the ambient pressure organic superconductor  $(\text{TMTSF})_2\text{ClO}_4$  in 1981 with  $T_C=1.4$  K [42].

The charge transfer complexes, mentioned above, represent quasi-one-dimensional electronic systems. As was forecast by Peierls in 1955, the one dimensionality involves a tendency to drive Fermi surface instabilities resulting in charge density (CDWs) and spin density wave (SDW) states rendering the material to be insulating at low temperature [43].

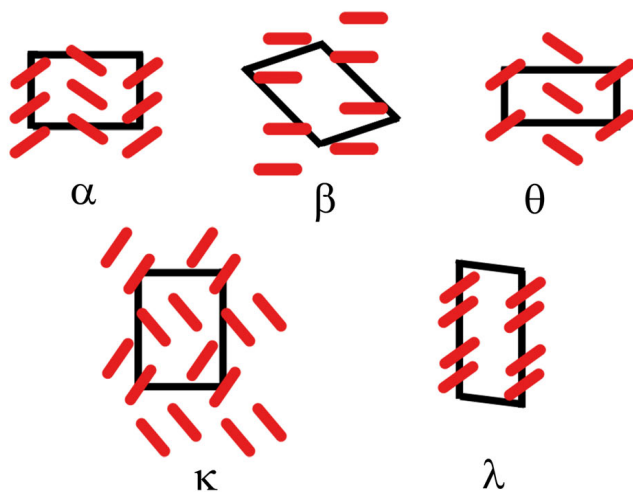


**Figure 2.3:** *Crystallographic modifications of the BEDT-TTF salts. The arrangement of the BEDT-TTF molecules is shown by red blocks. The unit cells are schematically shown by black lines.*

molecule. BEDT-TTF forms a rich variety of crystallographic phases with various anions. At the time of writing, crystal structures of more than two hundred BEDT-TTF salts have been reported in the literature [11–13]. The various crystal structures are classified as  $\alpha, \alpha'', \beta, \beta', \beta'', \theta, \kappa, \lambda$ . The most prominent motifs are illustrated in Fig. 2.3. Based on BEDT-TTF, a very rich family of organic charge transfer complexes was established. A new 2D organic charge transfer compound was found in the 80s:  $(\text{BEDT-TTF})\text{TCNQ}$  [14, 15], which is of interest to

To avoid the instabilities caused by the dimensionality effect, two-dimensional organic CT salts were studied. To form a two-dimensional organic CT complex, the building blocks based on TTF and TSF donor molecules were replaced by a new donor molecule BEDT-TTF (bis(ethylenedithio)tetrathiafulvalene), which was first synthesized in 1978 [44]. The structure of the molecule is shown in Fig. 1.2. It is a derivative of TTF having four extra sulphur atoms on the outer ends of the rings of the TTF



this thesis and will be discussed in chapters 4 and 7. Additionally, a new family of organic superconductors was found in the 90s:  $\kappa$ -(BEDT-TTF) $_2$ Cu[N(CN) $_2$ ]X, with X=Br, Cl.  $\kappa$ -(BEDT-TTF) $_2$ Cu[N(CN) $_2$ ]Br has the highest  $T_C = 11.6$  K for BEDT-TTF compounds at ambient pressure [45], while under applied pressure of 0.03 GPa  $\kappa$ -(BEDT-TTF) $_2$ Cu[N(CN) $_2$ ]Cl has an even higher  $T_C=12.5$  K [46]. The phase diagram for the  $\kappa$ -(BEDT-TTF) $_2$ X family of organic conductors, with examples of different ground states, is shown in Fig. 2.4.

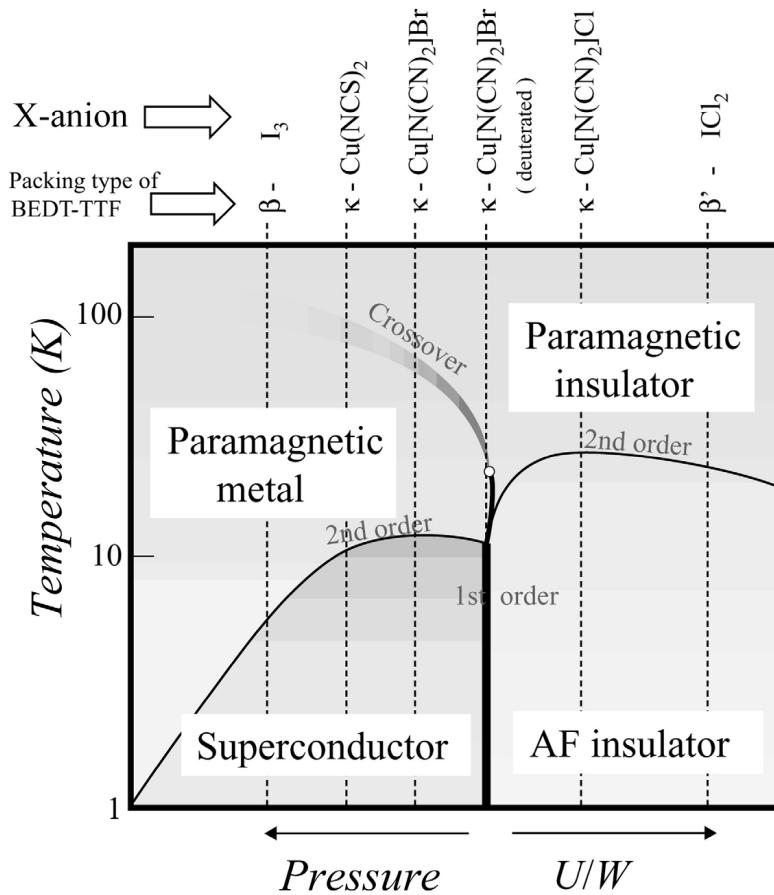


**Figure 2.4:** Phase diagram of the (BEDT-TTF) $_2$ X salts proposed by Kanoda [47]. AF is the abbreviation for antiferromagnetic.  $U$  is the on-site Coulomb repulsion,  $W$  is the bandwidth. The figure was adopted from [22].

The electronic transport properties of organic charge transfer complexes are strongly connected with the crystal structure of these materials, i.e. with the stacking arrangement of the donor and acceptor molecules in the CT complex. Qualitatively different stacking geometries of the molecules in organic CT complexes are

shown in Fig. 2.5. The segregated stack structure of donor and acceptor molecules,

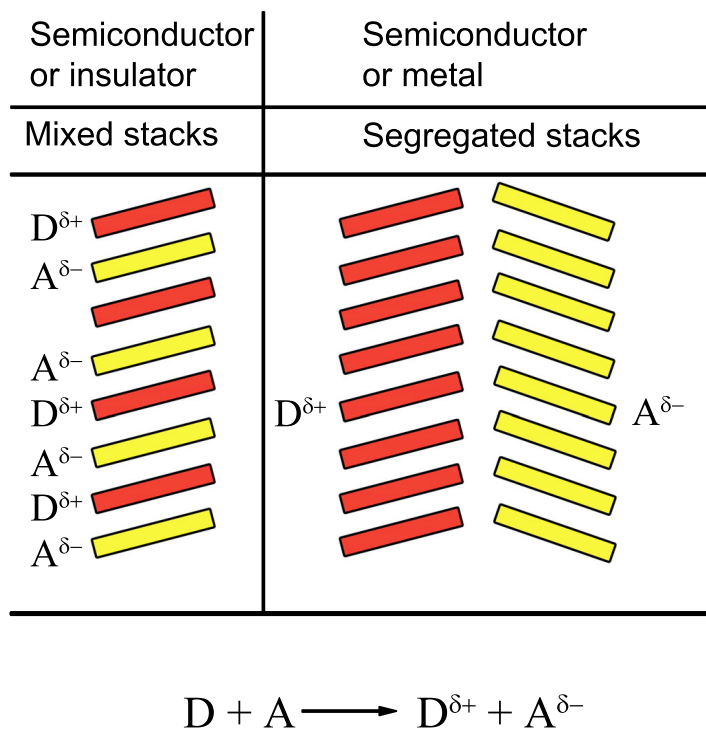


**Figure 2.5:** Possible stack structures of donor and acceptor molecules in the organic CT compounds. On the left side: the mixed stack structure; On the right: segregated stacking arrangement variant is presented.

with two types of separate stacks, leads to either semiconductor or metallic behavior of the electrical conductivity. Segregated stacks result in partially-filled bands of the overlapping  $\pi$ -orbitals, as the donors transfer a partial charge to the acceptor stacks (see Fig. 1). In the case of mixed stacks of donor and acceptor molecules organic CT complexes are isolators. TTF-TCNQ and TSF-TCNQ charge transfer compounds are examples of quasi-one-dimensional metals and have a segregated stack structure with the highest electrical conductivity axis along the stacking direction. TMTSF-TCNQ has two crystallographic phases, one corresponds to a mixed stack geometry and the other to the segregated stack structure. The molecule distribution in Bechgaard salts  $(TMTSF)_2X$  corresponds to stacks of TMTSF molecules ordered in sheets, which are separated by anion sheets. In  $\kappa$ -salts of BEDT-TTF, two BEDT-TTF molecules form a pair (dimer) with the central tetrathiafulvalene planes being nearly parallel. The BEDT-TTF pairs are almost perpendicular to each other and

form a sheet of donor molecules. The anions are arranged in insulating layers. Due to this specific arrangement, the electrical conductivity of these materials is strongly anisotropic. The formation of dimers favors the occurrence of frustration effects in the magnetic interactions. The wide spectrum of physical properties of organic charge transfer compounds stems from the variety of crystallographic modifications mentioned above.

## 2.3 Application of organic charge transfer thin films in modern electronics

In order to complete the overview of organic CT compounds, it is necessary to say a few words about their application in the electronic industry. This section gives a short outline of organic electronic devices, which can be fabricated based on thin films. The main advantage of organic compounds over the classical inorganic materials such as Si, GaAs etc. is that their components, i.e. the building blocks, are molecules, which can, in principle, be designed and synthesized according to the desired function of the device, albeit at significantly lower charge carrier mobilities. This holds the promise to reach the goal of molecular engineering to produce materials with predefined physical properties.

The most important device types are:

- Organic field effect transistors (OFET);
- Organic light emitting diodes (OLED);
- Organic photovoltaic cells (OPVCs) which are often called organic solar cells;

A brief description for each device follows below.

### OFET

OFETs represent a possible low-cost alternative to silicon-based field effect transistors (FETs) in the low-frequency domain. One of the main advantages of OFETs is the possibility for processing from solutions, using the spin coating methods and inject printing, which allows for low-cost fabrication on large areas. Furthermore, the physical vapor deposition growth of OFETs is performed at lower temperatures than for inorganic materials making this technique also attractive for mass production. Silicon can thus be substituted by organic materials even without using the

solvent-based methods, which can lead to the undesirable incorporation of the solvent molecules into thin film, for example with spin-coating. The working principle of OFET is similar to the FET based on inorganic materials, where the charge transporting channel is formed by organic film. The schematic structure of a back-gate, top-contact OFET is presented in Fig. 2.6.

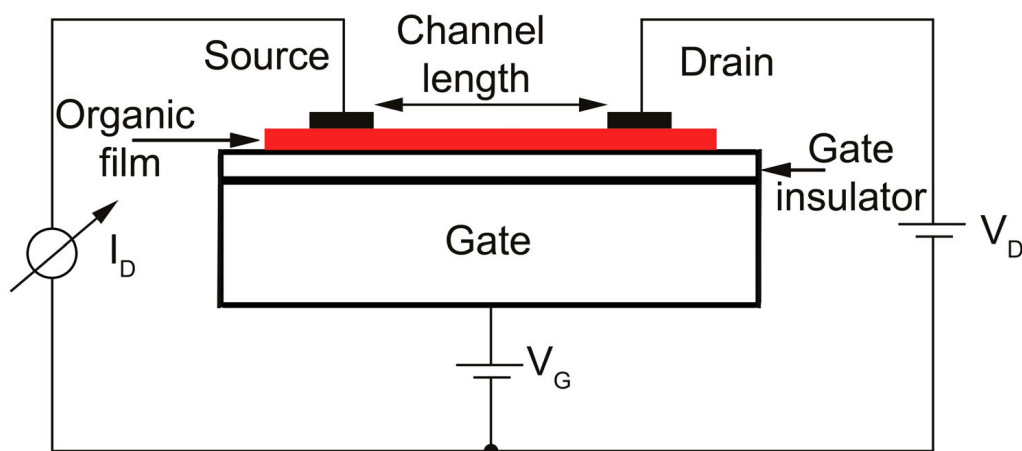


**Figure 2.6:** Schematic illustration of the working principle of organic field effect transistor with top contacts.  $V_G$  is the gate voltage,  $V_D$  is the drain-source voltage,  $I_D$  is the drain-source current.

The channel conductivity of organic semiconductors is rather small because no free charge is available and, at moderate voltage between drain and source, the current is negligible. By applying a negative (positive) gate voltage, positive (negative) charges are induced resulting in the increase of the current between the source and the drain. When a positive gate voltage is applied and electrons transport the current, the OFET is of the  $n$ -channel type. Negatively gated, the OFET is of the  $p$ -channel type. A highly doped silicon wafer with thermal oxide normally serves simultaneously as a dielectric substrate for the organic layer and as a gate electrode. The thickness of top oxide layer is important because it controls the leakage current. Bottom and top contact schemes for drain and source electrodes can be used. In the case of Au contacts, top contact devices give a better performance [48]. However, top contacts are not always straightforward to prepare on top of the organic

thin film because the film is heated during contact deposition and can be damaged. This problem is mitigated when, instead of the metal contacts, the contacts are made from organic materials. This reduces the carrier injection barrier between the electrodes and organic channel and consequently the contact resistance. This idea was supported by experiments performed on *n*-type OFETs with top TTF-TCNQ electrodes [49].

As an example, the *p*-channel materials with the highest mobility nowadays are pentacene ( $\mu = 3 \text{ cm}^2\text{V}^{-1}\text{s}^{-1}$ ) and rubrene ( $\mu = 20 \text{ cm}^2\text{V}^{-1}\text{s}^{-1}$ ) [48]. For comparison, Si has a hole mobility  $\mu \leq 450 \text{ cm}^2\text{V}^{-1}\text{s}^{-1}$  [50]. The *n*-channel OFET materials with the highest mobility are thiazole oligomers and thiazole/thiophene co-oligomers with trifluoromethylphenyl groups showing  $\mu = 1.83 \text{ cm}^2\text{V}^{-1}\text{s}^{-1}$  and N,N-dioctyl-3,4,9,10-perylene tetracarboxylic diimides with  $\mu = 1.7 \text{ cm}^2\text{V}^{-1}\text{s}^{-1}$  [51,52]. *n*-channel OFETs based on TTF-TCNQ have mobilities in the range of  $1.1 \dots 2.8 \text{ cm}^2\text{V}^{-1}\text{s}^{-1}$  [53]. Ambipolar transistors based on  $\beta'$ -(BEDT-TTF)TCNQ have a mobility of about  $2 \times 10^{-2} \text{ cm}^2\text{V}^{-1}\text{s}^{-1}$  [54]. The mobility of electrons for Si is  $\leq 1400 \text{ cm}^2\text{V}^{-1}\text{s}^{-1}$  [50]. Therefore, an increase of the mobility of organic semiconductor is needed to compete with silicon in all aspects. Organic charge transfer compounds have generally higher mobilities than either the donor or acceptor molecules from which they are formed. Consequently, the development of organic CT complexes is also relevant for furthering the development of OFETs.

## OLED

The first report on the electroluminescence of organic material was published by Martin Pope *et al.* in 1963 for a single crystal of anthracene inserted between two electrodes [55]. The large thickness of the crystal resulted in a strong self-absorption that prevented further development of the observed effect at that time. A breakthrough was reached only in the 80s, when the thin film evaporation technique was employed allowing the thickness of the active layer to be decrease [56,57]. The fabricated device was named organic light-emitting diode (OLED). Since that time monochrome and color displays based on OLEDs have been developed and are now commercially available. The working principle of an OLED is presented in Fig. 2.7a. In its simplest realization, it consists of two electrodes (cathode and anode) and organic thin film layers between them. To increase the efficiency of the device, the thickness of that layer should be less than 100 nm [31]. Materials with a high work function are normally used as anode (e.g. indium tin oxide (ITO)  $(\text{In}_2\text{O}_3)_{0.9}(\text{SnO}_2)_{0.1}$ ), while the cathode materials need to have low work function (e.g. Ca, Mg, Ag, Al). One of the electrodes must be semi-transparent to permit

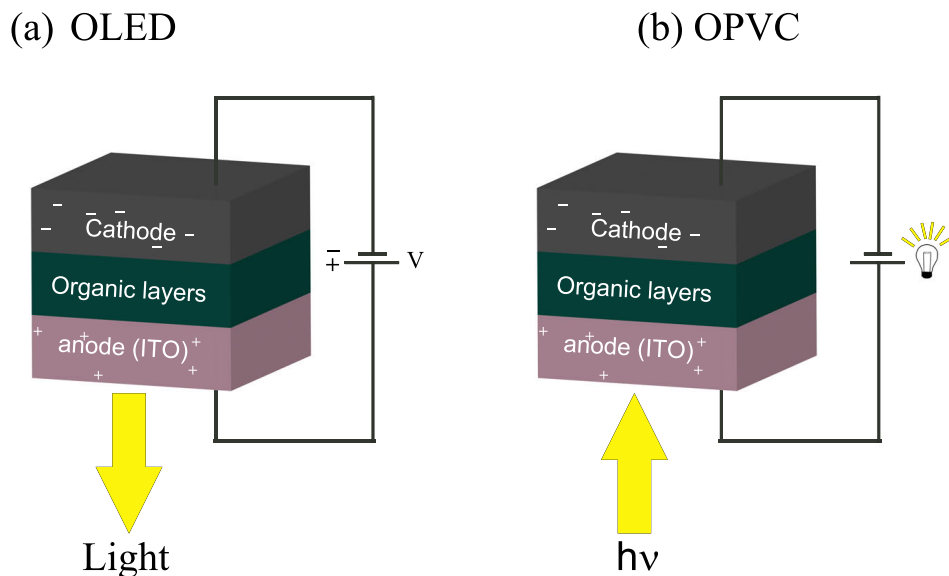


**Figure 2.7:** Working principle of: (a) OLED and (b) OPVC. The cathode, anode and organic layers are shown. The light direction is depicted by an arrow.

the light to exit the device. The following four processes take place in OLED:

- injection of charge carriers
- transport of the charge carriers
- binding of the charges to form an exciton
- recombination with subsequent light emission

By varying the different organic layers, the energy gap and the exciton energy can be tuned, therefore, the OLED emits at different wavelengths. By using organic CT complexes, the transport of the carriers and also binding of charge carriers into excitons can be improved, resulting in an enhanced efficiency of the devices.

## OPVC

In general, the OPVC has the same structure as the OLED (see Fig. 2.7b): two electrodes and organic layers in between. The two electrodes have different work functions and one of the electrodes is semi-transparent to incoming light. The light is absorbed by the organic layers and supplies the electrical power to the external circuit. The following physical processes take place in the OPVC:

- light absorption
- exciton creation and diffusion
- charge separation
- charge transport

The photovoltaic effect was detected for anthracene crystals in 1959 by Pope and Kallmann [58]. In 1975, the first organic solar cell was reported based on one layer of porphyrin and phthalocyanine [59], followed by the work in 1986, where the first two-layers solar cell was presented [60]. The combination of donor and acceptor layers allows to improve charge separation resulting in an increase of the efficiency of the device. In [60] copper-phthalocyanine (CuPc) was used as an electron donor and perylene-tetracarboxylic bis-benzimidazole as an electron acceptor. The charge carrier dynamics in donor-acceptor layers is very sensitive to the interaction between the donor and the acceptor. When the overlap between the ground-state electronic wave function of donor and acceptor is negligible, the charge separated state can be reached only through the excited state of donor (or acceptor) molecule. An increase in the donor-acceptor interaction leads to the formation of a charge transfer complex. In this case, charge separation can be reached directly after excitation from the charge transfer complex ground state to the charge transfer complex excited state. Therefore, the development of suitable charge transfer complexes is an important issue in the OPVC industry.





## TECHNIQUES FOR FABRICATION AND CHARACTERIZATION OF THIN FILMS OF ORGANIC CHARGE TRANSFER COMPOUNDS

This chapter gives an overview of the experimental techniques used for structure formation and characterization employed in the thesis. In section 3.1 the methods of fabrication of organic thin films and microcrystals are discussed. The advantages and disadvantages of the known growth methods are summarized and the main attention is directed to the organic molecular beam deposition technique, being the principal experimental method for the thin film fabrication used in the thesis. The methods for structure and morphology investigation of thin films and microcrystals employed in this study are presented in section 3.2 together with the focused beam patterning technique, which is needed for the fabrication of contacts on the grown microcrystals. The chapter is concluded in section 3.3, where the cryostat and electrical transport measurement techniques are described and the setup used for the low temperature transport measurements is discussed.

### 3.1 Thin film growth methods

This section is devoted to the techniques of thin film preparation. A short overview of the fabrication methods for organic thin films is given in the section 3.1.1 with a mention of their main advantages and disadvantages. The organic molecular beam deposition (OMBD) is one of the main techniques used in this work. It is discussed in section 3.1.2. The deposition setups are described in section 3.1.3. A newly

proposed method for testing the formation of organic charge transfer compound at the interface of the donor-acceptor bilayer is outlined in section 3.1.4 [19].

### 3.1.1 Principal methods for thin film preparation

The preparation of organic compounds in the form of thin films is a necessary step for the construction of organic material-based electronic devices, such as organic solar cells, electrochemical cells, organic light emitting diodes and organic field-effect transistors, as discussed in section 2.3. A common method for the fabrication of organic CT compounds is the solution growth method (see section 4.3), where single crystalline substances can be obtained (see e.g. Refs. [14,15,23]). An adopted variant of the solution growth for thin film preparation are the drop-casting [54,61] and spin-coating methods [62], respectively. Another widely-used method to grow organic thin films is the Langmuir-Blodgett technique, based on the formation of assemblies of monomolecular films on a liquid's surface, which is followed by its transformation into the thin film on the immersed substrate [63]. To form a monolayer thin film, the self-assembled monolayers method (SAMs) is employed. It is based on the formation of bonds between the substrate and dissolved organic materials: the end groups of molecules form covalent bonds, for example, with a gold layer on a substrate and the molecules form a film on the substrate surface [23].

Organic chemical vapor deposition (OCVD) is another technique to form organic thin films. In the OCVD technique, the precursor molecules are vaporized and transported by a carrier gas (argon or helium) through the heated lines to the precursor mixing area and after that to the deposition zone [23, 64]. The working pressure in the OCVD method is typically 1 mbar and the background pressure is in the range of  $10^{-6}$  mbar.

The main advantage of the methods mentioned above is their principle simplicity. However, all these methods also have certain disadvantages. In the case of the drop-casting and spin-coating method, as the solvent evaporates in the course of the crystallization process, solvent molecules may get incorporated in the growing film. In general, this will influence the material's electronic properties, which is typically not desirable. Inherent to the solvent-based methods is a second disadvantage for poorly soluble donor or acceptor species. In this case, not all the species can be used in the growth methods employing solutions. Defects and impurities introduced in the Langmuir-Blodgett technique as well as poor mechanical strength and thermal stability makes this method also rather limited for practical applications. In the SAM, method only certain substrate types can be used and also the thickness of the formed films is limited for practicality reasons. In using the OCVD method,

the growth rate can be controlled to some degree, but generally the growth rate is relatively high and the roughness of the formed films is significant. Another drawback of the OCVD method is in the possible incorporation of the carrier gas into the thin film.

To have a proper insight into the physical properties of thin films of organic CT complexes, one needs 1) to control the growth rate, 2) to reach a small concentration of impurities in the thin film, 3) to employ a vacuum compatible growth method in order to use freshly grown films in further studies.

Ordered thin films of CT systems can, in principle, be fabricated by physical vapor deposition of the donor and acceptor species without the disadvantages mentioned above, but other problems arise. *A priori* it is not clear whether a CT complex will form without the presence of a solvent. In the solvent-based growth methods, the dielectric properties of the solvent reduce the activation barrier for charge transfer. Moreover, careful selection of the solvent allows for biasing the nucleation rate towards the desired structural variant of the growing CT complex. In vapor-phase growth of thin films, the substrate's dielectric properties may play a significant role in CT, but this role is yet not well studied. In this thesis, the vapor phase deposition is chosen as a main technique. It allows to form organic thin films with sufficient purity in a controllable way and satisfies the conditions mentioned above. The detailed description of this technique is given in the following section 3.1.2.

For testing the formation of new organic CT complexes from donor and acceptor molecules, a new technique was proposed [19]. The bilayer sequential growth of acceptor/donor thin layers followed by a careful analysis of the acceptor/donor interface region can be efficiently used as discussed in chapter 7.

### 3.1.2 Organic molecular beam deposition

Organic molecular beam deposition (OMBD) is a technique used for the preparation of high-purity layers based on the evaporation of organic molecules in an ultra-high vacuum (UHV) chamber with a background pressure  $P \ll 10^{-6}$  mbar. The growth in an UHV chamber guarantees that a small amount of impurities will be incorporated into the formed film. The OMBD technique is an adaptation of the molecular beam epitaxy (MBE) method for organic materials. The MBE technique was first used in 1968 in the Bell Labs by J. R. Arthur and Alfred Y. Cho. The main difference between MBE and OMBD methods comes from the nature of the evaporated substances. MBE usually considers single atoms, while molecular complexes are used in OMBD. The forces acting in-between the deposited molecules and between the deposited molecules and the substrate in the OMBD method mostly are van der Waals

in nature [31]. As a sequence, the evaporation temperatures for organic molecular materials are much smaller than for metals or inorganic semiconductors.

By heating of the source material in an UHV chamber the molecular beam is produced, and the molecules are deposited on a substrate, kept at a certain temperature. The molecular flow is generated, for example, by Knudsen cells [65]. The sublimation temperature of organic materials is relatively low in comparison with metals and inorganic semiconductors and lies in the range  $[50 \dots 500]$  °C. The formation of a thin film takes place on the substrate surface, where the evaporated molecules interact with the surface atoms. Figure 3.1 illustrates schematically the main processes that occur on a substrate during the deposition:

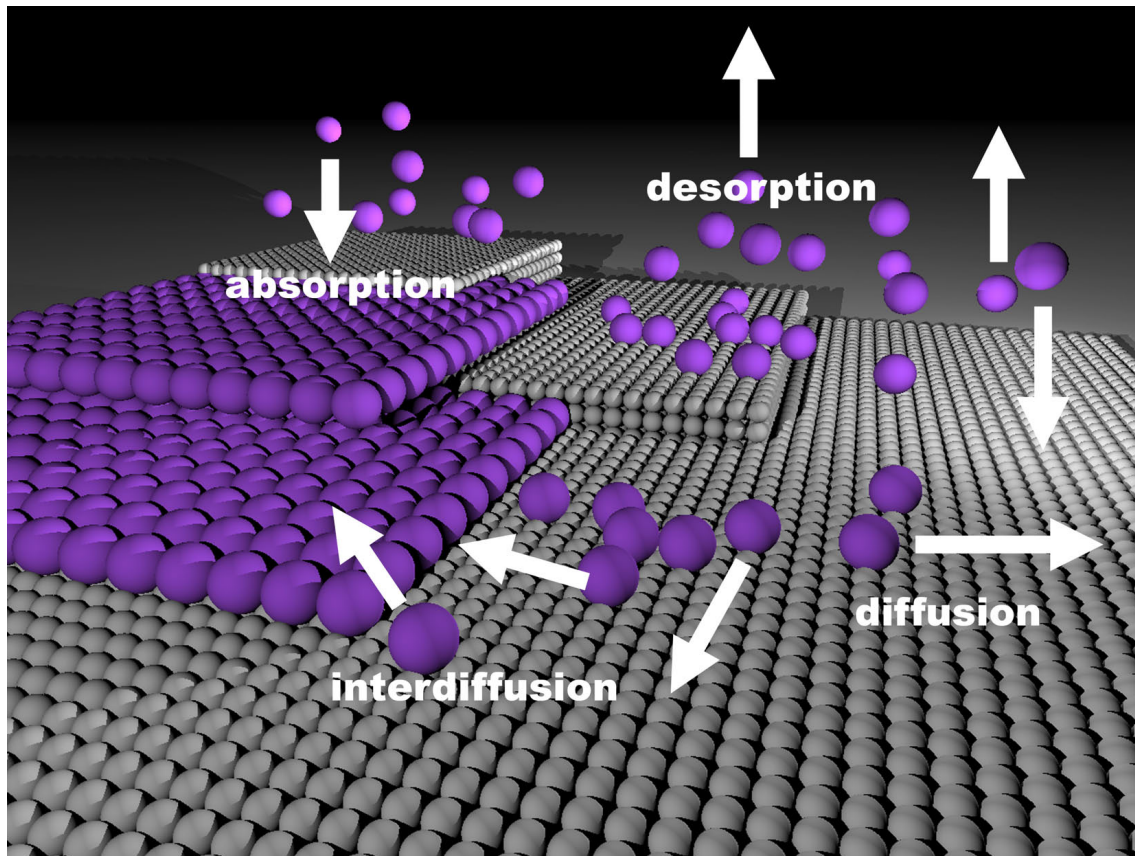


**Figure 3.1:** Various processes taking place during thin film formation. The grey spheres depict the substrate surface while violet spheres represent the deposited organic molecules.

- absorption of the evaporated molecules on the substrate surface;
- diffusion (and possible dissociation) of molecules on the substrate surface;

- interdiffusion of molecules in the growing layer;
- desorption of molecules from the substrate surface;

When a molecule reaches the surface it diffuses until it finds a favorable attachment site. If the molecule does not find an appropriate attachment site it desorbs from the substrate surface. In this case the impurities play an important role, because at certain conditions the formation of impurity layers is relatively fast, leading to the incorporation of impurities in the grown thin film. From the kinetic theory of gases, the time of adsorption of one monolayer of impurities can be estimated for background gas atoms of mass  $m$  at a pressure  $P$  [65, 66]:

$$\tau = \frac{N_s \alpha_c \sqrt{2\pi m k_B T}}{P}, \quad (3.1)$$

where  $N_s$  is the density of surface atoms required to form a complete monolayer,  $\alpha_c$  is the condensation (sticking) coefficient,  $P$  is the background pressure,  $k_B$  is the Boltzmann constant and  $T$  is the temperature. From Eq. (3.1) it follows that the formation time of one monolayer of impurities is inversely proportional to the pressure. If one assumes that the nitrogen impurities prevail in the evaporation chamber, then at a pressure of  $10^{-6}$  mbar one monolayer of impurities forms in about one second time. The normal working pressure in the OMBD process lies in the range  $10^{-7}$  to  $10^{-10}$  mbar which, in turn, corresponds to the time of formation of one monolayer of impurities in 10 to  $10^4$  s, respectively. This simple estimate shows the importance to keep the background pressure as low as possible in a growth experiment.

By using the kinetic gas theory one can model the organic molecular flow and predict the evaporation rate [65]. One of the most important parameter is the impingement rate  $z$  being the number of collisions per unit surface area per second:

$$z = \frac{P}{\sqrt{2\pi m k T}}, \quad (3.2)$$

where  $P$  is the vapor pressure,  $m$  is the particle mass and  $T$  is the evaporation temperature. The behavior of the thermal equilibrium vapor pressure of evaporated material in the Eq. (3.2) is given by the relation:

$$P \sim \exp\left(-\frac{\Delta H^0}{N_A k_B T}\right), \quad (3.3)$$

where  $\Delta H^0$  is a standard enthalpy of vaporization experimentally defined for each material,  $N_A$  is the Avogadro constant. From Eq. (3.3) it follows that the vapor pressure increases with increasing evaporation temperature.

From the impingement rate (see Eq. (3.2)), one can define the beam intensity  $J_\Omega$  for an ideal effusion cell shown in Fig. 3.2 as:

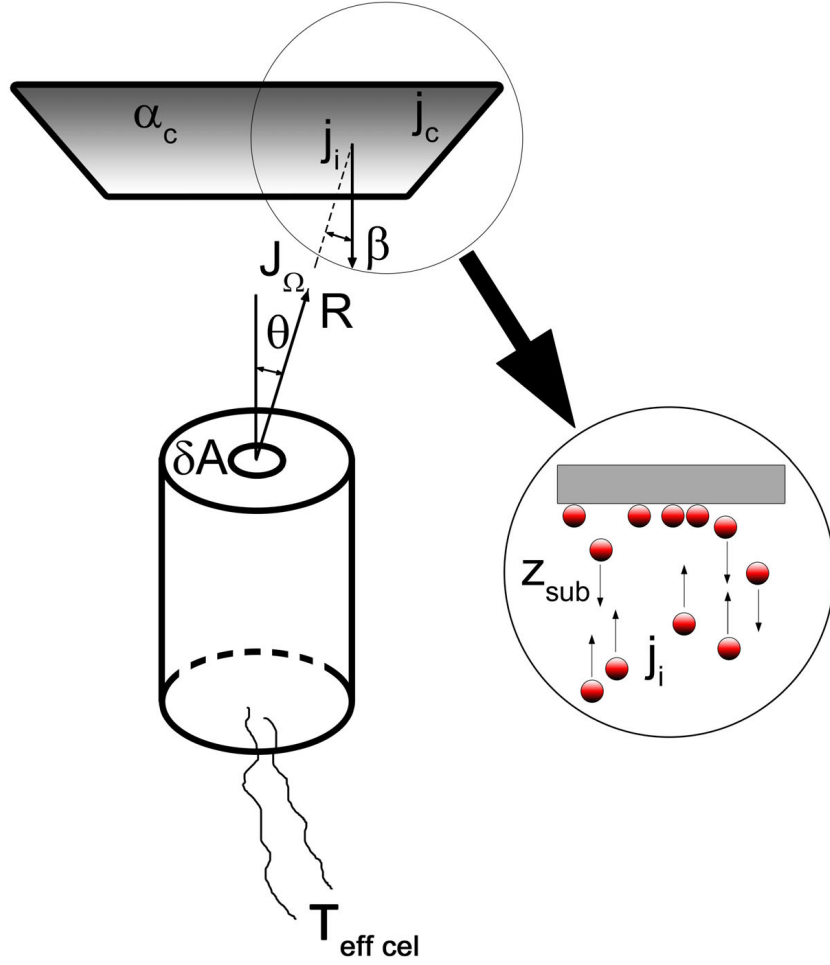


**Figure 3.2:** Schematic illustration of the Knudsen effusion cell and the deposition process of molecules on the substrate surface. The different quantities introduced in the figures are discussed in the text.  $T_{\text{eff cell}}$ , measured by, e.g., a thermocouple, is the effusion cell temperature.  $z_{\text{sub}}$  is the re-evaporation flux corresponding to the desorption of the previously absorbed molecules.

$$J_\Omega = \frac{z\delta A \cos \theta}{\pi}, \quad (3.4)$$

where  $\delta A$  is the orifice area of the effusion cell and  $\theta$  is the emission angle (see Fig. 3.2). Equation (3.4) obeys a cosine law of emission. It gives the total number

of particles per second per unit solid angle that are emitted in the direction specified by  $\theta$ . Using Eq. (3.4) the incident flux  $j_i$  on the substrate is:

$$j_i = \frac{J_\Omega \cos \beta}{R^2}. \quad (3.5)$$

Equation (3.5) gives the particle flux at the site on the substrate surface.  $\beta$  is the deposition angle and  $R$  is the distance from the effusion cell orifice to the substrate surface (see Fig. 3.2).

The total flux, or the condensation flux,  $j_c$  onto the substrate is combined from the incident flux given by Eq. (3.5), re-evaporation flux from the substrate surface,  $z_{sub}(T_{sub})$ , and condensation coefficient  $\alpha_c$  (or the sticking coefficient) of deposited material on the substrate. This coefficient shows the fraction of the molecules which are condensed on the substrate surface and is defined as:

$$\alpha_c = \frac{N_{cond}}{N_{tot}}, \quad (3.6)$$

where  $N_{tot}$  is the total number of molecules arriving on the substrate and  $N_{cond}$  is the fraction of the molecules which condense. The total flux is:

$$j_c = \alpha_c[j_i - z_{sub}(T_{sub})]. \quad (3.7)$$

The total flux  $j_c$  depends on several parameters, such as the vapor pressure and consequently the evaporation temperature. Furthermore, it follows from Eq. (3.5) that the flux is inversely proportional to the square of distance between the effusion cell opening and the substrate. Another factor influencing the sticking coefficient and re-evaporation flux, is the substrate material and substrate temperature. Therefore, taking into account the above-mentioned parameters, the total flux can be adjusted. The typical growth rates for organic materials range from 0.001 to 100 Å/s [66]. The smallest rate limit is not appropriate for practical application because it favors the increase of impurities in the grown film, while the highest rate limit is also not desirable due to kinetic limitations in the crystal growth.

Apart from the evaporation parameters, there are other aspects which need to be taken into account. While the flux of particles is defined within the framework of the kinetic gas theory, the thin film growth behavior is defined by the interaction between the forming film and the substrate. There are three main growth modes describing the formation of thin films on a substrate [67–69] (see Fig. 3.3). The layer-by-layer thin film growth mode is also called Frank-van der Merwe growth (see Fig. 3.3a). A strong interaction between the substrate and the deposited molecules leads to the formation of the first complete layer, which is then covered by the second

less bound layer etc. The monotonic decrease of the binding leads to a smooth film formation. In the Volmer-Weber growth mode (see Fig. 3.3c), islands are formed instead of smooth layers. This growth behavior takes place if the deposited molecules are more strongly bound to each other than to the substrate. A third type of growth is a combination of Frank-van der Merwe and Volmer-Weber growth: the Stranski-Krastanov growth mode (see Fig. 3.3b). In this case after some critical thickness is reached the layer-by-layer growth turns into island growth. It is worth noting that any factor, which disturbs the monotonic decrease of the binding, causes a change from layer-by-layer growth to island growth. The growth rate for the layer-by-layer growth needs to be controlled and kept small.

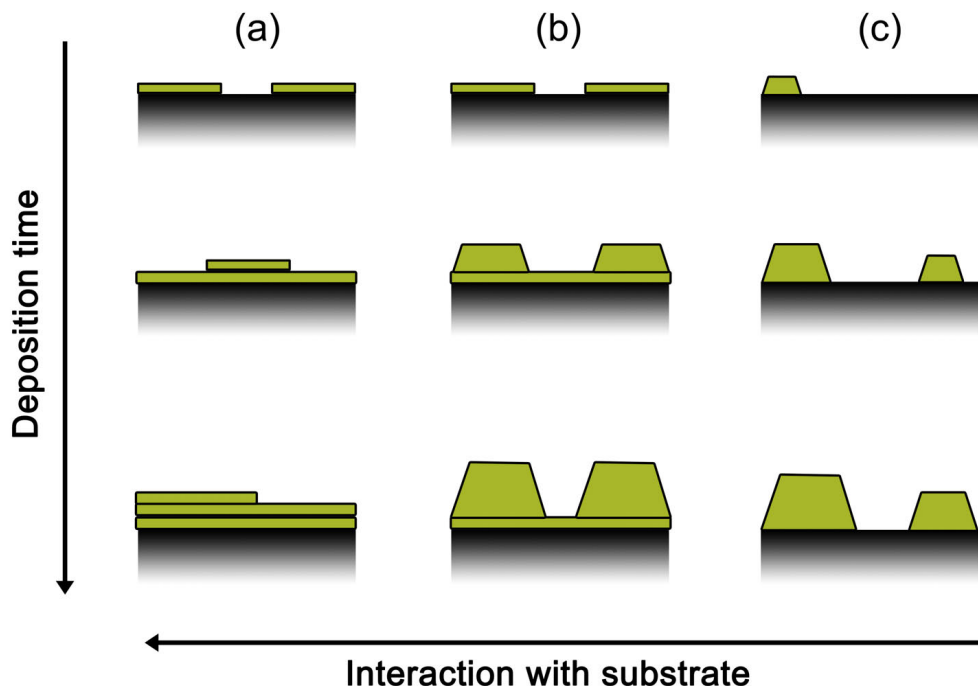


**Figure 3.3:** *Thin film growth modes on top of the substrate: (a) Frank-van der Merwe (layer by layer) growth mode, (b) Stranski-Krastanov (layer-island) growth mode, and (c) Volmer-Weber (island) growth mode.*

The choice of the substrate has a direct influence on the growth mode of thin films. Due to the importance of this factor, a significant attention is paid in the thesis to the study of the correlation between the substrate material and the growth mode of organic thin films, in particular for the TTF-TCNQ CT complex. The substrates used in this work are listed in section 4.4.



The microsize domain growth was studied as a subcase of the thin film growth by the physical vapor deposition method.

### 3.1.3 Ultra high vacuum chambers and effusion cells

The OMBD process takes place in an UHV chamber. Three different UHV chambers were used in this thesis. All chambers are equipped with turbo-molecular and fore-vacuum pumps. The general scheme of a deposition chamber is presented in Fig. 3.4. The temperature of effusion cells and substrates is measured with self-made Ni-NiCr-thermocouples coupled to the heated body of the effusion cells by copper wool, and controlled with a Eurotherm PID-controller (2208 or 2408). Below follows a more detailed description of the chambers used in this work:

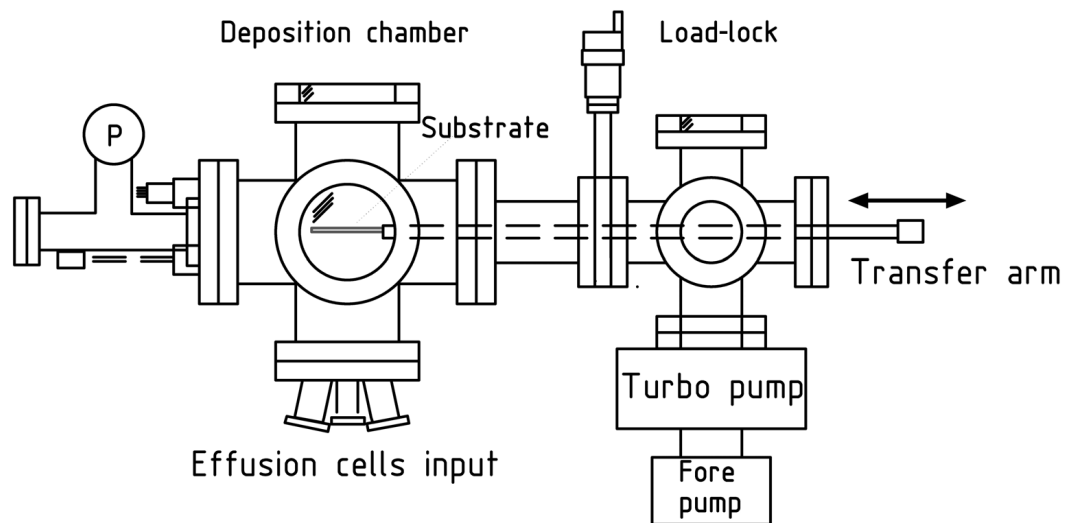


**Figure 3.4:** Schematic illustration of an UHV deposition chamber with load-lock chamber and deposition chamber. The transfer arm is used to transport the substrate holder with the substrate from the load-lock chamber to the deposition chamber.

#### “Multi-purpose” OMBD chamber

The OMBD chamber is equipped with substrate heating and cooling facilities. The substrate temperature can be varied from  $-50$  to  $>100$  °C. The OMBD chamber is part of an interconnected multi-chamber vacuum system with load-lock. The

background pressure in the OMBD chamber is about  $2 \times 10^{-9}$  mbar. A halogen lamp in the load-lock is used for substrate annealing up to 380 °C. This pre-heating of the substrate is important because it allows absorbed water to be removed from the substrate surface. Five Knudsen effusion cells are available in the OMBD chamber, with the distance from the effusion cell to the substrate varying from 2 to 25 cm. The chamber is equipped with a Low-Energy Electron Diffraction (LEED) system. The detailed description of the chamber is given in [70].

### **Test chamber**

The “test” chamber is a one chamber set-up, with background pressure in the range of  $2 \times 10^{-8}$  to  $5 \times 10^{-7}$  mbar depending on the pumping time. The chamber is equipped with one Knudsen effusion cell. The distance between the substrate surface and the effusion cell orifice is adjustable and can be varied in the range of 0.5 . . . 10 cm. Substrate heating was performed by Peltier elements (17A0021-Peltron GmbH) clamped to the substrate holder. The substrate temperature can be varied in the range of 23 . . . 70 °C.

### **“Mini”-OMBD chamber**

The “mini”-OMBD chamber is a new transportable OMBD system and load-lock equipped with three Knudsen effusion cells. Its design and assembly was carried out as part of this thesis in collaboration with Milan Rudloff. The distance between the substrate surface and the effusion cell orifice is fixed to 7 cm. The background pressure in the main chamber is in the range of  $7 \times 10^{-9}$  to  $2 \times 10^{-8}$  mbar. The pressure in the load-lock is  $\sim 10^{-6}$  mbar, allowing fast transfer of the sample from the load-lock into the main deposition chamber.

#### **3.1.4 Bilayer growth method**

A new method for testing of charge transfer phase formation was developed in the course of the experiments [19]. The main idea of this technique is to bring in direct contact donor and acceptor molecules at the interface between two thin film layers. Subsequently the bilayer structure is annealed. The direct contact between the donor and the acceptor layers favors organic CT complex formation. A significant advantage of this technique is in the easy testing of possible CT complex formation without long adjustment of the growth parameters in the co-evaporation method or in the case of the solution growth method.

The bilayer technique was successfully used for growing bilayers of TTF/TCNQ films. The charge transfer takes place at the bilayer interface even during the evaporation of the donor layer (TTF) on top of the acceptor (TCNQ) and the TTF-TCNQ CT complex forms. The group of Prof. Dr. Schönhense (Johannes Gutenberg-Universität Mainz) applied the proposed bilayer growth technique for the study of charge transfer phase formation of the coronene derivative molecules, where coronene-hexaone ( $C_{24}H_6O_6$ ) serves as an acceptor and hexamethoxycoronene ( $C_{30}H_{24}O_6$ ) as a donor. They showed that in the course of the growth of finite multilayer structure, a new charge transfer phase is formed [21].

In the thesis, experiments on BEDT-TTF/TCNQ bilayers of various thicknesses were performed by sequential physical vapor deposition of a TCNQ layer and a BEDT-TTF layer at a background pressure of  $3 \times 10^{-7}$  mbar or less in the “test” chamber. The materials were sublimated from a low-temperature effusion cell using a quartz crucible. TCNQ was deposited at 110 °C and BEDT-TTF at 155 °C. The growth rate for both layers was about 2 nm/s. These rather high growth rates were realized by having a small distance between the effusion cell lid and the substrate of about 10 mm. The TCNQ layer was deposited first because it has a higher vapor pressure than BEDT-TTF at any given temperature and tends to desorb from a substrate at even moderately elevated temperatures. The bottom TCNQ layer was exposed to air before the deposition of the top BEDT-TTF layer to check the surface morphology. Glass microscope slides and Si(100)/SiO<sub>2</sub> (300nm) substrates with and without Au template layers were used as substrate materials for the bilayers. During the growth process the substrate was held at room temperature. The post-growth annealing of the samples was performed in <sup>4</sup>He inert gas atmosphere at temperatures varying from 60 °C to 80 °C for up to 48 hours by employing a Peltier element (17A0021-Peltron GmbH) as a heater on which the substrates were glued with silver paint. The results for TCNQ/BEDT-TTF bilayers are presented and discussed in chapter 7.

## 3.2 Methods for structure and morphology investigation

The methods for inspection of structure and morphology of thin films used in the thesis are outlined in this section. X-ray diffraction was applied to find the crystallographic structure and/or orientation of the formed organic thin films (see section 3.2.1). Scanning electron microscopy (see section 3.2.2) and atomic force microscopy (see section 3.2.3) were used to characterize the surface morphology. In

section 3.2.2 energy-dispersive X-ray spectrometry (EDX) used for element analysis is discussed. Focused particle beam processing methods, such as electron (FEBID) and ion (FIBID) beam induced deposition, are described in section 3.2.4 together with the method of microcontact preparation.

### 3.2.1 X-ray diffraction

The organic thin films were *ex situ* characterized by X-ray diffraction. X-ray diffractometry was carried out by employing a Bruker D8 Discover diffractometer with a Cu anode (ceramic X-ray tube KFL-Cu-2K) in parallel beam mode using a Goebel mirror (see Fig. 3.5a). The main emitting wavelength of  $\text{CuK}_\alpha$  was 1.5406 Å. The operating voltage was 40 kV and the current was 40 mA. Mostly symmetric Bragg reflections were detected with an incident wave vector at an angle of  $\theta$  and detector angle at  $2\theta$ . The position of the reflections in this geometry is defined by Bragg's law (see Fig. 3.5b):

$$n\lambda = 2d_{hkl} \sin \theta, \quad (3.8)$$

where  $\theta$  is the angle between the incident ray and the scattering planes,  $\lambda$  is the emitting wavelength,  $d_{hkl}$  is the distance between crystallographic planes and  $n$  is the order of the reflection.

The measured XRD patterns were compared with reference diffraction patterns which were simulated using the Mercury 2.3 crystal structure visualization computer program [71] based on the known crystallographic structures. The structure data for BEDT-TTF, TCNQ, and TTF-TCNQ were taken from [38,72,73], respectively. The

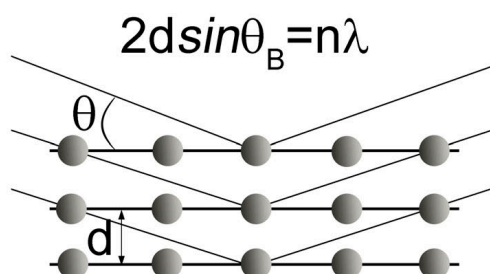
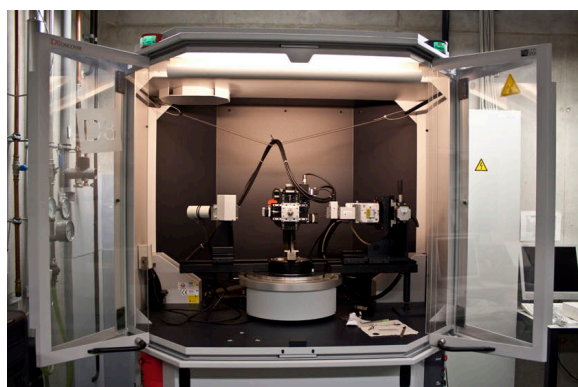


**Figure 3.5:** (a) X-ray diffractometer Bruker D8 Discover. (b) Illustration of Bragg's law.

structure for the monoclinic phase of (BEDT-TTF)TCNQ, the triclinic semiconductor  $\beta'$ -phase of (BEDT-TTF)TCNQ and the triclinic metal  $\beta''$ -(BEDT-TTF)TCNQ were adopted from [14–16], respectively. By comparison of the peak positions and intensities of the measured spectra with reference patterns one can draw conclusions about the crystallographic phases presented in the thin films.

By modifying the setup, grazing incidence diffraction (GID) [74,75] can be used for identification of the in-plane orientation of the thin films. At first in the  $\theta$ - $2\theta$  geometry, the position of the X-ray source and the detector are chosen according to the investigated crystallographic plane. Then in the GID mode, the X-ray pattern is recorded for an angle  $\varphi$  from  $0^\circ$  to  $360^\circ$  and for the angle of the incident and outgoing beams kept at very small values.  $\varphi$  is the rotation angle around the normal to the substrate surface used in the GID measurement. The results of the  $\varphi$ -scan makes it possible to obtain the in-plane orientation of the grown thin film. This was done for thin films of TTF-TCNQ (see section 5.2).

### 3.2.2 Scanning electron microscopy and energy-dispersive X-ray spectrometry

For this thesis, Scanning Electron Microscopy (SEM) was performed with a FEI xT Nova NanoLab 600 equipped with a Schottky electron emitter [76]. The FEI Nova 600 NanoLab is a dual-beam instrument that includes electron and Ga ion beams and energy-dispersive X-ray spectrometry units in one machine. The SEM is equipped with FEI's Gas Injection System (GIS) for focused electron and ion beam deposition of (granular) metals, semiconductors, and insulators [76]. The SEM is equipped with a through the lens detector (TLD) for secondary and backscattered electrons and an Everhart Thornley detector (ETD) for secondary electrons, respectively. The TLD detector is mounted within the lens and collects secondary or backscattered electrons from the scanned area of the sample. The electrons pass through the lens into the collector that is reflected in the detector name. The Everhart Thornley detector (ETD) is a standard scintillator type detector, which monitors the generated secondary electrons for collection outside of the lens. The detector is mounted in the chamber above and to one side of the sample.

In the course of the experiments on organic CT thin films, the TLD detector showed a better contrast and was used as a primary detector. The measurement resolution at small probe current of about 100 pA is 2 nm at an applied voltage of 5 kV. High electron fluxes destroy organic thin films, sometimes readily visible after the measurements, even by eye. Therefore, the applied current is a very important

parameter in the measurements and a low current value of 98 pA was normally used for SEM image acquisition.

Modern SEMs are equipped with energy-dispersive X-ray spectrometers, abbreviated as EDX, a powerful tool for quantitative X-ray microanalysis [77]. This method allows for a rapid and accurate evaluation of the specimen's elemental constituents. The electron beam excites the electrons from the sample with a certain energy, which is defined by the unique electronic structure of the atoms. The analysis of the obtained data allows to get the information about the composition of the investigated sample. The focus of an electron beam can vary and, therefore, the size of the investigated sample area is varied, as well. In the experiment, the focus of the electron beam was limited by 10 nm. Accordingly, the chemical composition of areas from microcrystals to thin films can be studied by EDX. The SEM FEI Nova NanoLab 600 was used in the experiments with an EDAX Genesis 2000 system. Silicon lithium crystal (Si(Li)) was used in the detection unit with Super Ultra Thin Window (SUTW). The lower detection element in this case is boron, corresponding to the threshold energy 0.185 keV. The voltage in the EDX measurements was 5 kV.

At best, EDX provides an accuracy of about 0.5 at%. Electron beam induced deposition of carbon from the residual gas in the SEM chamber during the measurements makes the quantitative identification of carbon difficult and the carbon content obtained from the spectra tends to be larger than the actual bulk carbon content of the thin film samples. For oxygen quantification, EDX should also be used critically due to possible oxidation of the films in the course of transportation. Therefore, if possible other atoms in the organic materials should be used as markers. In the case of tetrathiafulvalene the marker atom is sulphur with  $K_\alpha$  line energy equals to 2.307 keV, and for the cyano group the marker atom is nitrogen with  $K_\alpha$ -line energy equals to 0.392 keV. The Monte Carlo simulation program Casino [78] was used to reproduce the experimental conditions for determination of the minimum film thickness necessary to prevent undesired excitation from the substrate.

### 3.2.3 Atomic force microscopy

For this thesis, AFM measurements were performed with a Nanosurf easyScan 2 AFM System in non-contact mode. NANOSENSORS<sup>TM</sup> PPP-NCLR-50 AFM cantilevers were used. The sample is mounted on a sample holder, which is placed on a micrometer translation stage. The stage is fixed on the isolating table, which reduces the influence of external vibration. The stage allows the sample to be moved along two directions parallel to the substrate surface. The morphology of the sam-

ple surface is obtained from the measured  $x, y$  and  $z$  coordinates. The resolution of an AFM is generally limited by the tip radius of curvature which can be less than 10 nm.

### 3.2.4 Focused particle beam processing

The SEM FEI xT Nova NanoLab 600, used in this work, is equipped with a Ga ion column, which broadens the experimental capabilities. The ion beam technique was employed for thin film cross-sectioning in order to measure the thickness [19]. The thickness of organic thin films cannot always be accurately measured by other *in situ* or *ex situ* techniques. This problem arises in the course of evaporation due to the bad sticking of organic molecules on the surface of a quartz microbalance, which generally monitors the thickness of the growing films *in situ*. In the case of *ex situ* AFM measurements, the large surface roughness does not allow accurate thickness measurements very often. Focused ion beam (FIB) cross-sectioning, as used here, allows the measurement of the thickness, even of rough layers. The voltage employed in the course of cross-sectioning was 30 kV and the current was  $\leq 1.6$  nA. Due to the high operating voltage, the FIB can be also used for cutting of thin films and cleaning certain defined areas of the sample. This can be used, for example, to separate pre-defined electrodes from unwanted connection to microcrystals.

A focused ion beam can also be used for induced material deposition (called as FIBID). A precursor material, for example tungsten hexacarbonyl ( $W(CO)_6$ ), is injected into the SEM and is allowed to physisorb onto the sample surface. By scanning a pre-defined surface area, covered with the precursor by means of the ion beam, the precursor is decomposed into volatile and non-volatile components. The non-volatile component, such as amorphous W-C-O in case of  $W(CO)_6$ , remains on the sample surface as a deposit. The rest is pumped away. The same procedure can be performed with a focused electron beam (FEBID). A lower voltage can be used by using FEBID in comparison to FIBID. The choice of either ion or electron beam induced deposition is governed by the experimental needs and deposit requirement. For example, tetramethylsilane ( $Si(CH_3)_4$ ) and neopentasilane ( $Si_5H_{12}$ ) precursors can be used for the preparation of  $SiO_2$  and Si deposits, respectively. The deposited material can be used as a passivation layer to protect the underlying structure from the destructive environment influence, for example, from oxidation.

The techniques of FIBID and FEBID were used in the thesis for microcontact fabrication. The contacts for electrical transport measurements on TTF-TCNQ microcrystals were formed by combination of FIBID with  $W(CO)_6$  and FEBID with trimethyl-methylcyclopentadienyl-platinum ( $MeCpPt(Me)_3$ ) as precursor gases, re-

spectively. The results are discussed in chapter 6. For FEBID and FIBID experiments valuable support was provided by Roland Sachser.

### 3.3 Electrical conductivity measurements

The electrical conductivity measurement techniques used in the thesis are described in section 3.3.1. The contact fabrication is also discussed in this section. In section 3.3.2 details of the temperature-dependent measurements are presented.

#### 3.3.1 Electrical transport measurement technique

Two- and four-probe measurement techniques were employed to determine the electrical conductivity of the samples. The four-probe technique allows to remove the influence of the contact resistance. However, in the case of organic thin films with minimal resistance, typically at least in the kilo Ohm range, the two-probe technique can also be used. The contacts for the measurements were done either on top of the formed film or before the film deposition directly on the substrate.

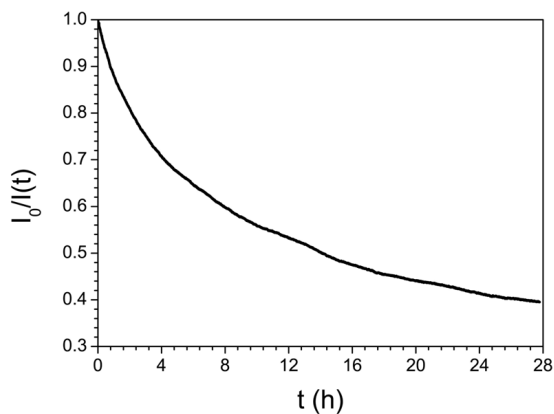


**Figure 3.6:** *The degradation of a TTF-TCNQ thin film grown on  $\text{SrLaGaO}_4(100)$  substrate in the course of a current measurement at fixed bias voltage of 0.1 V.*

the substrate was glued by VGE-7031 varnish onto an intermediate contact plate with pre-fabricated Cu-contacts (see Fig. 3.7). The plate was then glued onto the measurement chip, having 24 contacting pins, as shown in Fig. 3.7b. The contacts between the Cu plate and the TTF-TCNQ thin film were done by using a bonding machine. The contacts between the cryostat holder and the contact plate were

The electrical conductivity of organic CT thin films and microcrystals were measured either in UHV or in helium atmosphere to account for degradation effects. A degradation of the electrical conductivity on air was observed and is exemplarily shown in Fig. 3.6 for a TTF-TCNQ thin film grown on  $\text{SrLaGaO}_4(100)$ . The current measured at a fixed applied voltage of 0.1 V during 28 hours shows a gradual drop of 60%.

For conductivity measurements on TTF-TCNQ thin films grown on different substrates (see Tab. 4.2) the



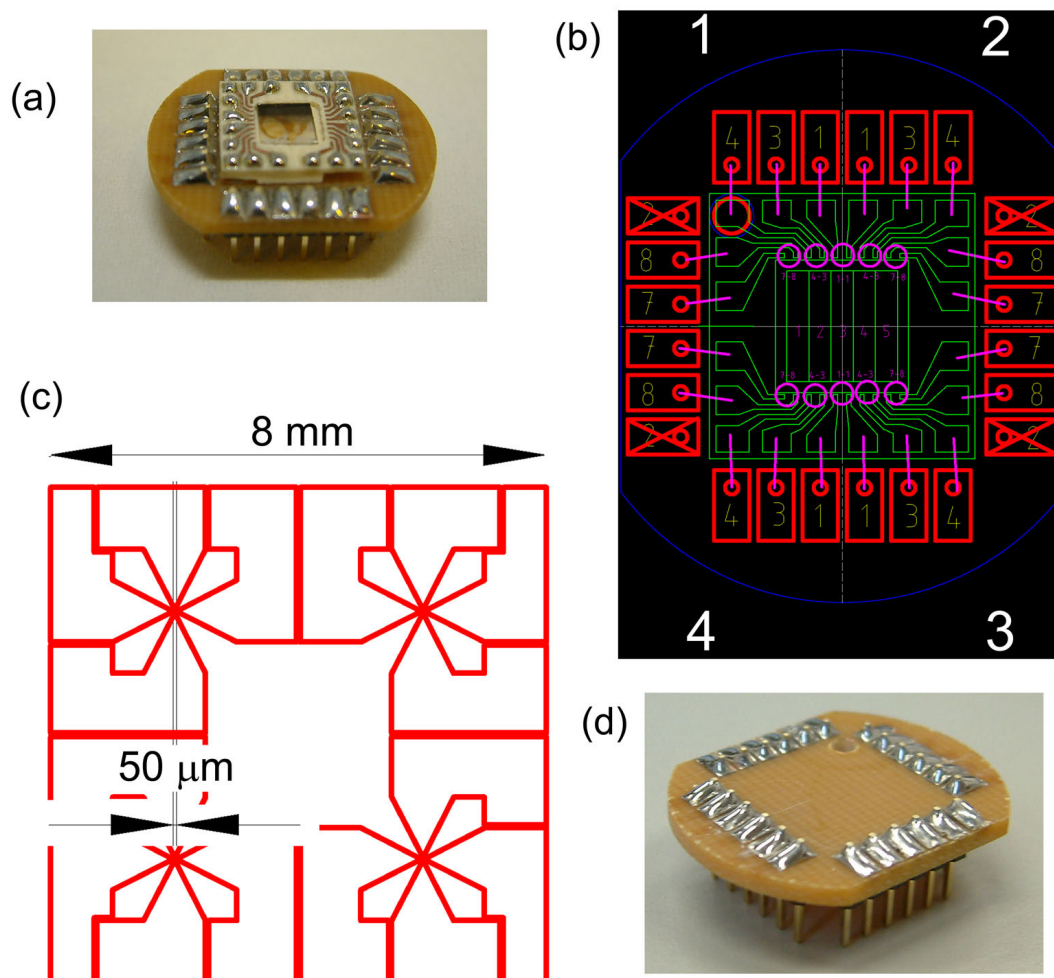


**Figure 3.7:** Transport measurement chips and contact schemes: (a) Cryostat chip with the sample containing 5 stripes, (b) the drawing of the contacts on the cryostat chip and on the plate with the Cu-contacts. The measurement sectors and pin numbers are indicated. (c) Photolithography mask with four opening areas for four-probe measurements of the electrical conductivity of TTF-TCNQ microcrystals, (d) the cryostat chip.

soldered. Al wires with a diameter of  $25\ \mu\text{m}$  were used to contact the plate with TTF-TCNQ thin films. As a last step, the contacts on the TTF-TCNQ thin film were strengthened for robustness with silver paint. Small drops of silver paint were placed on the sites where the wire touched the thin film surface.

Conductivity measurements on TTF-TCNQ microcrystals were performed on the same cryostat chip type as was used for the TTF-TCNQ thin films. The TTF-

TCNQ microcrystals were formed via evaporation in the UHV chamber through a shadow mask on NaCl(100) or Si(100)/SiO<sub>2</sub>(285 nm) substrates with pre-patterned Au(100 nm)/Cr(20 nm) contacts (see Fig. 3.7c). Au and Cr layers were grown either in a Pfeiffer Classic 500 coating system by means of electron beam evaporation or in a gold sputtering chamber. Photolithography and lift-off processes were used to form the contacts with predefined geometry on the substrate surface (see Fig. 3.7c). The details of the photolithography, lift-off and sputtering processes are outlined in Appendix A. After the crystal formation on the substrate with pre-patterned Au/Cr contacts, selected microcrystals and the gold contacts were connected by combination of FEBID and FIBID.

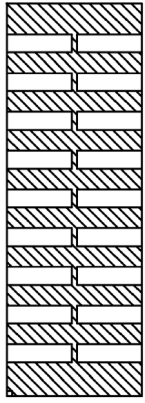


**Figure 3.8:**  
*The mask for  
the bilayer.*

For the electrical conductivity measurements on BEDT-TTF/TCNQ bilayers glass slide substrates with pre-patterned Au(100 nm)/Cr(20 nm) contacts were used. Contacts were formed on the glass substrate with a shadow mask (see Fig. 3.8) in the Pfeiffer Classic 500 coating system. The distance between the contacts was 1 mm. As a next step the glass slide with the Au/Cr contacts were covered with the shadow mask separating the neighboring contacts. Subsequently the TCNQ and BEDT-TTF layers were deposited on top. The heating of the bilayer samples was done in <sup>4</sup>He atmosphere by a Peltier element (17A0021-Peltron GmbH). The temperature regime supported by this heating element is in the range 18...90 °C. Conductance measurements were done in the heating-cooling cycles, at a heating speed of about ~1 K/min.

### 3.3.2 Conductivity measurements at low temperatures

The series of phase transitions in TTF-TCNQ single crystal is visible in conductivity measurements at low temperature. Consequently, electrical conductivity measurements were carried out on TTF-TCNQ thin films and microcrystals in an Oxford <sup>4</sup>He cryostat with variable temperature insert (see Fig. 3.9) using the two- and four-probe technique. The temperature was controlled in the range from room temperature down to 4.2 K. The measurements were performed at fixed bias voltage due to the low conductivity of the samples at low temperature. Voltage of 0.1 V, 0.2 V and 0.5 V were applied. The temperature of the sample was measured by a Cernox sensor (SD-1010 SN: X52935). The average cooling rate was ~ 3 K per minute and the average heating rate was ~1 K per minute. The heating cycle was consistently used to derive the Peierls transition temperature, because of smaller temperature

change rate.

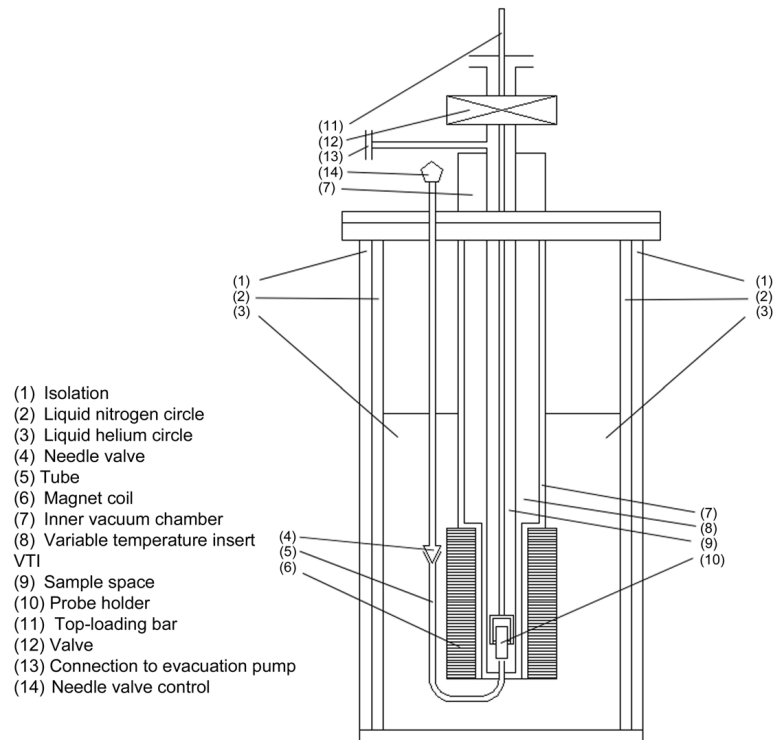


**Figure 3.9:** Scheme illustrating the working principle of the Oxford  $^4\text{He}$  cryostat with liquid nitrogen shielding (2), liquid helium (3) and variable temperature insert (8).

It is worth noting that the heating/cooling of the sample during the experiments did not induce any damage to the thin films, as follows from the measurements reproducibility.



## ORGANIC MATERIALS AND SUBSTRATES USED FOR THIN FILM FABRICATION

This chapter describes the organic charge transfer materials used in the thesis and discusses their physical properties. Out of a variety of donor molecules studied in the last decades, tetrathiafulvalene (TTF) and its derivative bis-(ethylenedithio)tetrathiafulvalene (BEDT-TTF) were chosen in the work because of the interesting CT complexes they form with tetracyanoquinodimethane (TCNQ) as acceptor. TTF-TCNQ is a quasi one-dimensional metal and (BEDT-TTF)TCNQ in contradistinction is a two-dimensional charge transfer salt. The dimensionality of the compound defines the properties of these materials. In the case of TTF-TCNQ, the presence of the Peierls transition is ascribed to the one-dimensional structure of the CT complex. On the other hand, (BEDT-TTF)TCNQ has several crystallographic modifications: an insulator, a semiconductor and a metal. One of the modifications shows a Mott metal-insulator transition almost at room temperature and another one shows a high electrical conductivity when compared to other organic CT salts.

The physical properties of TTF-TCNQ are discussed in section 4.1. The crystal structure and physical properties of (BEDT-TTF)TCNQ are outlined in section 4.2. The charge transfer compounds or the components used in the work are commercially available. Crystal growth from solution was used in some instances. Details on the solution growth method are given in section 4.3. In addition, the used substrate materials are briefly addressed in section 4.4.

## 4.1 TTF-TCNQ

The fabrication of the strong acceptor TCNQ (7,7,8,8-Tetracyanoquinodimethane,  $C_{12}H_4N_4$ ) in 1960 [79] (see Fig. 1.1a) with electron affinity  $E_A = 2.84$  eV [80] gave rise to a new era of organic material science. Later, new donor molecules were synthesized, which showed good compatibility with TCNQ in forming organic charge transfer compounds (for Refs. see [27, 81]). In 1970, the group of Prof. Wudl at the State University of New York synthesized the new sulphur-containing molecule [82] TTF (1,4,5,8-Tetrathiafulvalene  $C_6H_4S_4$ ) (see Fig. 1.1b). TTF has a low ionization energy  $I_D = 6.85$  eV [83] which makes it a promising donor molecule. Three years later, the groups from Johns Hopkins University and University of Pennsylvania independently reported the discovery of a new highly conductive TTF-TCNQ CT salt containing TTF and TCNQ [3, 4] in stoichiometric ratio 1:1. The amount of charge transfer in this CT complex at ambient pressure is  $0.59e$ . TTF-TCNQ has a monoclinic structure ( $P2_1/c$  space group,  $a = 12.298$  Å,  $b = 3.819$  Å,  $c = 18.468$  Å, and  $\beta = 104.46^\circ$ ) and consists of parallel homoseric stacks of acceptor (TCNQ) and donor (TTF) molecules as schematically illustrated in Fig. 2.2 [38]. The normal direction to the TTF molecular plane is tilted  $24.5^\circ$  with respect to the  $b$ -axis of TTF-TCNQ and to the TCNQ molecular plane the tilt is  $34.0^\circ$  in the opposite direction.

It was demonstrated that due to the interaction between the  $\pi$ -orbitals arising along the stack direction, as presented in Fig. 1 (corresponding to the  $b$ -direction in Fig. 2.2b), the electrical conductivity of TTF-TCNQ is strongly anisotropic with  $\sigma_b/\sigma_a > 10^2$  at room temperature, where  $\sigma_a$  and  $\sigma_b$  are the electrical conductivities along the  $a$ - and  $b$ -directions, respectively [5]. TTF-TCNQ has a remarkably high room temperature conductivity of about  $500 (\Omega\text{cm})^{-1}$  along the  $b$ -axis in comparison with other known organic CT materials.

Electrical transport measurements revealed metallic behavior down to 54 K with a maximum conductivity of  $1.47 \times 10^4 (\Omega\text{cm})^{-1}$ . Below 54 K, a phase transition drives the material into a semiconducting state [3]. In contrast to the results reported in [3], the Pennsylvania group claimed that the maximum of conductivity reaches  $10^6 (\Omega\text{cm})^{-1}$  for some single crystals of TTF-TCNQ [4]. However, such a giant increase could not be reproduced. Further investigation showed that TTF-TCNQ single crystals exhibit metallic behavior down to about 60 K and undergo a series of phase transitions at  $T_H = 54$  K,  $T_I = 49$  K and  $T_L = 38$  K [6, 8, 9], which successively lead to a suppression of the metallic conductivity of the TTF and TCNQ chains. The transitions were attributed to the one-dimensional structure of TTF-TCNQ complex.

It was first theoretically suggested by Sir Rudolph Peierls that one dimensional molecular chains with small intrasite interaction are not stable at  $T=0$  K against a periodic lattice distortion with a wave vector  $2k_F$  [43]. The ensuing periodic distortion of the electron gas results in the opening of a gap equal to  $2\Delta$  at the Fermi level. The formation of the gap at the Fermi level turns the material from metallic to semiconducting. Later it was shown that the structural instability is driven by  $2k_F$  lattice fluctuations of the one-dimensional material. These fluctuations result in the formation of a charge density wave via electron-phonon interaction. The period of the charge density wave is  $\frac{\pi}{k_F}$ . In the case of a partially-filled electron band, the period of the distortion is incommensurate with the underlying lattice. An example of the periodic lattice distortion for a bandstructure with a half-filled band is shown in Fig. 4.1 for temperatures above and below the Peierls transition.

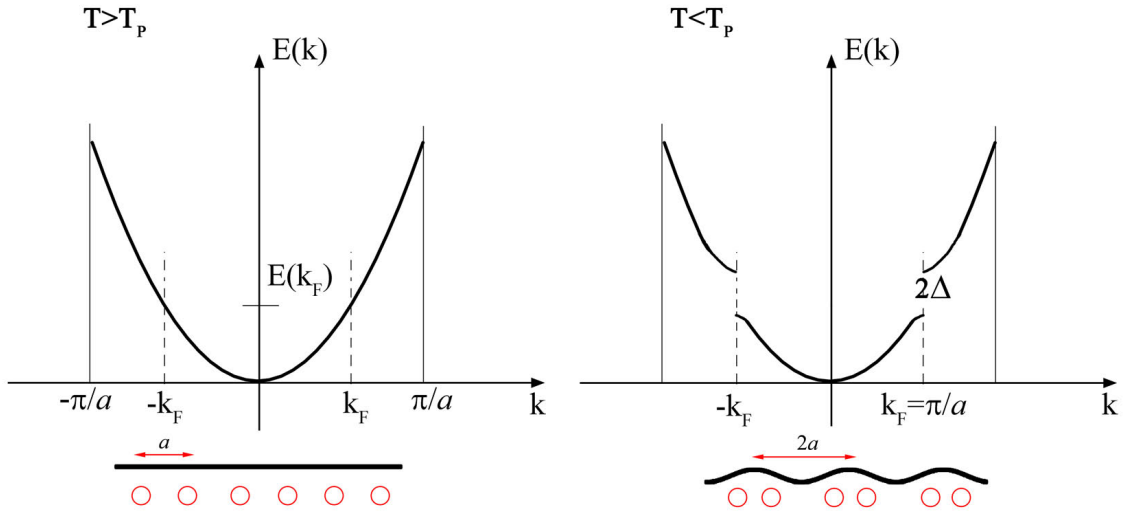


**Figure 4.1:** Bandstructure for a half-filled band at different temperatures (a) above  $T_P$ , (b) at  $T < T_P$ . The electron density and lattice distortion are schematically shown.

The instabilities come from the special form of the Fermi surface of a one-dimensional metal, consisting of only two points (or sheets) at  $+k_F$  and  $-k_F$  separated by distance of  $2k_F$ . This form of the Fermi surface causes such instabilities as discussed above and this particular topology is called perfect nesting [84]. In the case of one dimension, the Fermi surface is totally nested with nesting vector  $Q = 2k_F$  and the energy satisfies the condition [34]:

$$E(\vec{k} + \vec{Q}) = E(\vec{k}). \quad (4.1)$$

The phonon spectrum shows phonon softening  $\omega(2k_F) \rightarrow 0$  at Peierls transition temperature, named Kohn anomaly [85].

For the case of strong intrasite electron-electron repulsion, each lattice point cannot be occupied by more than one electron (in the case of non-degenerated orbitals) and the electrons now have to fill the band from  $-2k_F$  to  $+2k_F$  instead of  $-k_F$  to  $+k_F$ . Accordingly, the system with strongly correlated electrons is also unstable against a periodic lattice distortion with a wave vector of  $4k_F$ . It was shown that materials with two different stacks of molecules, as for example TTF-TCNQ, can exhibit both instabilities at  $2k_F$  and  $4k_F$ .

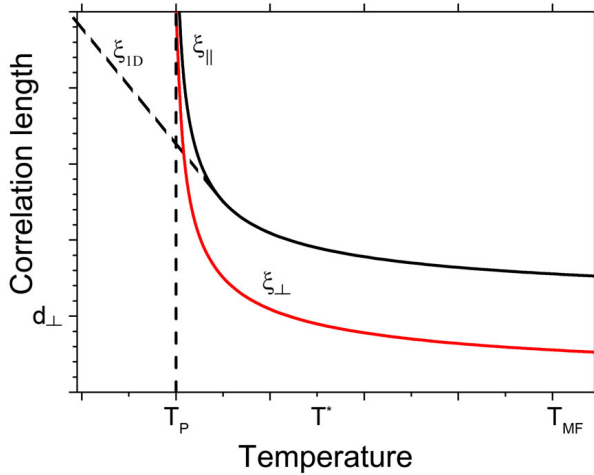


**Figure 4.2:** Temperature dependence of the intra-chain ( $\xi_{||}$ ) and inter-chain ( $\xi_{\perp}$ ) correlation lengths.  $\xi_{1D}$  is the correlation length of the ideal one dimensional chain.  $d_{\perp}$  is the distance between the neighboring chains.  $T_P$  is the transition temperature,  $T^*$  is a crossover temperature where the correlations among the neighboring chains develop and  $T_{MF}$  is the mean field temperature, where the correlations start to form along the chain direction.

transition temperature and the zero temperature gap (see for example [33]). However, in real materials  $T_P < T_P^{MF}$  because the MF approach ignores fluctuation effects and furthermore, the inter-chain coupling is not taken into account. Due to the reduced dimension, quasi 1D systems are particularly prone to fluctuations and these fluctuations hinder the formation of long range order and decrease the transition temperature [84]. In the case of a real material with coupled chains, with decreasing temperature, the intra-chain and inter-chain correlation lengths increase and finally diverge at the Peierls transition temperature  $T_P$  (see Fig. 4.2).

Mean field theory (MF) can be used to describe the qualitative behavior of the charge density waves and the Peierls transition in one-dimensional materials [84]. In MF theory, an average interaction replaces the interaction between the investigated particle and all other particles in the system. This reduces the many-body problem to an effective one particle problem. Within MF theory the Peierls transition takes place at [84]:

$$T_P^{MF} = \frac{2\Delta}{3.52k_B}. \quad (4.2)$$

This expression is well known for the Bardeen, Cooper, and Schrieffer theory for the superconducting



Below the Peierls transition  $T_P$  the charge density waves become easily pinned. There are several pinning mechanisms: impurity pinning, lattice potential pinning, i.e. commensurability pinning, and pinning by Coulomb interaction between oppositely charged chains in the case of a two-chain system. The effectiveness of impurity pinning is defined by the dimensionless parameter  $\epsilon$  introduced by Fukuyama and Lee [86]:

$$\epsilon = \frac{V_{pot}}{V_{el}} = \frac{V_0 \rho_1}{\hbar v_F n_I}, \quad (4.3)$$

where  $V_0$  is the strength of the impurity potential,  $n_I$  is the number of impurities in the material per unit length,  $v_F$  is the Fermi velocity,  $\rho_1$  is the charge density wave modulation amplitude. The numerator defines the gain of potential energy with respect to the undisturbed lattice ( $V_{pot}$ ). The denominator defines the increase of elastic energy which is a consequence of the lattice distortion ( $V_{el}$ ). In the case of a strong impurity potential and when impurities are far apart, CDWs can adjust themselves leading to a strong pinning effect ( $\epsilon > 1$ ). On the other hand,  $\epsilon < 1$  is the case of weak pinning. At large  $n_I$  CDWs need to undergo a lot of short-wavelength distortions for phase matching on all impurity sites which is energetically costly [84].

The above-mentioned theoretical outline is directly related to TTF-TCNQ. First theoretical studies of the anomalous behavior of the electrical conductivity of TTF-TCNQ predicted that TTF-TCNQ exhibit three phase transitions at about 54 K, 47 K and 38 K [87]. Experimentally, two phase transitions in TTF-TCNQ were observed at  $T_H$  (54 K) and  $T_L$  (38 K) in conductivity-temperature measurements at ambient pressure (see Fig. 4.3) [88–90]. The phase transition at 54 K is a second order transition, while the phase transition at 38 K is hysteretic, signifying a first order phase transition [7]. The phase transition at  $T_I$  (49 K) was first theoretically predicted in [87] and later found by high-resolution neutron scattering experiments [91].

The investigation of TTF-TCNQ single crystals by diffusive X-ray and elastic neutron scattering showed [89,91] that at  $T_H$ , a three-dimensional superlattice forms with period  $2a \times 3.4b \times c$  [92], where  $a, b, c$  are the parameters of the underlying lattice. The period was also measured precisely by scanning tunneling microscopy [92]. Between  $T_H$  and  $T_I$ , the period along the  $a$ -axis is constant and equal to  $2a$ . As the temperature decreases further, no noticeable change in the lattice modulation along the  $b$ -axis was observed, while transverse modulations along the  $a$  direction become incommensurate and the period of the modulations continuously increases. At  $T_L$  the period of modulation along the  $a$ -axis jumps discontinuously to  $4a$  [7,92].

At temperatures higher than 54 K, two anomalies in the X-ray diffusive patterns of TTF-TCNQ crystals were found: at  $0.295b^*$  (corresponding to  $2k_F$ , where  $k_F$  is the Fermi vector) and at  $0.59b^*$  (corresponding to  $4k_F$ ). Here  $b^*$  is a reciprocal lattice vector.  $2k_F$  fluctuations (or sliding CDWs) emerge on the TCNQ chains below 150 K.  $4k_F$  fluctuations were observed for TTF chains [94] and are visible even at room temperature. Strong Coulomb interaction in the TTF chains is one of the possible explanations for the formation of the  $4k_F$  instability [81]. The  $4k_F$  instability appears only on the TTF stacks presumably because the bandwidth of the TTF chains is smaller than the one for the TCNQ chains [9].

For temperatures higher than  $T_H$ , CDW fluctuations exist on the molecular chains (TTF and TCNQ), but they are not phase-correlated. As the temperature decreases, the correlation length of the charge density wave fluctuations grows along the chain and at  $T_P$  the CDWs become long-range ordered and are, in general, collectively pinned. The energy gap for the CDW state of TTF-TCNQ at temperatures below 38 K is  $2\Delta \approx 460$  K [9]. Using Eq. (4.2) one can calculate the transition temperature as  $T^{MF} = \Delta/1.76 \approx 125$  K, whereas the Peierls transition in TTF-TCNQ single crystals is observed at temperature around 54 K. This discrepancy underlines the importance of fluctuations and the correlations between the molecular chains. The fluctuations result in the suppression of the transition temperature as compared to  $T^{MF}$  until the weak interchain coupling fixes the phase of the CDWs and at  $T_H$  the formation of three dimensional order starts.

As discussed above, TTF-TCNQ shows a series of phase transition and is an attractive object for investigation. TTF-TCNQ single crystals were first grown in acetonitrile [82]. In the last decades, TTF-TCNQ single crystals were thoroughly studied (see for example [6,9,81,95]). At the same time, the arising interest in organic electronics and in the investigations of structures with low dimensions promoted the

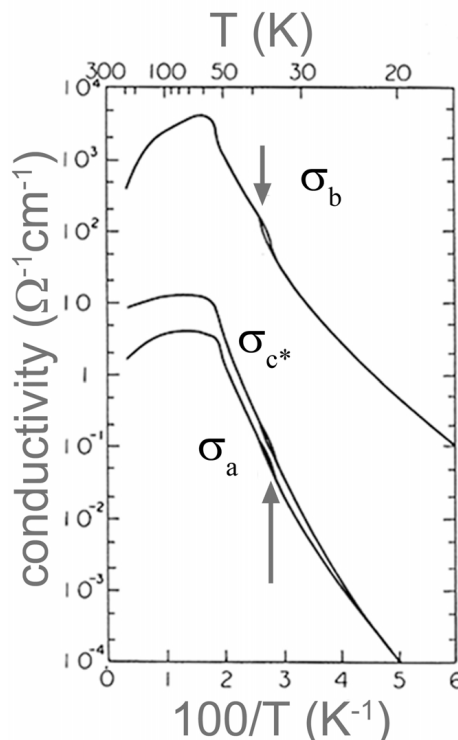


**Figure 4.3:** Conductivity of TTF-TCNQ single crystals along the  $a$ ,  $b$  and  $c^*$ -axes.  $c^*$ -axis is the axis perpendicular to the  $(ab)$  plane of TTF-TCNQ. The arrows show the position of the first order phase transition  $T_L$ . The figure is adopted from [93].

work on microcrystals and thin films.

TTF-TCNQ thin films deposited from pre-reacted TTF-TCNQ crystals preserve the stoichiometric ratio of TTF to TCNQ equal to 1:1 [96]. Therefore, a co-evaporation of donor and acceptor molecules is not needed in the case of TTF-TCNQ, simplifying the preparation process and making this CT complex attractive for experiments on the thin film growth by physical vapor deposition. The pre-reacted TTF-TCNQ powder was purchased from Sigma-Aldrich (Fluka, purity  $\geq 97.0\%$ ) and tested. Energy-dispersive X-ray spectrometry (EDX) was employed to analyze the composition the thin films. For this purpose, the atomic ratio of sulphur and nitrogen in the films was determined. The evaporation characteristics were analyzed and it was found that a suitable evaporation temperature range for this material lies within  $85\text{ }^{\circ}\text{C}$  and  $130\text{ }^{\circ}\text{C}$ . This is in agreement with earlier studies [96,97]. The decomposition temperature of TTF-TCNQ is about  $210\text{ }^{\circ}\text{C}$  [96]. The influence of the evaporation temperature and substrate material on the Peierls transition of the resulting TTF-TCNQ thin films was investigated and will be discussed later.

## 4.2 (BEDT-TTF)TCNQ

One of the strongest donor molecules, which forms CT compounds with TCNQ is TTF (see section 4.1). The TTF molecule was modified in 1978 to form the new donor bis(ethylenedithio)tetrathiafulvalene, later abbreviated to BEDT-TTF (or ET) ( $\text{C}_{10}\text{H}_8\text{S}_8$ ) (see Fig. 1.2) with an ionization energy  $I_D = 6.21\text{ eV}$  [44, 98]. An important property of BEDT-TTF is that this molecule forms a rich variety of crystallographic phases with various acceptors. Based on BEDT-TTF as donor and TCNQ as acceptor the new charge transfer salt (BEDT-TTF)TCNQ ( $\text{C}_{22}\text{H}_{12}\text{N}_4\text{S}_8$ ) was synthesized in 1978 [44].

The various crystal structures of BEDT-TTF-based CT salts are classified as  $\alpha$ ,  $\alpha''$ ,  $\beta$ ,  $\beta'$ ,  $\beta''$ ,  $\theta$ ,  $\kappa$ ,  $\lambda$  (see Fig. 2.3) [11, 12]. During the last three decades, three structural modifications of (BEDT-TTF)TCNQ were found, which can be classified according to their crystallographic structure as:

- monoclinic ( $\text{P}2_1/\text{n}$ ) insulator phase [14]. It was discovered in 1987 and has a mixed-stack structure of donor and acceptor molecules, as shown in Fig. 4.4a.
- triclinic  $\beta'$  ( $\text{P}\bar{1}$ ) semiconductor phase [15], discovered in 1986 with segregated stacks, as shown in Fig. 4.4b.

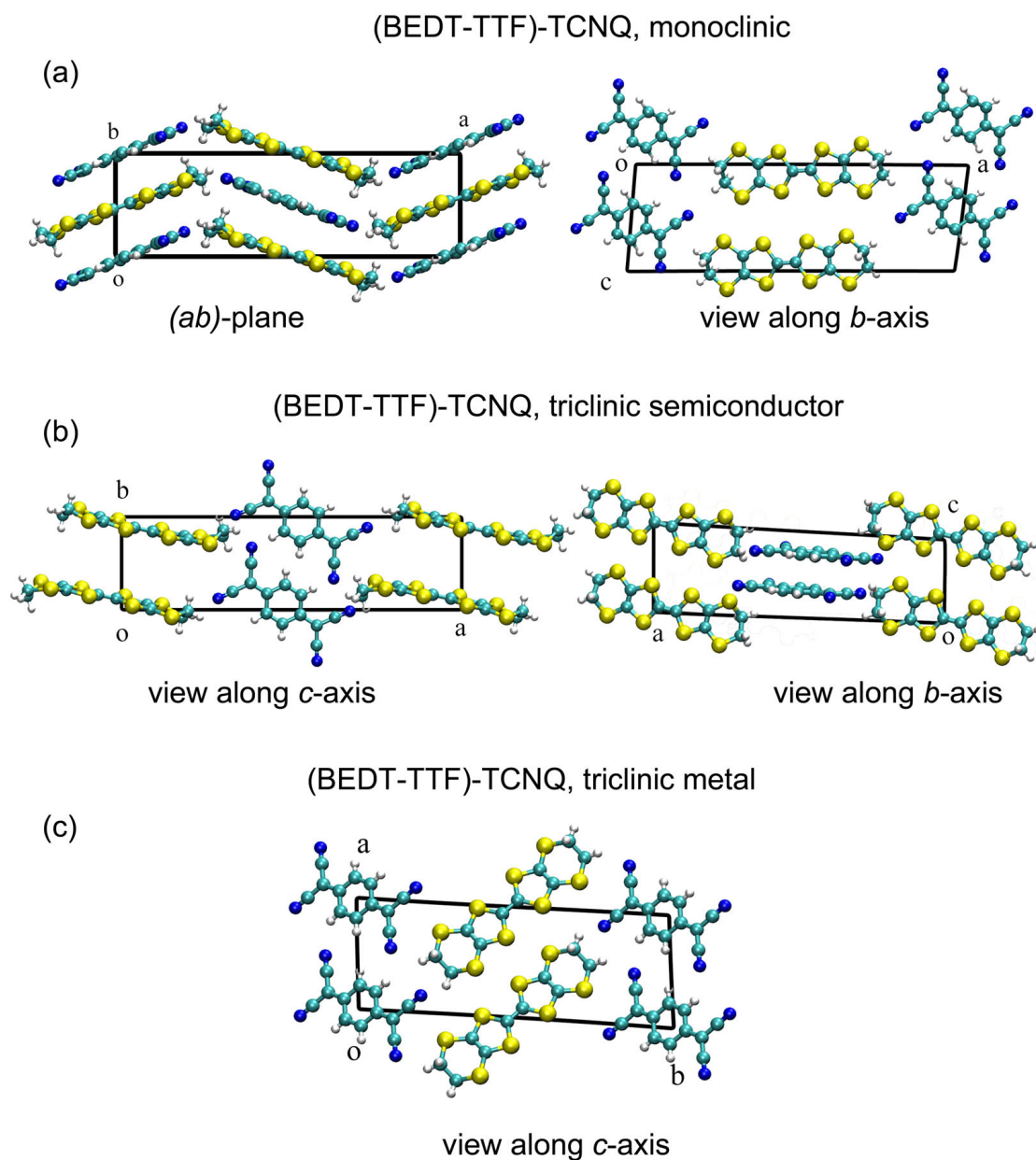


**Figure 4.4:** Crystallographic phases of the (BEDT-TTF)TCNQ CT complex: (a) monoclinic phase, (b) triclinic semiconductor  $\beta'$ -phase, and (c) triclinic metallic  $\beta''$ -phase. The VMD visualization program was used to represent the molecules [10].

- triclinic  $\beta''$  ( $P\bar{1}$ ) metallic phase [16], discovered in 2003 also with segregated stacks, as shown in Fig. 4.4c.

First experiments on the crystal growth of (BEDT-TTF)TCNQ were performed by means of solution growth. To form the monoclinic phase and the semiconductor  $\beta'$ -phase trichlorethane, dichlorethane (DCE) or tetrahydrofuran (THF) solvents were used [14, 15]. To get the  $\beta''$ -phase of (BEDT-TTF)TCNQ one needs to use a solvent with addition of tetraiodoethylene ( $C_2I_4$ ). Because of the different crystal structures the physical properties of the phases differ strongly as outlined below.

### Monoclinic phase

The monoclinic phase of (BEDT-TTF)TCNQ is an isolator with an electrical conductivity of about  $10^{-6} (\Omega\text{cm})^{-1}$  at room temperature. The high resistivity originates from the mixed-stack structure of TCNQ and BEDT-TTF molecules (see Fig. 4.4a) along the  $b$ -axis of the crystal [31]. The charge transfer amounts to  $\sim 0.2e$  [27].

### Semiconductor triclinic $\beta'$ phase

The  $\beta'$ -phase of (BEDT-TTF)TCNQ consists of 2D BEDT-TTF sheets and of 1D columns of TCNQ. The room temperature conductivity is about  $10 (\Omega\text{cm})^{-1}$ , being remarkably high for a semiconducting organic material.  $\beta'$ -salts of BEDT-TTF usually have a dimeric structure where two BEDT-TTF molecules form a dimer. The  $\beta'$ -phase of (BEDT-TTF)TCNQ experiences a series of phase transitions: an antiferromagnetic transition at 20 K due to the ordering of the localized spins on each BEDT-TTF dimer [99] and ordering at 3 K on the TCNQ chains [100, 101]. In contrast to the bandstructure calculations, which predict for this material metallic properties at ambient pressure, a metal-insulator transition drives the system into the semiconducting state below  $T \approx 330$  K [15]. First temperature-dependent resistivity measurements performed under pressure in 1994 showed that the insulating behavior is suppressed with increasing pressure (see Fig. 4.5a) [101]. It was demonstrated that under applied pressure of 1 GPa the transition temperature shifts down to 40 K. Below 40 K the (BEDT-TTF)TCNQ crystals do not show metallic behavior. However, in contradiction to these resistivity measurements performed in 1994, recent reports show that the metallic behavior spans the whole temperature range at pressures of 1 GPa and higher [102, 103]. Therefore, to date it is not clear if the suppression of the insulating state persists at the lowest temperatures.

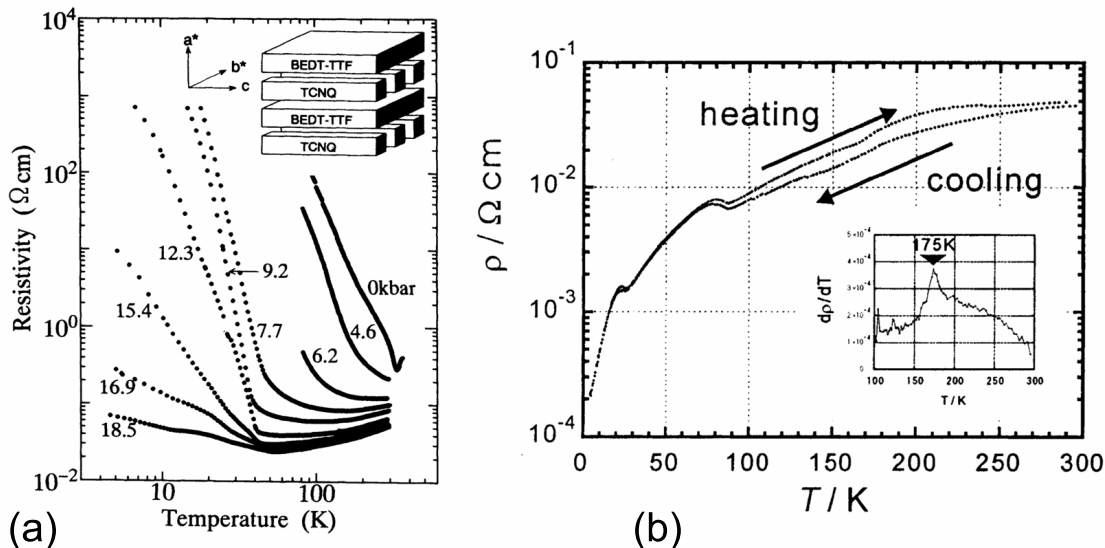


**Figure 4.5:** Transport characteristics of  $(BEDT-TTF)TCNQ$  CT complexes. (a) Temperature dependence of the resistivity along the  $c$ -axis of a crystal of the  $\beta'$ -phase for different pressures, taken from [101]. (b) Resistivity of a  $\beta''$ -phase single crystal of  $(BEDT-TTF)TCNQ$  at ambient pressure, taken from [104].

The resistivity was measured for  $\beta'$ - $(BEDT-TTF)TCNQ$  single crystals and anisotropic behavior was found with the resistivity being a few times larger along the  $b^*$ -axis of the crystal than along the  $c$ -axis. This indicates that the BEDT-TTF sheets have a dominating contribution to the electrical conductivity [101]. The amount of charge transfer is about  $0.5e$  [27, 103]. The reproducibility of the metal-insulator transition at  $T \approx 330$  K is arguable at the moment and could not be demonstrated to take place in all studied  $\beta'$   $(BEDT-TTF)TCNQ$  single crystals [70, 105]. In conclusion, it is noted that ambipolar behavior of OFET transistors based on  $\beta'$ - $(BEDT-TTF)TCNQ$  single crystal was observed with electron and hole mobilities of about  $2 \times 10^{-2} \text{ cm}^2 \text{V}^{-1} \text{s}^{-1}$  [54].

### Metallic triclinic $\beta''$ -phase

The  $\beta''$ -phase of the  $(BEDT-TTF)TCNQ$  is at present the last found crystallographic modification of this CT compound. It was obtained in 2003 from a  $\text{CH}_2\text{Cl}_2$  (or  $\text{CH}_2\text{Br}_2$ ) solution containing BEDT-TTF, TCNQ and tetraiodoethylene ( $\text{C}_2\text{I}_4$ ) by slow evaporation of the solvent [16]. The  $\beta''$ -phase of  $(BEDT-TTF)TCNQ$  has a triclinic crystal structure and exhibits metallic behavior down to low temperatures as

shown in Fig. 4.5b [104]. The room temperature conductivity is about  $30 (\Omega\text{cm})^{-1}$ . Donor and acceptor stacks of the  $\beta''$ -phase form separate layers parallel to the  $(ac)$  plane of the crystal (see Fig. 4.4c). The  $\beta''$ -complex has a very exotic Fermi surface at room temperature: two quasi one-dimensional Fermi surfaces cross each other at a  $90^\circ$  angle. One Fermi surface is associated with the BEDT-TTF layers and is composed of parallel sheets being perpendicular to the  $k_a$ -axis [106]. The second Fermi surface stems from the TCNQ layers and has sheets parallel to the  $k_c$ -axis. At low temperature, the  $\beta''$ -complex has an anisotropic quasi two-dimensional Fermi surfaces. Resistivity measurements revealed three anomalies at temperatures of 170 K, 80 K and 20 K. It is believed that the anomalies at 20 K and 80 K are caused by a partial nesting of the quasi one-dimensional Fermi surface, which was supported by measurements of Shubnikov-de-Haas oscillations [16, 107]. The structural phase transition at 170 K is interpreted as a destruction of a charge ordered state of the holes in the BEDT-TTF layer [108]. The amount of charge transfer in the  $\beta''$ -phase of (BEDT-TTF)TCNQ is  $0.5e$  [108].

For the formation of the  $\beta''$ -phase, the use of an additional catalytically active tetraiodoethylene component in the solution appears to be essential. Without this component, only the monoclinic and the  $\beta'$ - phases emerge. In the presence of the catalyst the metallic  $\beta''$ -(BEDT-TTF)TCNQ crystals grow on tetraiodoethylene crystals. Tetraiodoethylene works as a nucleation center for the growth of the new phase. A possible explanation to this effect was suggested as follows: the iodine atoms covalently bind to carbon atoms and interact with the electronegative nitrogen atoms of TCNQ. They thus work as a template for the new phase formation by fixation of the nitrogen atoms of TCNQ during the initial crystallization step [16].

Among the three crystallographic phases of (BEDT-TTF)TCNQ, the  $\beta''$ -metallic phase and the  $\beta'$ -semiconductor phase are the most interesting candidates for further studies.

The (BEDT-TTF)TCNQ CT complex is not commercially available. Therefore, the solution growth method from mixtures of BEDT-TTF and TCNQ was employed (see section 4.3). BEDT-TTF powder was purchased from Sigma-Aldrich (Fluka, purity 97%). TCNQ is supplied by Sigma-Aldrich (Fluka, purity 98%). The pre-reacted material, as well as separate donor and acceptor molecules, were evaporated in the OMBD chamber to obtain thin films of (BEDT-TTF)TCNQ.

The evaporation temperature for BEDT-TTF was determined to be within the range of  $120 \dots 160^\circ\text{C}$  (see section 7.1). This is in good agreement with previously reported values in [109], but show a severe discrepancy with the work [110], where the evaporation temperature was given as  $200^\circ\text{C}$ . The melting point of BEDT-TTF

is 242 °C [111]. The evaporation temperature for TCNQ was determined within the range 100...150 °C (see section 7.1), being in good agreement with reported data (for example [112]). The melting point of TCNQ is 293 °C.

In the experiments performed here, the evaporation temperature of the components were chosen with regard to the evaporation rate and growth conditions needed for the respective experimental purpose. The bilayer growth (see section 3.1.4) and the co-evaporation methods were used to investigate the formation of the (BEDT-TTF)TCNQ charge transfer complex. The results are presented in chapter 7.

### 4.3 Merging of organic charge transfer compounds in the solution growth method

Solution growth is a proven method to grow organic molecular crystals [23]. The advantage of this method is that it works at ambient temperatures and allows for controllable growth. The main disadvantage of this method is the possible inclusion of solvent molecules into the grown crystal. However, in the process of the growth of an organic charge transfer complex, the use of a solvent allows the activation energy barrier to be decreased and the shifting of the reaction balance to the CT phase side. The heating of the solvent with dissolved donor and acceptor molecules decreases the importance of the activation energy barrier as well and, therefore, the probability of CT phase formation increases.

The solution growth method was employed here to obtain crystalline powder of (BEDT-TTF)TCNQ following the procedure of Mori et al. [15]. The employed solvents are listed in Tab. 4.1.

**Table 4.1:** *Different phases of (BEDT-TTF)TCNQ charge transfer complex obtained using the solution growth method depending on the choice of the solvent and on the growth conditions. The boiling point for each used solvent is given.*

Solvent	Boiling point (°C)	$T_{solvent}$ (°C)	Evaporation time	Emerged phase
Dichlorethane (DCE) (C <sub>2</sub> H <sub>4</sub> Cl <sub>2</sub> )	84	50	2-25 days	$\beta'$ -phase
Tetrahydrofuran (THF) (C <sub>4</sub> H <sub>8</sub> O)	66	50	7-13 days	$\beta'$ -phase



Tetrahydrofuran	66	50	1 day	monoclinic + $\beta'$ -phase
-----------------	----	----	-------	---------------------------------

The donor and acceptor crystals were powdered in a mortar by a pestle and separately dissolved in organic solvent, then mixed together in a ratio of 1:1, heated on the hot plate and stirred by a magnetic stirrer for about 1.5 h at a temperature of 50 °C. After that the prepared solution was left under the exhaust hood to evaporate at room temperature in the glass beaker with an aluminum foil cap

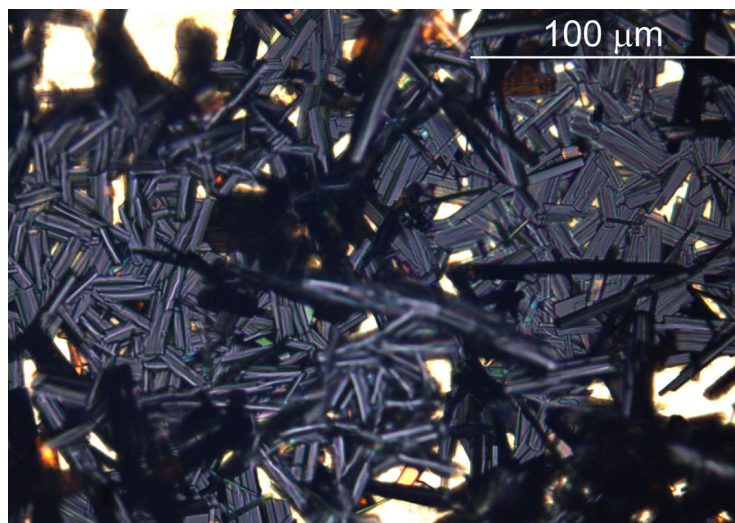


**Figure 4.6:** Crystals of the  $\beta'$ -phase of (BEDT-TTF)TCNQ grown in DCE solution.

punched with holes. After several days, new crystals of the CT phase emerged on the walls and bottom of the beaker as is shown for in Fig. 4.6 for the growth from DCE solvent. The crystals were collected and for further experiments. The crystallographic phase of the emerged crystals was determined by X-ray powder diffraction from the powdered and pressed samples (see Fig. 4.7).

From the X-ray diffraction analysis it is apparent that mixtures of the monoclinic and the  $\beta'$ -phases occur and it is difficult to separate the phases after the growth. Fast solvent evaporation leads to a preferred growth of the monoclinic phase (see Fig. 4.7b), while slow evaporation favors the emergence of the  $\beta'$ -phase (see Fig. 4.7a,c). Based on these experimental observations it is fair to assume that the  $\beta'$ -phase formation has a slower kinetic than the monoclinic phase [19]. The dependence of the preferred phase formation on the solvent type and evaporation time is given in Tab. 4.1.

The pre-reacted (BEDT-TTF)TCNQ crystals obtained from the solution growth were powdered with mortar and pestle and used further as a source material for thin film growth experiments.

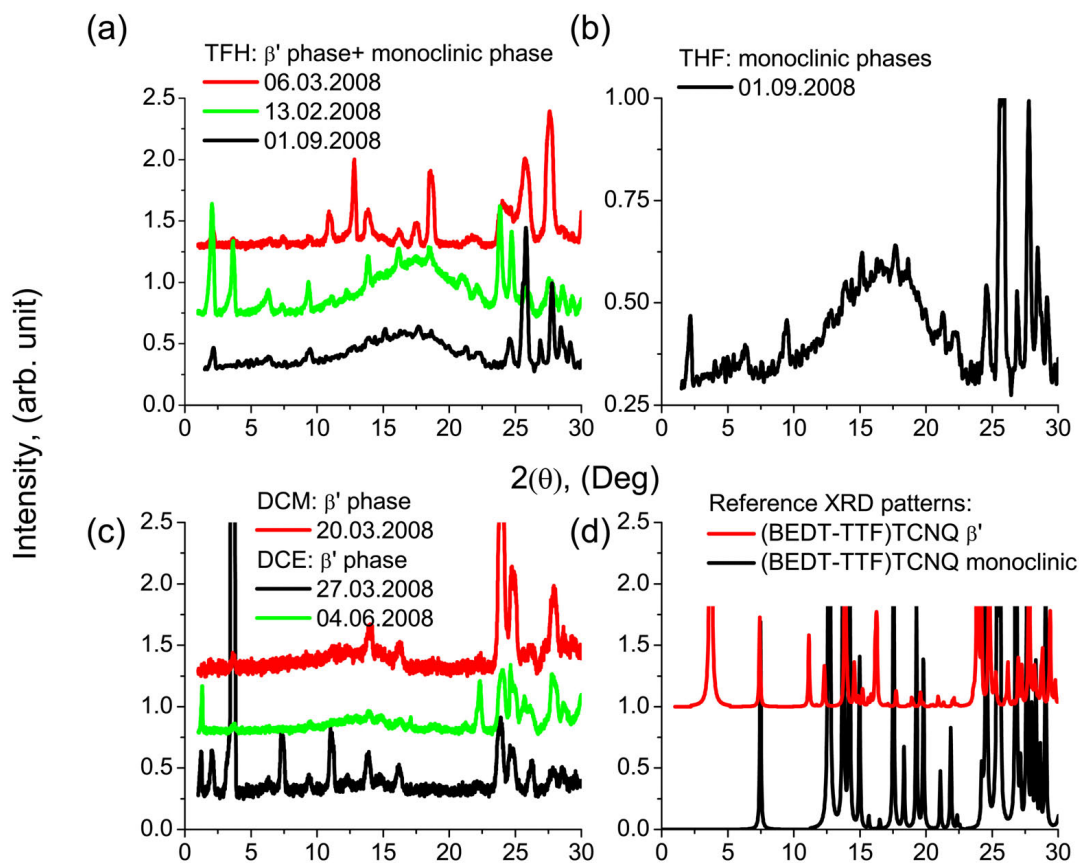


**Figure 4.7:** XRD patterns of *(BEDT-TTF)TCNQ* solution grown crystals from different solvents: (a) tetrahydrofuran, (b) fast evaporation from tetrahydrofuran solvents, (c) dichloroethane and dichlormethane, and (d) the references for *(BEDT-TTF)TCNQ* monoclinic and  $\beta'$ -phases [14, 15].

## 4.4 Substrates used for thin film growth

The initial experiments, which were done to determine the appropriate evaporation conditions for TCNQ, BEDT-TTF, TTF-TCNQ, *(BEDT-TTF)TCNQ*, were performed on glass microscope slides. An example of a microscope slide with deposited thin films is presented in Fig. 4.8 for the monoclinic phase of *(BEDT-TTF)TCNQ*. The evaporation starts on one side of the slide. Then the glass slide is shifted during the evaporation process as the temperature of the effusion cell is increased. Therefore, different areas on the slide correspond to different evaporation temperatures. By X-ray diffraction and by inspection of the samples in the light microscope, the appropriate evaporation parameters for each material was determined. The root mean square (RMS) roughness of the glass slide was determined by AFM measurements

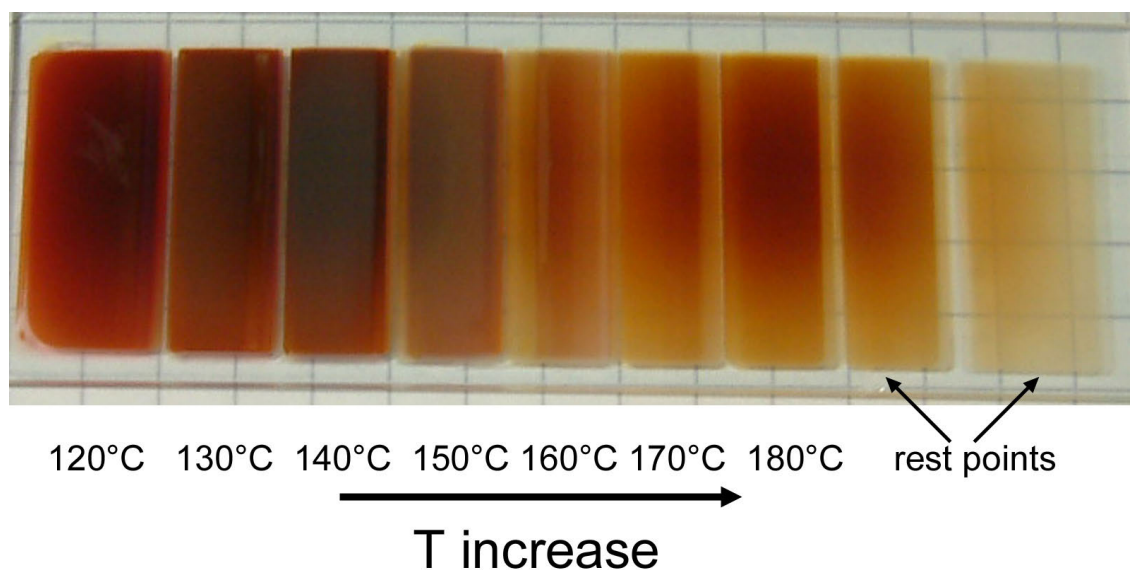


**Figure 4.8:** Example of a microscope slide with (BEDT-TTF)TCNQ thin films, grown in the test chamber from the pre-reacted material. The different evaporation temperature areas were separated by a shadow mask during the deposition.

to be 6 nm for a scan range of  $10\ \mu\text{m} \times 10\ \mu\text{m}$ .

Microscope glass slides proved to be ideal substrates at the initial experimental stage, when the evaporation parameters of the studied materials needed to be established. For further growth studies, the choice of the substrate becomes important. The substrates used in this work are summarized in Tab. 4.2. It was reported that epitaxial growth of TTF-TCNQ takes place only on alkali halide substrates in specific crystallographic orientations, such as NaCl(100) and KCl(100) [20, 97, 113, 114]. Therefore, NaCl(100) substrates with the RMS roughness of 0.16 nm were used as a reference. NaCl(210) and NaCl(110) substrates were tested as well. The RMS roughness of these substrates were found to be 0.12 nm and 0.17 nm, respectively. SrLaGaO<sub>4</sub>(100) (RMS roughness 0.176 nm) and SrLaAlO<sub>4</sub>(100) (RMS roughness 0.202 nm) were also used and chosen because of the lattice match with the lattice parameters of TTF-TCNQ (see the Tab. 4.2) that should favor the epitaxial growth of the TTF-TCNQ thin film. MgO(100) (RMS roughness 0.224 nm), MgF<sub>2</sub>(001) (RMS roughness 0.103 nm), MgF<sub>2</sub>(100) (RMS roughness 0.132 nm), and  $\alpha$ -Al<sub>2</sub>O<sub>3</sub>(11 $\bar{2}$ 0) (RMS roughness 0.067 nm) substrates were used, too.

In the case of oxide substrate the interaction with organic molecules is only van der Waals. Therefore, for these substrates either Stranski-Krastanov or Volmer-Weber growth is expected (see chapter 3). The halide substrates are polar and the

interaction between the substrate and the molecules is stronger, favoring Frank-van der Merwe growth (see section 3.1.2).

**Table 4.2:** *Substrate materials used in growth experiments of TTF-TCNQ thin films. TTF-TCNQ lattice parameters are included for illustration purpose.*

Substrate material and crystallographic orientation	$a$ (nm)	$b$ (nm)	$c$ (nm)	crystalline structure	Ref.
<i>TTF-TCNQ</i>	<i>1.2298</i>	<i>0.3819</i>	<i>1.846</i>	<i>monoclinic</i>	<i>[38]</i>
SrLaGaO <sub>4</sub> (100)	0.384	0.384	1.268	tetragonal	[115]
SrLaAlO <sub>4</sub> (100)	0.375	0.375	1.263	tetragonal	[116]
MgO(100)	0.421	0.421	0.421	cubic	[117]
MgF <sub>2</sub> (001), (100)	0.464	0.464	0.306	tetragonal	[118]
$\alpha$ -Al <sub>2</sub> O <sub>3</sub> (11 $\bar{2}$ 0)	0.476	0.476	1.299	rhombohedral	[119]
NaCl(100), (110), (210)	0.564	0.564	0.564	cubic	[120]
Si(100)/SiO <sub>2</sub>	0.543	0.543	0.543	cubic	[121]

In experiments on the bilayer growth of (BEDT-TTF)/TCNQ, three types of substrates were used: (i) Si(100) with 300 nm thermal silicon oxide layer (ii) Si(100) with 300 nm thermal silicon oxide layer covered with 20 nm Cr and 50 nm Au and (iii) glass slides. The RMS roughness of the Si/SiO<sub>2</sub> substrates was found to be 0.6 nm, while the RMS roughness of the Si/SiO<sub>2</sub> substrates covered with gold was  $\sim$ 1 nm.

Si(100)/SiO<sub>2</sub> and  $\alpha$ -Al<sub>2</sub>O<sub>3</sub>(11 $\bar{2}$ 0) substrates were chemically cleaned in an ultrasonic bath in acetone for 15 min, then rinsed with distilled water, cleaned once more in acetone for 5 min, followed by the step with distilled water for 5 minutes and the final cleaning step was performed in isopropanol for 10 min. An extra isopropanol step was used to insure the cleanliness of the substrates. The cleaning procedure for MgO, MgF<sub>2</sub>, SrLaGaO<sub>4</sub> and SrLaAlO<sub>4</sub> substrates was different. The steps with acetone were omitted, because acetone influences the surface of the substrate. Acetone was substituted by isopropanol. NaCl(100), NaCl(110) and NaCl(210) substrates were *ex situ* cleaved and polished, no other treatment was performed. All the used substrates were purchased from Crystec GmbH. RMS measurements are given for the  $1\mu\text{m}\times 1\mu\text{m}$  area.

## **DEFECT-INDUCED SHIFT OF THE PEIERLS TRANSITION IN TTF-TCNQ THIN FILMS**

**T**his chapter is devoted to the investigation of thin films of TTF-TCNQ. The transport properties of TTF-TCNQ single crystals are well established. However, there are many aspects, the study of which is not possible for single crystals, but which are accessible in thin films, such as substrate-induced strain and electron irradiation effects. The study of TTF-TCNQ thin films allows to illuminate these aspects and to compare the results with the known data for single crystals. In this work, TTF-TCNQ thin film growth studies are performed, the substrate-induced strain is calculated and the influence of defects in the thin films on the Peierls transition is analyzed.

In section 5.1, the critical factors influencing the Peierls transition in TTF-TCNQ single crystals are outlined, giving the starting point for the experiments performed in this work. The growth and characterization of TTF-TCNQ thin films is discussed in section 5.2. A detailed analysis of the grown thin films was performed by angle resolved photoelectron spectroscopy (ARPES) via a collaboration with the group of Prof. Dr. Martin Aeschlimann (University of Kaiserslautern). The results of these measurements are presented in section 5.3. Section 5.4 is devoted to the investigation of strain in TTF-TCNQ thin films. The substrate's influence on the electrical conductivity of TTF-TCNQ thin films is discussed in section 5.5. The study of the Peierls transition temperature of TTF-TCNQ thin films and factors, which cause a shift of the phase transition temperature in thin films, are considered in section 5.6.

## 5.1 Factors influencing the Peierls transition in TTF-TCNQ single crystals

In this section, a brief account is given on the factors which influence the phase transitions in TTF-TCNQ single crystals.

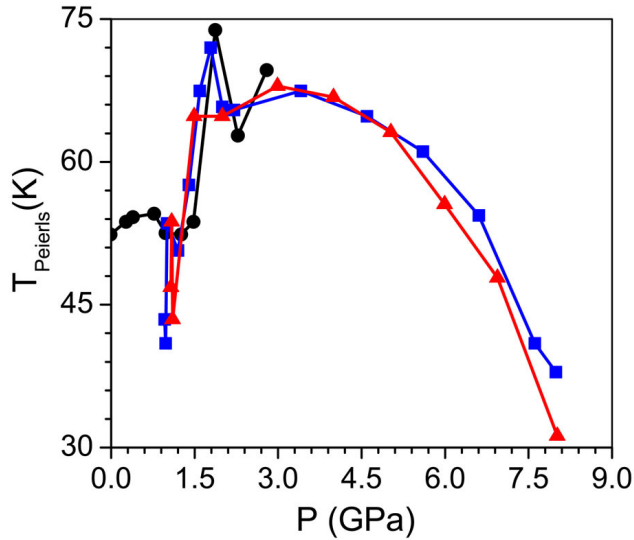


**Figure 5.1:** Pressure-temperature phase diagram for TTF-TCNQ single crystals: circles show the results from [6], while squares and triangles are taken from [122].

the dependence of the Peierls transition temperature on hydrostatic pressure  $P$  for TTF-TCNQ single crystals. The phase transition temperature at pressure of 3 GPa is shifted to the higher temperature values ( $\sim 70$  K) [6] and, under extremely high pressures ( $\gtrsim 3$  GPa), a suppression of the CDWs is taking place [122]. When the pressure reaches 1.9 GPa, a sharp peak in the pressure-temperature phase diagram is observed. In the region above 1.5 GPa, the lattice distortions become commensurate with the underlying lattice and the period of the distortion becomes  $3b$  in contrast to the incommensurate value  $3.4b$  in the absence of external pressure. The degree of the charge transfer increases with the increase of pressure from its ambient pressure value of  $\rho = 0.59$  to  $\rho = \frac{2}{3}$  under pressure when the CDW becomes commensurate. However, for the low pressure regime the incommensurate state is preferred.

The concentration of defects in TTF-TCNQ is another important factor which influences the CDWs and the Peierls transition. A increase of the concentration of defects in TTF-TCNQ single crystals leads to a lowering of the Peierls transi-

In recent studies the influence of hydrostatic pressure on TTF-TCNQ was investigated [6, 122, 123]. Pressure increases the overlap of the electronic wave functions between the TTF and TCNQ stacks and thus alleviates the quasi-one-dimensional conductivity of TTF-TCNQ, which in turn suppresses the Peierls instability [95] and presumably permits superconductivity [122]. It was demonstrated that at higher pressures ( $\gtrsim 1.5$  GPa), only one phase transition associated with the CDW exists. Figure 5.1 gives an illustration of

tion temperature because the long-range order in the 1D crystal becomes disturbed and the coherence length associated with CDW state is reduced [84, 124, 125]. A phenomenological similar behavior is known to occur in superconductors with paramagnetic defects. An increase of the defect concentration also affects the CDW pinning. As follows from Eq. (4.3) for high defect concentration the pinning is weak and more energy is needed to undergo a series of short-wavelength distortions for CDWs phase matching on all impurities sites leading to a decrease of the transition temperature.

In [125], the defects in a TTF-TCNQ single crystal were induced by 8 MeV deuteron irradiation of the sample. It was experimentally demonstrated that the Peierls transition temperature shifts towards lower temperature with increasing radiation dose. The temperature range of the Peierls transition became broadened and the transition was completely suppressed when the defect concentration in the TTF-TCNQ single crystal reached a few percent [126]. In this case the electrical conductivity of the crystal showed thermo-activated behavior.

In the effects mentioned above [6, 122, 125–127], hydrostatic pressure or irradiation applied to a TTF-TCNQ single crystal exert constant isotropic forces in the system or affect the crystal uniformly. The quasi-one-dimensional conductivity of TTF-TCNQ motivated further experimental and theoretical studies involving anisotropic forces [128, 129]. Attempts to reduce or increase the intermolecular distances along a certain direction of the TTF-TCNQ crystal were made by applying uniaxial stress to the system [129–131]. The bent-beam (bar) technique [130] was used to study the influence of uniaxial stress in TTF-TCNQ single crystals and it was demonstrated that the change of transport properties at room temperature strongly depends on the crystalline axis along which uniaxial tensile stress is applied. The resistivity along the  $b$ -axis of the TTF-TCNQ single crystal was measured for tensile strains applied along the  $a$ - and  $b$ -axes of the crystal. In the case of the tensile strain applied along the  $a$ -axis, the resistivity along the  $b$ -axis decreases, while in the case of the  $b$ -axis tensile strain the resistivity increases.

The effect of uniaxial stress on the band structure of TTF-TCNQ was considered theoretically in [128] using the local-density approximation (LDA) [132, 133] and the generalized gradient approach (GGA) [134]. According to these theoretical studies, a change of the inter- or intrastack distances affects the electronic structure in TTF-TCNQ. The system studied in [128] was considered at 100 K. It was shown that the change of the molecular structure of TTF and TCNQ depends on the compression direction and, depending on the compression direction, electronic bandstructure of TTF-TCNQ is differently changed [128]. For the temperature of 100 K, the

experimental value of the charge transfer in TTF-TCNQ at ambient pressure is  $0.59e$  [8], while LDA calculations give 0.813 and GGA gives 0.768. The calculated numbers are somewhat overestimated compared with the experimental values. A possible reason is the lack of a description of the electronic exchange correlation and thermal vibrations in the theoretical models [135]. The theoretical calculations deliver the value of the charge transfer in the case of 10% compression along the  $a$ -axis equal to 0.925 for LDA and 0.87 for GGA methods, being larger than the values calculated without any compression. The increase of the charge transfer can be ascribed to the increase of the coupling between TTF and TCNQ stacks as compression perpendicular to the stack axis is applied. The compression along the  $b$  or  $c^*$  (axis perpendicular to  $(ab)$ -crystallographic plane of TTF-TCNQ) axes does not lead to any significant increase of the charge transfer amount [128]. Uniaxial compression induces a change in the intercolumnar coupling. The change of the coupling and the charge transfer can affect transport properties of the CT compound, thereby providing a possible mechanism to tune the transport properties of the crystal by external pressure.

The above-mentioned methods were applied to study single crystals of organic charge transfer salts. In contradistinction to these investigations, works studying microcrystals of organic charge transfer salts utilize substrate-induced strain. Recently, a clamping effect was used to modify the electronic properties of microcrystals of the organic CT salt  $\kappa$ -(BEDT-TTF)<sub>2</sub>Cu[N(CN)<sub>2</sub>]Br [136]. Microcrystals of the organic CT salt were dropped on the substrate and fixed by van der Waals forces. The difference in the thermal expansion of the organic microcrystal and substrate imposes either compressive or tensile strain as the system is cooled down. By changing the substrate material and consequently thermal expansion properties, the temperature-induced strain changes and the material becomes either superconductor (for polystyrene substrate) or insulator (for Si/SiO<sub>2</sub> substrate).

There are several aspects which hinder the study of TTF-TCNQ thin film properties with regard to substrate-induced effects. Unlike in the case of single crystal growth, the crystallographic growth preferences in organic thin films strongly depend on the growth conditions and on the substrate material and is difficult to control. Typically TTF-TCNQ thin films grown by physical vapor deposition, or related techniques [64, 96, 114, 137], show a  $(00\ell)$  growth preference. The  $b$ -axis can be either randomly oriented in the plane of the substrate, such as for Si(100) and sapphire (random oriented) [96, 114], or can have two preferential orientations. The latter case typically occurs for alkali halide substrates with cubic symmetry, such as NaCl(100), KCl(100) [114]. The influence of the substrate on the transport proper-



ties was not discussed before for TTF-TCNQ with regard to the thermal contraction effect. One of the aims of this work was to investigate the influence of the substrate material and the interaction between the substrate and the thin film on the transport properties of TTF-TCNQ, especially on the Peierls transition temperature.

## 5.2 TTF-TCNQ thin film growth and characterization

First studies on thin films of TTF-TCNQ were published in the late seventies (see for example [96]). It was demonstrated that TTF-TCNQ forms epitaxial thin films on alkali halide substrates with (100) orientation [113], where TTF-TCNQ crystallites grow with their  $b$ -axis oriented parallel to the  $\langle 110 \rangle$  and  $\langle \bar{1}10 \rangle$  axes of the substrates. Subsequently, many experiments aimed for growing epitaxial films on other substrate. However, this is still an open question. Another challenging task is the formation of TTF-TCNQ thin films consisting of microcrystals oriented in-plane only along the  $b$ -axis, which is the highest conductivity axis in the crystal (see section 4.1). This would allow the study of the transport properties of TTF-TCNQ thin films along one crystallographic direction.

During the thesis work, preliminary experiments aimed to find the evaporation conditions of TTF-TCNQ by PVD were performed in the “mini”-OMBD chamber on microscope glass slides. According to the results reported in the previous studies, the use of pre-reacted TTF-TCNQ as a single evaporation source in physical vapor deposition experiments results in the formation of thin films consisting of TTF-TCNQ [96, 138, 139]. Therefore, at first TTF-TCNQ crystalline powder was tested as a source material in the experiments. The sampled temperature range was 100...200 °C. X-ray diffraction of the films exhibits the peaks corresponding to the (002 $l$ ) crystallographic planes of TTF-TCNQ, as is exemplarily shown in Fig. 5.2. EDX characterization of the TTF-TCNQ thin films grown from the pre-reacted CT salt reveals the S:N ratio to be close to 1:1 (see Fig. B.1), corresponding to the expected value for TTF-TCNQ. Therefore, for the further experiments the powdered pre-reacted TTF-TCNQ crystals were used and evaporation took place from a single effusion cell.

To study the epitaxial growth of TTF-TCNQ thin films, different substrates, listed in Tab. 4.2, were used. Sodium chloride substrates with (100) orientation were taken as a reference because it is known to be suitable for the epitaxial growth of TTF-TCNQ thin films [113]. The substrate preparation steps are described in section 4.4 in detail.

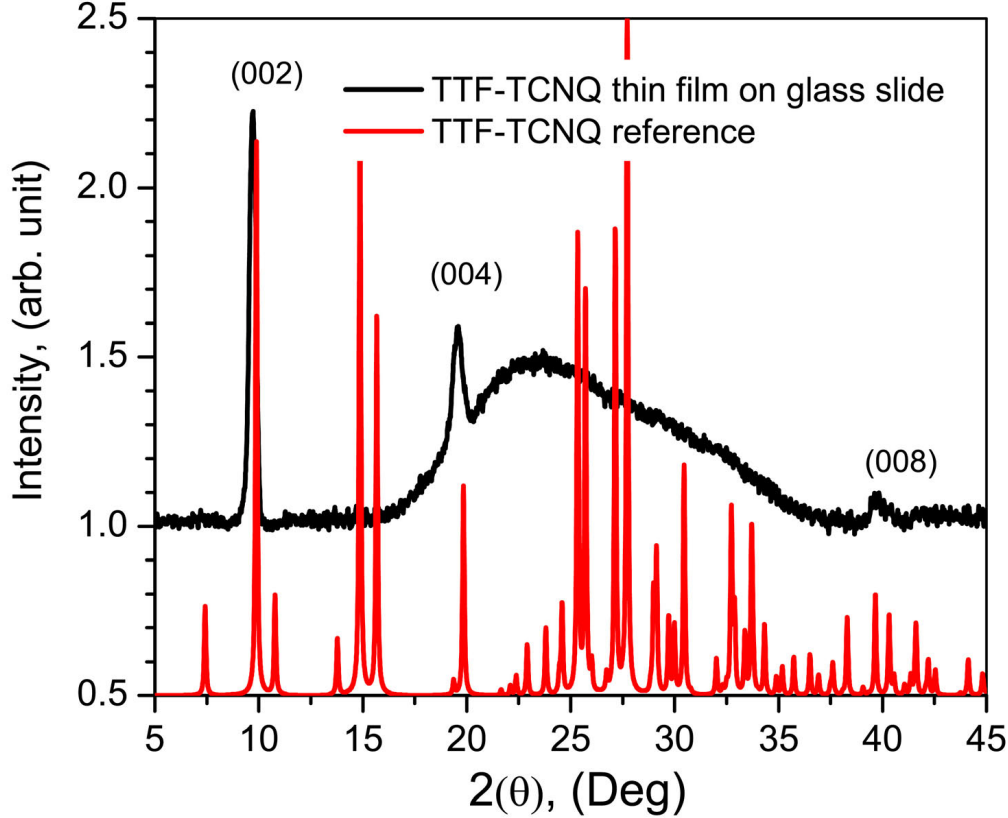


**Figure 5.2:** X-ray diffraction pattern of TTF-TCNQ thin film. The black line shows the diffractogram for the TTF-TCNQ thin film grown on a glass substrate. The evaporation temperature was  $110^\circ$ . The red line is the reference XRD pattern for TTF-TCNQ [38].

In the course of the experiments, two domains' growth of TTF-TCNQ microcrystals was observed on the NaCl(100) substrates (see Fig. 5.3). TTF-TCNQ microcrystals in these domains have their  $b$ -axis oriented parallel to the  $\langle 110 \rangle$  and  $\langle \bar{1}10 \rangle$  axes of NaCl(100). NaCl substrates with (110) and (210) crystallographic orientations were also tested. Figure 5.4 shows SEM images of TTF-TCNQ films grown under identical conditions on NaCl substrates with different crystallographic orientations. From this comparison, one can readily conclude that, in contrast to NaCl(100), the orientations (110) and (210) of NaCl do not favor any in-plane preferential growth. It is also important to note that the sticking coefficients for the three NaCl substrate substrates differ significantly, as is shown in Fig. 5.4.

Strontium oxide substrates, such as SrLaGaO<sub>4</sub>(100) and SrLaAlO<sub>4</sub>(100), are not commonly used for organic thin film preparation. Here they were chosen due

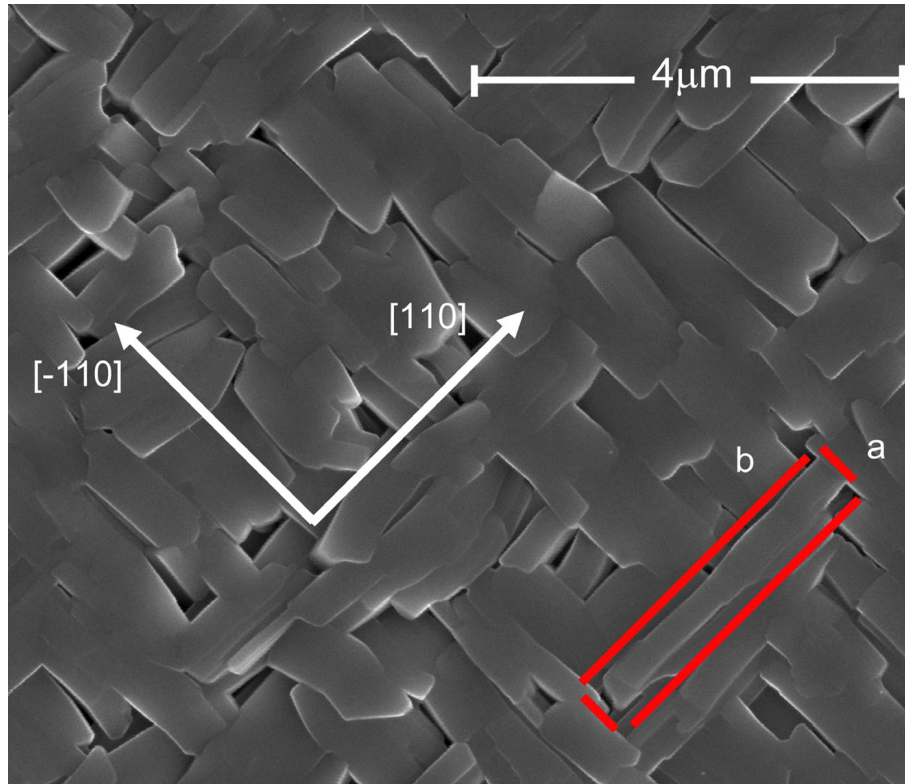


**Figure 5.3:** Two domain growth of microcrystals of TTF-TCNQ on NaCl(100). The  $\langle 110 \rangle$  and  $\langle \bar{1}10 \rangle$  axes of the NaCl(100) substrate are indicated in white. The  $a$ - and  $b$ -axes of the TTF-TCNQ microcrystal are also shown in red.

to the matching of their lattice parameters with TTF-TCNQ (see Tab. 4.2) that could presumably favor the oriented growth of TTF-TCNQ thin films on these substrates [115, 116]. The in-plane alignment of TTF-TCNQ thin films grown on SrLaGaO<sub>4</sub>(100) substrate was studied by Grazing Incidence X-ray Diffraction (GID). The diffraction pattern of the GID- $\varphi$  scans for the (100) crystallographic plane of TTF-TCNQ and for the (002) crystallographic plane of the substrate are shown in Fig. 5.5a. The reflection from the (100) crystallographic plane of TTF-TCNQ describes the relative orientation of the crystal  $a$ -axis in the plane of the substrate with respect to the  $c$ -axis of the SrLaGaO<sub>4</sub>(100) substrate, which is defined by the (002) crystallographic plane.

Figure 5.5a (red line) shows four weak peaks at  $\varphi \approx -90^\circ, 0^\circ, 90^\circ, 180^\circ$ , which correspond to the reflection from the (100) crystallographic plane of the TTF-TCNQ thin film. The peaks are indicated by small vertical arrows in Fig. 5.5a and coincide with the two-fold symmetric substrate reflections (black line) demonstrating that the

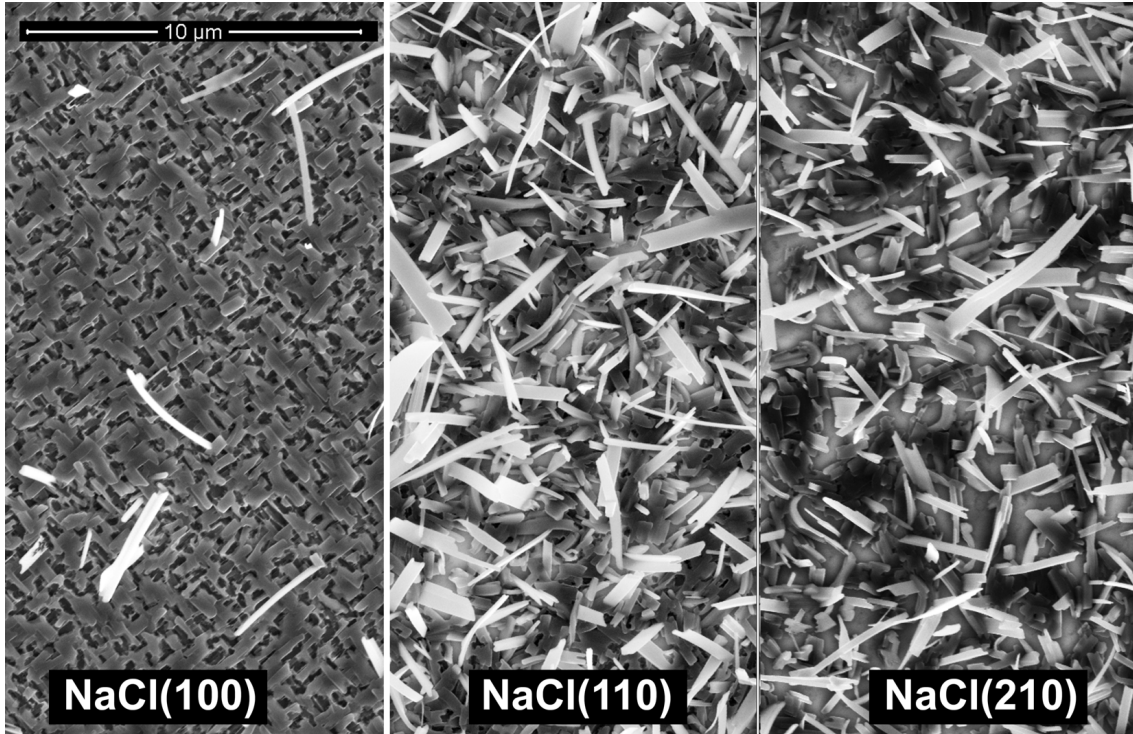


**Figure 5.4:** SEM images of TTF-TCNQ thin films grown with an effusion cell temperature  $90\text{ }^{\circ}\text{C}$  on (a) NaCl(100) for 5 min, (b) NaCl(110) for 6 min and (c) NaCl(210) for 6 min. The scale bar applies to all panels.

$a$ -axis of the TTF-TCNQ crystallites has a weak in-plane preferred orientation co-directional with the  $b$ - and  $c$ - crystallographic axes of the SrLaGaO<sub>4</sub>(100) substrate. This weak effect cannot be corroborated by SEM imaging. Figure 5.5b-d shows  $\theta - 2\theta$  X-ray diffraction pattern and SEM images of the TTF-TCNQ thin film grown on SrLaGaO<sub>4</sub>(100). From these figures, one concludes that no appreciable preferential orientation can be identified in the case of the SrLaGaO<sub>4</sub>(100) substrate and that the matching of the lattice parameters does not play a significant role in the growth of TTF-TCNQ films. The same growth type was observed on SrLaAlO<sub>4</sub>(100).

The oxide substrates MgO(100),  $\alpha$ -Al<sub>2</sub>O<sub>3</sub>(11 $\bar{2}$ 0), Si(100)/SiO<sub>2</sub>(285 nm) and fluoride substrates MgF<sub>2</sub>(001) and MgF<sub>2</sub>(100) were also tested. These substrates are often used in MBE growth experiments. The oxide substrates interact with TTF-TCNQ only via van der Waals forces, favoring the Volmer-Weber growth mode (see section 3.1.2). The binding between the MgF<sub>2</sub> substrate and the TTF-TCNQ thin film has an ionic component. Therefore, for MgF<sub>2</sub> substrate, as well as for the case of the NaCl(100), the interaction between the substrate and the TTF-TCNQ thin

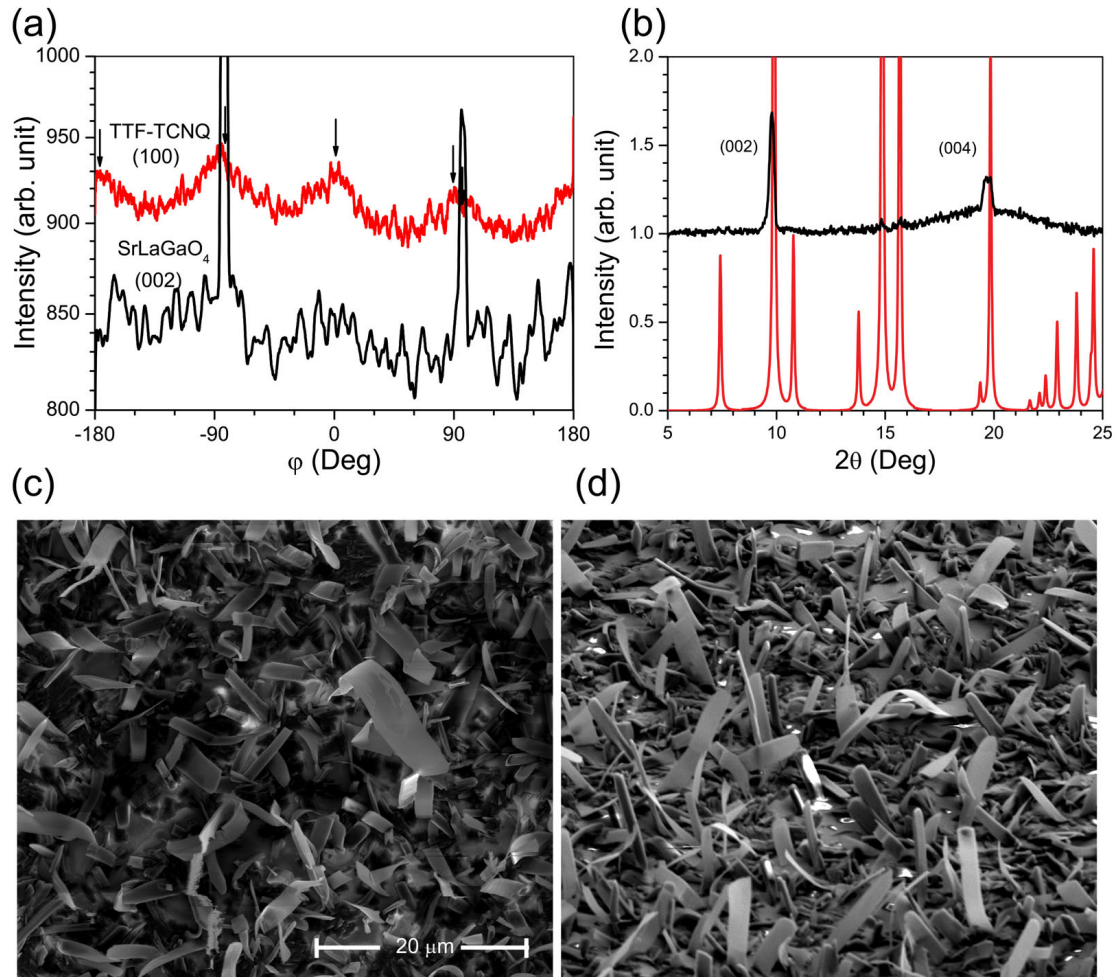


**Figure 5.5:** (a) GID- $\varphi$  scans for TTF-TCNQ film (red line) grown on SrLaGaO<sub>4</sub>(100) (black line) with an effusion cell temperature of 120 °C. The peaks corresponding to the (100) crystallographic plane of the TTF-TCNQ film and the (002) plane of the SrLaGaO<sub>4</sub>(100) substrate are indicated with arrows.  $\varphi$  is the rotation angle around the normal to the substrate surface used in the GID measurement. (b) XRD pattern in symmetric Bragg condition of TTF-TCNQ thin film grown on SrLaGaO<sub>4</sub> (black line), compared with the reference pattern for TTF-TCNQ (red line) [38]. (c)-(d) SEM images of the TTF-TCNQ thin film, normal view and tilted view with 52° tilt angle. The scale bar in (c) applies to both panels.

film is stronger, possibly influencing the growth mode.

To study the growth of TTF-TCNQ thin films, a series of samples was fabricated. The samples were prepared as follows: 5 stripes of TTF-TCNQ films with different

thickness were deposited on each substrate. The first stripe was grown for 1 hour, the second one for two hours, the third one for three hours etc. Thus, for each substrate, 5 film stripes with different thickness increasing from one edge of the substrate to the other were fabricated. A shutter construction was used for this purpose. The growth was performed with an effusion cell temperature of 110 °C and substrate temperature of 26 °C. The distance between the effusion cell orifice and the substrate was kept at 50 mm.

Several growth modes of TTF-TCNQ thin films could be distinguished. The first growth mode is typical for cubic alkali halide substrates with the (100) crystalline orientation. Figure 5.6 shows the morphology of a TTF-TCNQ film grown on NaCl(100) with a thickness of about 175 nm, 350 nm, 525 nm, 700 nm and 825 nm, respectively. The film thickness was measured by FIB cross-sectioning, as is described in section 3.2.4. TTF-TCNQ thin films of a certain thickness self-assemble on the NaCl(100) substrate into a characteristic two-domain pattern as seen in Figs. 5.6a-d. After the film thickness reaches a critical value, the thin film morphology acquires a pronounced 3D character (see Fig. 5.6e). In this example, the critical thickness of the TTF-TCNQ thin film is about 600 nm.

The thickness of the TTF-TCNQ film grown for 1 hour deposition on NaCl(100) is about 175 nm as determined by FIB cross sectioning. In this case, AFM measurements allowed to distinguish two different areas in the film's morphology (see Fig. 5.7), which are hardly detectable in the SEM measurements due to substrate charging effect caused by the electron beam. The chemical composition of both areas was analyzed by means of EDX. The experimental data are presented in Appendix B. The first area corresponds to the top layer of the thin film where TTF-TCNQ crystallites with their *b*-axis oriented parallel to the  $\langle 110 \rangle$  and  $\langle \bar{1}10 \rangle$  axes of the NaCl(100) substrate could be identified (see Fig. 5.3 and Fig. 5.7d). The ratio of TTF:TCNQ  $\approx 1:1$  was verified by selected area EDX (see Fig. B.2a). The second area observed in AFM corresponds to a layer below the TTF-TCNQ crystallites of the grown thin film. The orientation of the crystallites in this region is parallel to the  $\langle 010 \rangle$  and  $\langle 001 \rangle$  directions of the NaCl(100) substrate (see Fig. 5.7b-c). The chemical composition of the crystallites of the lower layer of the thin film was measured by EDX and showed only the presence of nitrogen, demonstrating that this layer consists to a large extent of TCNQ molecules (see Fig. B.2b). This result is in agreement with [140], where it was demonstrated that during the growth process of TTF-TCNQ thin films on KCl(100), a wetting layer of TCNQ is formed on the substrate surface. The increase of the thickness of the deposited TTF-TCNQ film on NaCl(100) substrate leads to a covering of the TCNQ-domains in the bottom

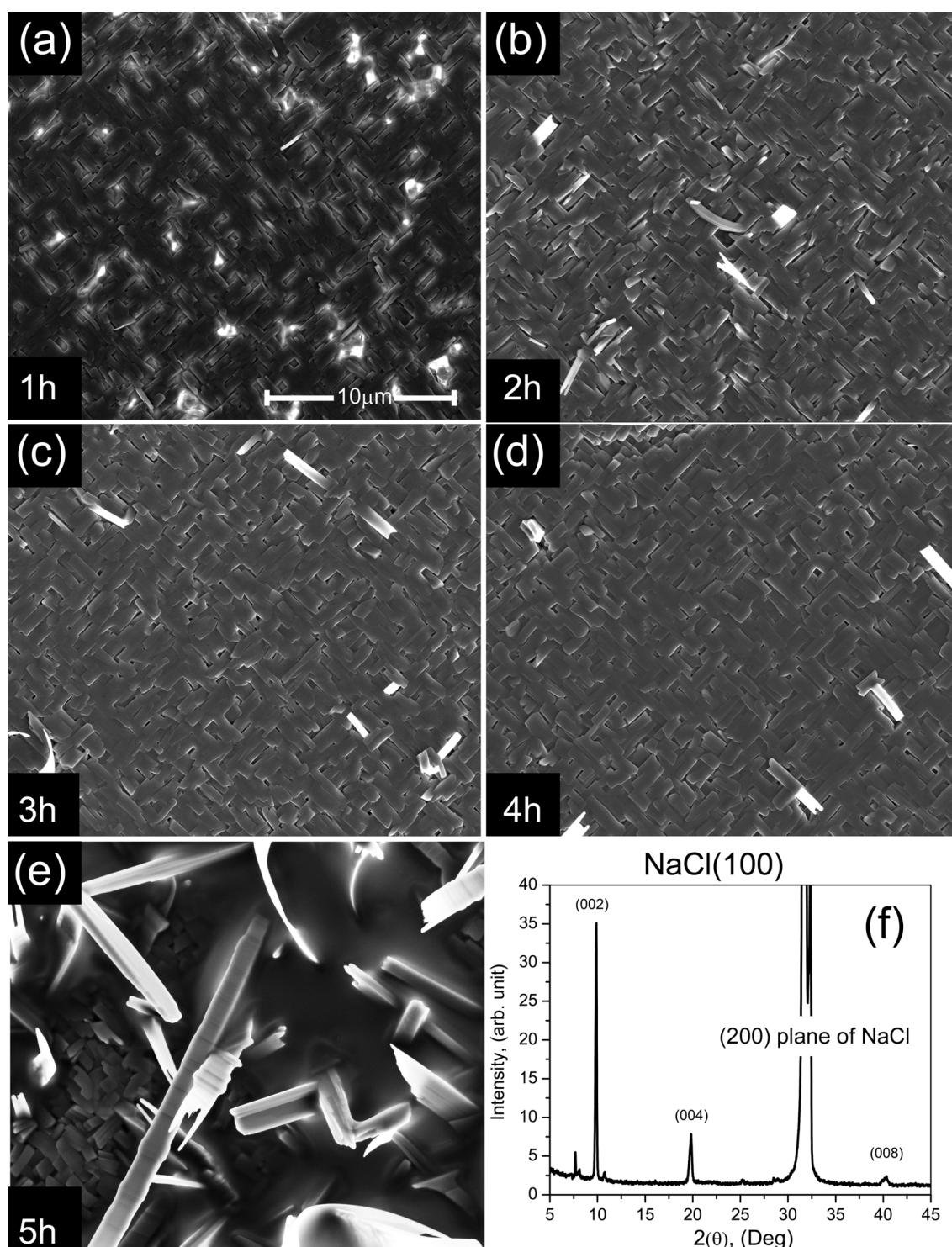


**Figure 5.6:** SEM images of TTF-TCNQ thin films grown on NaCl(100) after (a) 1h deposition (corresponding to 175 nm thickness), (b) 2h deposition (corresponding to 350 nm), (c) 3h deposition (corresponding to 525 nm), (d) 4h deposition (corresponding to 700 nm) and (e) 5h deposition (corresponding to 825 nm). (f) XRD pattern of the sample. The scale bar in (a) applies to all panels.

layer.

In contrast to the TTF-TCNQ films grown on NaCl(100), TTF-TCNQ films grown on NaCl(210) show a different growth mode, further referred to as the second growth mode. This growth is not epitaxial, but with planar microcrystals and a critical thickness of the layer of about 400 nm. The films formed after 1 h, 2 h, 3 h, 4 h and 5 h deposition time are shown in Fig. 5.8. Accurate thickness measurements for the TTF-TCNQ thin films grown on NaCl(210) are hindered due

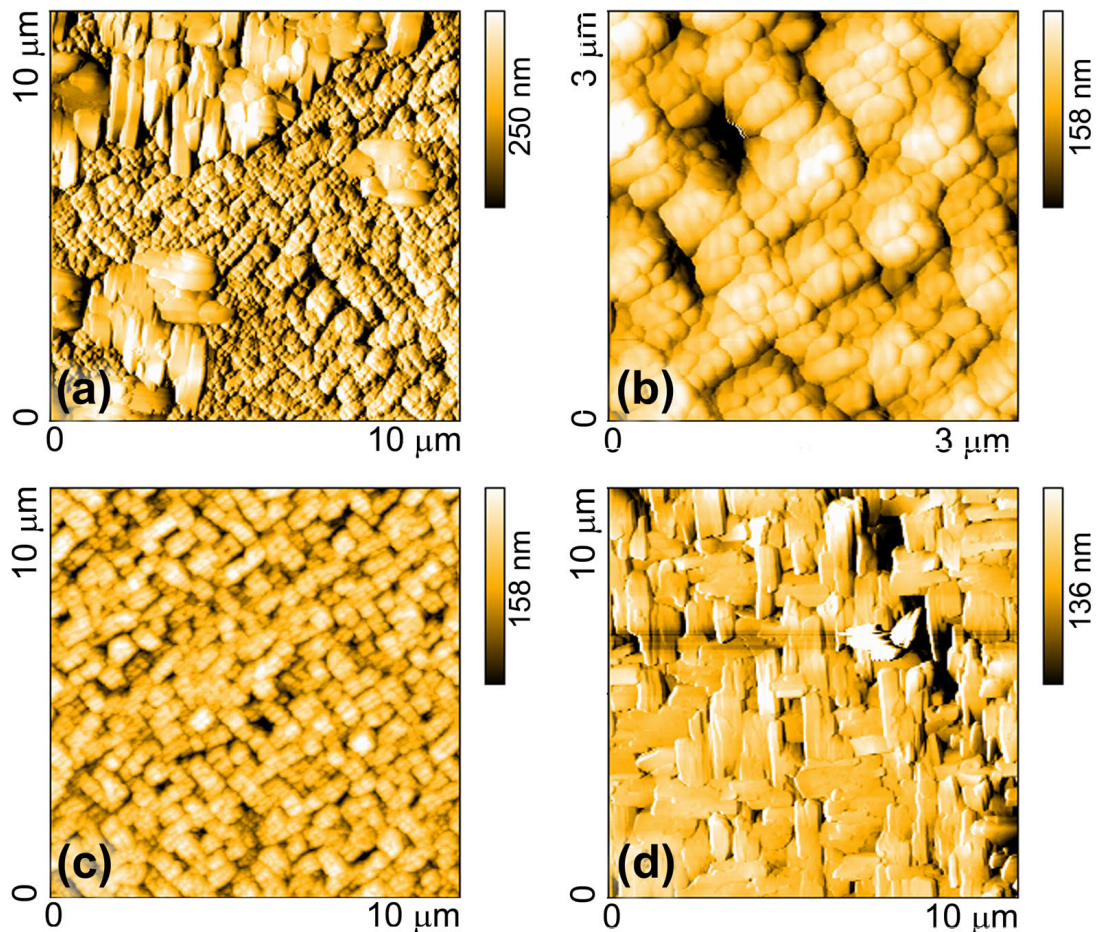


**Figure 5.7:** AFM images of TTF-TCNQ thin film grown on the NaCl(100) after 1 hour of deposition at 110 °C effusion cell temperature. Plot (a) illustrates the mixed area of the TTF-TCNQ thin film, where both, TCNQ and TTF-TCNQ crystallites are observed. Plots (b) and (c) illustrate regions of the lower layer of the thin film, which to a large extent consists of TCNQ crystals. Plot (d) illustrates selected regions showing the upper layer of the thin film, consisting of TTF-TCNQ crystallites.



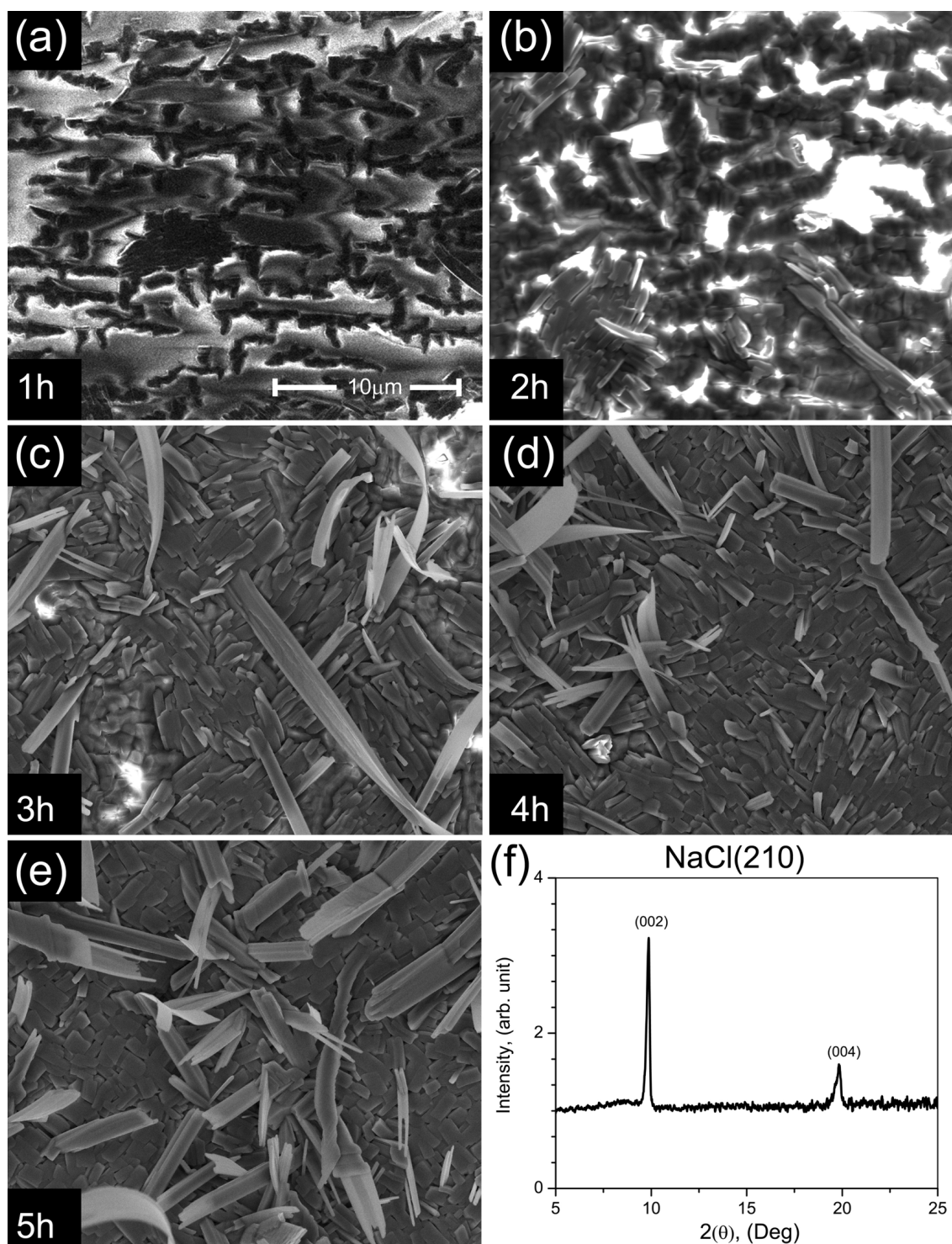


**Figure 5.8:** SEM images of TTF-TCNQ thin films grown on NaCl(210) after (a) 1h deposition, (b) 2h deposition, (c) 3h deposition, (d) 4h deposition and (e) 5h deposition. (f) XRD pattern of the sample. The scale bar in (a) applies to all panels.

to the three-dimensional growth mode. By increasing the substrate temperature, epitaxial growth on NaCl(210) was expected. However, the self-organization process of the TTF-TCNQ thin films is apparently much more complicated than expected, and the heating of NaCl(210) substrate up to 35 °C during the evaporation did not lead to the formation of an oriented film.

TTF-TCNQ microcrystals also form flat arrays of crystallites without a preferred orientation on the MgF<sub>2</sub>(001) substrate (see Fig. 5.9). This growth behavior is similar to TTF-TCNQ thin film self-organization on KCl(100) kept at an elevated temperature of 325 K and annealed at 360 K as observed in [114]. Therefore, an oriented growth of the TTF-TCNQ thin film may be expected to occur if, during the growth process, the MgF<sub>2</sub>(001) substrate is kept at reduced temperature. However, the cooling of the MgF<sub>2</sub>(001) substrate down to 260 K during the evaporation did not lead to the formation of an oriented film, indicating the complicated process of TTF-TCNQ thin film self-organization.

In contrast to the NaCl(100), NaCl(210) and MgF<sub>2</sub>(001) substrate, TTF-TCNQ thin films grown on other substrates such as MgO(100), MgF<sub>2</sub>(100), SrLaGaO<sub>4</sub>(100), SrLaAlO<sub>4</sub>(100), Si(100)/SiO<sub>2</sub> and  $\alpha$ -Al<sub>2</sub>O<sub>3</sub>(11 $\bar{2}$ 0) do not show any in-plane oriented growth for all investigated thickness ranges (see Fig. 5.10–5.14). For these substrates, the growth of the thin film originates from TTF-TCNQ islands (see Fig. 5.10a–5.14a). On increase the deposition time, the islands coalesce and pronounced three-dimensional bar-shaped TTF-TCNQ crystallites are formed (see Fig. 5.10d–e–5.14d–e). Although, the discussed substrates lead to the formation of thin films with similar morphology, the sticking coefficient  $\alpha_c$  of the TTF-TCNQ molecules on the different substrates varies, thereby influencing the effective thin film growth rate. It is also important to stress that heating and cooling of the substrate during the growth process does not affect the growth preferences in the system, influencing only the size of the formed microcrystals, being dependent on the sticking coefficient. The sticking coefficient itself depends on the substrate temperature. With increasing the substrate temperature, the sticking coefficient decreases due to the higher mobility of the molecules on the substrate surface and desorption processes.

The measurements of the thickness of the TTF-TCNQ films grown on MgO(100), SrLaAlO<sub>4</sub>(100), SrLaGaO<sub>4</sub>(100),  $\alpha$ -Al<sub>2</sub>O<sub>3</sub>(11 $\bar{2}$ 0) and MgF<sub>2</sub>(100), Si(100)/SiO<sub>2</sub> substrates are difficult or even impossible due to the irregular and very pronounced three-dimensional growth starting already at an early stage. Therefore, the results of measurements on the film thickness for TTF-TCNQ for these substrates are not presented here.

A study of the influence of the evaporation temperature on the TTF-TCNQ

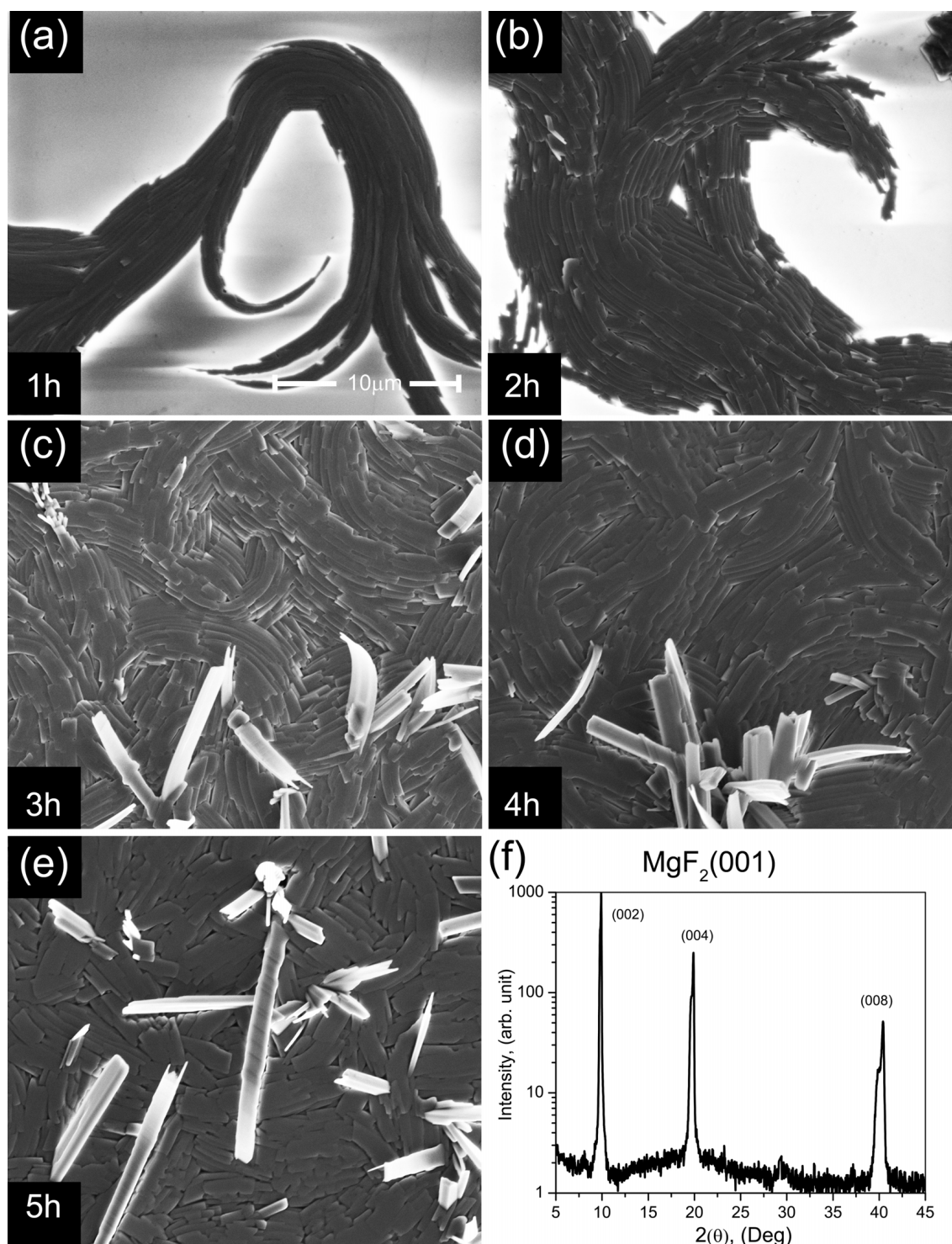


**Figure 5.9:** TTF-TCNQ thin films grown on MgF<sub>2</sub>(001) after (a) 1h deposition (corresponding to 0.375 μm film thickness), (b) 2h deposition (corresponding to 0.7 μm), (c) 3h deposition (corresponding to 1.125 μm), (d) 4h deposition (corresponding to 1.5 μm) and (e) 5h deposition (corresponding to 1.875 μm). (f) XRD pattern of the sample. The scale bar in (a) applies to all panels.

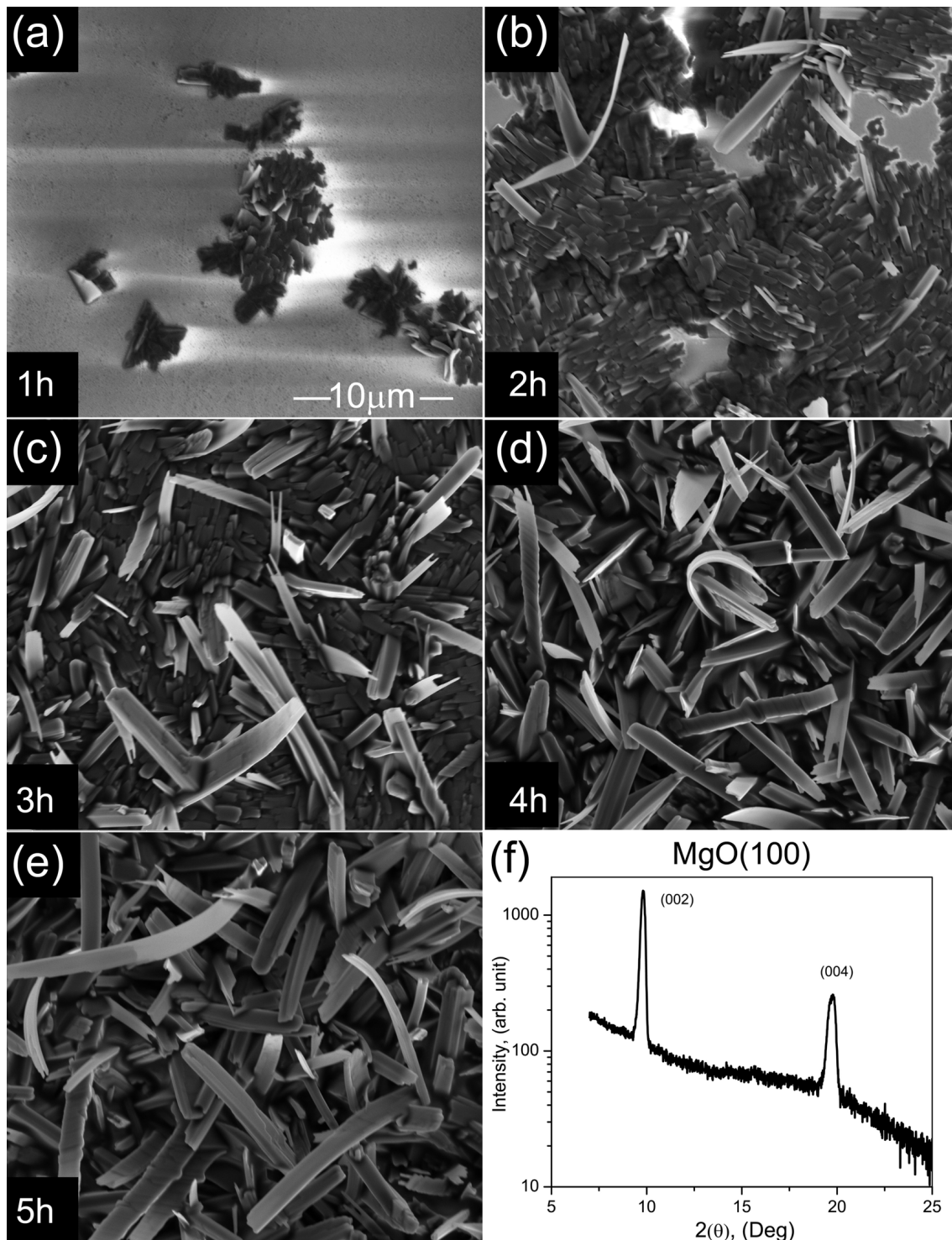


**Figure 5.10:** SEM images of TTF-TCNQ thin films grown on MgO(100) after (a) 1h deposition, (b) 2h deposition, (c) 3h deposition, (d) 4h deposition and (e) 5h deposition. (f) XRD pattern of the whole sample. The scale bar in (a) applies to all panels.

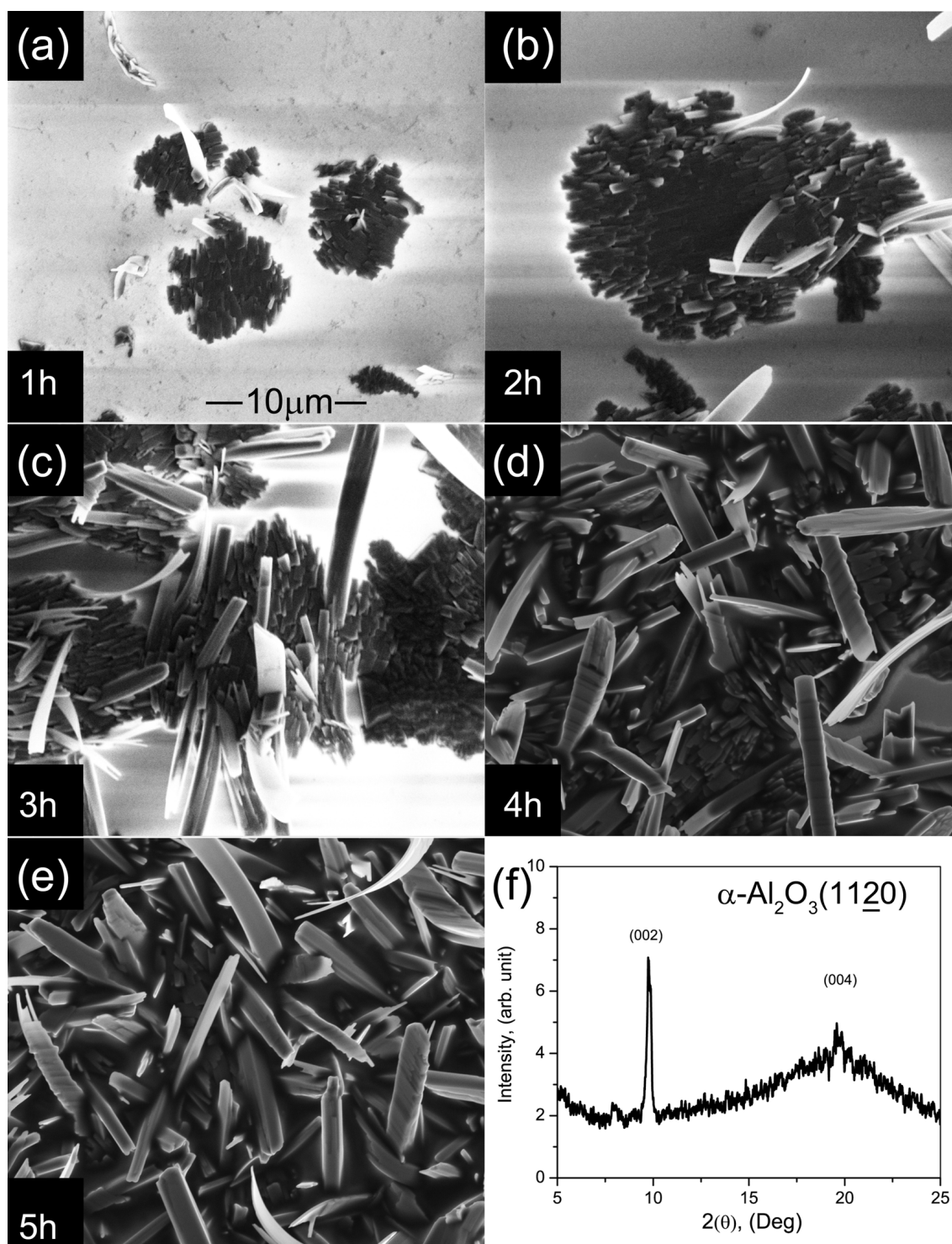


**Figure 5.11:** SEM images of TTF-TCNQ thin films grown on  $\alpha\text{-Al}_2\text{O}_3(11\bar{2}0)$  after (a) 1h deposition, (b) 2h deposition, (c) 3h deposition, (d) 4h deposition and (e) 5h deposition. (f) XRD pattern of the sample. The scale bar in (a) applies to all panels.

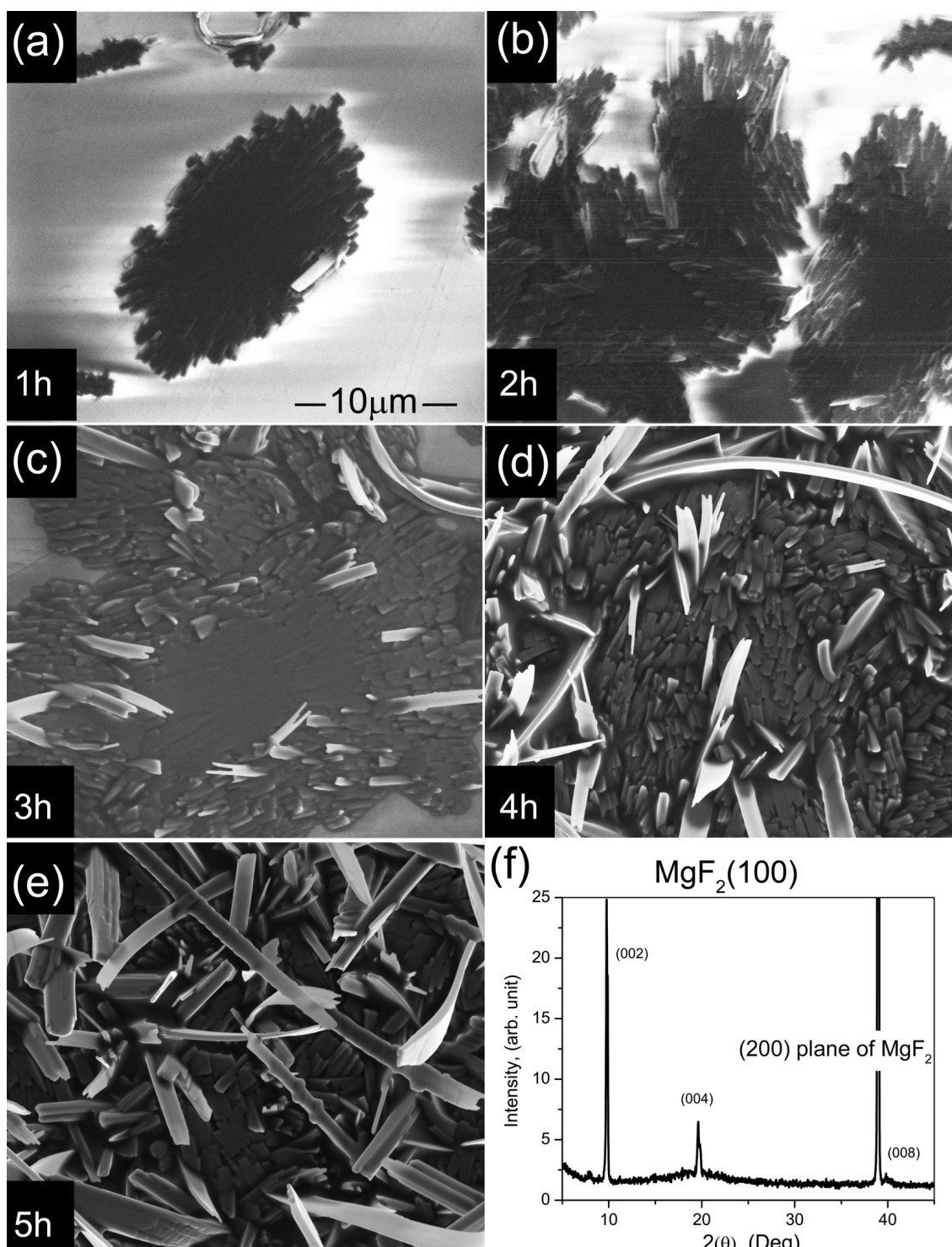


**Figure 5.12:** SEM images of TTF-TCNQ thin films grown on MgF<sub>2</sub>(100) after (a) 1h deposition, (b) 2h deposition, (c) 3h deposition, (d) 4h deposition and (e) 5h deposition. (f) XRD pattern of the sample. The scale bar in (a) applies to all panels.

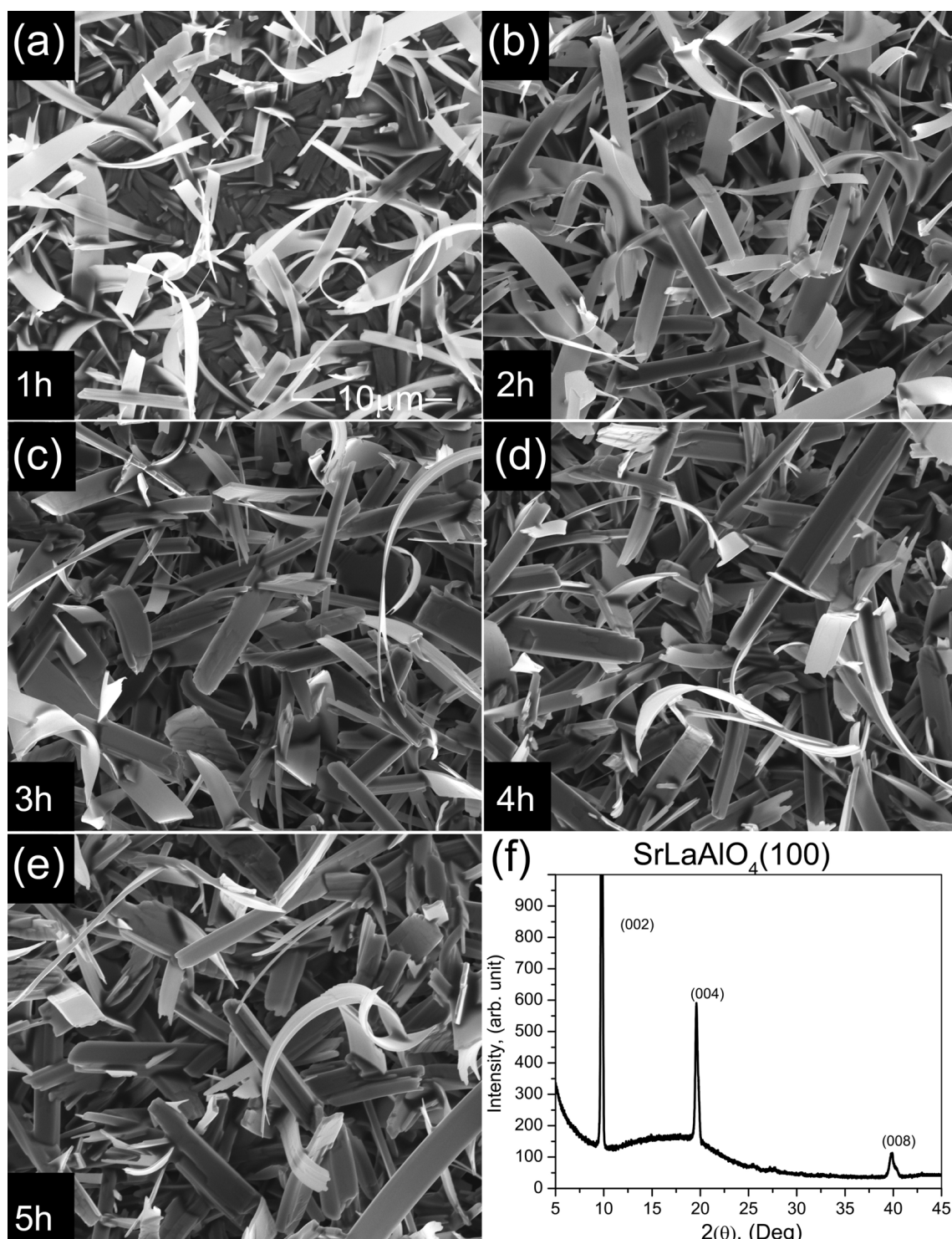


**Figure 5.13:** SEM images of TTF-TCNQ thin films grown on SrLaAlO<sub>4</sub>(100) after (a) 1h deposition, (b) 2h deposition, (c) 3h deposition, (d) 4h deposition and (e) 5h deposition. (f) XRD pattern of the sample. The scale bar in (a) applies to all panels.

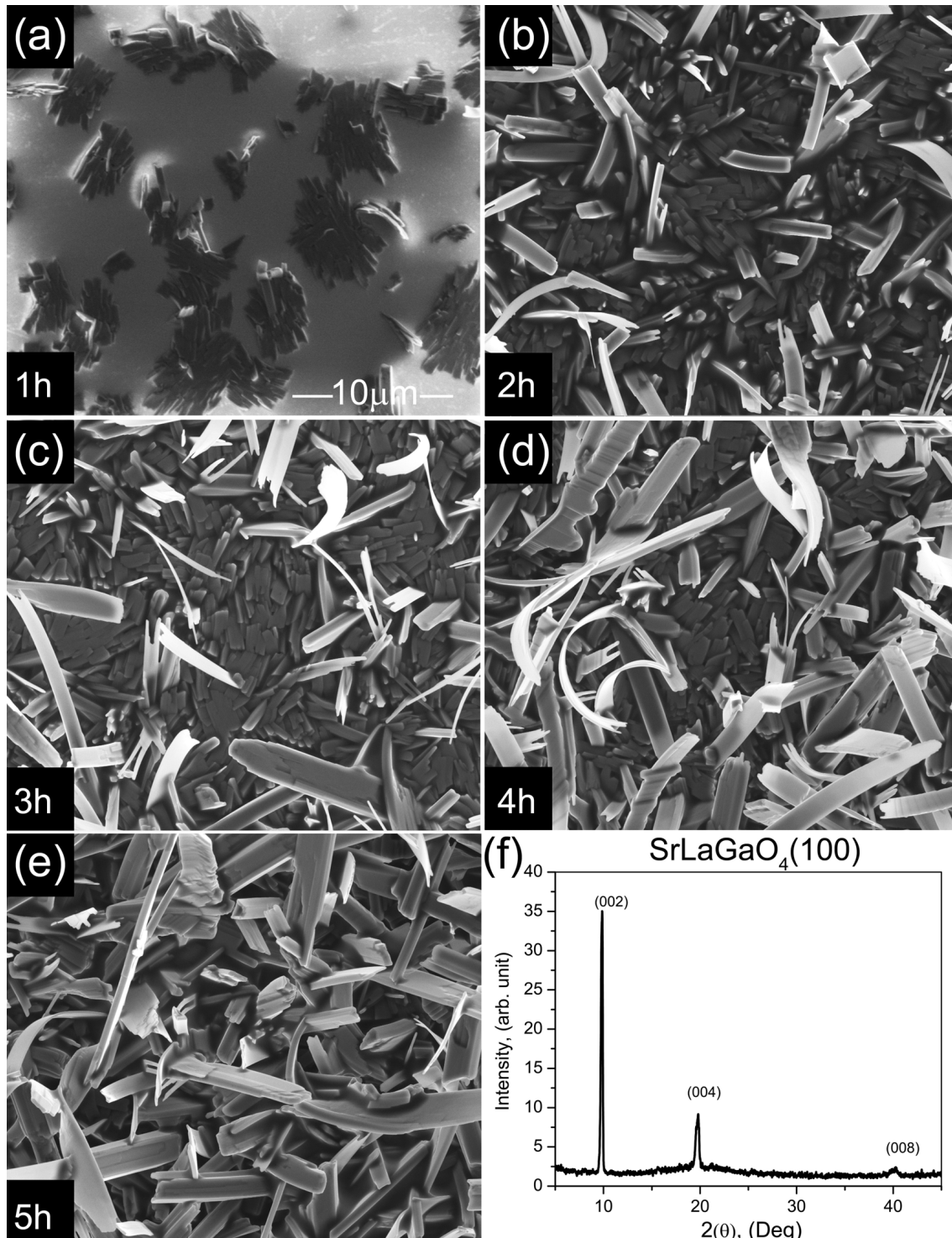


**Figure 5.14:** SEM images of TTF-TCNQ thin films grown on SrLaGaO<sub>4</sub>(100) after (a) 1h deposition, (b) 2h deposition, (c) 3h deposition, (d) 4h deposition and (e) 5h deposition. (f) XRD pattern of the sample. The scale bar in (a) applies to all panels.



thin film morphology was performed for the Si(100)/SiO<sub>2</sub>(285 nm) substrate. Figure 5.15 shows a series of SEM images recorded for TTF-TCNQ thin films grown on Si/SiO<sub>2</sub> with evaporation temperatures of 90 °C, 110 °C, and 130 °C. From Fig. 5.15, it follows that the size of the TTF-TCNQ crystallites varies with the evaporation temperature, such that the higher the evaporation temperature is, the higher the crystallite density becomes. From the FIB cross-sectioning, one concludes that the critical thickness for TTF-TCNQ thin films also depends on the evaporation temperature: it decreases with increasing evaporation temperature. For higher evaporation temperature the growth rate is also higher and the diffusion of the molecules on the substrate surface is affected. The growth mode itself does not depend on the evaporation temperature as follows from Fig. 5.15. The results of the experiments for TTF-TCNQ thin films grown on different substrates are summarized in Tab. 5.1.

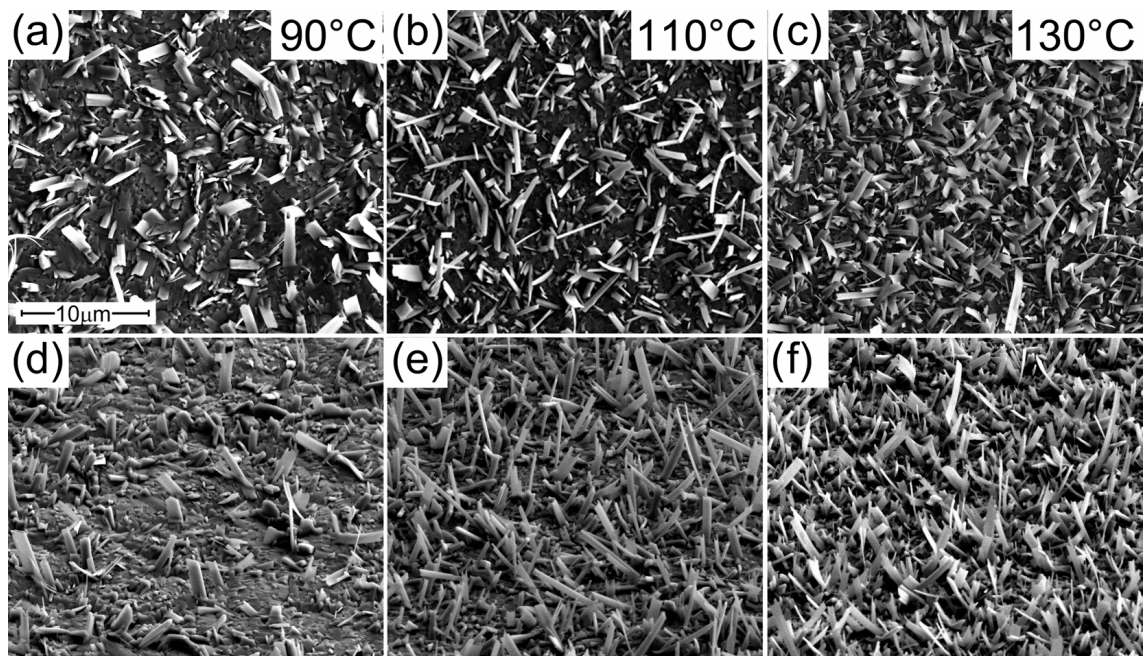


**Figure 5.15:** SEM images of TTF-TCNQ thin films grown on Si(100)/SiO<sub>2</sub> with an effusion cell temperature (a), (d) 90 °C; (b), (e) 110 °C; (c), (f) 130 °C. (a)-(c) normal view and (d)-(f) tilted view with 52 ° tilt angle. The scale bar applies to all panels.

**Table 5.1:** *Different growth modes of TTF-TCNQ thin films observed for the investigated substrates.*

Substrate	Growth type	Example ref.
Si(100)/SiO <sub>2</sub>	Volmer-Weber	[96, 141]
Au(111)	Volmer-Weber	[142]
NaCl(100)	Frank-van der Merwe	[114]
NaCl(110)	Volmer-Weber	–
NaCl(210)	Volmer-Weber	–
SrLaGaO <sub>4</sub> (100)	Volmer-Weber	–
SrLaAlO <sub>4</sub> (100)	Volmer-Weber	–
MgO(100)	Volmer-Weber	–
MgF <sub>2</sub> (001)	Stranski-Krastanov	–
MgF <sub>2</sub> (100)	Volmer-Weber	–
TiO <sub>2</sub> (100)	Volmer-Weber	–
$\alpha$ -Al <sub>2</sub> O <sub>3</sub> (11 $\bar{2}$ 0)	Volmer-Weber	[96]

The X-ray diffraction patterns for all investigated TTF-TCNQ thin films (see Figs. 5.6f, 5.8f-5.14f) shows reflections from the  $(00\ell)$  crystallographic plane of TTF-TCNQ for even numbers of  $\ell$ . The presence of the  $(00\ell)$  reflections in the XRD indicates that the  $(ab)$ -molecular planes of the TTF-TCNQ thin films are parallel to the substrate surface and consequently the stacking direction  $b$  is aligned within the substrate surface (see Fig. 2.2). The  $c^*$ -axis is the axis perpendicular to the  $(ab)$ -plane of TTF-TCNQ. The XRD pattern recorded for a typical TTF-TCNQ thin film grown on MgO(100) is shown in Fig. 5.16. The in-plane orientation is random except for the NaCl(100) case, where two preferred orientations occur.

The performed analysis using X-ray diffraction data, EDX measurements, SEM images and GID measurement shows that one can classify the substrates in three groups each corresponding to one growth mode of TTF-TCNQ thin films, which depends on the substrate material: (1) thin films grown on the NaCl(100) substrate have two preferential orientations of the TTF-TCNQ crystals; (2) thin films grown on MgF<sub>2</sub>(001) and NaCl(210) do not have any preferential orientation of the crystals, although the crystals self-assemble flat on the substrate surface; (3) islands without any pronounced preferential orientation of TTF-TCNQ crystals grow on the MgF<sub>2</sub>(100), MgO(100),  $\alpha$ -Al<sub>2</sub>O<sub>3</sub>(11 $\bar{2}$ 0), Si(100)/SiO<sub>2</sub>(285 nm), NaCl(110), SrLaAlO<sub>4</sub>(100) and on SrLaGaO<sub>4</sub>(100) substrates.

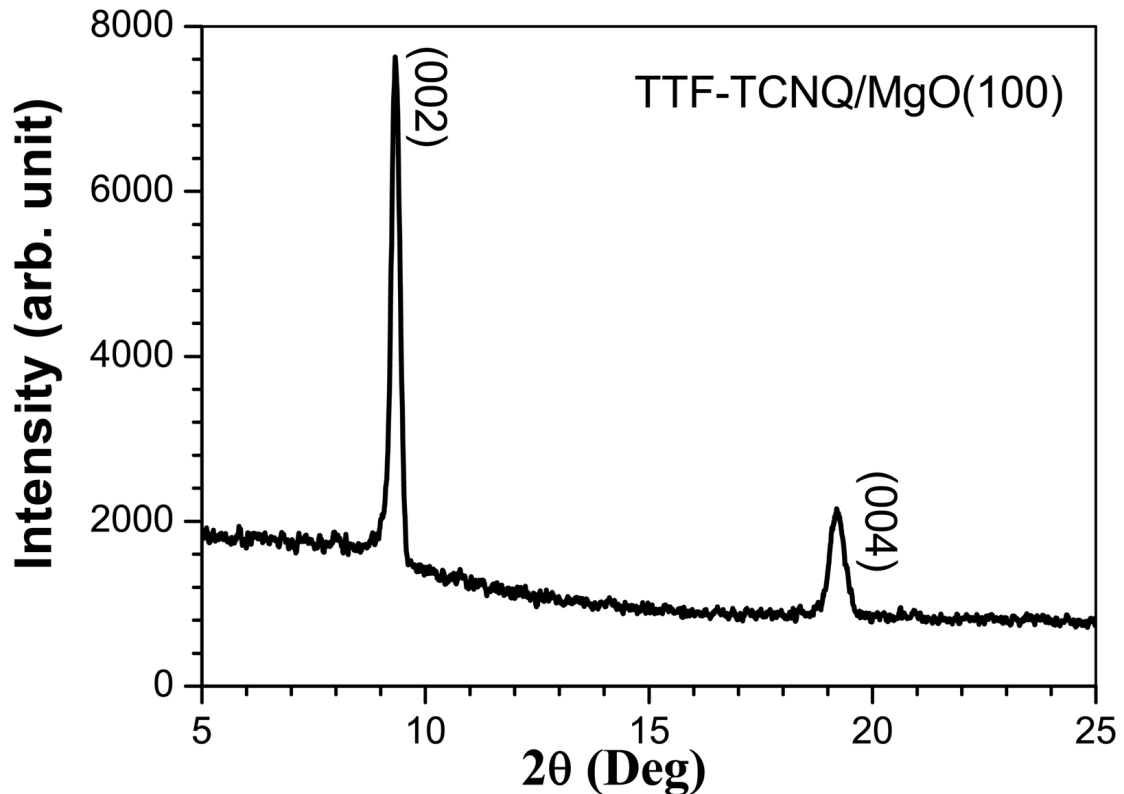


Figure 5.16: X-ray pattern for TTF-TCNQ thin film grown on MgO(100).

### 5.3 Angle-resolved photoelectron spectroscopy of TTF-TCNQ thin films

Angle resolved photoelectron spectroscopy (ARPES) was used to show that the grown TTF-TCNQ thin films exhibit 1D electronic behavior as is the case for TTF-TCNQ single crystals [20]. ARPES can measure the band structure of the sample and also provide insight into the specific electronic states at defined energy. In 1991, by means of ARPES, non-Fermi liquid behavior was shown for 1D metallic systems. A strong suppression of the spectral weight at the Fermi level and no Fermi edge were observed [143].

ARPES measurements were performed in collaboration with Prof. Dr. Martin Aeschlimann (University of Kaiserslautern) on TTF-TCNQ films grown on KCl(100) substrates using physical vapor deposition. The first experiments were performed in Kaiserslautern in the “multi-purpose” OMBD chamber constructed in Frankfurt (see section 3.1.3). Thereupon the effusion cell constructed in Frankfurt was directly

attached to the UHV-system where the ARPES measurements were done by Dr. Indranil Sarkar. The samples were transferred into the ultra high vacuum ARPES chamber from the sample preparation chamber using a transfer arm in a vacuum of  $1 \times 10^{-9}$  mbar. The samples were mounted on a  $^4\text{He}$  flow cryostat. The HeI spectral line with an energy of 21.2 eV was used as excitation source. A 150 mm hemispherical energy analyzer (SPECS Phoibos 150) was used for the ARPES measurements with energy and angular resolution of 40 meV and  $0.03 \text{ \AA}^{-1}$ , respectively.

Figure 5.17 shows the energy dispersive curve obtained by integration of the ARPES measurement over the wave vector  $[-0.26, 0.26] \text{ \AA}^{-1}$ . Because of the two domain structure of TTF-TCNQ films grown on alkali halide substrates, the bands

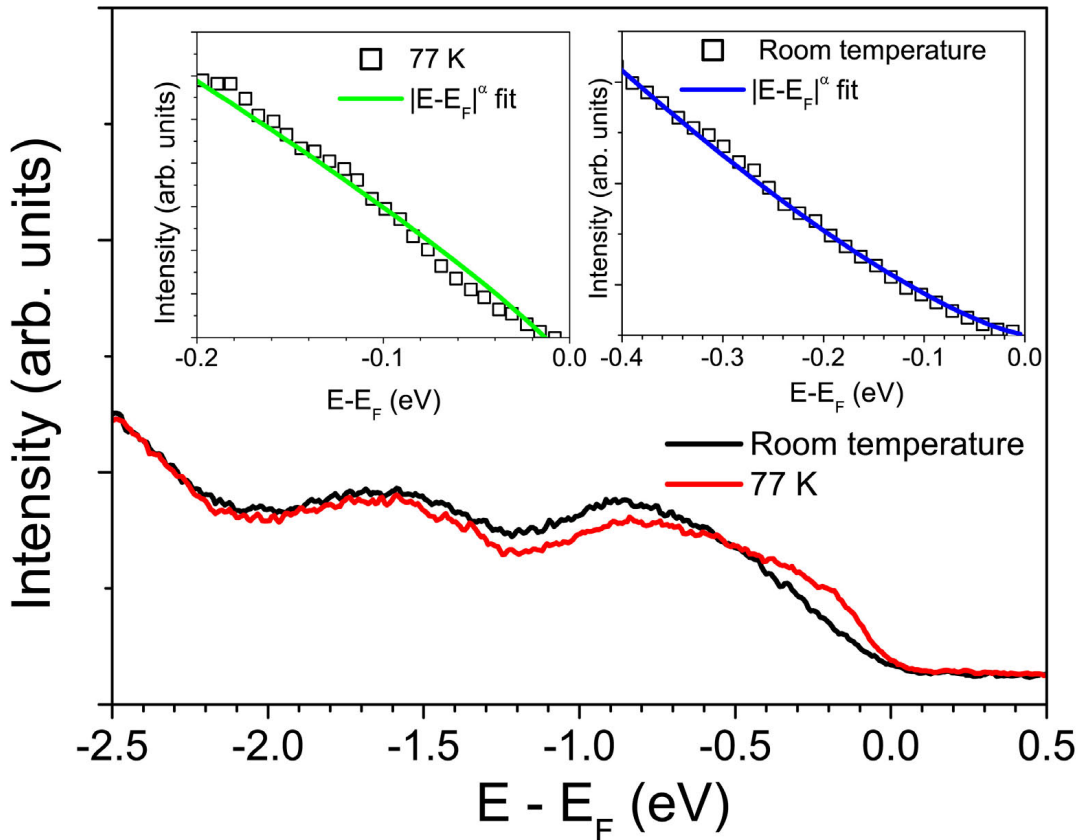


**Figure 5.17:** Integrated energy dispersive curves for TTF-TCNQ thin films measured at room temperature and at 77 K. The insets show the fit of the low energy part by a power law for the curves measured at 77 K and at room temperature.  $\alpha(300 \text{ K}) = 1.2$ .  $\alpha(77 \text{ K}) = 0.85$ .

are mapped simultaneously along the  $a$ -axis ( $\Gamma B$ ) and the  $b$ -axis ( $\Gamma Y$ ) and do not correspond to a single high conductivity  $b$ -axis, but to a superposition of the measurement along  $\Gamma B$  and  $\Gamma Y$ .

The energy dispersive curve measured at room temperature is shown in Fig. 5.17 by a black line. No signature of a Fermi edge is observed and the result clearly deviates from Fermi liquid behavior of typical three-dimensional metals. The absence of a sharp Fermi edge is a well-known characteristic of 1D metals and was already observed for TTF-TCNQ single crystals [144–146]. The energy dispersive curve is shown in the inset to Fig. 5.17 at low binding energies and follows a power law  $|E - E_F|^\alpha$  with  $\alpha=1.2$ . A power law behavior is expected in the case of a one-dimensional metal. Figure 5.17 (red line) shows the energy dispersive curve of the TTF-TCNQ film measured at 77 K. With decreasing temperature, a large redistribution of spectral weight near the Fermi energy is observed, enhancing the spectral weight near  $E_F$  (compare result in Fig. 5.17 for room temperature and 77 K). As the temperature is reduced, the low energy spectrum no longer obeys the power law  $|E - E_F|^\alpha$ . The observed spectral weight redistribution is much larger than the change in thermal energy  $k_B T$  due to variations in temperature. A similar unusual spectral weight transfer has been observed earlier in TTF-TCNQ single crystals [145,146] and is attributed to strong electronic correlations due to Coulomb interaction and can be described by the single-band 1D Hubbard model.

## 5.4 Strain in TTF-TCNQ thin films

The growth conditions and morphology are very different for TTF-TCNQ single crystals and thin films. This leads to new physical effects in thin films. For example, due to the inhomogeneous structure and non-equilibrium growth, the TTF-TCNQ thin films (see e.g. Fig. 5.12) have an enhanced defect density. The defects can be classified into three groups: (i) point defects, i.e. vacancies, impurities etc.; (ii) linear defects, i.e. edge and screw dislocations ; (iii) planar defects, like stacking faults, grain boundaries etc. [147]. Due to the reciprocity between crystal and reciprocal space there is a connection between the type of defects and the strain which they cause. Different types of strain, on the other hand, cause different types of scattering contribution in XRD. For point defects, diffusive Huang scattering takes place [148]. Huang scattering describes the distortion scattering caused by the long-range part of the displacement field produced by point defects and the diffraction effects for this scattering mechanism lie far from the Bragg reflections. Linear defects produce extended strain fields, therefore, the diffraction effects they make are concentrated

around the Bragg reflections and result in diffraction peak broadening, which is studied by line profile analysis. Planar defects are homogenous in the crystal (film), therefore, they cause a shift of the Bragg reflections with regard to non-disturbed material. The defects in thin films can be divided into two groups, depending on the effects they produce: the first one causes Bragg peak broadening and the second one causes Bragg peak shifts.

Two effects caused by the defects in TTF-TCNQ thin films are considered here. Bragg peak shifts are readily deduced from the X-ray diffraction patterns, while the peak broadening is extracted from a peak profile analysis according to Williamson and Hall [75, 149].

The X-ray diffraction measurements of TTF-TCNQ thin films show in all cases that the  $(00\ell)$  crystallographic planes of TTF-TCNQ are aligned with the substrate surface, where  $\ell$  is an even number (see Fig. 5.16). The reflection corresponding to  $(002)$ ,  $(004)$  and  $(008)$  are present in almost all X-ray patterns of TTF-TCNQ thin films. The intensity of the peaks varies with the quality of the films. The best one is observed for TTF-TCNQ thin films grown on NaCl(100) and MgF<sub>2</sub>(001) due to the planar structure of the films in these cases, which results in a higher peak intensity. The Bragg peak corresponding to the  $(002)$  crystallographic plane is shifted non-systematically for different samples. This happens due to the difficulty in alignment of the substrate with the TTF-TCNQ thin film in the diffractometer. A laser alignment, as routinely used in our lab, allows the sample to be positioned most accurately, but is not possible to use for TTF-TCNQ films, because the rough surface morphology of most TTF-TCNQ thin films prevent specular reflection. Accordingly, the macrostrains in TTF-TCNQ thin films cannot be defined properly and only microstrain is left to be deduced from the X-ray diffraction data.

Microstrain is produced by linear defects, such as dislocations, and causes a Bragg peak broadening. Strain fields introduced by dislocations may extend over many hundreds of unit cells of the crystal. As follows from the Bragg equation Eq. (3.8), if the interplanar spacing is subject to a variation, the diffraction angle is not limited to a fixed value, therefore, the Bragg peak is getting broadened. The microscopic strain expands on the length scale which is smaller than the inverse linear attenuation coefficient  $1/\mu$  of the X-ray beam in the material, which illuminate the sample [75]. In the case of TTF-TCNQ the attenuation coefficient can be calculated by using Eq. (5.1).

$$\mu/\rho = \left( \sum x_i A_i \mu_i / \rho_i \right) / \sum x_i A_i, \quad (5.1)$$

where  $x_i$  is an atomic fraction of each atom type,  $A_i$  is the mass of each atom and

$\mu_i/\rho_i$  is the mass attenuation coefficient of each atom type. The inverse attenuation coefficient gives an average thickness of the layer to be irradiated. The data for the mass absorption coefficients for the atoms contained in TTF-TCNQ ( $C_{18}H_8N_4S_4$ ) are given in Tab. 5.2. From Eq. (5.1) and the density for TTF-TCNQ ( $1.62 \text{ g/cm}^3$  [38]) one obtains the value of the absorption coefficient  $\mu = 1/186 \text{ } \mu\text{m}^{-1}$ . From this estimate it follows that the length scale of the microscopic strain in the case of organic materials is smaller than the total volume irradiated by the X-ray beam. This allows the use of the line profile analysis technique here [75].

**Table 5.2:** Mass attenuation coefficients  $\mu/\rho$  ( $\text{cm}^2/\text{g}$ ) for atoms contained in TTF-TCNQ [150].

X-ray energy	H	C	N	S
$K_\alpha$ , $E=8.04 \text{ keV}$	0.3914	4.576	7.562	94.65

X-ray diffraction line profile analysis is a powerful characterization technique to obtain microstructural changes of the thin films [75, 147]. Usually it is applied to inorganic materials. The application of the line profile analysis to organic thin films is a complicated task. The main difficulty is the lack of sufficient diffraction peak intensity. In the case of organic thin films, the diffraction peaks are obtained only for the large  $d$ -values, corresponding to small  $2\theta$  angles. The small mass attenuation coefficients of the elements in organic materials (see Tab. 5.2) result in a low diffracted intensity. For comparison, the mass attenuation coefficient for cobalt is  $3.248 \times 10^2 \text{ cm}^2/\text{g}$ . Also the method is not accurate enough for materials with large unit cell [151]. The structure of the TTF-TCNQ thin films is inhomogeneous and, except for the films grown on NaCl(100), the films do not grow in uniform closed layers. Therefore, the line profile analysis can only be used for TTF-TCNQ thin films grown on NaCl(100). The method for the calculation of microstrains in thin films is discussed below and the numerical results for TTF-TCNQ films are given in section 5.6. Here it is important to note that, knowing the strains for the TTF-TCNQ thin films and the Peierls transition temperature for the strained films, one can analyze how strain influences the Peierls transition.

The main parameter in line profile analysis is called the integral breadth:

$$\beta = \frac{1}{I_0} \int_{-\infty}^{\infty} I(2\theta) d(2\theta), \quad (5.2)$$

where  $\beta$  is the modified width of the diffraction peak, which is calculated for a

rectangular box of the same integral intensity as the Bragg peak with the height  $I_0$  and width  $\beta$ , as is schematically displayed in the inset to Fig. 5.18. There are many possible mathematical functions which can be used to fit the Bragg peaks. The commonly employed functions for modeling of the integral breadth are compiled in Tab. 5.3. All functions given in Tab. 5.3 fit Bragg peaks quite accurately, although the pure Gauss and Cauchy functions have larger errors compared to the mixed functions [75]. Therefore, the mixed profile functions, like Pearson and Pseudo Voigt, are preferable in profile analysis.

**Table 5.3:** *Integral breadth for the model functions in line profile analysis.  $2w$  is the full width at half maximum of the peak,  $\Gamma(m)$  is the gamma function,  $A=0.9039645$ ,  $B=0.7699548$ ,  $C=1.364216$ ,  $D=1.136195$  and  $E=2(\ln 2\pi)^{\frac{1}{2}}=0.9394372$  are constants,  $m$  is the adjustment parameter in the Pearson function. The parameter  $\eta$  is the amount of the Cauchy contribution in the Pseudo Voigt function, which represents a mixture of Gauss and Cauchy profiles.  $k = \frac{\beta_C}{\sqrt{\pi}\beta_G}$  is the scaling factor between the Cauchy and Gauss profiles.*

Model function	Integral breadth
Cauchy	$\pi w$
Gauss	$\sqrt{\frac{\pi}{\ln 2w}}$
Pearson	$\frac{\pi 2^{2(1-m)} \Gamma(2m-1)}{(2^{\frac{1}{m}} - 1) \Gamma^2(m)} w$
Voigt	$\frac{2(1 + Ck + Dk^2)}{E(1 + Ak + Bk^2)} w$
Pseudo-Voigt	$(\eta\pi + (1 - \eta)\sqrt{\pi \ln 2})w$

The results of the fit by the Pearson function look most accurate and this function was used in the thesis for line profile analysis to fit the data of X-ray diffraction measurements on TTF-TCNQ thin films. The Project1 X-ray analysis program was used for the X-ray analysis [152]. The striped sample of TTF-TCNQ grown on NaCl(100) was used (see Fig. 5.6). The data for the whole sample was acquired and deconvoluted for each stripe under the assumption that a thicker film gives Bragg peaks of higher intensity. The result of the fit of the (002) peak for the striped sample is shown in Fig. 5.18. The integrated breadth is deduced from the fitting of the peak. Knowing the integrated breadth one can find the relative strain ( $K_D \varepsilon_{rms}$ ) as follows [153]:



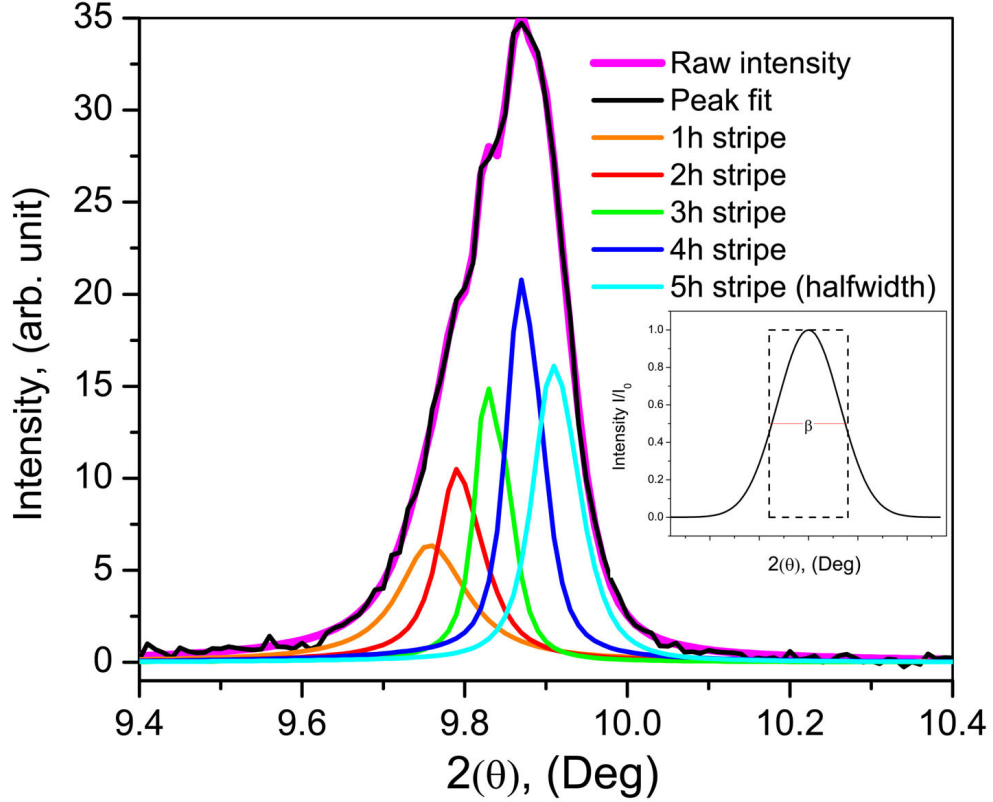


**Figure 5.18:** Bragg reflection for the (002) crystallographic plane of the striped TTF-TCNQ thin film grown on NaCl(100) (see Fig. 5.6) fitted by the Pearson function (see Tab. 5.3) for each stripe separately. The width of the stripe corresponding to 5h deposition time equals to a half width of other stripes. The inset illustrates the principle of the integrated breadth calculation.

$$\beta \frac{\cos \theta}{\lambda} = \frac{1}{\langle D \rangle} + K_D \varepsilon_{rms} \frac{2 \sin \theta}{\lambda}, \quad (5.3)$$

where  $\langle D \rangle$  is the average crystallite size,  $K_D$  is a scaling factor depending on the nature of the microstructural changes [75].  $\varepsilon_{rms} = \sqrt{\langle \varepsilon^2 \rangle}$  with  $\varepsilon = \Delta d/d_0$ ,  $\Delta d$  is the variation of interplanar spacing and  $d_0$  is the undistorted spacing. If the X-ray pattern has more than two peaks, then the plot of the function  $\beta \cos \theta/\lambda$  versus  $2 \sin \theta/\lambda$  can be parameterized and used to define the  $K_D \varepsilon_{rms}$  being the slope of the linear function.

The relative microstrain in TTF-TCNQ thin films is calculated in section 5.6, where the dependence of the Peierls transition temperature on the microstrain in TTF-TCNQ thin films grown on NaCl(100) is discussed.

## 5.5 Influence of substrate material and film thickness on electrical conductivity of TTF-TCNQ thin films

As a next step in the characterization of TTF-TCNQ thin films the electrical conductivity was measured. The conductivity vs temperature  $\sigma(T)$  measurements were performed in a  $^4\text{He}$  cryostat from room temperature down to 4.2 K. The two- and four-probe technique was used with constant applied voltage of 0.1 V corresponding to an electric field in the thin films that did not exceed 0.2 V/cm.

At first room temperature conductivity measurements of the TTF-TCNQ thin films with striped geometry were performed. The scheme of the sample connection is presented in Fig. 3.7 and the detailed description is given in section 3.3. Already from electrical conductivity measurements at room temperature it is apparent that the growth mode of the TTF-TCNQ thin films exerts a strong influence on their electrical properties. The minimal  $\sigma_{min}$  and the maximal  $\sigma_{max}$  values of the room temperature conductivity measured for various TTF-TCNQ thin films obtained for the striped samples are given in Tab. 5.4.

**Table 5.4:** *The minimal ( $\sigma_{min}$ ) and the maximal ( $\sigma_{max}$ ) values of the room temperature electrical conductivity  $\sigma$  recorded for TTF-TCNQ thin films grown on different substrates. 5 different samples were measured for each substrate. The reference conductivity of TTF-TCNQ for single crystals is  $\sigma_b \approx 500 (\Omega \text{ cm})^{-1}$ ,  $\sigma_a \approx 3 (\Omega \text{ cm})^{-1}$  [5].*

Substrate	$\sigma_{min}, (\Omega \text{ cm})^{-1}$	$\sigma_{max}, (\Omega \text{ cm})^{-1}$
NaCl(100)	1.32	30
SrLaGaO <sub>4</sub> (100)	0.08	0.35
SrLaAlO <sub>4</sub> (100)	0.02	0.03
MgO(100)	0.48	1
MgF <sub>2</sub> (001)	3.19	9.68
MgF <sub>2</sub> (100)	0.58	0.86
$\alpha$ -Al <sub>2</sub> O <sub>3</sub> (11 $\bar{2}$ 0)	0.01	2.4

As discussed in section 5.2, the substrate influences the film morphology, which in turn determines the electrical conductivity. The maximal conductivity is observed for TTF-TCNQ thin films grown on NaCl(100) and MgF<sub>2</sub>(001). This is mainly

due to the better quality of the TTF-TCNQ films having enhanced ordering of the crystallites. Quasi-two-dimensional TTF-TCNQ thin films grown on NaCl(100) (see Fig. 5.3) shows higher conductivity in comparison with the disordered structures formed on other substrates, because grain boundaries and weak inter-grain coupling reduces the conductivity. Nevertheless, the conductivity for all studied TTF-TCNQ thin films  $\sigma$  is in all cases significantly smaller than the conductivity of the TTF-TCNQ single crystals,  $\sigma_b \approx 500 (\Omega\text{cm})^{-1}$ . The existence of grain boundaries hinders the metallic behavior and promotes the semiconductor-like conductivity. This is also true for films on NaCl(100) because of the two-domain structure. This results in a thermo-activated behavior of the electrical conductivity.

The influence of the film thickness on the room temperature conductivity for thin films grown on NaCl(100) was studied in more detail. It was found that the room temperature conductivity depends non-monotonously on film thickness, as is presented in Fig. 5.19. The room temperature conductivity shows a maximal

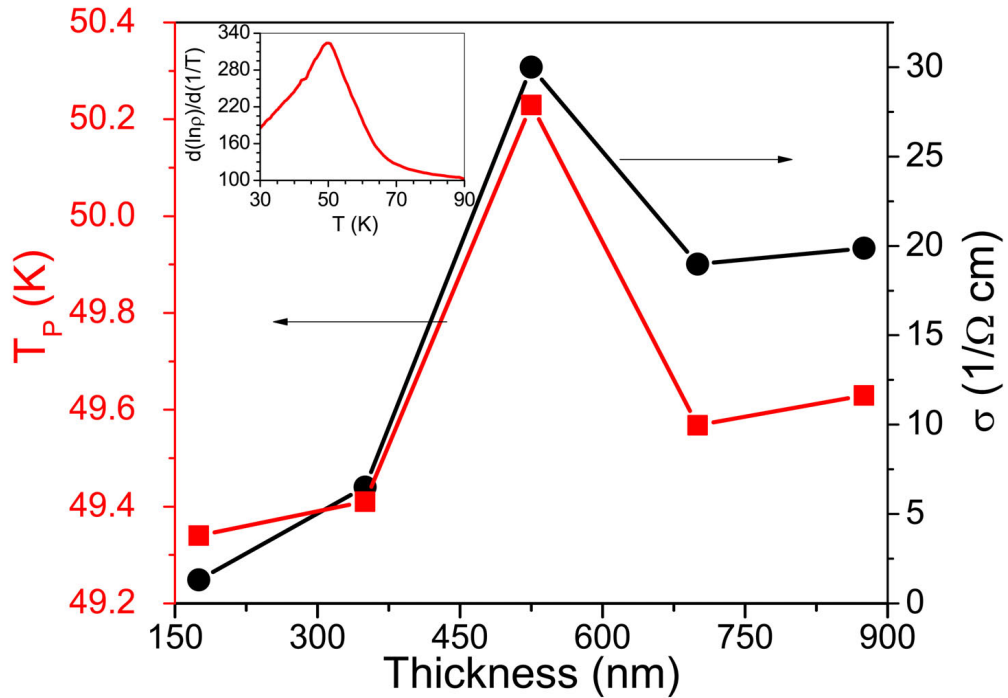


**Figure 5.19:** Electrical conductivity (circles) and the Peierls transition temperature (squares) measured for TTF-TCNQ thin films with different thicknesses grown on the NaCl(100). The inset shows the dependence of the logarithmic derivative of the resistivity on temperature, Eq. (5.4), for the films grown for 4 hours.

value at a thickness of about 525 nm. The likely reason for this behavior can be

deduced from AFM and SEM measurements (see Figs. 5.6-5.7). The increase of the thin film thickness eventually leads to the coalescence of TTF-TCNQ islands on the substrate surface, enhancing the conductivity. When the coalescence occurs the film thickness is about 500 nm and the electrical conductivity is maximal. A further increase of the film thickness results in the decrease of the conductivity because the growth mode is changed into a disordered growth that yields three-dimensional bar-shaped crystallites partly pointing out of the surface. A similar dependence was reported in [97] for TTF-TCNQ thin films grown on alkali halide and glass substrates. Although the non-monotonic dependence of the conductivity of TTF-TCNQ films on thickness was also observed for all other substrates investigated in this work, a reliable thickness measurement is severely hindered or even impossible due to the irregular and very pronounced three-dimensional growth already in early stages of film growth.

## 5.6 Dependence of the Peierls transition temperature on the defects in TTF-TCNQ thin films

The Peierls transition temperature  $T_P$  can be extracted from the temperature dependence of the electrical conductivity  $\sigma(T)$ . For illustrative purposes, the inset to Fig. 5.19 shows the logarithmic derivative of the resistivity on temperature for one chosen thin film. The Peierls transition temperature corresponds to the temperature where the function

$$\frac{d(\ln \rho(T))}{d(1/T)} = \frac{d(\ln 1/\sigma(T))}{d(1/T)} \sim \frac{d \ln(1/I(U = const))}{d(1/T)}, \quad (5.4)$$

exhibits a maximum [84]. Here  $\rho(T)$  is the resistivity of the thin film. For analysis, the data taken on the heating branch of the full thermal cycle were used. The heating rate was  $\sim 1$  K/min.

The appearance of the Peierls transition also becomes apparent from the current-voltage characteristics for TTF-TCNQ thin films measured at low temperature. Several  $I(U)$  curves for TTF-TCNQ thin films grown on NaCl(100) for 1 hour measured at different temperatures are collected in Fig. 5.20a. From the performed analysis it follows that, below a certain temperature, a non-linear behavior of the  $I(U)$  curves, deviating from Ohm's law, starts to develop. This observation is in good agreement with the results for TTF-TCNQ single crystals. From the  $I(U)$  curves, a threshold electric field was deduced and summarized in Fig. 5.20b for TTF-TCNQ thin films grown on NaCl(100) and on Si(100)/SiO<sub>2</sub> substrates. One can see that at

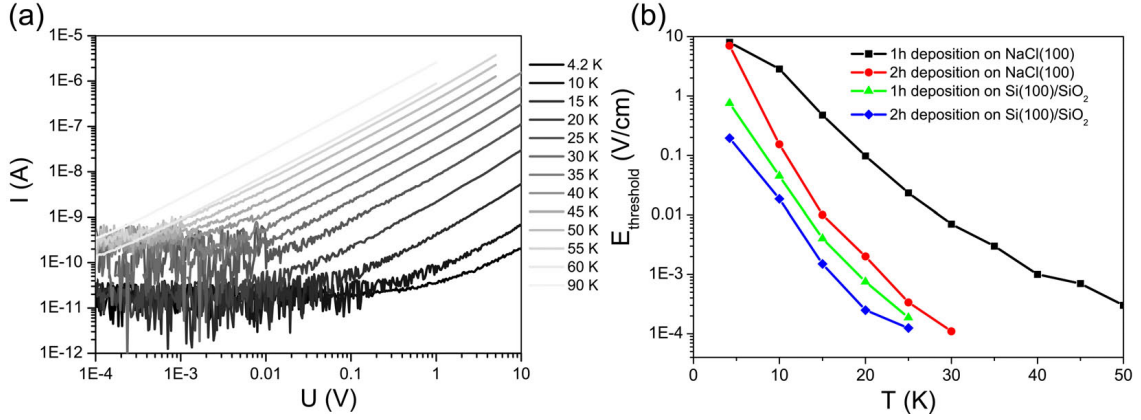


**Figure 5.20:** (a) Current-voltage characteristics for a TTF-TCNQ thin film grown on NaCl(100) after 1 hour growth. (b) Threshold electric field for TTF-TCNQ thin films grown on NaCl(100) and on Si(100)/SiO<sub>2</sub> after 1 and 2 hours growth.

a temperature less than 50 K, the threshold field increases, which is a sign of the depinning of CDWs in TTF-TCNQ, which start to move under the applied voltage at temperatures lower than the Peierls transition temperature.

It is observed that the Peierls transition temperature for all TTF-TCNQ thin films grown at an evaporation temperature of 110°C is close to 50 K. Note that no systematic dependence of the Peierls transition temperature on the substrate material and thickness could be observed. Films grown on NaCl(100) substrate are an exception to this rule and will be discussed separately. This observation can be qualitatively explained by the relatively weak forces acting between the substrate and the TTF-TCNQ thin films. Indeed, exempting the NaCl(100) substrate, the forces acting between the TTF-TCNQ thin film and the substrate are mainly van der Waals in nature leading to a three-dimensional Volmer-Weber growth mode [69]. Due to three-dimensional Volmer-Weber growth, the cooling of the sample does not induce tensile biaxial strain in the thin film, and no significant influence of the substrate material on the Peierls transition temperature is expected.

The binding between the NaCl(100) substrate and the TTF-TCNQ thin film has an ionic component. Therefore, an influence of the thin film thickness on the Peierls transition temperature is likely to occur. With increase of the thin film thickness, the interaction of the growing layers with the substrate weakens. The thicker the film, the more dislocations nucleate to compensate for the lattice misfit. At some critical thickness, the gained energy is enough to cross the Peierls barrier and the lattice constants of the film relax to their bulk value (see e.g. [154] and references therein). This critical thickness for TTF-TCNQ thin films in the experiment is

presumably about 525 nm including the TCNQ wetting layer. The dependence of the Peierls transition temperature and electrical conductivity on TTF-TCNQ film thickness grown on NaCl(100) are shown in Fig. 5.19. The dependence of the electrical conductivity on the film thickness is followed by the dependence of the Peierls transition temperature on thickness. This observation can be explained by a correlation between the defect density and the Peierls transition temperature. As known for TTF-TCNQ single crystals an increase of the defect density leads to a decrease of the Peierls transition temperature [125]. Here, the interaction of the thin film with the substrate can induce defects in the film. The inverse conductivity can be used as a measure of the defect density [155]. Figure 5.19 shows that the Peierls transition temperature increases with increasing electrical conductivity (or, equivalently, decreasing defect density) being in agreement with the result observed for TTF-TCNQ single crystals [125].

An indicator of the defect presence is the formation of defect-induced microstrain in the films which can be deduced from a line profile analysis of the X-ray diffraction patterns for films grown on NaCl(100). The detailed analysis is presented in section 5.4. The analysis provides  $K_D \varepsilon_{rms}$ , where  $\varepsilon_{rms}$  is the root mean square microstrain in the films and  $K_D$  is a scaling factor depending on the nature of the microstructural changes [75]. The result of the line profile analysis is shown in Fig. 5.21.

As follows from Fig. 5.21, thinner films experience a larger microstrain and, therefore, possess more defects, presumably because the influence of the substrate increases as the thickness of the thin film decreases. The Peierls transition temperature also increases as the strain decreases (see Fig. 5.21) for thin films with a thickness up to 525 nm, supporting the hypothesis that the defects have a critical impact on this transition. The increase of the microstrain in the case of the TTF-TCNQ film with thickness of 700 nm as compared to the film with thickness of 525 nm is caused by the interplay of two effects: a decrease of the microstrain due to the relaxation of the film by dislocation formation and an increase of strain caused by the increasingly disordered film microstructure (see Fig. 5.6).

Figure 5.22 shows the normalized distribution of the Peierls transition temperature. The presented statistic was accumulated for 40 different samples grown at varied growth conditions and having different film thicknesses. The Peierls transition temperature exhibits a pronounced maximum at  $\sim 50$  K, which is smaller than the one reported for single crystals at 54 K [3, 4].

It is worth noting that if one considers thin films of the blue-bronze ( $\text{Rb}_{0.30}\text{MoO}_3$ ) which also exhibit charge density waves, the Peierls transition temperature for this

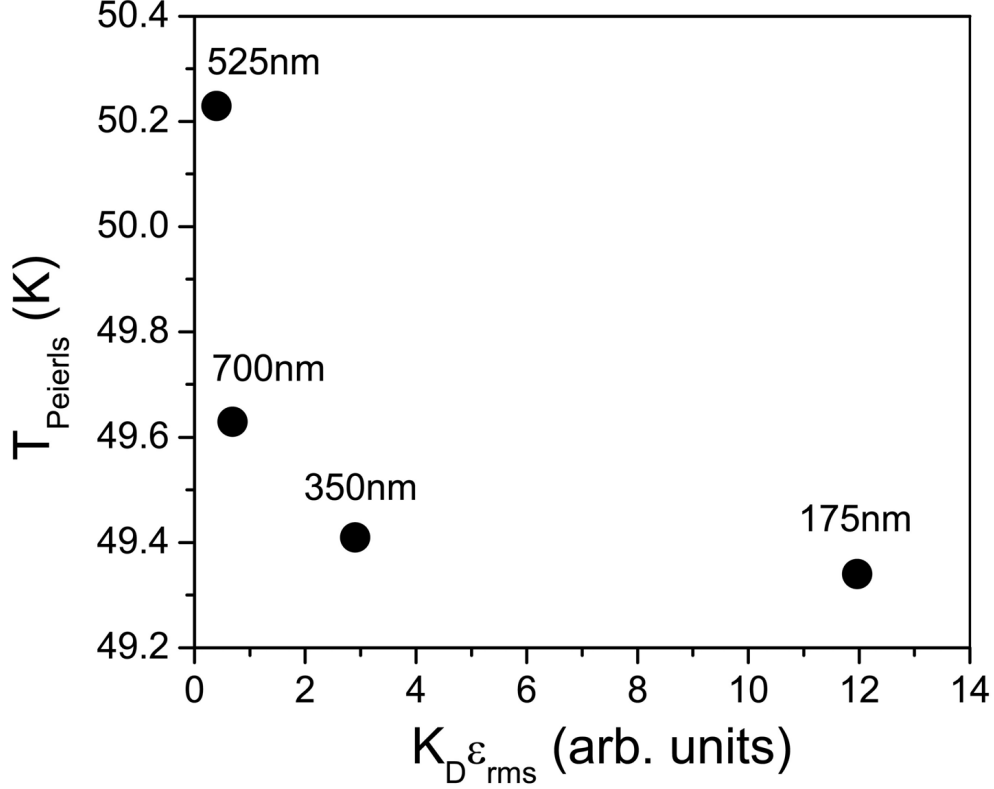


**Figure 5.21:** *Dependence of the Peierls transition temperature on the root mean square microstrain in TTF-TCNQ thin films, extracted from a line profile analysis (see sections 5.4). The film thicknesses are indicated.*

material is also shifted towards lower values as compared to single crystals [156]. Therefore, it is suggested that the shift observed here can be ascribed to the presence of defects in the TTF-TCNQ thin films.

To estimate the defect concentration from the Peierls transition temperature shift, the microscopic calculation approach introduced in [157, 158] was used. The decrease of the Peierls transition temperature due to defects obeys the following relation:

$$\ln \left( \frac{T_{P0}}{T_P} \right) = \Psi \left( \frac{1}{2} + \frac{\hbar}{2\pi k_B \tau T_P} \right) - \Psi \left( \frac{1}{2} \right), \quad (5.5)$$

where  $T_{P0}$  and  $T_P$  are the transition temperatures in the absence of defects and with defects, respectively.  $k_B$  is the Boltzmann constant,  $\hbar$  is the reduced Planck constant.  $\Psi(x)$  is the digamma function, defined as the logarithmic derivative of the gamma function,  $\tau$  is the scattering time due to the presence of defects.  $\tau$  can be

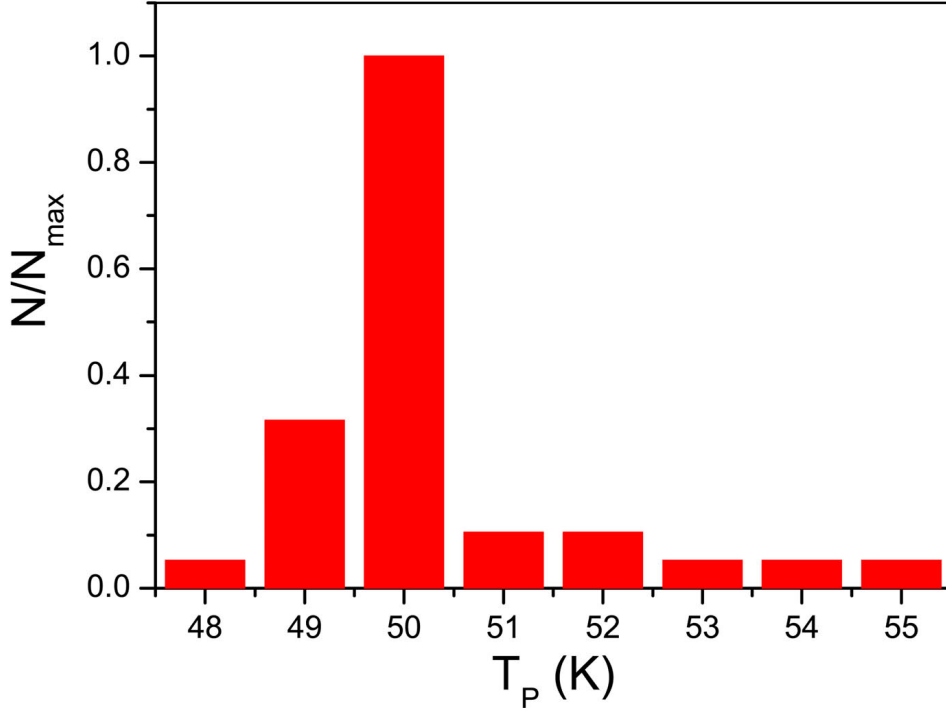


**Figure 5.22:** Normalized distribution of the Peierls transition temperature of different TTF-TCNQ thin films grown at different conditions.  $N_{max}$  is the number of samples for which the distribution has a maximum. The total number of investigated TTF-TCNQ samples is 40.

estimated as

$$l = \tau v_F. \quad (5.6)$$

Here  $l$  is the average distance between the defects and  $v_F$  is the Fermi velocity. From Eq. (5.5) for  $T_{P0}=54$  K and  $T_P=50$  K one obtains  $\tau = 1.52 \times 10^{-12}$  s. The Fermi velocity for TTF-TCNQ is  $\sim 1.82 \times 10^7$  cm/s [159]. Using Eq. (5.6) one obtains  $l \approx 2.7 \times 10^{-5}$  cm which corresponds to 0.14 % defect concentration. This can be compared with the single crystal analysis performed in [125] for different defect concentrations induced by deuteron irradiation of the sample: a decrease of the Peierls transition temperature of 4 K, as observed in the present experiments, corresponds to a defects concentration of about 0.1...1%. This agrees favorably with the results of the analysis presented here. The uncertainty in defect concentration for single crystal stems from the uncertainty in converting the deuteron flux into induced defect concentration, as detailed in [125].



As mentioned above, the irradiation defects cause a shift of the Peierls transition temperature in TTF-TCNQ single crystals. It was therefore indicated to study how the irradiation of TTF-TCNQ thin films by electrons influences the phase transition and compare the results with the results for single crystals. In order to investigate the influence of the electron irradiation on the transport properties of TTF-TCNQ thin films, the following experiment was performed on a thin film with a thickness of about 450 nm grown on NaCl(100). After the growth, the sample was divided into two parts, one was irradiated by the electron beam in the SEM with an operating current of 9.5 nA and a voltage of 30 kV. The area of the irradiated surface was 2.5 mm $\times$ 2.5 mm. The irradiation dose was 17.3 C/m<sup>2</sup> corresponding to 1.4 GGy. The second part of the sample was not irradiated. During the irradiation process the electrical conductivity of the thin film was measured. In the course of the electron beam irradiation, the conductivity decreased linearly as function of time which allows to speculate that the number of defects was increasing linearly (see Fig. 5.23a).

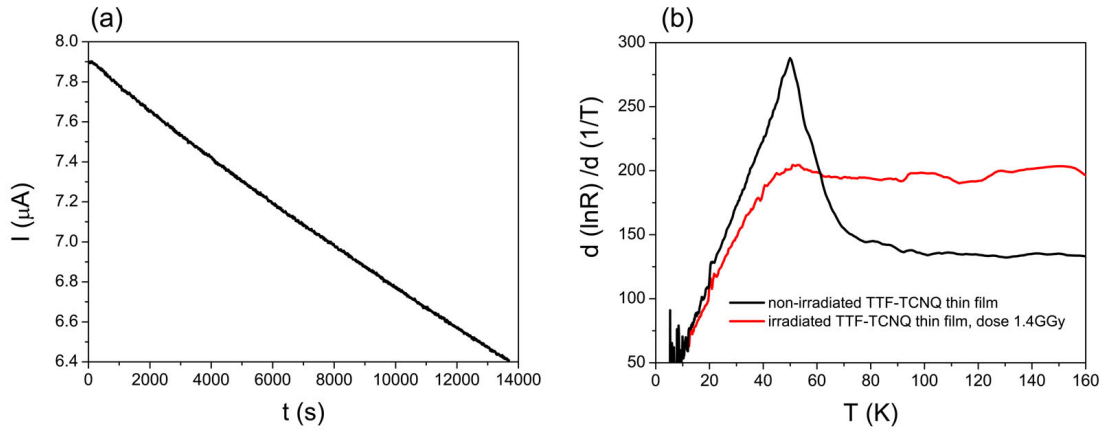


**Figure 5.23:** (a) The change of the electrical current measured at fixed bias voltage in a TTF-TCNQ thin film as function of time of irradiation. (b) The Peierls transition for the non-irradiated and irradiated TTF-TCNQ thin film. The irradiation dose was 1.4 GGy.

After the irradiation, the sample was transferred into the cryostat for temperature dependent conductivity measurements. The temperature dependence of logarithmic derivative of the resistance for the non-irradiated and the irradiated TTF-TCNQ thin film is shown in Fig. 5.23b. The logarithmic derivative of the resistance of the non-irradiated TTF-TCNQ thin film (curve 1) demonstrates a sharp peak at the Peierls transition and thermo-activated behavior at temperatures above the

phase transition. For the irradiated films, no such peak occurs (curve 2). However, the irradiated film still shows Arrhenius behavior for temperatures above 50 K. The Peierls transition temperature is indicated by a slope change in the logarithmic derivative, whereas the sharp maximum, typical for non-irradiated TTF-TCNQ thin films, is suppressed.

## 5.7 Summary

The preferential growth of TTF-TCNQ thin films for various substrate materials and crystallographic orientations was investigated. The morphology of the thin films was studied for different film thicknesses. It was shown that for some critical thickness, the morphology of the TTF-TCNQ films changes from two-dimensional into a three-dimensional structure when grown on NaCl(100) and MgF<sub>2</sub>(001).

The Peierls transition temperature was analyzed for TTF-TCNQ thin films of varied thicknesses, grown on different substrate materials and for different crystalline orientations. It was demonstrated that the influence of most substrate materials on the Peierls transition temperature is negligible and no clamping between the thin film and the substrate takes place. In contrast, if the interaction between the TTF-TCNQ thin film and the substrate is strong, as is the case for NaCl(100), the Peierls transition temperature depends on the thin film thickness. The interaction between thin film and substrate leads to the formation of microstrain in the films.

It was also demonstrated that the Peierls transition temperature of non-irradiated TTF-TCNQ thin films is systematically shifted towards lower values, as compared to the transition in TTF-TCNQ single crystals. The defects, which emerge in TTF-TCNQ microcrystals due to the non-equilibrium growth process, may destroy the long range order and be partly responsible for the observed temperature shift. Using a theoretical framework developed in [157, 158] the concentration of defects was estimated as  $\sim 0.14\%$ .

In order to compare the influence of the irradiation-produced defects on the Peierls transition in TTF-TCNQ thin films with the results for single crystals, a long-term electron irradiation of a selected thin film was performed. It is concluded that the electron irradiation affects the Peierls transition in the same manner as for TTF-TCNQ single crystals. The Peierls transition becomes suppressed in the course of the irradiation, but for the temperature range above the Peierls transition the electrical conductivity still follows an Arrhenius behavior as for non-irradiated samples.

**INFLUENCE OF THE SUBSTRATE-INDUCED  
STRAIN AND IRRADIATION DISORDER ON  
THE PEIERLS TRANSITION IN TTF-TCNQ  
MICRODOMAINS**

In this chapter, the dynamics of low-lying charge excitations in TTF-TCNQ domains with micrometers size exhibiting large defect densities induced by electron irradiation is studied, both above and below the Peierls transition temperature. Using electron irradiation for the creation of defects is advantageous for several reasons, one of which is the possibility to deposit locally large doses (reaching into the GGy regime) with very high lateral resolution and control within an scanning electron microscope. Primary electron energies of several keV at a flux density of about 250 C/m<sup>2</sup> have been employed. Due to the limited penetration depth of the electrons of about 400 nm at 5 keV, the studies need to be performed on layers of TTF-TCNQ with thicknesses below about 200 nm in order to ensure a homogenous distribution of the induced defects. It is possible to grow epitaxial, *c*-axis oriented thin films of TTF-TCNQ on alkali-halide substrates and study the irradiation effect as shown in chapter 5. However, the epitaxy is of the two-domain type which inevitably leads to two complications. First, low-lying charge excitations originating from domain or grain boundaries will contribute to the measured transport properties. Considering the typical domain size for TTF-TCNQ, which is below 3  $\mu\text{m}$ , this can only be avoided by high-resolution lithographic techniques. However, resist-based photo- or electron-beam lithography is not readily applicable to organic charge transfer materials due to the damage they induce. Second, if the transport data are taken over multiple domains, a mixture ensues (series and parallel circuiting) of the con-

tributions along the highly-conducting  $b$ -axis and the much less conducting  $a$ -axis. In this case, the data analysis is much more complicated.

Therefore, in order to study the transport properties of TTF-TCNQ along the highest conductivity  $b$ -axis in dependence of the induced defects, a new fabrication technique was employed. The investigation of transport properties of TTF-TCNQ domains combines the physical vapor deposition technique as the growth method and ion and electron beam induced deposition (IBID and EBID, respectively) as contact fabrication methods [18]. This technique allowed us to fabricate samples which are of unusual geometry and sizes. The different factors influencing the electrical conductivity of individual TTF-TCNQ domains are: (i) irradiation-induced defects associated with electron beam irradiation; (ii) finite-size effects, and as a consequence (iii) strain, induced by the hindered thermal contraction of an organic microcrystal grown on a stiff substrate. Using transport measurements, the influence of these factors on the Peierls transition temperature is studied here.

This chapter is organized as follows: state of the art experiments on TTF-TCNQ microcrystals and nanowires are outlined in section 6.1. The fabrication parameters and techniques used in this work are discussed in section 6.2. The calculation of the deposited radiation dose in the TTF-TCNQ domains is performed in section 6.3. The results of electrical conductivity measurements and the determination of the Peierls transition temperature are discussed in section 6.4. In section 6.5 the influence of finite-size effects in conjunction with substrate-induced strain and electron irradiation of the sample on the Peierls transition is discussed. Section 6.6 summarizes the chapter.

## 6.1 Experimental studies of TTF-TCNQ microcrystals

The fabrication of microobjects consisting of the TTF-TCNQ charge transfer complex has been so far achieved by two methods: PVD growth of TTF-TCNQ nanowires from TTF and TCNQ molecules on a substrate with pre-patterned contacts under an applied  $dc$  or  $ac$  electric field, or using the so called drop-casting method.

One of the first studies of TTF-TCNQ nanowires was performed already in 1998. TTF-TCNQ nanowires were formed in an UHV chamber during the co-evaporation of TTF and TCNQ molecules. The nanowires were grown on a Si/SiO<sub>2</sub> substrate between two gold electrodes at a constant voltage of 350 V [160]. The electrodes serve also as contacts in the transport measurements. The electrical transport measurements showed an antisymmetric growth of nanowires from the cathode and

anode sides: the electrical conductivity of the nanowires grown from the cathode side exceeded  $100 (\Omega\text{cm})^{-1}$ , while for the nanowires emerged on the anode side it was  $\sim 0.3 (\Omega\text{cm})^{-1}$ . This asymmetric growth was explained by the lack of TTF-molecules on the anode side [161]. To overcome this problem, the vapor pressure of TTF was enhanced during co-evaporation [162]. Thereupon the technique was modified and an *ac* electric field of 10 V with a frequency of 140 Hz was used. Organic field effect transistors were prepared based on the TTF-TCNQ nanowires and *n*-channel characteristics for the OFET was observed [163]. The estimated carrier mobility of TTF-TCNQ OFETs was determined to be within the range of  $1.1 \dots 2.8 \text{ cm}^2\text{V}^{-1}\text{s}^{-1}$  [53].

The method of nanowire growth under an external electric field was further modified and used for transport measurements of TTF-TCNQ nanowires at low temperature. Nanowires obtained by the evaporation technique in UHV from a single TTF-TCNQ source under applied electric field were investigated. The Peierls transition was extracted from electrical transport measurements [164]. The room temperature conductivity of these samples was determined to be in the range  $10 \dots 12 (\Omega\text{cm})^{-1}$ . The electrical conductivity of the nanowires showed Efros-Shklovskii hopping behavior and no indication of a conductivity maximum at 54 K. Instead, a change of the slope of the  $\sigma(T)$  curve was observed in the range  $37 \dots 55$  K, which was attributed to the Peierls transition. A threshold electric field of 300 V/cm was determined from the current-voltage characteristics for the TTF-TCNQ nanowire at 10 K [165], being appreciably larger than the threshold electric field of TTF-TCNQ single crystals (10 V/cm [166]) and of TTF-TCNQ thin films (3 V/cm, see Fig. 5.20b). According to [167], enhanced defect concentrations in these quasi-one-dimensional metals are responsible for an increase of the threshold electric field  $E_{th}$ . Therefore, presumably the impurities and defects also enhanced the threshold field in the TTF-TCNQ nanowires studied in [165].

The drop-casting method was used to form TTF-TCNQ nanowires of a length exceeding  $10 \mu\text{m}$  on Si/SiO<sub>2</sub> substrates. TTF was dissolved in hexane and TCNQ was dissolved in acetonitrile. The solution of TCNQ was dripped into TTF solution with a certain rate and stirred. With this deposition method the TTF-TCNQ nanowires were aligned across two pre-patterned gold contacts [168]. In order to improve the contacts between the pre-fabricated Au electrodes and the TTF-TCNQ nanowires, focused ion beam induced deposition of a Pt-C composite was used. The room temperature conductivity of the TTF-TCNQ nanowires formed by the drop-casting method is rather small, about  $0.26 (\Omega\text{cm})^{-1}$ , though the authors claim that they have measured single microcrystals of TTF-TCNQ by using Selected Area

Electron Diffraction (SAED) to prove the monocrystalline structure. Such a small conductivity is not typical for TTF-TCNQ single crystals, which normally have room temperature electrical conductivities of about  $500 (\Omega\text{cm})^{-1}$ . The result was explained by the high energy barrier between two different TTF-TCNQ columns along the current path.

The experiments mentioned above were performed on TTF-TCNQ micro- and nanowires. However, a metallic behavior of the electrical conductivity and a distinct signature of the Peierls transition was not observed for these samples. The conductivity measurements were performed by the two-probe method. In the work presented here, an alternative approach was used to study the transport properties of single TTF-TCNQ domains. These TTF-TCNQ domains were formed using the physical vapor deposition technique and electrical contacts were prepared with the deposition techniques available in our SEM. The employed methods allowed to contact individual TTF-TCNQ microdomains and study their transport properties. The strain-induced effects due to the interaction of TTF-TCNQ microcrystals with the substrate (which were not considered in earlier studies) were also taken into account.

## 6.2 Fabrication of TTF-TCNQ microcrystals and contacts

An in-depth inspection of the growth of TTF-TCNQ thin films shows that their formation starts from the agglomeration of microcrystals (further referred to also as domains) as was shown in section 5.2 (see Figs. 5.8a-5.14a). In the case of NaCl(100) as the substrate material, the growth of TTF-TCNQ thin films is planar and microcrystals in two domain orientations are formed. The long axis of the formed microcrystals coincides with the crystallographical  $b$ -axis of TTF-TCNQ [114]. In the case of other substrates used in this work, no epitaxial growth was obtained and a well-defined orientation of the crystallographic  $b$ -axis was not observed. However, the growth of TTF-TCNQ thin films has some similarities in the initial stage for all studied substrate materials. First, isolated TTF-TCNQ domains form without grain boundaries and in the course of evaporation the deposited TTF-TCNQ domains coalesce and the typical three-dimensional film morphology emerges. By tuning of the evaporation temperature and distance between the substrate and the effusion cell, one can achieve suitable conditions to form individual TTF-TCNQ domains on the substrate surface. TTF-TCNQ domains were formed during a very short time compared to the formation time of TTF-TCNQ thin films. The size of a typical mi-

microcrystal used in the measurements varied within the range of 1.5 . . . 3  $\mu\text{m}$  in length, 110 . . . 550 nm in width and 10 . . . 110 nm in thickness. The evaporation temperature of the TTF-TCNQ precursor was 88  $^{\circ}\text{C}$ , the distance between the substrate surface and the effusion cell orifice was 1 cm and the evaporation time was 2.5 min. The deposition was performed in the “test” chamber (see section 3.1.3). The background pressure was  $8 \times 10^{-8}$  mbar. The experimental conditions were chosen according to the measurements performed on TTF-TCNQ thin films grown on NaCl(100) and Si(100)/SiO<sub>2</sub> substrates.

NaCl(100) and Si(100)/SiO<sub>2</sub> (285 nm) substrates were used in the experiments. NaCl(100) was chosen because it induces epitaxial growth of TTF-TCNQ. The silicon/silicon oxide substrate was used in order to reduce the charging of the substrate which severely complicates the work in the SEM for NaCl(100). Au/Cr contacts were pre-patterned on the substrates before the domain deposition as described in section 3.3. A shadow mask was used to define the region for TTF-TCNQ domain growth on the substrate between the metallic electrodes (see Fig. 6.1). The opening

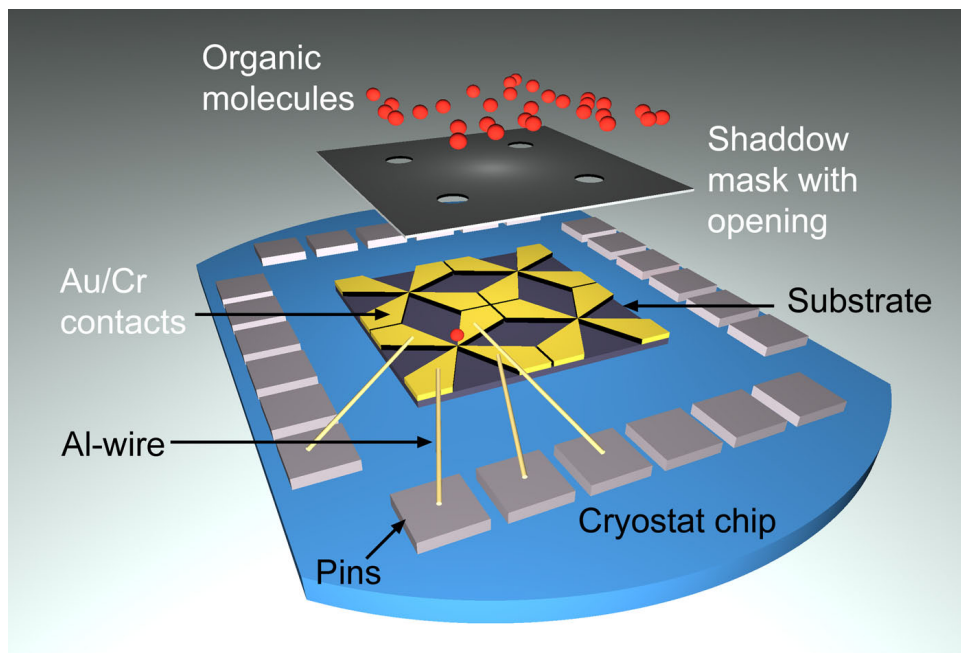


**Figure 6.1:** Schematic illustration of the deposition process of the TTF-TCNQ microdomains on the substrate through a shadow mask. The substrate with bonded Au/Cr contacts is shown on the chip used for *in situ* conductivity measurements in the electron microscope during the irradiation experiment, as well as for the low-temperature measurements.

of the mask was about 130  $\mu\text{m}$  which allowed to cover the surface area between the pre-patterned Au/Cr contacts. This proved to be sufficient for choosing a suitable domain for contacting. After the deposition process the substrate with the deposited microcrystals was glued on a cryostat holder (see Fig. 3.7). The holder pins were connected with the Au/Cr contacts using Al-wire of 25  $\mu\text{m}$  diameter using a bonding machine. The main difficulty was to select a suitable microcrystal for measurement and make contacts with the pre-formed Au/Cr pads. To simplify the following description the fabricated samples are named according to their fabrication order. A summary of the investigated microdomains' parameters, i.e. electrical conductivity, geometrical dimensions and the applied processes, is given in Tab. 6.1.

**Table 6.1:** Summary of the geometrical parameters, electrical conductivity  $\sigma_b$  and employed processes for the individual TTF-TCNQ microdomains. The process description is given in the text. TMS is the abbreviation for tetramethylsilane. NPS is the abbreviation for neopentasilane.

Substrate material	Sample number	Length/width/thickness (nm)	$\sigma_b$ ( $\Omega\text{cm}$ ) <sup>-1</sup> at RT	Used process	Passivation
NaCl(100)	1	700/140-150/150-200	950	FIBID	–
NaCl(100)	2	1250/115/150	210	FIBID	–
Si/SiO <sub>2</sub> (100)	3	2000/330/10-30	210	FIBID	TMS
Si/SiO <sub>2</sub> (100)	4	2400/380/30	240	FIBID	NPS
Si/SiO <sub>2</sub> (100)	5/6	1650/110/120	10	FEBID/ FIBID	NPS
Si/SiO <sub>2</sub> (100)	7	2500/530/15	30	FEBID/ FIBID	NPS

In preliminary experiments (samples 1-5) tungsten hexacarbonyl ( $\text{W}(\text{CO})_6$ ) was used as a precursor material for contact fabrication [169, 170]. The contacts were made by a FIBID process using the Ga-ion source under a voltage of 30 kV. The operating current was 10 pA. The tungsten metal content was 53%, as measured by EDX. The areas between the contacts were etched by FIB. In order to decrease the irradiation damage on the domains during the contact formation, the contacting method was later modified and a combined FEBID and FIBID contact fabrication method was employed for samples 6 and 7. At first the contacts on top of the TTF-TCNQ



microcrystals were deposited by FEBID with trimethyl-methylcyclopentadienyl-platinum ( $\text{MeCpPt}(\text{Me})_3$ ) as precursor [171] and then extended by a FIBID process up to the pre-patterned Au/Cr contacts with  $\text{W}(\text{CO})_6$  as precursor. The operating voltage for the FEBID-process was 5 kV and the current was 1.6 nA. The width of the contacts formed on the microcrystals was 100 nm and the thickness was 40 nm. The parameters of the electron and ion beams used in the experiments are collected in Appendix C in more detail.

The first samples (1&2) were fabricated on  $\text{NaCl}(100)$ . These samples lost their electrical contacts during transportation to the cryostat, presumably due to oxidation. Therefore, no temperature-dependent measurements of the electrical conductivity for these samples could be performed. Another possible explanation for the sample damage could be the humidity of air which detonates the sensitive alkali halide substrate and thus creates strain in the microcrystal which causes its breakage (see Fig. 6.2). Sometimes in the course of the experiments the cracks appeared in the  $\text{NaCl}$  substrate itself.

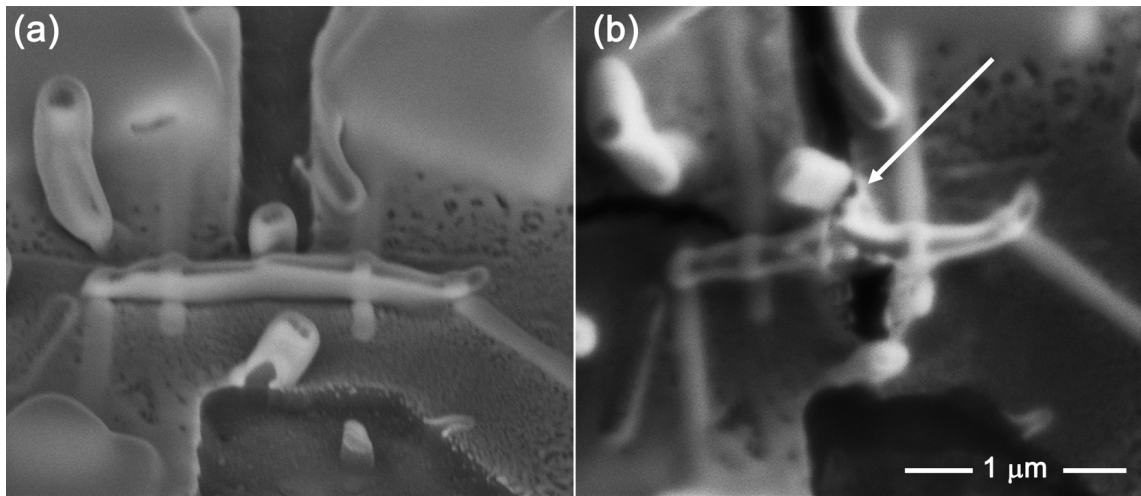


**Figure 6.2:** Contacted *TTF-TCNQ* microcrystal grown on  $\text{NaCl}(100)$  (sample 1): (a) domain with attached contacts, (b) broken *TTF-TCNQ* domain after transportation to the cryostat. The arrow indicates the site of crystal breakage. The scale bar applies to both panels.

To protect the microcrystals from breaking due to the air humidity, oxidation and cracks of the  $\text{NaCl}$  substrate,  $\text{Si}(100)/\text{SiO}_2$  substrates were used instead. Sample 3 was also passivated with a 100 nm layer of tetramethylsilane ( $\text{Si}(\text{CH}_3)_4$ ) by a FEBID process at a voltage of 5 kV and a current of 0.4 nA directly after W-composite contact deposition. The electrical conductivity of sample 3 after the

passivation decreased from  $210 (\Omega\text{cm})^{-1}$  to  $153 (\Omega\text{cm})^{-1}$ . The transportation of the sample to the  $\text{He}^4$  cryostat through ambient air took about 10 min. Afterward the pumping of the probe space in the cryostat was started immediately. The electrical conductivity of the sample dropped to  $135 (\Omega\text{cm})^{-1}$  after the transportation. It was concluded that TTF-TCNQ microcrystals grown on Si/SiO<sub>2</sub> allow for transportation through ambient air. Therefore, the following samples were fabricated on Si/SiO<sub>2</sub> and passivated.

Samples 4-7 were passivated only locally on the areas where the Pt-composite contacts were deposited on the TTF-TCNQ domains in order to decrease the sample irradiation damage. Also the precursor for passivation was changed to neopentasilane ( $\text{Si}_5\text{H}_{12}$ ) which forms highly resistive Si(O) layers. The thickness of the passivation layer was about 10 nm. The operating voltage was 5 kV and the current was 1.6 nA.

The temperature dependence of the electrical conductivity of sample 4 showed only the characteristic behavior of the W-composite and no features from TTF-TCNQ. Therefore, it was concluded that in this case a co-deposit from the  $\text{W}(\text{CO})_6$  precursor covered the entire sample. Samples 5 and 6 were fabricated on the same substrate (see Tab. 6.1). Sample 5 was contacted with a FIBID process, while sample 6 was contacted by a combination of FIBID and FEBID techniques, as described above. The microcrystal contacted with FIBID alone did not show any characteristic feature of TTF-TCNQ. Neither the Peierls transition nor a threshold voltage was observed. A co-deposit effect was observed as was for sample 4. Therefore, the pure FIBID cycle for contact preparation was judged as not appropriate for the electrical conductivity measurements of TTF-TCNQ domains. The combined process was used in the next experiments.

Figure 6.3 illustrates step by step the formation of contacts on a selected TTF-TCNQ microcrystal using FEBID and FIBID. First, the area with TTF-TCNQ microcrystals is scanned by the electron beam in order to find a microcrystal which is suitable for further experiments. When a good candidate is found (see Fig. 6.3b), electric contacts are formed on top by FEBID, as shown in Fig. 6.3c,d. The formed contacts are lengthened and extended towards the pre-patterned Au/Cr contacts by FIBID (see Fig. 6.3e,f). After that the area between the contacts is etched with FIB to erase the remaining TTF-TCNQ microcrystals, which can cause a short circuit (see Fig. 6.3e,f). As a last step a Si(O) protection layer is formed on top of the contacts. In order to reduce the sample irradiation in the course of contact fabrication only snapshot SEM images were taken. The dwell time was  $3 \mu\text{s}$ . AFM measurements were performed at the very end after the temperature-dependent

conductivity measurements (see Fig. 6.3h,j).

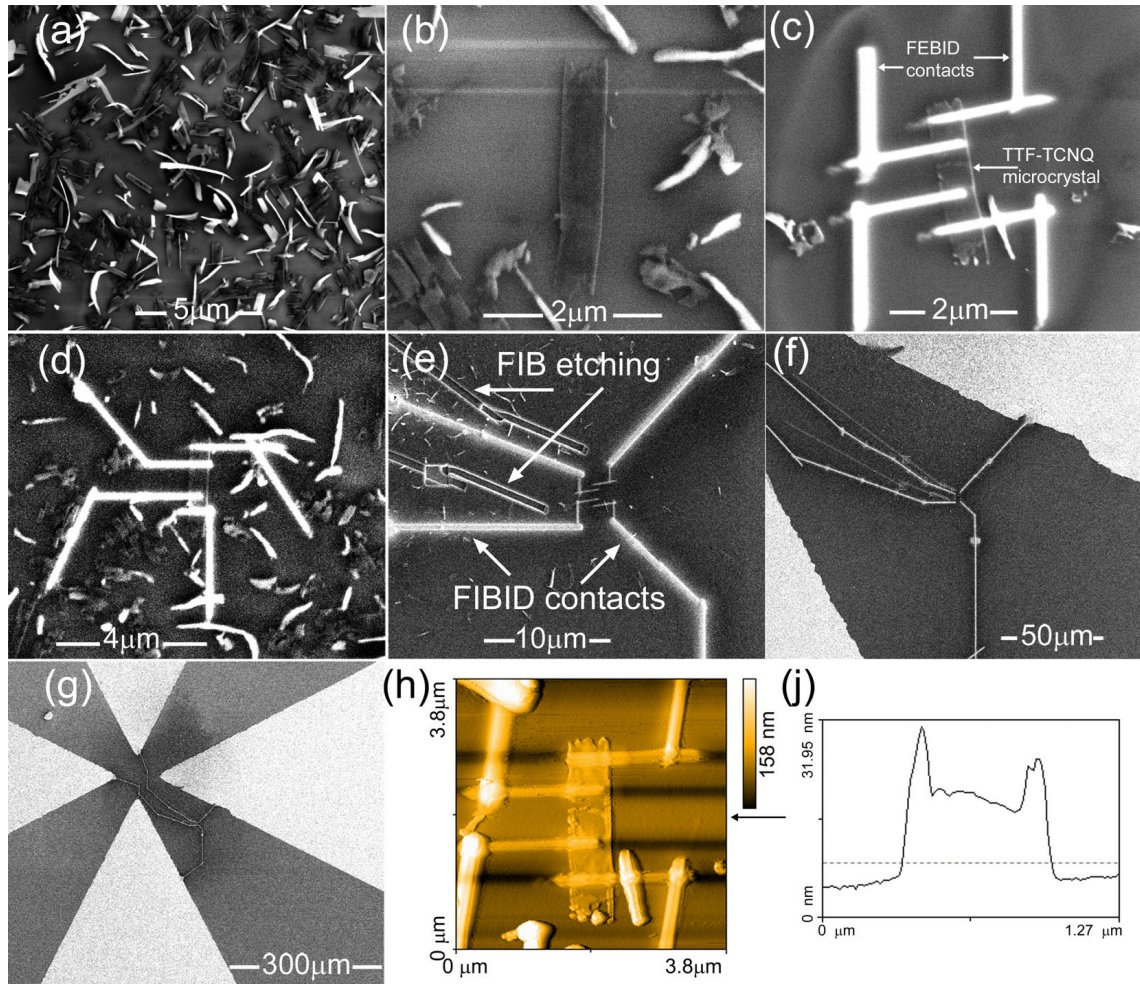


**Figure 6.3:** Schematic illustration of the contact fabrication process on a TTF-TCNQ microcrystal. SEM images of (a) the TTF-TCNQ microcrystals formed on the substrate (see Fig. 6.1), (b) a TTF-TCNQ microcrystal is chosen for contacting, (c) TTF-TCNQ microcrystal with Pt contacts attached, (d) contacts extension by FEBID, (e)-(f) contacts extension by FIBID, (g) a zoomed-out SEM image of the TTF-TCNQ microcrystal with FEBID/FIBID contacts together with the pre-patterned Au/Cr contacts. (h) AFM image of the TTF-TCNQ microcrystal and (j) AFM cross section view of the TTF-TCNQ domain. The position of the cross section is shown by arrow in (h). AFM images were taken after the transport measurements.

Samples 6 and 7 are considered in greater detail in the following sections. The electrical conductivity measurements on TTF-TCNQ microcrystals were performed along the long axis, coinciding with the crystallographic  $b$ -axis of TTF-TCNQ [114].

They were carried out in a  $^4\text{He}$  cryostat with a variable temperature insert allowing to cool down the sample from room temperature (300 K) to 4.2 K. The four-probe scheme for the transport measurement was applied. Temperature-dependent resistivity measurements were performed at a fixed bias voltage of 0.2 V corresponding to an electric field of about 8000 V/cm. This rather large excitation level was needed to generate sufficient current. It is also related to the enhanced threshold voltage in the microdomains. The fixed bias voltage mode was used due to the high resistivity of the samples at low temperatures. Cooling-heating cycles of the samples were repeated several times and the conductivity showed no indication of either hysteretic behavior or thermal-stress-induced damage formation in the domains.

### 6.3 Radiation-induced defects in TTF-TCNQ microcrystals

The irradiation of TTF-TCNQ microcrystals during the contact formation procedure causes defect formation. In order to estimate the defect concentration a calculation of the irradiation dose is necessary.

The defect concentration induced in sample 3 was estimated from the ion beam parameters. The calculation of the defect concentration was performed by using the simulation software SRIM (Stopping and Range of Ions in Matter) [172]. Knowing the deposition time and current one can evaluate the number of ions which irradiated the sample. The SRIM program calculates the energy which one ion loses in the TTF-TCNQ microdomain. The beam parameters for the tungsten deposition are given in Tab. C.1. From the SRIM calculation, it follows that one ion loses about 21.1 keV in the TTF-TCNQ microcrystal. The energy which is needed to introduce one defect in TTF-TCNQ single crystals is 21.2 keV as reported in [155] for X-ray radiation. There are no literature reports of such measurements for gallium ion radiation. Therefore, the calculation was carried out based on a quality factor for gallium ions. The quality factor for gallium ions is assumed to have the value 20, as in the case for  $\alpha$ -particles [173]. The calculated number of defects per one molecule is about 1200. This number is too large and does not seem to be reasonable, only allowing one to speculate that the defect density induced by ion beam in TTF-TCNQ microcrystal is very high. The performed estimation was the basic motivation which suggested the use of FEBID instead of FIBID for contact preparation.

Sample 3 whose electrodes were fabricated via the FIBID method, yields the highest defect concentration of the three considered microcrystals (samples 3, 6 and 7), which were measured in the cryostat. For the deposition of W-composite

electrodes, snapshots of the whole domain had to be taken with the ion beam. In addition, TMS covered the sample completely, resulting in the increase of the defect concentration, especially in the region between the voltage electrodes, where the transport properties were measured.

In the following discussion, the irradiation doses are calculated for samples 6 and 7, which were irradiated with the electron beam only. The doses of irradiation were determined by Monte-Carlo simulation using the Casino program [78]. The irradiation parameters and the calculated irradiation doses are compiled in Tab. 6.2. The parameters of the electron beam for the Pt-composite deposition and irradiation, passivation and also snapshots of the domains can be found in Tab. C.2. Since the electrical conductivity of the microcrystals was measured by the four-probe technique, the evaluation of the radiation dose caused by the deposition of the electrodes and passivation onto the contact areas is irrelevant and only the damage of the current path is important for microcrystals 6 and 7. The current path areas were exposed to the electron beam for snapshot images and are taken into account in Tab. 6.2.

**Table 6.2:** *Radiation doses of TTF-TCNQ domains caused by the electron beam when the snapshot images of the sample were taken.*

Domain parameters	sample 6	sample 7
Width	110 nm	530 nm
Length	480 nm	600 nm
Hight	120 nm	15 nm
Width (pixels)	5.63	27.14
Length (pixels)	21.22	26.52
Dell time $t_D$	3 $\mu$ s	3 $\mu$ s
Passes/number of snapshots	50	30
Operating current $I$	1.6 nA	1.6 nA
Operating voltage $U$	5 kV	5 kV
Charge	$2.87 \times 10^{-11}$ A s	$6.48 \times 10^{-10}$ A s
Charge in $e$	$1.79 \times 10^8$	$4.04 \times 10^8$
Irradiated area	$5.28 \times 10^{-2}$ $\mu$ m <sup>2</sup>	$3.18 \times 10^{-1}$ $\mu$ m <sup>2</sup>
Electron density (el/m <sup>2</sup> )	$2.12 \times 10^{21}$	$1.27 \times 10^{21}$
Current density (A s/m <sup>2</sup> )	340	204
Deposited energy	$5.59 \times 10^{11}$ eV	$2.02 \times 10^{12}$ eV

Amount of absorbed energy	27.12 %	3.098 %
<b>Absorbed dose</b>	<b>2.36 GGy</b>	<b>1.3 GGy</b>
Number of defects	$7.16 \times 10^6$	$2.95 \times 10^6$
Volume of damaged area	$6.34 \times 10^{-21} \text{ m}^3$	$4.77 \times 10^{-21} \text{ m}^3$
Defect concentration	$1.13 \times 10^{19} \text{ cm}^{-3}$	$0.62 \times 10^{19} \text{ cm}^{-3}$

The electric charge that goes through a microcrystal during one snapshot is determined by multiplying the beam current with the number of points scanned by the electron beam and the dwell time (the time which the electron beam spends on each point):

$$q = It_D w(\text{pixels}) \times l(\text{pixels}), \quad (6.1)$$

where  $q$  is the charge,  $I$  is the operating current,  $t_D$  is the dwell time. The electron density can be estimated by dividing the number of electrons by the size of the affected microcrystal area. The accumulated beam energy is calculated by multiplying the electrical charge obtained from Eq. (6.1) by the applied voltage as follows:

$$E = qU, \quad (6.2)$$

where  $E$  is the irradiation energy and  $U$  is the operating voltage. A fraction of the irradiation energy is absorbed by the TTF-TCNQ domain and is calculated within the Monte Carlo simulation. The results of the simulation by the Casino computer program are presented in Fig. 6.4. By integrating the values of the deposited energy

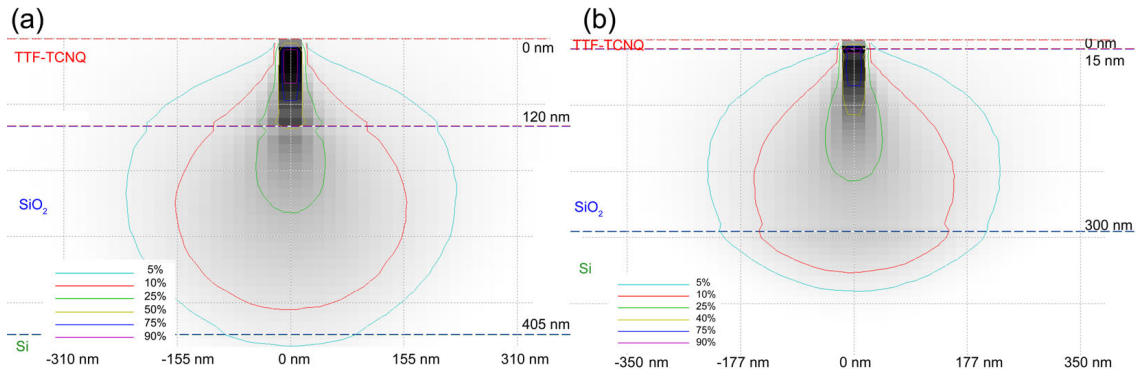


**Figure 6.4:** Cross-section view of absorbed energy by TTF-TCNQ microcrystal grown on a Si(100)/SiO<sub>2</sub>(285 nm) substrate for (a) sample 6 and (b) sample 7. The grey shade ranges from light to dark as the density increases; the 10% line, for example, is the frontier between the area containing 90% of the absorbed energy and the rest of the sample.

for each volumetric element in the domain region, the fraction of energy absorbed by the TTF-TCNQ crystal is calculated. The energy absorbed by sample 6 is about 27% of the deposited energy, while for microcrystal 7 this value is smaller and equal to about 3% of the total energy (see Fig. 6.4). The difference in the absorbed energy stems from the geometry of the samples. Thinner samples absorb less than thicker ones and also from the experiment parameters: sample 7 was less irradiated, because less snapshots were taken (30 instead of 50). Using the calculated energy distribution the radiation dose for TTF-TCNQ microcrystal 6 is 2.36 GGy and for sample 7 it is 1.3 GGy (see Tab. 6.2). The large values of the absorbed doses are the result of the small irradiated volume. By taking into account the volume of the domain, the defect density is  $1.13 \times 10^{19} \text{ cm}^{-3}$  for sample 6, and  $0.62 \times 10^{19} \text{ cm}^{-3}$  for sample 7.

## 6.4 Temperature dependence of electrical conductivity of TTF-TCNQ microdomains

After the contact fabrication the sample was moved into the cryostat to perform the temperature-dependent measurements of the electrical conductivity and current-voltage characteristics, which allows one to determine the Peierls transition temperature and the threshold electric field.

The measurements of the electrical conductivity of sample 3 did not show any signature related to the Peierls transition, which is easily observed in TTF-TCNQ single crystals or in TTF-TCNQ thin films. However, a threshold electric field could be determined from the current-voltage characteristic. Samples 4 and 5 with the contacts fabricated by means of the FEBID process show neither a metallic nor thermo-activated dependence of the conductivity on temperature and no threshold voltage. The decrease of the current with temperature is very small, less than 20%. For instance, the reduction of the current at fixed bias voltage in TTF-TCNQ thin films from room temperature down to 4.2 K is about 1000. The behavior of the electrical conductivity of samples 4 and 5 is therefore ascribed to the FEBID deposit itself which is further corroborated by the presence of a superconducting transition at  $T=5.5 \text{ K}$ .

The electrical resistivity of TTF-TCNQ domains fabricated with the combined FEBID and FIBID processes (samples 6 and 7) shows a variable-range hopping (VRH) behavior starting from room temperature down to low temperature [174]:

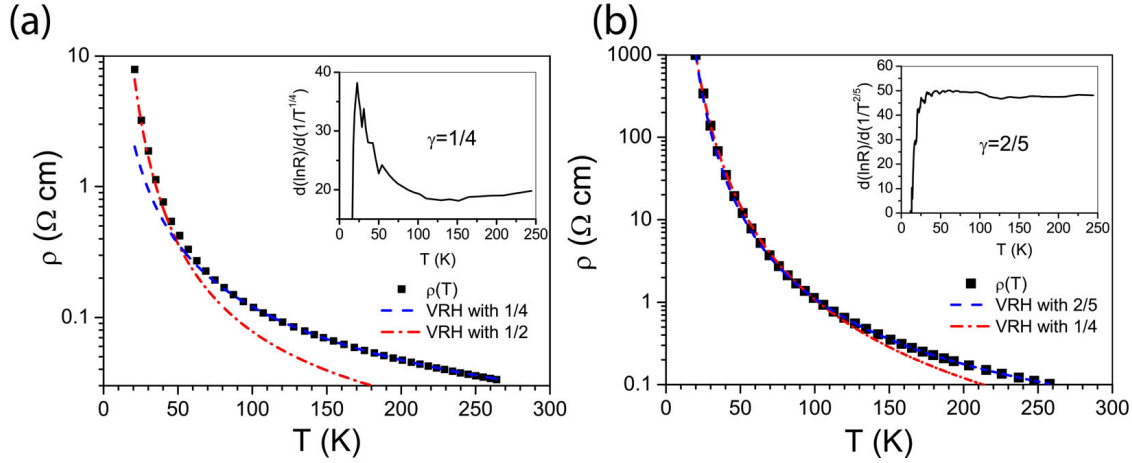


**Figure 6.5:** Temperature dependence of the resistivity (squares) measured for two TTF-TCNQ domains irradiated by the electron beam with (a) 1.3 GGy radiation dose (sample 7) and (b) 2.36 GGy radiation dose (sample 6). The exponents  $\gamma$  used in Eq. (6.3) are given for each graph. The applied voltage is 0.2 V. The insets show the temperature dependence of the logarithmic derivative  $d(\ln R)/d(1/T)^\gamma$  with  $\gamma$  as indicated. Detailed results of the fits are given in Appendix D.

$$R(T) = R_0 \exp\left(\frac{T_0}{T}\right)^\gamma, \quad (6.3)$$

where  $T_0$  and  $R_0$  are constants,  $\gamma$  is the variable-range hopping exponent. In the present case the exponent  $\gamma$  varies for different irradiation doses and experiences a change at a temperature of about 50 K as is shown in Fig. 6.5. The values of the exponent for different temperatures and for different samples including non-irradiated and irradiated TTF-TCNQ thin films are summarized in Tab 6.3. It is important to note that the precise values of the exponents  $m$  should be treated with some caution. The respective fitting ranges, above and below about 50 K, are rather small. Nevertheless, the exponents given in Tab. 6.3 yielded significantly better fits than other physically plausible choices taken from the set  $m \in (1, \frac{1}{2}, \frac{2}{5}, \frac{1}{3}, \frac{1}{4})$ . The results of the fit are given in Appendix D. Also, the crossover temperature of about 50 K is quite well-defined as this is the temperature where the fits for the high- and low-temperature data tended to deviate from the experimental values, respectively.



**Table 6.3:** Exponent  $\gamma$  and  $T_0$  (K) characterizing the electrical transport behavior of TTF-TCNQ thin films and microcrystals at temperatures (1)  $T \geq 50$  K and (2)  $T < 50$  K.

Sample	Thin film	Thin film	Domain	Domain
	0 GGy	1.4 GGy	1.3 GGy	2.4 GGy
$\gamma, T_0$ ( $T < 50$ K)	1/4, 8503056	2/5, 13995	1/2, 1225	1/4, 3992363
$\gamma, T_0$ ( $T \geq 50$ K)	1, 137	1, 197	1/4, 130321	2/5, 15962
$l(\text{\AA})$	$2.3 \times 10^3$	13	15	8

The manifestation of the Peierls phase transition in the TTF-TCNQ domains is smeared out in the resistivity-temperature dependence shown in Fig. 6.5. The absence of a minimum in the resistivity at about 54 K, i.e. the typical indication of the Peierls transition in TTF-TCNQ single crystals, is a result of the electron irradiation of the samples in the SEM, which induces defects in the TTF-TCNQ microcrystal. The thermo-activated behavior of the resistivity generally found for TTF-TCNQ thin films [17] also does not fit the resistivity-temperature dependence of the TTF-TCNQ domains. The TTF-TCNQ thin films irradiated with a similar dose (about 1.4 GGy) still show Arrhenius behavior (see Fig. 5.23). This observation leads to the assumption that the VRH behavior is caused by an interplay of the high concentration of defects in the domains which induce localized states near the Fermi level and the specific geometry of the individual domains.

For all cases presented in Tab. 6.3 the transport regime changes at a temperature below about 50 K. For reference purposes the data for non-irradiated and irradiated TTF-TCNQ thin films are included. In order to explain the change of the VRH exponent the theoretical model suggested by Fogler, Teber and Shklovskii (FTS) in [175] for a quasi-one-dimensional electronic system was used. At temperatures below the phase transition the electronic charge distribution of an assumed Wigner crystal in the material is divided by impurities into metallic rods. Between the rods the electronic transport is performed via variable-range hopping. The transport regime in the material is impurity dependent and also changes with temperature. The authors introduce an average length of the segment of the chain which is not disturbed by impurities  $l = 1/(Na_{\perp}^2)$ , where  $N$  is the defect concentration and  $a_{\perp}^2$  is the area per chain. While in the theoretical model chains of the same type are considered, in the case of TTF-TCNQ two types of chains should be taken into account. The Peierls transition studied here refers to the TCNQ chains resulting in  $a_{\perp} \approx 10.4 \text{ \AA}$  [38].

For each sample the average length of the segment  $l$  was calculated and is given

in Tab. 6.3. For the non-irradiated thin film sample the concentration of the defects was defined from the scattering time given by Eq. (5.5). The average length of the segment is responsible for the transport regime in the quasi-one-dimensional metal. Figure 6.6 shows the transport regimes in a quasi-one-dimensional system depending on the average segment length for different temperatures as was suggested in the model [175]. The parameter  $l_S$  is the characteristic length of the distortion around impurities for TTF-TCNQ defined as:

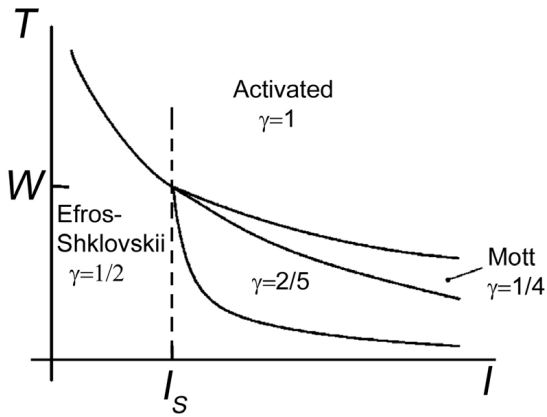


**Figure 6.6:** *Transport regimes in quasi-one-dimensional Wigner crystal with defects depending on the average segment length. The figure is adopted from [175].*

The results for the exponents given in Tab. 6.3 can be explained fairly well by the framework of the metallic rods model formulated in [175]. For temperatures below 50 K the Mott behavior describes the transport behavior of non-irradiated TTF-TCNQ thin films, while for irradiated thin films the average segment is shorter, therefore, the transport regime is changed and the position in the diagram in Fig. 6.6 is shifted to the left and the value of the exponent equals 2/5. The individual TTF-TCNQ domains studied here were irradiated with comparable irradiation doses and the inevitable uncertainty in the  $l$  estimation does not allow for a clear statement concerning a crossover in the transport regime, which was possible in the case of irradiated and non-irradiated TTF-TCNQ thin films. Sample 7 irradiated with 1.3 G Gy shows a Efros-Shklovskii behavior and sample 6 irradiated with 2.4 G Gy

$$l_S = \frac{a_{\perp}}{\sqrt{\alpha}}, \quad (6.4)$$

where  $\alpha$  is a dimensionless anisotropy parameter. The anisotropy parameter is estimated for TTF-TCNQ as  $\alpha \sim 10^{-2} \dots 10^{-4}$  [175]. This results in a broad range of the length:  $105 \text{ \AA} \leq l_S \leq 1050 \text{ \AA}$ . The variable-range hopping exponent  $\gamma$  in Tab. 6.3 can be parameterized as follow [175]:

$$\gamma = \frac{\mu + 1}{\mu + d + 1}, \quad (6.5)$$

where  $d$  is the dimensionality and  $\mu = 0, 1, 2$  according to the physical situation were suggested in [175]. For the case of the finite coupling between the chains  $d = 3$ ,  $\mu = 0$  corresponds to  $\gamma = 1/4$  and Mott behavior,  $\mu = 1$  corresponds to  $\gamma = 2/5$ , and  $\mu = 2$  corresponds to  $\gamma = 1/2$  and Efros-Shklovskii variable-range hopping behavior. When  $\gamma = 1$  the transport regime is thermo-activated.

The results for the exponents given in Tab. 6.3 can be explained fairly well by the framework of the metallic rods model formulated in [175]. For temperatures below 50 K the Mott behavior describes the transport behavior of non-irradiated TTF-TCNQ thin films, while for irradiated thin films the average segment is shorter, therefore, the transport regime is changed and the position in the diagram in Fig. 6.6 is shifted to the left and the value of the exponent equals 2/5. The individual TTF-TCNQ domains studied here were irradiated with comparable irradiation doses and the inevitable uncertainty in the  $l$  estimation does not allow for a clear statement concerning a crossover in the transport regime, which was possible in the case of irradiated and non-irradiated TTF-TCNQ thin films. Sample 7 irradiated with 1.3 G Gy shows a Efros-Shklovskii behavior and sample 6 irradiated with 2.4 G Gy

displays a Mott behavior at temperatures below 50 K. Both these regimes are probable for strongly irradiated quasi-one-dimensional electronic systems [175]. In any case, the strong electron irradiation of the TTF-TCNQ domains does cause a complete suppression of the simple Arrhenius behavior commonly observed in thin films. From the calculated values for the parameter  $l$  and from the variable-range hopping exponents the length scale  $l_S$  is reconsidered. The calculated value is presumably overestimated and for the studied case  $l_S \sim 8 \text{ \AA}$  seems more appropriate.

Also, the observed crossover between transport regimes stemming from the change of the VRH exponent  $\gamma$  at temperatures of about 50 K for the measured TTF-TCNQ domains is ascribed to the presence of the slightly suppressed Peierls transition in the system which is assumed to persist despite the increased defect concentration.

In order to get more information about CDW contributions below  $T_P$  (within the FTS scenario) and above  $T_P$  (via CDW fluctuations), current-voltage  $I(U)$  measurements were performed and any possible threshold behavior was analyzed. Several  $I(U)$  curves for individual domain measured at different temperatures are collected in Fig. 6.7. The  $I(U)$  curves exhibit a non-linear behavior as the temperature is

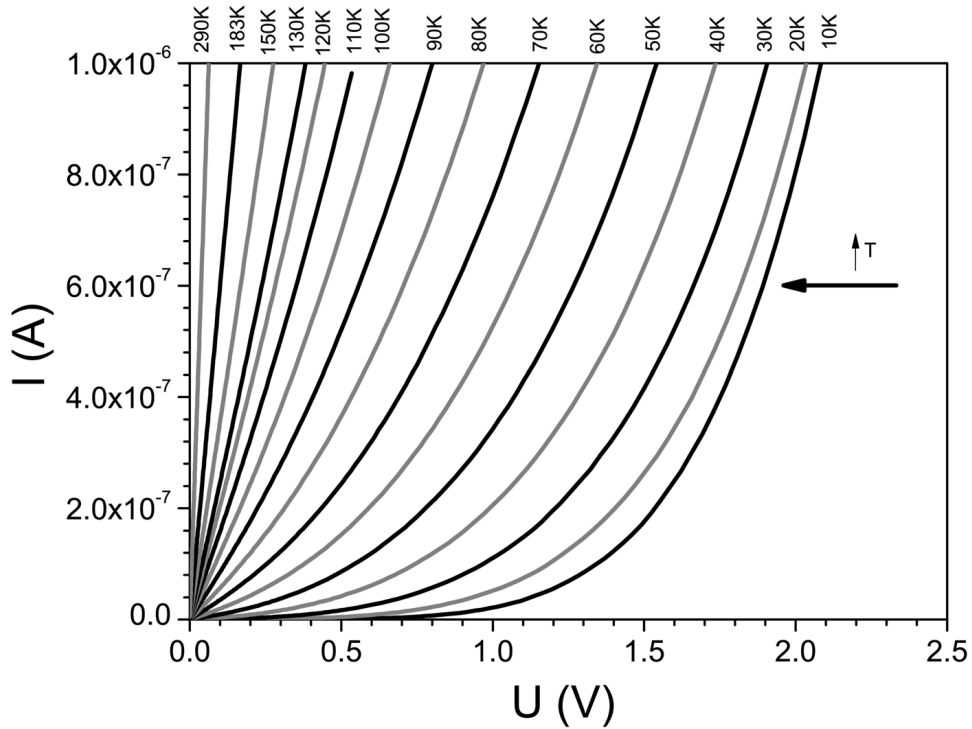


**Figure 6.7:** Current voltage characteristics for a TTF-TCNQ microcrystal (sample 6) measured in the temperature range of 10...290 K.

reduced to below about 100 K. The measured  $I(U)$  characteristics were used to obtain the threshold electric field for the TTF-TCNQ domain. In particular, Fig. 6.8 shows the differential resistance derived from the data presented in Fig. 6.7. The threshold electric field was defined from the dependence of the differential resistance on the electric field as the field where the differential resistance changes its behavior from constant, corresponding to Ohm's law, to a non-linear behavior. The results of the threshold field measurements for samples 3, 6 and 7 are presented in the inset to Fig. 6.8. For samples 7 and 6 the obtained threshold electric field at 10 K (800 V/cm and 8000 V/cm) is several orders of magnitude larger than commonly observed for TTF-TCNQ single crystals (10 V/cm [166]) and for TTF-TCNQ thin films (3 V/cm) as shown in Fig. 5.20b. This increase of the threshold electric field is thought to be caused by two effects: (i) the relatively high concentration of defects in the domains [166], and (ii) the finite-size of the sample, which can have a drastic influence on the threshold electric field in one-dimensional conductors [176].

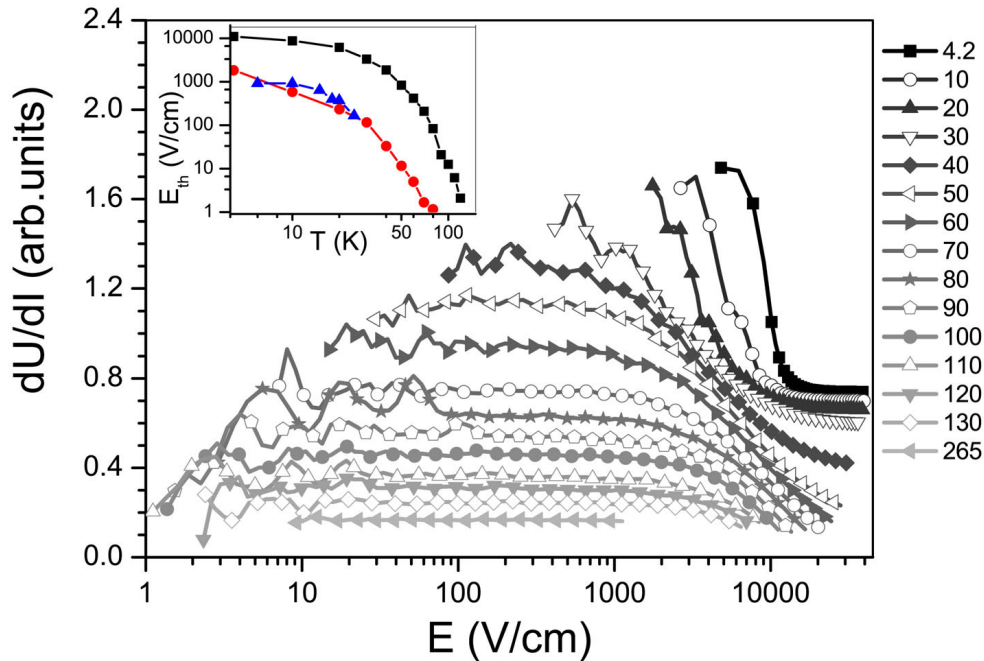


**Figure 6.8:** *Differential resistance of a TTF-TCNQ domain (sample 6) measured in the temperature range of 4.2... 265 K. The irradiation dose of the microcrystal was 2.36 GGy. The inset shows the temperature dependence of the threshold electric field for sample 3 (shown by triangles), sample 6 (shown by squares) and sample 7 (shown by circles).*

At this stage the persistence of the threshold voltage at temperatures substantially higher than the Peierls transition temperature (50 K) is attributed to the pin-

ning of fluctuating CDW regions which are known to dominate the charge transport in bulk crystals even far above  $T_P$ . If these CDW fluctuation components persist despite the large defect density, it would arguably be subjected to the same segmentation of the chains as assumed in the FTS-model [175] – albeit here an additional length scale enters, namely the average CDW-fluctuation correlation length.

## 6.5 Substrate-induced shift of the Peierls transition in TTF-TCNQ microcrystals

As final point in the analysis, an additional aspect which may be of relevance in developing a comprehensive understanding of the presented data is addressed. In [136] the influence of a substrate-induced strain on the transport properties of the organic charge transfer salt  $\kappa$ -(BEDT-TTF)<sub>2</sub>Cu[N(CN)<sub>2</sub>]Br was studied. It was shown that by introducing either compressive or tensile strain the superconducting ground state of the material can be dramatically changed from superconducting to insulating. Thus, substrate-induced effects need also to be taken into account here.

In the experiments TTF-TCNQ domains were grown on top of a Si(100)/ SiO<sub>2</sub> substrate. The Si/SiO<sub>2</sub> substrate has a negligibly small thermal contraction when compared to the thermal contraction of TTF-TCNQ [177]. Due to the difference of the thermal expansion properties of the substrate and the charge transfer complex a tensile biaxial strain is produced when the sample is cooled down as is schematically illustrated in Fig. 6.9. This does, of course, imply the assumption that the TTF-TCNQ microcrystals are fully clamped on the substrate. A direct proof of clamping, as can, in principle, be provided by temperature-dependent X-ray diffraction experiments, is not feasible for individual microcrystals. However, due to the very small thickness of the microcrystals and in view of the results obtained of thin films (see chapter 5 and [17]), a clamped state is highly likely.

A rough estimation of the strain produced due to the difference in the thermal expansion coefficients of the substrate and organic microcrystal can be given. In the general case the macrostress in a thin film at a certain temperature can be calculated as:

$$\sigma_{total} = \sigma_{th} + \sigma_i + \sigma_e, \quad (6.6)$$

where  $\sigma_{th}$  is the thermal stress, arising from the difference in the thermal expansion coefficients of the thin film or microcrystal and the substrate.  $\sigma_i$  is an intrinsic stress induced during the deposition process, originating from defects which occur in the

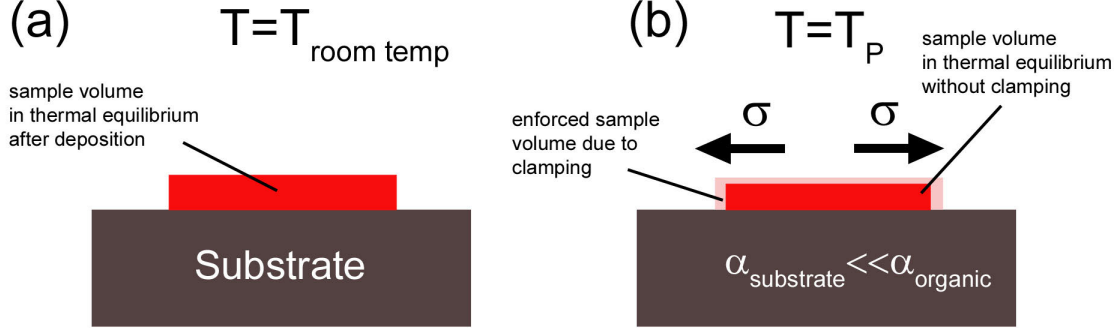


**Figure 6.9:** Schematic illustration of the clamping principle. (a) organic microcrystal at room temperature and (b) at the Peierls transition temperature.

course of the growth. The intrinsic stress depends on the deposition parameters like substrate temperature, pressure in the deposition chamber, evaporation temperature etc.  $\sigma_e$  in Eq. (6.6) is the extrinsic stress induced by external factors, e.g. water adsorption. It is omitted here.

To estimate the macrostrain in TTF-TCNQ domains some assumptions need to be made. The X-ray diffraction patterns of all the TTF-TCNQ microcrystals grown on Si(100)/SiO<sub>2</sub> substrate show that there is no shift of the Bragg peak (002) at room temperature. Therefore, the intrinsic strain induced during the deposition process is considered to be negligible. At the Peierls transition temperature thermal strain causes the main contribution. If the microcrystal is clamped to the substrate then the microcrystal experiences a tensile stress in the (*ab*)-plane at low temperatures and due to the Poisson effect it is contracted in the *c*\* direction which also strengthens the finite-size effects. Here the thermal expansion coefficient of silicon is taken to be zero [178]. The values of the thermal expansion coefficient for TTF-TCNQ along the principal crystallographic directions were taken from [177,179] and are given in Tab. 6.4.

The tensile strain created in the TTF-TCNQ domain during the cooling is:

$$\epsilon_{th} = (\langle \alpha_s \rangle - \langle \alpha_f \rangle) \Delta T \approx -\langle \alpha_f \rangle \Delta T, \quad (6.7)$$

where  $\Delta T = -244$  K for  $T_P = 50$  K. Using the thermal expansion coefficients from Tab. 6.4, from Eq. (6.7) one obtains the values  $\epsilon_a = 7.4 \times 10^{-3}$  and  $\epsilon_b = 2.3 \times 10^{-2}$ .

The tensile stress at the temperature of the Peierls transition is [67]:

$$\sigma_{tens} = \epsilon \frac{E_f}{1 - \nu_f}, \quad (6.8)$$

where  $E_f$  is the elastic modulus of TTF-TCNQ and  $\nu_f$  is the Poisson ratio.  $E_f$  at the room temperature is equal to  $2.2 \times 10^{10}$  Pa and at 54 K it is about  $3.3 \times 10^{10}$  Pa [180–185]. The Poisson ratio was taken as 0.4 [130, 184, 186]. Based on these values the tensile stress along the  $a$ -axis of a TTF-TCNQ domain was estimated as  $\sigma_a^{tens} = 0.4$  GPa and along the  $b$ -axis as  $\sigma_b^{tens} = 1.3$  GPa. The calculated tensile strain and stress in the TTF-TCNQ domains are compiled in Tab. 6.4.

**Table 6.4:** *Thermal expansion coefficients of TTF-TCNQ and calculated values for tensile strain and stress in TTF-TCNQ microcrystals at 50 K along  $a$ - and  $b$ -crystallographic axes.*

Axis	Thermal expansion coefficient ( $\text{K}^{-1}$ )	Strain	Stress (GPa)
$a$	$3.05 \times 10^{-5}$	$7.4 \times 10^{-3}$	0.4
$b$	$9.4 \times 10^{-5}$	$2.3 \times 10^{-2}$	1.3

TTF-TCNQ single crystals compressed by hydrostatic pressure of the same order of magnitude as calculated above experience a slight shift of the Peierls transition temperature of about  $\pm 4$  K [6, 122]. It is not proper to naively compare the possible effects of biaxial strain with results for hydrostatic pressure quantitatively. However, it may provide a qualitative idea about the range of changes of the Peierls transition temperature in the case of the biaxial strain as is expected to occur in the TTF-TCNQ microcrystals. The thermal tensile strain caused by the substrate-induced interaction decreases the overlap of the electronic wave function in TTF-TCNQ along the stack direction and one might rather expect an increase of the Peierls transition temperature. However, as of this writing, the influence of biaxial strain on the Peierls transition temperature has not been studied by theoretical means. Therefore, we are left with the qualitative statement that the strain effect is most likely not significant against the background of the change of the phase transition due to the induced defects. The Peierls transition temperature in TTF-TCNQ domains irradiated with electrons is attributed to the point where the exponent in the variable-range hopping behavior changes, i.e. at about 50 K. Due to the interplay of the effects caused by defects (decrease of  $T_P$ ) and by biaxial strain (possible increase of  $T_P$ ), each individual aspect cannot be separated in the present case. Theoretical support is needed at this point to shed further light on the open questions.

## 6.6 Summary

In this chapter the charge carrier dynamics in individual TTF-TCNQ domains fabricated by physical vapor deposition was discussed. The individual domain represents a system in which thin-film-specific aspects, like substrate-induced strain, size effects and disorder-induced changes in the electronic structure, are combined. The results obtained on TTF-TCNQ domains are compared with data obtained on epitaxial, as-grown TTF-TCNQ films of the two-domain type.

The contact fabrication process employed in this work is associated with defect incorporation which is caused by electron irradiation of the organic microcrystals. The manifestation of the Peierls phase transition in the TTF-TCNQ domains is smeared out in the resistivity-temperature dependence. The relatively high defect concentration results in a variable-range hopping behavior of the resistivity, instead of the commonly observed metallic or thermo-activated one. A non-linear behavior in the current-voltage characteristics develops below about 100 K.

The properties of TTF-TCNQ domains differ dramatically from those of TTF-TCNQ single crystals and thin films. The influence of the substrate on the grown domains is appreciable. The development of tensile strain in the domain upon cooling may lead to an increase of the Peierls transition temperature. In contrast to this, the possible change of the Peierls transition temperature due to the developed biaxial strain is counterbalanced by the influence of defects, which leads to a net reduction of the phase transition temperature. For the individual domains, variable-range hopping behavior of a different kind above and below a temperature of about 50 K, corresponding to a slightly suppressed Peierls transition temperature, was observed. The data below 50 K can be explained in the framework of the segmented metal-rod model of Fogler, Teber and Shklovskii developed for a quasi-one-dimensional electron crystal [175]. The observed threshold voltage for TTF-TCNQ domains is assumed to correspond to a depinning of the charge density wave below  $T_P$ , which persists as a fluctuating contribution at temperatures above  $T_P$  despite the relatively large defect concentration.

The approach followed in this work provides a new pathway to the isolation of individual TTF-TCNQ (or other organic charge transfer) domains for studying size effects and clamping. The electron-beam-induced effects are very useful for studying the influence of irradiation-induced defects. The combination of all of these aspects leads to additional complexities and it is concluded that (i) the combined action of finite-size effects and disorder causes a crossover from Arrhenius-like to variable-range hopping transport in TTF-TCNQ; (ii) the influence of biaxial strain has to be disentangled from the finite-size and irradiation effects. It would be desirable



to optimize the domain contact fabrication such that it can be performed without excessive defect formation.



**ORGANIC CHARGE-TRANSFER PHASE  
FORMATION IN THIN FILMS OF THE  
BEDT-TTF/TCNQ DONOR-ACCEPTOR  
SYSTEM**

**W**ithin the many different organic charge transfer compounds, which have been studied during the last decades, the complex (BEDT-TTF)TCNQ (bis(ethylenedithio)-tetrathiafulvalene-tetracyanoquinodimethane) is particularly interesting [61, 101, 104]. It exists in three different structural variants, namely as monoclinic semiconductor [14], triclinic semiconductor  $\beta'$  [15] or triclinic metal  $\beta''$  [16] phases. The triclinic semiconductor phase experiences a correlation-driven metal-insulator transition at 330 K [15, 101], while the triclinic metallic  $\beta''$  phase shows anomalies in its electrical conductivity, which are assumed to be of magnetic origin [104]. A detailed description of the physical properties and peculiarities of the crystallographic phases of the (BEDT-TTF)TCNQ charge transfer complex is given in section 4.2.

In spite of the interesting properties of (BEDT-TTF)TCNQ, a systematic study of this material concerning its phase formation via vapor phase route has not been reported so far. Moreover, to date there have been no literature reports about the growth of (BEDT-TTF)TCNQ thin films by means of OMBD. In the present work, physical vapor deposition was used to form acceptor (TCNQ) – donor (BEDT-TTF) bilayer films. The subsequent post-growth annealing of the sample promotes the formation of the (BEDT-TTF)TCNQ charge transfer compound at the layer's interface. Here, the phase formation of (BEDT-TTF)TCNQ at the layers' interface was studied by inspecting the interface region employing focused ion beam (FIB) cross-section

analysis (for details see section 3.2.4). Additional information was received from the investigation of the formation of (BEDT-TTF)TCNQ by co-evaporating of BEDT-TTF and TCNQ molecules, as well as by using (BEDT-TTF)TCNQ crystallites from solution growth as a source material [19].

The main result of the investigation is that a charge transfer phase does form at the interface region of bilayer samples under proper annealing conditions. The composition of the CT crystals was analyzed by energy dispersive X-ray spectroscopy and employing X-ray diffraction. The charge transfer phase was identified as the monoclinic variant of (BEDT-TTF)TCNQ.

## 7.1 Evaporation parameters of the BEDT-TTF donor and TCNQ acceptor molecules

Before the fabrication of BEDT-TTF/TCNQ bilayer samples, several experiments for establishing the donor and acceptor evaporation parameters were performed. For this purpose the BEDT-TTF and TCNQ thin films were grown at different evaporation temperatures. X-ray diffraction patterns and optical microscopy images are presented in Fig. 7.1 and Fig. 7.2 for BEDT-TTF thin films grown at 120...180 °C and TCNQ thin films grown at 90...170 °C, respectively. Glass slides were used as substrates and kept at room temperature. The optical images show the evolution of the films' morphology for different evaporation temperatures. From the X-ray peak intensities, peak ratios and their form the appropriate evaporation temperatures for donor and acceptor molecules were determined.

In the case of BEDT-TTF, an evaporation temperature of 155 °C was found to be appropriate, being the value between 150 °C and 160 °C (see curves (c) and (d) in Fig. 7.1). The literature value for the BEDT-TTF evaporation temperature lies in the range 80...200 °C [109,110,188]. However, we observed that, despite the high melting point ( $\sim 242$  °C [111]), BEDT-TTF tends to dissociate already for effusion cell temperatures above 170 °C. The BEDT-TTF dissociation became apparent from characteristic sulphur ( $0\ell\ell$ ) Bragg reflections at  $15.5^\circ$  and  $30^\circ$  (see Fig. 7.1c,f). The sulphur peaks are indicated in Fig. 7.1e. Also signs of the decomposition are evident from a color change of the source material from red-orange to dark brown and the occurrence of a specific smell of hydrogen sulphide  $H_2S$  in the vacuum pump exhaust. The same observation was mentioned in [188], where it was shown that due to a partial dissociation of BEDT-TTF into fragments it prevents an ordered growth of BEDT-TTF thin films [188]. For the sample growth, we decided to use the lower limit for the evaporation temperature of BEDT-TTF in order to achieve the highest

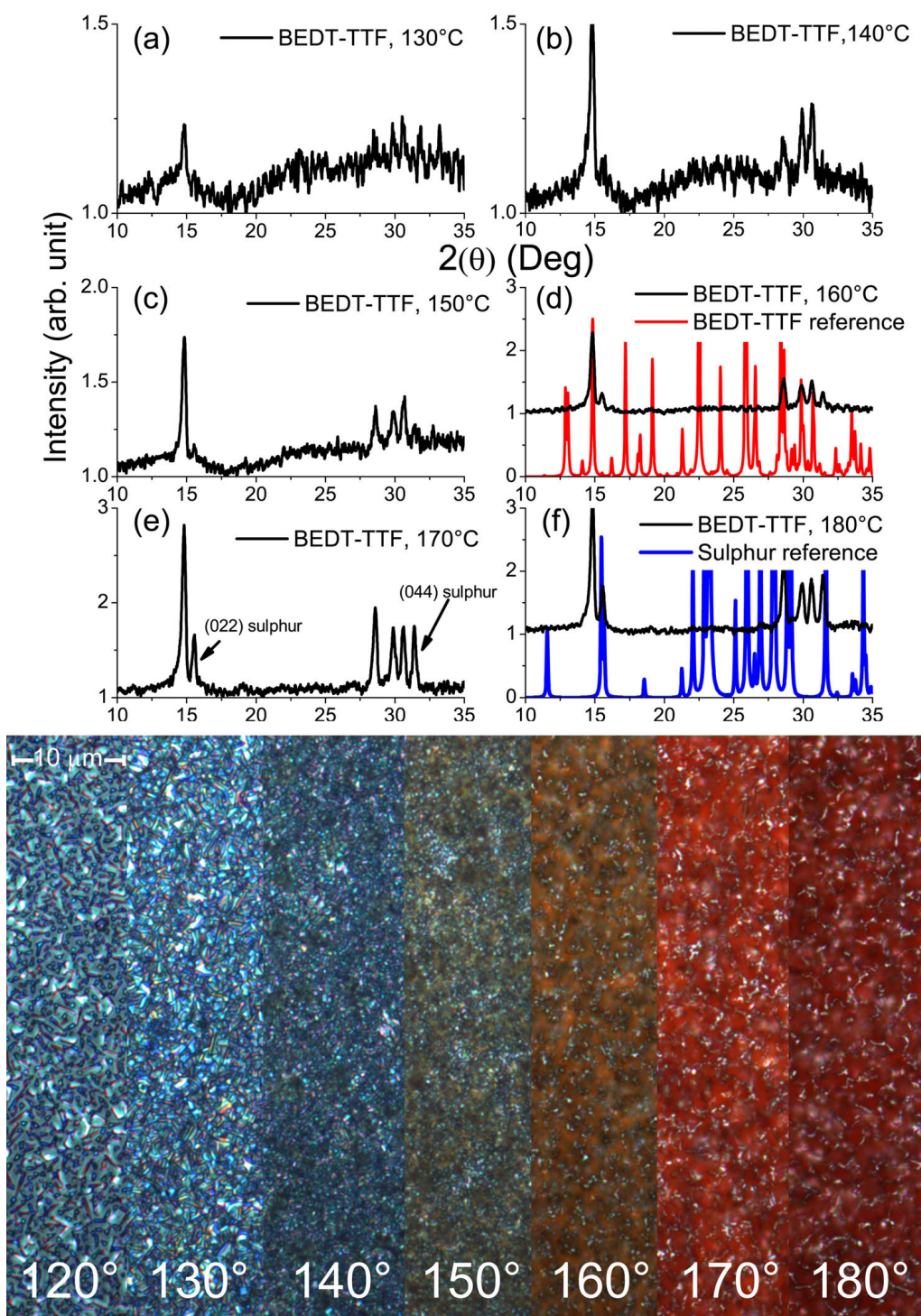


**Figure 7.1:** *BEDT-TTF* thin films, grown in the “test” chamber: (top) X-ray diffraction patterns for *BEDT-TTF* thin films grown at evaporation temperature (a) 130 °C, (b) 140 °C, (c) 150 °C, (d) 160 °C, (e) 170 °C and (f) 180 °C. The reference XRD pattern for *BEDT-TTF* [72] is shown by the red line in (d). The reference XRD pattern for sulphur [187] is shown by the blue line in (f). (bottom) Optical images of *BEDT-TTF* thin films. Each indicated temperature corresponds to 1 hour deposition time.

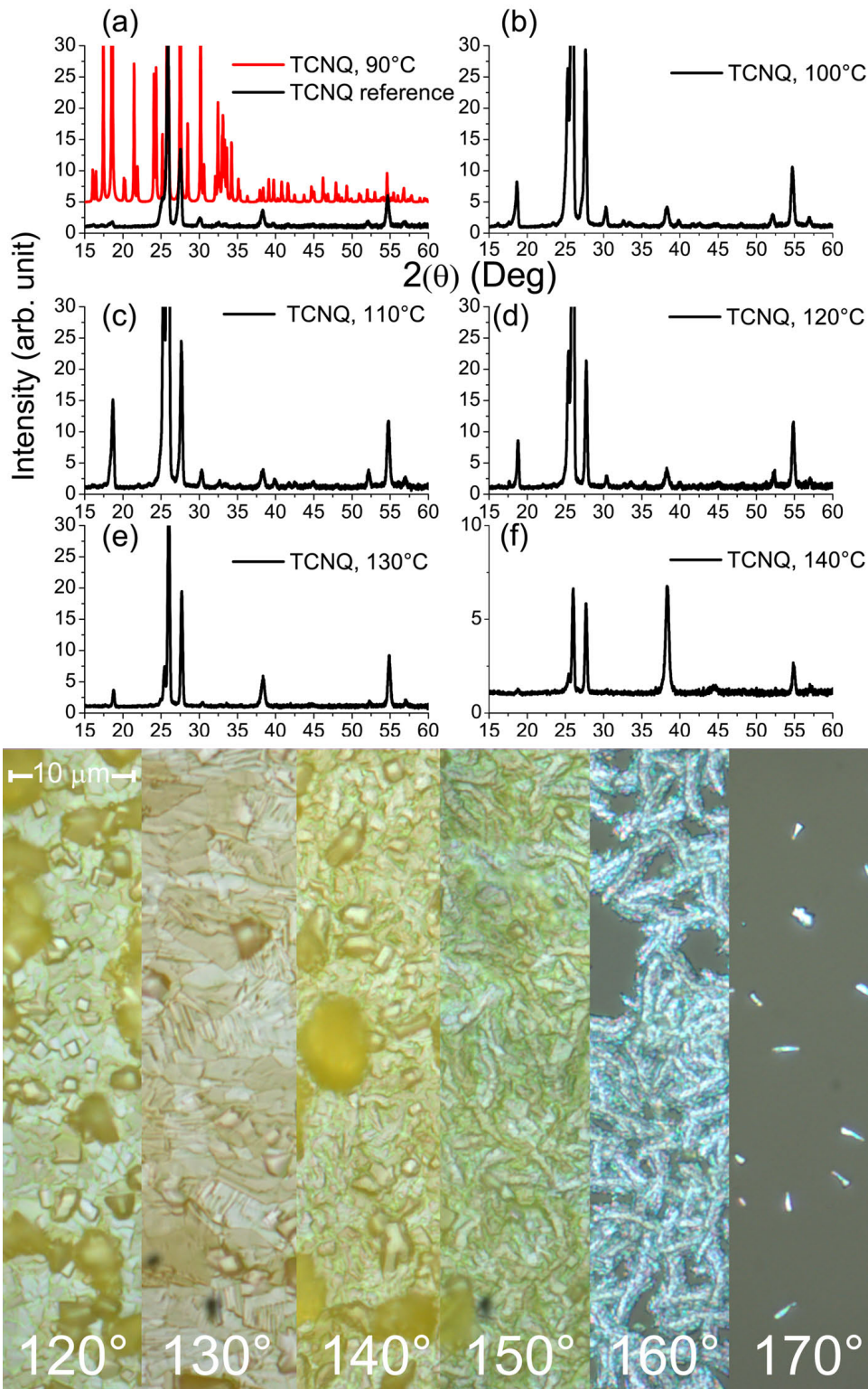


**Figure 7.2:** *TCNQ thin films, grown in the “test” chamber: (top) X-ray diffraction patterns for TCNQ thin films grown at evaporation temperature (a) 90 °C, (b) 100 °C, (c) 110 °C, (d) 120 °C, (e) 130 °C and (f) 140 °C. The XRD reference pattern for TCNQ [73] is shown by the red line in (a). (bottom) Optical images of TCNQ thin films. Each indicated temperature corresponds to 1 hour deposition time.*

film quality, as which was judged from X-ray diffraction data (see Fig. 7.1).

TCNQ shows more stability against decomposition during evaporation up to 170 °C (see Fig. 7.2). Evaporation temperatures higher than 170 °C were not investigated because the evaporation rate at this temperature is very high and does not allow thin films to be grown in a controllable way. Therefore, the temperature range appropriate for TCNQ evaporation is 100...170 °C. From the shape of the X-ray peaks and their ratio, the temperature range 100...140 °C is preferable because of the better film crystallization. This temperature range is in good agreement with reported data for TCNQ thin films (e.g. [112]). For the bilayer experiments the evaporation temperature for the TCNQ component was chosen to be 110 °C (see graphs (c) and (d) in Fig. 7.2). These experiments were performed with a 10 mm distance between the effusion cell orifice and the substrate surface.

## 7.2 BEDT-TTF/TCNQ bilayer growth

With the determined deposition parameters for donor and acceptor molecules, bilayer films were fabricated. BEDT-TTF/TCNQ bilayers of various thicknesses were prepared by sequential physical vapor deposition of, first, TCNQ and, second, BEDT-TTF at a background pressure of  $3 \times 10^{-7}$  mbar or less in the “test” chamber (see section 3.1.3). TCNQ was deposited at 110 °C and BEDT-TTF at 155 °C, which corresponds to growth rates of about 2 nm/s and 1 nm/s, respectively. The deposition rate was determined from FIB cross-section measurements done after film growth. The TCNQ layer was deposited first because it has a higher vapor pressure than BEDT-TTF and tends to desorb from a substrate, even at moderately elevated temperature. The TCNQ layer was exposed to air before the deposition of the subsequent BEDT-TTF film because the deposition chamber contains only one effusion cell and the source material needed to be changed after the first deposition. As a substrate material, glass microscopy slides with pre-patterned Au/Cr contacts and Si(100)/SiO<sub>2</sub> (300 nm)–with and without Au template layers–were used. The substrates were held at room temperature during the entire growth process. In order to stimulate the CT phase formation at the bilayer interface, post-growth annealing of the samples was done in <sup>4</sup>He inert gas environment at 60...80 °C for up to 48 hrs employing a Peltier element. The substrate was glued on top of the Peltier element by silver paint. Photographs of glass slides with BEDT-TTF/TCNQ bilayers before and after annealing are shown in Fig. 7.3. The color change of the bilayer after annealing is evident. The red color, characteristic for BEDT-TTF (see Fig. 7.3a), is changed into a dark brown-black color of the annealed bilayer (see Fig. 7.3b).

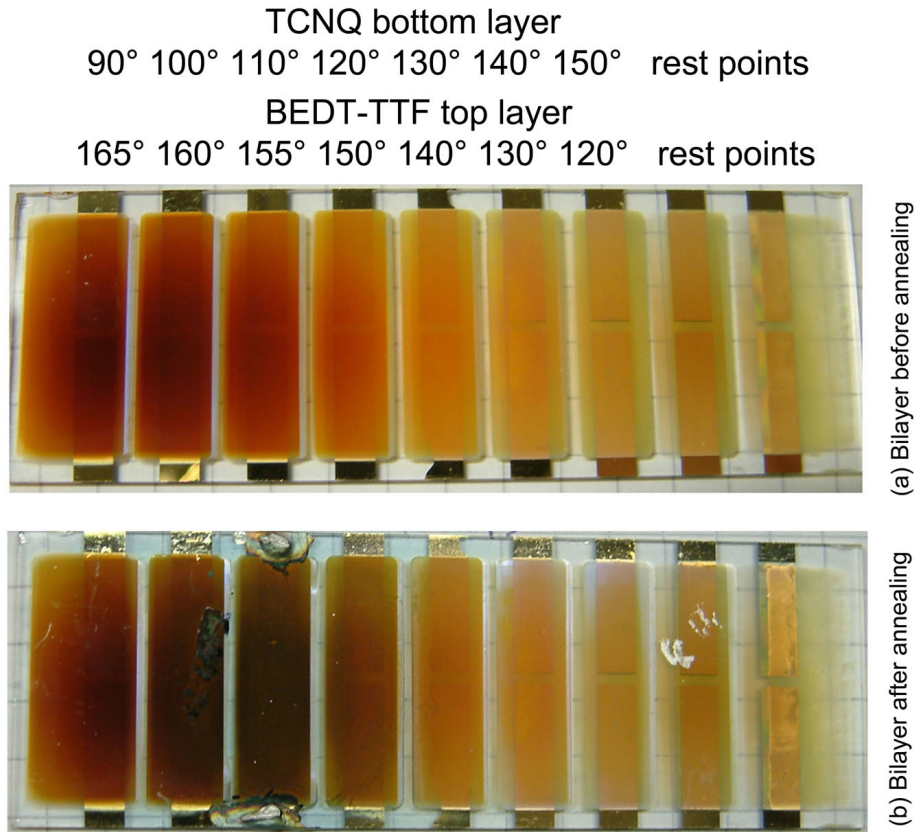


**Figure 7.3:** *BEDT-TTF/TCNQ bilayers grown on glass substrates with prefabricated Au/Cr contacts (a) before and (b) after annealing. The color change of the film indicates the formation of a CT phase.*

### 7.3 BEDT-TTF/TCNQ bilayer characterization

To characterize the BEDT-TTF/TCNQ bilayers the techniques outlined in chapter 3 were used. A Leica DM 4000M optical microscope was used for optical inspection to track the changes taking place after the annealing. X-ray diffractometry was done to study the crystallographic phases. SEM was done with a FEI xT Nova NanoLab 600 at 5 kV and a beam current of 98 pA. A Ga ion source FIB operating at 30 kV with beam currents between 30 pA and 1 nA was used for the preparation of cross-sections. EDX at 5 keV was employed for determining the composition of the grown structures. Additional information about the composition was derived from Hard X-Ray photoemission spectroscopy (HAXPES) measurements performed at the DESY HASYLAB synchrotron in Hamburg.



### 7.3.1 Optical microscopy

The bilayer samples were inspected by optical microscopy at different stages of the experiment, i. e. after the deposition of each layer and after the post-growth annealing. Typical images, as recorded after the deposition of the second layer and after the post-growth annealing of a bilayer grown on a glass substrate, are shown in Figs. 7.4a and 7.4b, respectively. Figure 7.4b shows that after the post-

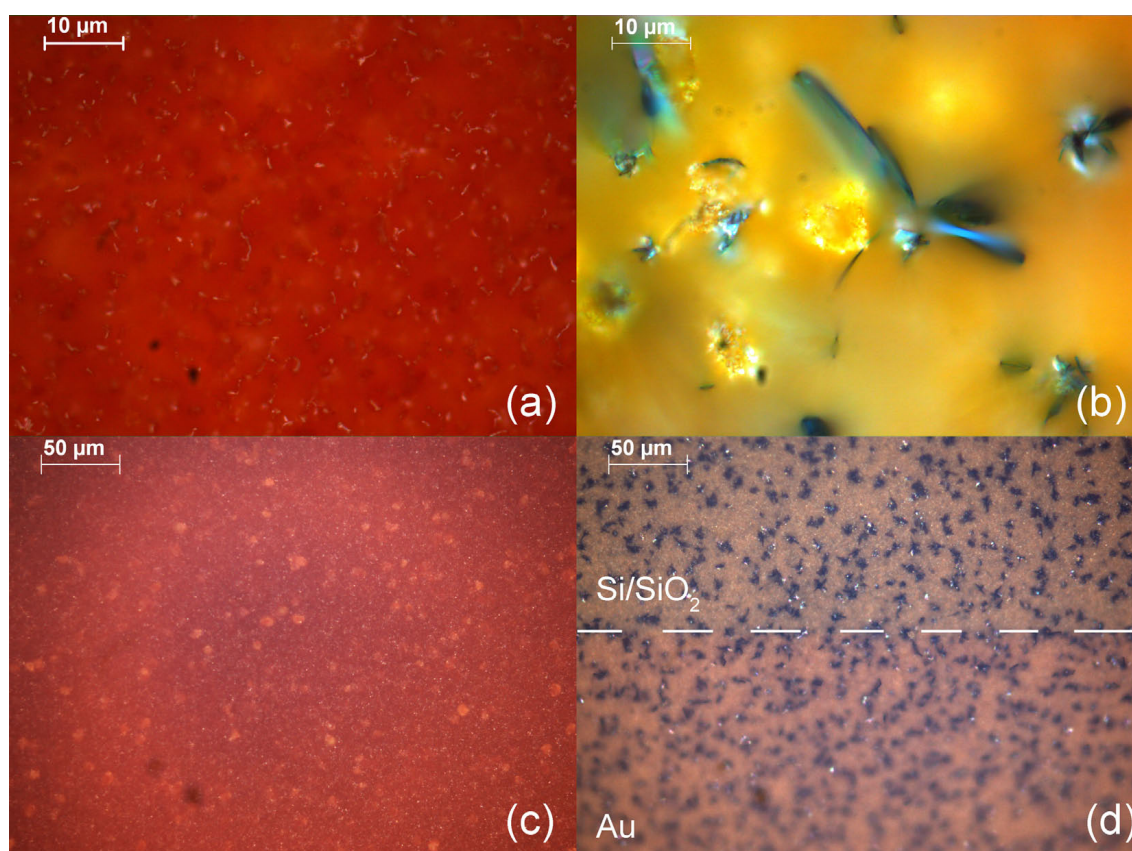


**Figure 7.4:** Optical microscopy images of (BEDT-TTF)TCNQ bilayer samples. Top row: bilayer grown on a glass substrate. Bottom row: bilayer grown on a Si/SiO<sub>2</sub> substrate one half of which is covered with a gold layer. Images (a) and (c) show the bilayer after the deposition of the BEDT-TTF layer on top of the TCNQ layer. Image (c) shows the bilayer grown on the bare Si/SiO<sub>2</sub>. Images (b) and (d) show the bilayer after the post-growth annealing. The dashed line in (d) indicates the border between the bare Si/SiO<sub>2</sub> and Au-covered Si/SiO<sub>2</sub> surface.

growth annealing black crystals are formed originating from the interior of the top BEDT-TTF-layer as compared with the not yet annealed sample (see Fig. 7.4a), where no newly formed crystals could be observed. This was a first indication for

a CT phase transformation in the system after the post-growth annealing. The same observation was made for bilayers grown on Si(100)/SiO<sub>2</sub> substrates one half of which was covered by a gold layer. Comparing Fig. 7.4c and Fig. 7.4d for non-annealed and annealed bilayers, respectively, black crystals are observed to emerge in the annealed bilayer. Based on the observations made in the optical microscope, a more detailed analysis was carried out.

### 7.3.2 SEM and EDX investigations of BEDT-TTF/TCNQ bilayers

The size and morphology of the crystallites formed after annealing for bilayers grown on different substrate materials were investigated by SEM. The characteristic size of crystals grown from layers on the glass substrate is  $\gtrsim 10 \mu\text{m}$ , as is exemplarily shown in Fig. 7.5a. The crystals have typically a prismatic shape and are oriented inclined to the film surface, as also follows from optical microscopy (see Fig. 7.4b). Crystals

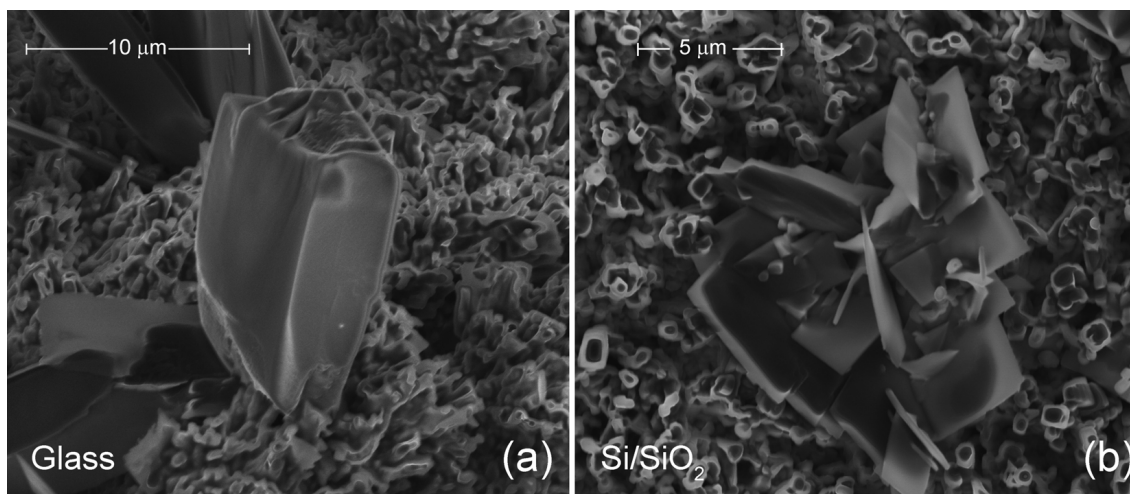


**Figure 7.5:** (a) SEM image of individual (BEDT-TTF)TCNQ crystal formed in the course of the post-growth annealing procedure of a bilayer grown on a glass substrate. The characteristic size of the crystal is  $\sim 10 \mu\text{m}$ , as indicated in the figure. (b) A group of (BEDT-TTF)TCNQ crystals which had been formed during the post-growth annealing of a bilayer grown on a Si(100)/SiO<sub>2</sub> substrate. The characteristic size of one crystal in this case is  $< 5 \mu\text{m}$ , as indicated in the figure.

obtained on Si(100)/SiO<sub>2</sub> and Si(100)/SiO<sub>2</sub>/Au substrates show a plate-like shape and their characteristic size is smaller than  $5 \mu\text{m}$  (see Fig. 7.5b). Note that for the Au-covered and bare part of the Si/SiO<sub>2</sub> substrate the crystals' average size and

inclination to the surface do not appear to depend systematically on the underlying substrate surface. Presumably, the observed morphological differences between the crystallites formed on glass and Si/SiO<sub>2</sub> are due to the different RMS-roughnesses of the respective substrate surfaces. From atomic force microscopy measurements in non-contact mode, the RMS-roughnesses was determined to be 6 nm and 0.6 nm (scan range 10 μm×10 μm) for the glass and Si/SiO<sub>2</sub> substrates, respectively.

As a further step in the course of the experiment the chemical composition of the black crystallites was analyzed. Calculations of the necessary thickness of the BEDT-TTF top layer that would prevent undesired X-ray fluorescence (by penetrating electrons from the primary beam from the bottom TCNQ layer) were performed by Monte Carlo simulations using Casino [78]. At 5 kV the minimal needed thickness of the BEDT-TTF top layer was estimated to be 450 nm (see Fig. 7.6) being approximately one order of magnitude less than the thickness of the BEDT-TTF thin films in the experiment. Therefore, neither the bottom TCNQ nor the sub-

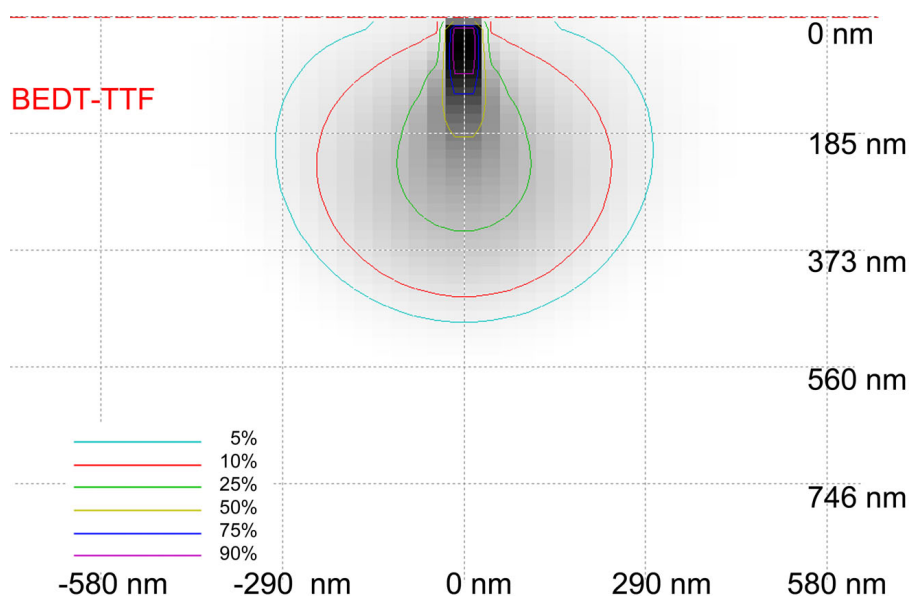


**Figure 7.6:** *Casino simulation [78]: cross-section view of absorbed electron energy caused by the BEDT-TTF thin film. The operating voltage is 5 kV. The electron penetration depth is below 500 nm.*

strate should have influenced the EDX measurements of the crystal composition and the results of the EDX measurements reliably reflect the chemical composition of the sample. EDX was used to determine the abundance of sulphur, nitrogen and carbon of the black crystallites in the bilayer grown on the Si/SiO<sub>2</sub> substrate. The result is S:N:C=21.0:9.8:69 (in atomic percents) with an estimated error margin of

$\pm 0.5$  for each component. The abundance of hydrogen atoms cannot be quantified by this method. The expected values for (BEDT-TTF)TCNQ ( $C_{22}H_{12}N_4S_8$ ) are S:N:C=23.5:11.8:64.7, if one considers the stoichiometry of the molecule. The measured proportion of carbon is higher than expected, which is attributed to carbon deposition induced by the electron beam dissociating adsorbed residual gases in the SEM vacuum chamber in the course of the EDX measurement. The ratio of sulphur to nitrogen in the measurement is  $2.15 \pm 0.15$ , which is, within the estimated error margin, in accordance with the expected ratio of 2.0 for the (BEDT-TTF)TCNQ compound.

Supplementary EDX element mapping experiments were performed to identify regions of high abundance of nitrogen and sulphur. They are presented in Fig. 7.7. In these experiments the EDX data acquisition covers an area greater than one crystal. As follows from the EDX element maps overlaid with the SEM micrograph of a group of crystallites formed after annealing, the enhanced abundance of nitrogen atoms coincides with the location of the new crystallite group (shown in red). The sulphur element map (green color) shows a rather homogenous distribution over the complete bilayer surface. From these observations, it is concluded that TCNQ molecules diffuse through the BEDT-TTF top layer during annealing. The element maps furthermore support the assumption that the black crystallites represent a CT phase of (BEDT-TTF)TCNQ.

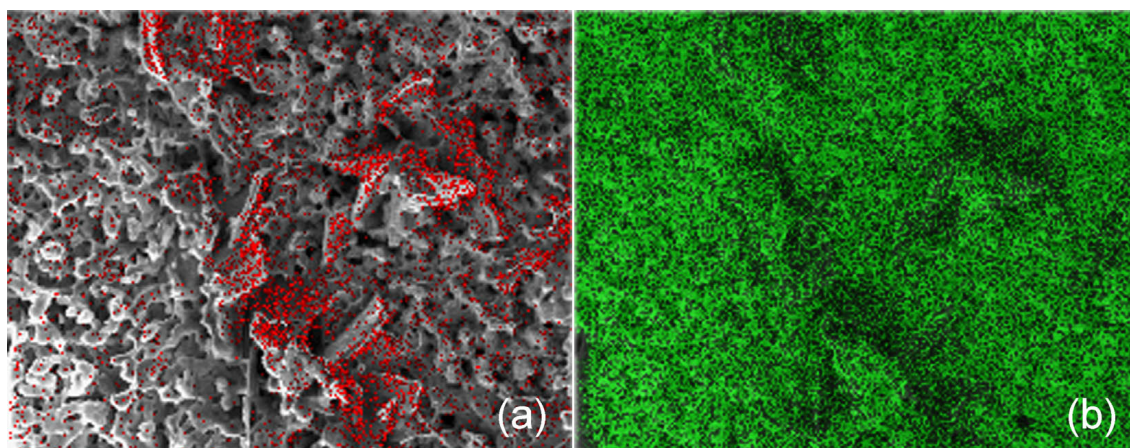


**Figure 7.7:** EDX element maps. (a) Overlay of the nitrogen element map (K-line) with a SEM image of a crystallite group protruding from the annealed bilayer grown on Si/SiO<sub>2</sub>. Nitrogen indicates the presence of TCNQ molecules. (b) Overlay of the sulphur element map (K-line) with the SEM image of the same crystallite group. Sulphur indicates the presence of BEDT-TTF molecules.

### 7.3.3 Hard X-ray photoelectron spectroscopy

Hard X-ray photoelectron spectroscopy (HAXPES) is a technique developed during the last decades [189], which uses higher excitation energy than conventional photoelectron spectroscopy. Therefore, HAXPES has the advantage of being more bulk sensitive, with electron inelastic attenuation lengths in the 50-150 Å range. It allows one to investigate samples fabricated *ex-situ*.

The HAXPES measurements, on bilayer samples grown on Si/SiO<sub>2</sub>(300 nm) substrates covered with gold (Au/Cr 100 nm/20 nm), were performed at DESY synchrotron in Hamburg, during the beam time in spring 2009. For HAXPES experiments valuable support was provided by Dr. Andrei Hloskovskyy. The gold layer on the Si/SiO<sub>2</sub> substrate is necessary for the HAXPES measurements because it decreases the charging effects of the thin films, which can have a severe influence on the measurement accuracy. The excitation energy of the X-ray photons was 3.5 keV. A SPECS Phoibos HSA15000 DLD 225 R6-HV hemispherical electrostatic energy analyzer was used. It allows to record the energy spectra for negative particles (electrons) and positive particles (ions) in the kinetic energy range from 0 eV to 3.5 keV. The resolution was 50 meV. The binding energy is determined using Eq. (7.1)

$$E_{bind} = E_{photon} - (E_{kin} + W), \quad (7.1)$$

where  $E_{bind}$  is the binding energy of the electron, being unique for each atom type,  $E_{photon}$  is the energy of the incident photons,  $E_{kin}$  is the measured kinetic energy of the photoelectron and  $W$  is its work function.

The measurements of the samples fabricated in Frankfurt were performed at DESY in an UHV chamber with a background pressure of about  $10^{-9}$  mbar. A photoelectron energy spectrum was acquired for each sample. The measured spectra of the core level electrons for carbon (C), sulphur (S) and nitrogen (N) of non-annealed and annealed bilayer samples are shown in Fig. 7.8a,b, and Fig. 7.8c, respectively. Comparing the spectra for the non-annealed and annealed BEDT-TTF/TCNQ bilayer samples one can see that a very weak nitrogen peak appears for the annealed sample (see Fig. 7.8c). This peak corresponds to the formation of CT crystals of (BEDT-TTF)TCNQ at the bilayer interface. In the HAXPES measurements the beam size was about 200  $\mu\text{m}$  and, therefore, it averaged over a large surface area resulting in a small intensity of the nitrogen peak as compared to the carbon and sulphur peaks. The experiments performed on annealed BEDT-TTF thin films do not reveal any trace of nitrogen. The emergence of nitrogen at the surface of the annealed bilayer is therefore in good agreement with the observations

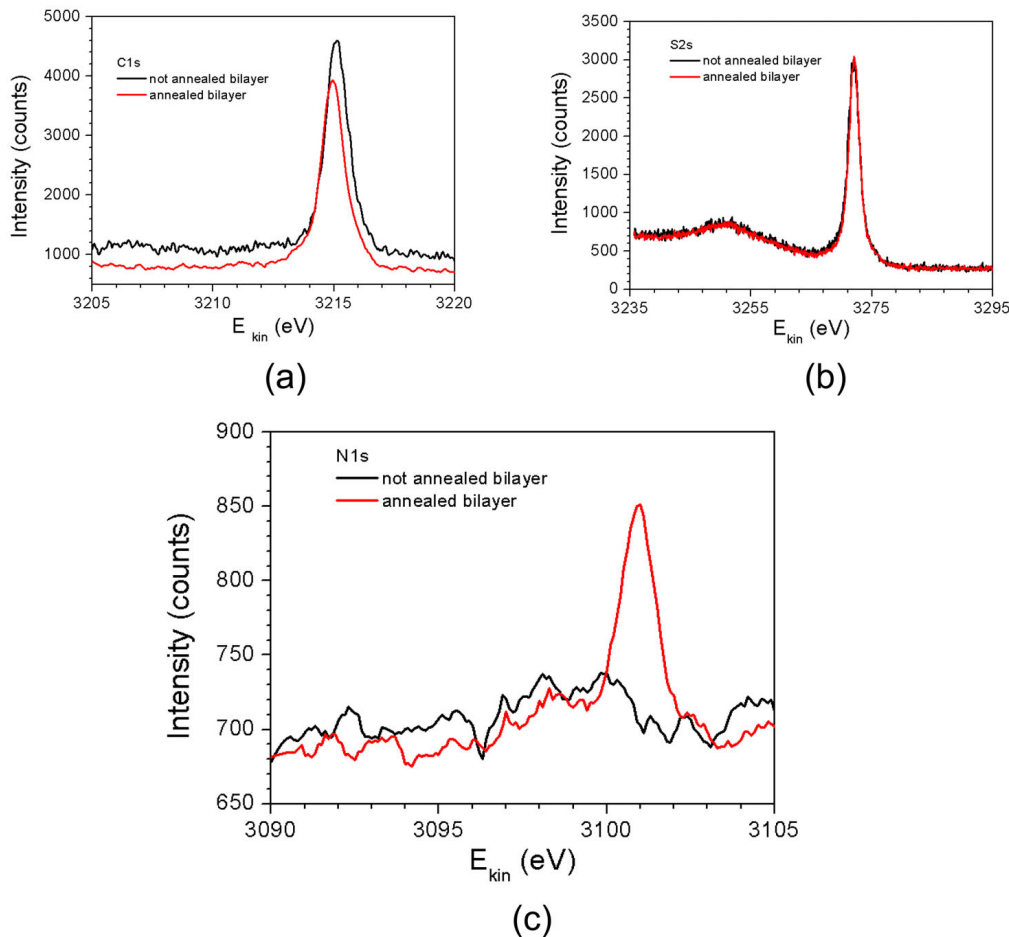


**Figure 7.8:** Results of the HAXPES measurements: core levels spectra for (a) carbon (C), (b) sulphur (S), (c) nitrogen (N) of the annealed (red line) and not annealed (black line) BEDT-TTF/TCNQ bilayers grown on a Si/SiO<sub>2</sub> substrate covered with Au/Cr layer.

from the EDX measurements described in section 7.3.2.

### 7.3.4 Focused ion beam cross-sectioning and X-ray diffraction

In order to obtain additional information about the TCNQ diffusion and charge transfer phase formation process, FIB cross-sections of the as-grown bilayer and of the bilayer after the post-growth annealing (see Figs. 7.9a-b) were prepared. In the cross-sections the individual TCNQ and BEDT-TTF layers can be easily identified,

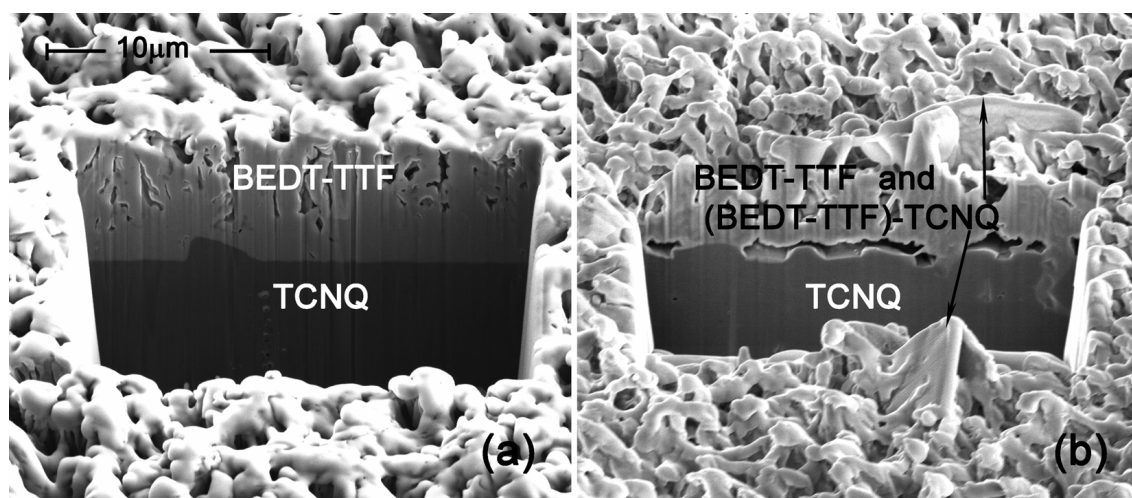


**Figure 7.9:** SEM images of FIB cross-section through the bilayers grown on a  $\text{Si}(100)/\text{SiO}_2$  substrate, (a) before and (b) after the post-growth annealing. The images were recorded for the sample being inclined to the electron beam by  $52^\circ$ . BEDT-TTF/TCNQ layers and (BEDT-TTF)TCNQ crystals are indicated. The scale bar applies to both panels.

with the BEDT-TTF layer appearing brighter because the average atomic number for this layer is higher than for the TCNQ layer. It is also apparent that the TCNQ layer is rather smooth whereas the BEDT-TTF layer is rough. In the as-grown sample the interface between the TCNQ and BEDT-TTF layers is smooth and planar. After annealing, cavities have been formed at the layers' interface (see Fig. 7.9b), which are attributed to diffusive transport of the highly mobile TCNQ molecules into the rough, capillaric BEDT-TTF top layer, in the course of which the charge transfer phase formation occurred. The thus formed CT crystals grow upward from the interface region and extend beyond the BEDT-TTF top layer as also shown in Fig. 7.5. From these cross-section measurements, the thickness of the top BEDT-TTF layer before and after annealing was determined. A noticeable reduction of the BEDT-TTF layer thickness from about  $6.4 \mu\text{m}$  to  $3.3 \mu\text{m}$  takes place. For TCNQ it is only possible to specify a lower limit of  $6.5 \mu\text{m}$  for the layer thickness, because the cross-section depth was not sufficiently extended to reach the substrate surface. The reduction in the BEDT-TTF layer thickness was attributed to the CT phase formation and also to partial desorption of BEDT-TTF from the rough top-layer surface during the annealing process.

To determine which of three crystallographic phases of the (BEDT-TTF)TCNQ charge transfer complex forms, X-ray diffraction measurements of the bilayers grown

on glass and Si/SiO<sub>2</sub> substrates were performed (see Fig. 7.10). After annealing, a

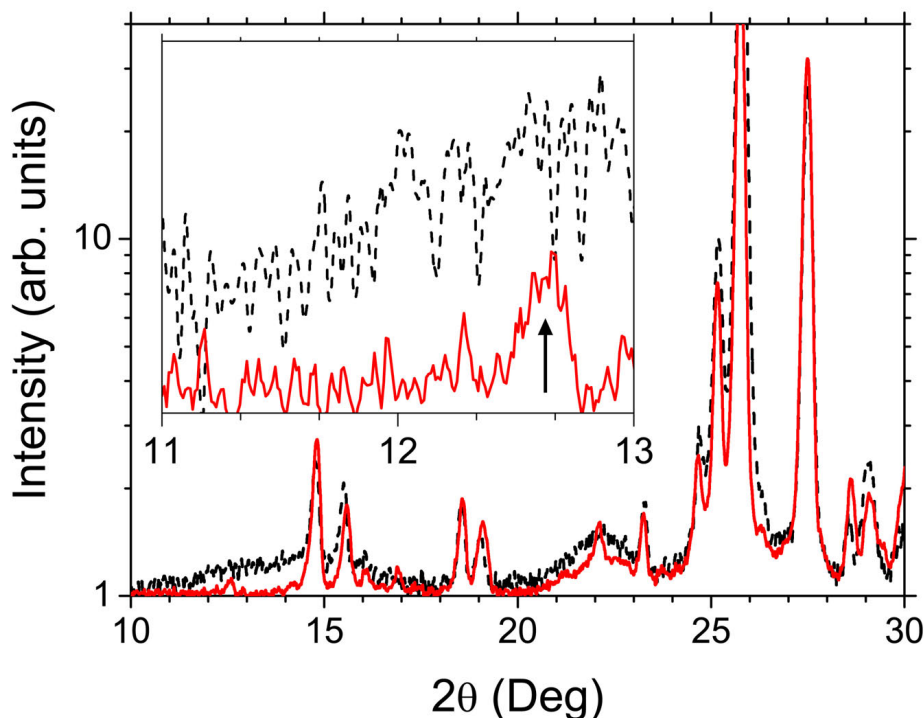


**Figure 7.10:** X-ray diffraction patterns for the as-grown and annealed BEDT-TTF/TCNQ bilayer grown on Si(100)/SiO<sub>2</sub> substrate shown by dashed and solid lines, respectively. Inset: Angular range in which a small new Bragg peak (indicated by the arrow) appears at 12.66° after annealing. See text for details.

new Bragg peak at  $2\theta = 12.66^\circ$  were observed, which could be tentatively attributed to the (10 $\bar{1}$ ) reflection of the monoclinic (BEDT-TTF)TCNQ phase. However, the small volume fraction of the black crystallites within the remaining layers of TCNQ and BEDT-TTF materials after annealing results in a correspondingly weak intensity of the X-ray diffraction pattern, which is furthermore overlaid with the strong BEDT-TTF and TCNQ Bragg reflections. The volume fraction of the CT phase can be enhanced if the contact area between the donor and acceptor layer is increased. This can be done best by co-evaporation of donor and acceptor, which is discussed in section 7.4.



### 7.3.5 Conductivity measurements

The electrical conductivity of the BEDT-TTF/TCNQ bilayer samples grown on glass substrates with pre-patterned Cr/Au contacts was measured (see Fig. 7.3). The contact preparation details are given in section 3.3. The measurements were performed by the two-probe method using Cr/Au contacts during sequential heating and cooling of the bilayer samples. The temperature dependence of the current measured at fixed bias voltage of 0.1 V for the as-grown bilayer and for the bilayer annealed for 12 hrs are shown in Fig. 7.11 by squares and dots, respectively. It

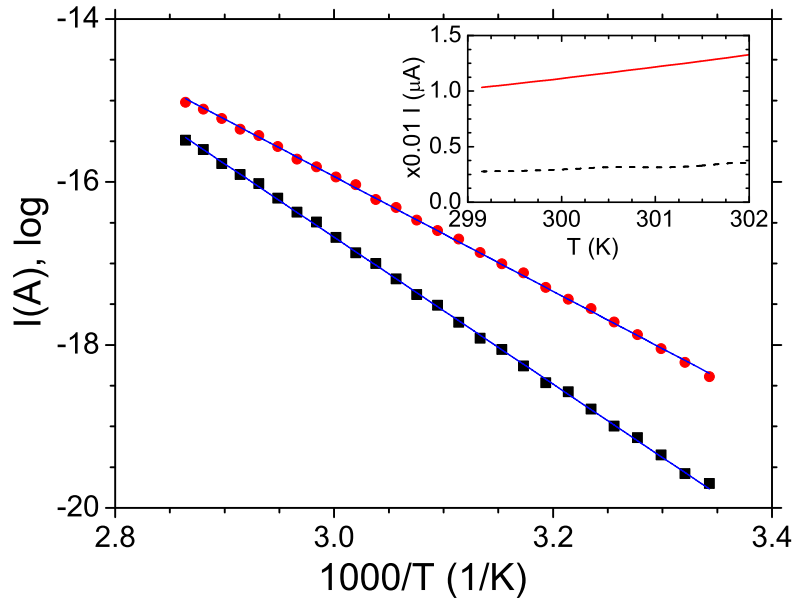


**Figure 7.11:** *Temperature dependence of the current through the TCNQ/BEDT-TTF bilayer in  $\ln \sigma$  vs.  $1/T$  representation at a fixed bias of 0.1 V. The squares represent data before bilayer annealing and the dots show data after 12 hrs annealing of the bilayer. The solid lines show the results of a linear fit. Room-temperature currents are shown in the inset for the sample before and after annealing by dashed and solid lines, respectively.*

is important to note that such a measurement, which was taken over the course of about 1 h, does represent a short annealing procedure in itself. Evidently, the current through the bilayer increases approximately by a factor of four at 300 K (see inset in Fig. 7.11) after the post-growth annealing. This increase is more pronounced if the number of heating cycles, the annealing time and the annealing temperature are increased.

The temperature-dependent conductivity  $\sigma$  shows thermally activated behavior, as is evident from Fig. 7.11 where  $\sigma$  is plotted in Arrhenius representation. Using Ohm's law  $I = \sigma ES$  ( $E$ : electric field,  $S$ : effective cross-section) and taking [31]:

$$\sigma = \sigma_0 \exp\left(-\frac{\Delta}{k_B T}\right), \quad (7.2)$$

where  $\Delta$  is the activation energy,  $k_B$  is the Boltzmann factor,  $T$  is the temperature and  $\sigma_0$  is the pre-exponential factor, one obtains the activation energy for non-annealed and annealed bilayers as  $\Delta_{non-anneal} = 0.77$  eV and  $\Delta_{anneal} = 0.61$  eV, respectively.

However, the conductivity measurements of the bilayer do not reflect the transport properties of the newly formed crystals of (BEDT-TTF)TCNQ, because of their small volume fraction in the film. The TCNQ layer is grown directly on top of the Cr/Au contacts and is more than  $6.5 \mu m$  thick. As follows from the SEM study (see Fig. 7.5 and Fig. 7.9) the CT crystals do not penetrate into the TCNQ layer, and the crystals make up only a small volume fraction and do not form a connected network. Thus, the derived activation energies mostly represent values for TCNQ alone without appreciable contributions of the BEDT-TTF and of the CT phase. The reference value for the activation energy of TCNQ single crystals obtained from the temperature-dependent measurements of the dark conductivity lies within the range of 0.48...0.6 eV [190–192], which is in good agreement with the results obtained for the bilayer. The decrease of the activation energy of the bilayer after annealing can be explained by the improvement of the TCNQ film structure in the course of the heating-cooling cycles. The results of conductivity measurements on BEDT-TTF/TCNQ bilayers do not give insight into the transport properties of the CT phase.

## 7.4 Preparation of (BEDT-TTF)TCNQ thin films by the co-evaporation method

As a comparison to the bilayer growth, where the formation of the CT phase takes place at the interface between donor and acceptor layers, experiments on the physical vapor deposition of thin films from the single component (BEDT-TTF)TCNQ salt prepared by solution growth (see section 4.3) and on the simultaneous co-evaporation of donor and acceptor molecules are discussed here.

To distinguish between the investigated samples, thin films prepared by single-source evaporation from (BEDT-TTF)-TCNQ crystallites are called sample type

“single-CT”, by co-evaporation of TCNQ and BEDT-TTF are called “co-A/D”, and by co-evaporation of TCNQ with (BEDT-TTF)TCNQ are called “co-A/CT”. The samples “single-CT” and “co-A/D” were deposited on glass substrates. The samples “co-A/CT” were grown in parallel on Si(100)/SiO<sub>2</sub> and  $\alpha$ -Al<sub>2</sub>O<sub>3</sub>(11 $\bar{2}$ 0) substrates. The film deposition took place in different MBE chambers depending on the respective experimental task. The “single-CT” samples were prepared in the “test” chamber as well as in the OMBD chamber (see section 3.1.3) where a heating of the substrate was performed. The distance between the sample surface and the effusion cell orifice in the “test” chamber was about 1 cm and in OMBD chamber it was about 2 cm. The background pressure in the “test” chamber was about 10<sup>-7</sup> mbar, while in the OMBD chamber the background pressure was 3×10<sup>-9</sup> mbar. The “co-A/D” and “co-A/CT” samples were deposited in the OMBD chamber, where the heating possibility was combined with the use of the two effusion cells, which are necessary for co-evaporation. The distance between the TCNQ effusion cell and the substrate surface was 16 cm, and between the BEDT-TTF cell and the substrate it was 2 cm. The details of the co-evaporation experiments are fully described in [70].

The growth of the “co-A/D” samples is appreciably hindered by the fact that BEDT-TTF tends to dissociate for effusion cell temperatures above 170 °C as discussed above. However, the higher effusion cell temperature for BEDT-TTF was required because in the co-evaporation experiments the cell-to-substrate distance was by a factor of two larger than in the bilayer experiments.

As the source material, the monoclinic phase of (BEDT-TTF)TCNQ grown in THF was used (see section 4.3). The growth of the “single-CT” samples on substrates held at room temperature results in the formation of thin films of the monoclinic CT phase of (BEDT-TTF)TCNQ albeit in badly crystallized form with the incorporation of pure BEDT-TTF and TCNQ. For these experiments a wide range of effusion cell temperatures was tested. The optical images of the films obtained in the course of the evaporation of the pre-reacted (BEDT-TTF)TCNQ are shown in Fig. 7.12 for the temperature range 120...180 °C. In the range of 130...150 °C the monoclinic phase of (BEDT-TTF)TCNQ is observed in X-ray diffraction (see Fig. 7.13a). The growth method, which employs the pre-reacted CT material, was inspired by experiments previously performed on TTF-TCNQ (see chapter 5). In this case it was shown that for physical vapor deposition, thin films of TTF-TCNQ CT phase form easily, although it remained unclear whether the vapor contains donor-acceptor dimers or individual donor and acceptor molecules and, therefore, where the formation of CT phase takes place. For BEDT-TTF/TCNQ it is considered to be highly unlikely that the flux contains (BEDT-TTF)TCNQ dimers because

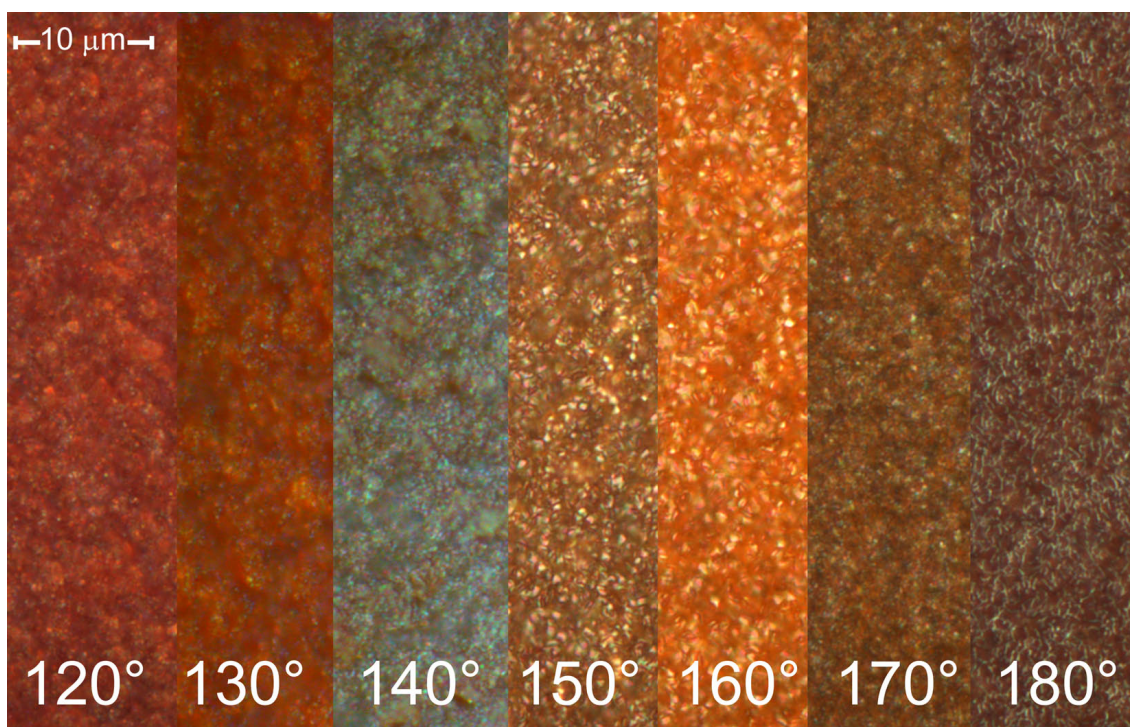


**Figure 7.12:** *Optical microscopy image of “single-CT” thin films grown on glass slides kept at room temperature. The effusion cell temperature was within the range of 120...180 °C.*

of the associated large mass. This assumption receives experimental support from the observation that pure, oriented and well-crystallized BEDT-TTF layers can be grown via the “single-CT” route as well as “co-A/CT” route if the substrate is held at elevated temperature about 100 °C. This is depicted in Fig. 7.13b for a layer grown on  $\alpha\text{-Al}_2\text{O}_3(11\bar{2}0)$ . The EDX measurements on a reference sample grown in parallel on Si/SiO<sub>2</sub> showed no trace of nitrogen. It is possible to speculate that during evaporation the TCNQ flux acts as a carrier gas for the BEDT-TTF molecules because TCNQ has orders of magnitude larger vapor pressure at any given temperature. On the substrate surface the TCNQ molecules then readily desorb at elevated substrate temperature whereas the BEDT-TTF molecules mostly stick to the surface. Even if the substrates are held at room temperature, it was observed that TCNQ layers tend to desorb easily. With regard to the optimal route towards CT layer growth it is concluded that the partial loss of TCNQ for the “single-CT” samples could be compensated in the co-evaporation experiments. The arguments outlined above suggest that the co-evaporation route is promising with regard to the growth of CT compounds via PVD.

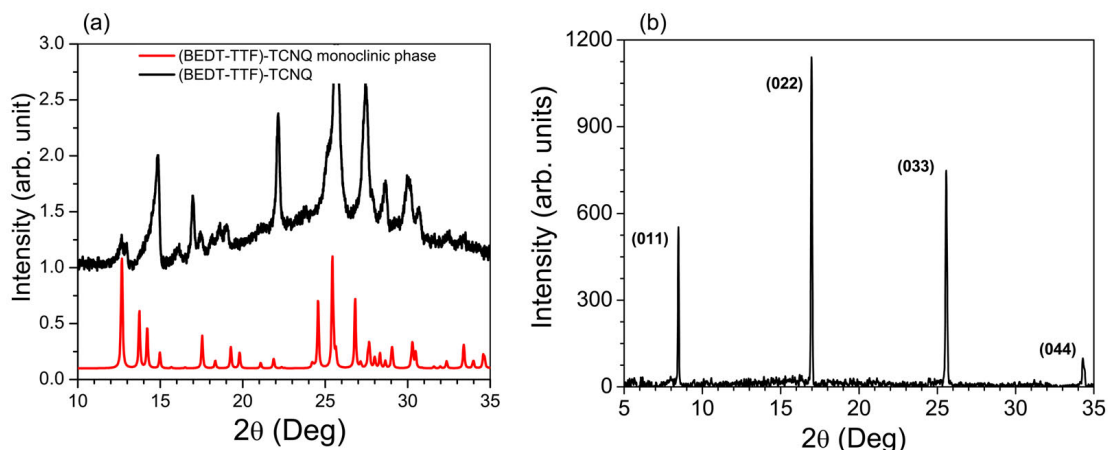


**Figure 7.13:** (a) The XRD pattern recorded for the “single-CT” thin film sample grown on glass substrate held at room temperature. The effusion cell temperature is 150 °C. (b) X-ray diffraction pattern of the “co-A/CT” sample grown on  $\alpha$ - $\text{Al}_2\text{O}_3$  (*a*-plane) substrate kept at 100 °C. (0*ll*) reflections of BEDT-TTF can be identified up to fourth order. The intensity of the peaks is shown in arbitrary units.

Instead of pure BEDT-TTF in the co-evaporation experiments also (BEDT-TTF)TCNQ grown in solution was used together with TCNQ. In this case (“co-A/CT” growth), the (BEDT-TTF)TCNQ of the monoclinic variant formed much better crystallized layers. The layers were prepared at effusion cell temperatures of 130 . . . 138 °C for TCNQ and 136 °C for (BEDT-TTF)TCNQ. Simultaneous thin film growth was done on  $\alpha$ - $\text{Al}_2\text{O}_3$ (11 $\bar{2}$ 0) and Si(100)/SiO<sub>2</sub> substrates, which were held at room temperature. Isolated small black crystals formed on the substrate surface (see Fig. 7.14). The determined sulphur-to-nitrogen ratio for a sample grown on Si/SiO<sub>2</sub> by EDX was  $1.89 \pm 0.13$ , which is, within the error margin, in accordance with the expected ratio of 2.0 for the (BEDT-TTF)TCNQ. X-ray diffraction patterns for the samples are shown in Fig. 7.15. In the X-ray pattern of the sample grown on  $\alpha$ - $\text{Al}_2\text{O}_3$  (11 $\bar{2}$ 0) the peaks at 12.66° and at 13.73° correspond to the (10 $\bar{1}$ ) and (101) reflections of the monoclinic phase of (BEDT-TTF)TCNQ. The corresponding second order diffraction peaks occur at 25.53° and 27.66°. For the Si/SiO<sub>2</sub> substrate only first order diffraction peaks can be resolved hinting towards a poor crystallization of (BEDT-TTF)TCNQ as compared to the other substrate material. Comparing with the BEDT-TTF/TCNQ bilayer the volume of the CT phase is enhanced and no trace of the pure moieties is observed.

In the bilayer growth experiments no indication of CT phase formation at the

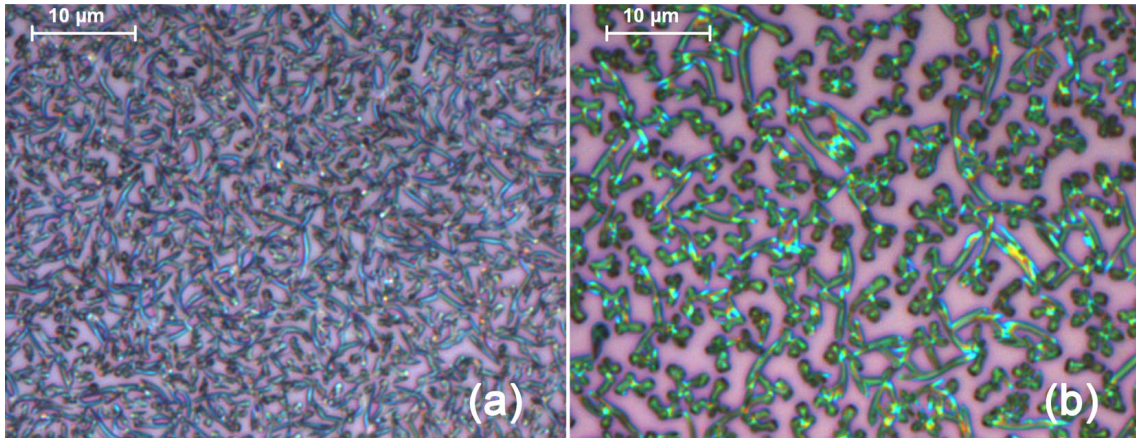


**Figure 7.14:** Optical microscopy images of the “co-A/CT” samples grown on  $\alpha$ - $\text{Al}_2\text{O}_3(11\bar{2}0)$  (a) and on  $\text{Si}(100)/\text{SiO}_2$  (b) substrates taken in differential interference contrast. Average crystal size is about  $4\ \mu\text{m}$  and  $6.5\ \mu\text{m}$  for  $\alpha$ - $\text{Al}_2\text{O}_3(11\bar{2}0)$  and for  $\text{Si}(100)/\text{SiO}_2$  substrates, respectively. Images were taken at  $500\times$  magnification.

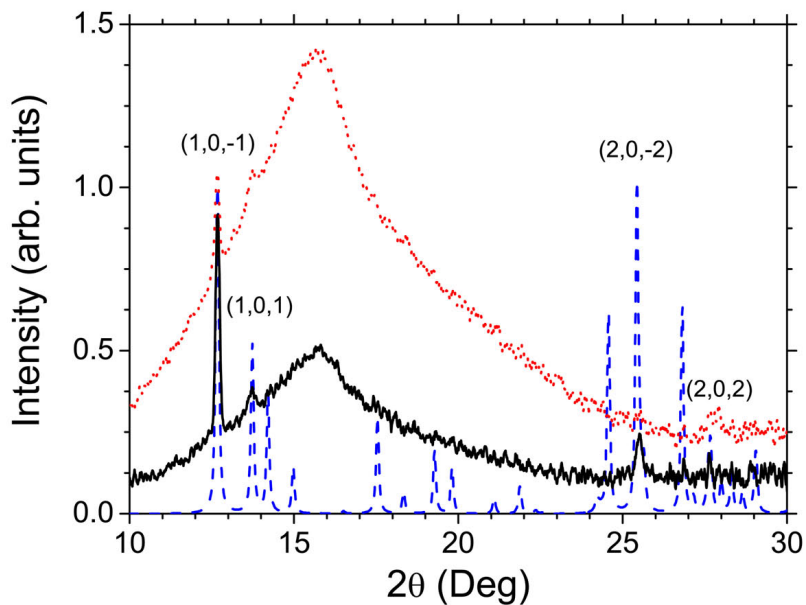


**Figure 7.15:** X-ray diffraction pattern of “co-A/CT” (BEDT-TTF)TCNQ samples grown on  $\text{Si}/\text{SiO}_2$  (dotted line) and on  $\alpha$ - $\text{Al}_2\text{O}_3$  (a-plane) (solid line). The intensity of the peaks is given in arbitrary units. Dashed line: Reference diffraction pattern simulated using Mercury 2.3 [71] for the monoclinic phase of (BEDT-TTF)TCNQ.

donor/acceptor interface for the as-grown (not annealed) samples could be detected within the resolution of the electron microscope (about 4 nm at the given settings). Nevertheless, the co-evaporation route proved to be successful. It is assumed that this is due to the overall enlargement of the number of directly touching donor and acceptor molecules as compared to the bilayer structure. The released heat during the CT process may be sufficient to drive further reactions by enhancing the mobility of the molecules and helping to overcome the activation barrier for the charge transfer process.

To conclude the section it is interesting to comment on possible reasons why the monoclinic variant of the CT-phase was formed in the performed experiments: in the bilayer growth, as well as in the co-evaporation. In the case of bilayer growth the CT-phase formation is close to equilibrium at the interface region. For the co-evaporation the growth occurs with large supersaturation that strongly suppresses the formation of CT-phase with slow kinetics. In both experiments only the monoclinic phase of (BEDT-TTF)TCNQ was detected. As it is known from solution growth (see section 4.3), the monoclinic variant of (BEDT-TTF)TCNQ is formed in the course of fast growth, while if the process is slow enough the  $\beta'$ -phase of (BEDT-TTF)TCNQ is more likely to occur. One may therefore conclude that the formation of the  $\beta'$ -phase is kinetically hindered.

## 7.5 Summary

A study of the formation of a charge transfer phase in the (BEDT-TTF)TCNQ donor-acceptor system prepared by physical vapor deposition was performed. A donor/acceptor bilayer approach was used and comparative investigations were performed for the layer interface for the as-grown and annealed bilayers. In this context focused ion beam cross-sectioning delivered valuable information about the charge transfer phase formation initiated at the interface. It was found that the monoclinic (BEDT-TTF)TCNQ charge transfer complex forms at the interface of the donor/acceptor bilayer.

It was also demonstrated that a charge transfer phase formation can be initiated by evaporation experiments from the pre-reacted charge transfer phase, as well as from the co-evaporation experiments of the donor/acceptor and acceptor/CT-phase. The results show that the pre-reacted CT phase can serve as a source material for the preparation of oriented BEDT-TTF layers at elevated substrate temperature on  $\alpha$ -Al<sub>2</sub>O<sub>3</sub> (11 $\bar{2}$ 0). In the case of (BEDT-TTF)TCNQ the use of pre-reacted (BEDT-TTF)TCNQ as one of the source materials is considered to be advantageous as

compared to evaporation from pure BEDT-TTF source material and it is possible to speculate that the TCNQ component acts as a carrier gas and thus allows for higher BEDT-TTF evaporation rates at moderate effusion cell temperature. More important for the present study is that the co-evaporation of the pre-reacted CT phase supplemented by TCNQ results in the direct formation of the monoclinic CT phase on substrates held at room temperature.

The bilayer approach used in the experiments here can be a valuable method for a systematic study of charge transfer reactions in donor/acceptor systems prepared by the vapor phase approach. In particular, this approach can be extended to other donor/acceptor combinations. In order to improve the efficiency of the method, finely modulated donor/acceptor multilayers can be applied which may serve as an intermediate of the bilayer and co-evaporation technique combining the advantages of both methods.



## CONCLUSION

The thesis is focused on the study of two charge transfer compounds systems grown from the tetrathiafulvalene (TTF) donor and tetracyanoquinodimethane (TCNQ) acceptor and from the bis(ethylenedithio)tetrathiafulvalene (BEDT-TTF) as donor and, again, TCNQ as acceptor. TTF-TCNQ and (BEDT-TTF)TCNQ charge transfer compounds were fabricated by using the physical vapor deposition method and their properties were comprehensively studied.

Thin films and microcrystals (i.e. individual domains) of TTF-TCNQ were studied. TTF-TCNQ is a well-known one-dimensional organic charge transfer complex. The thesis shows that some of the physical properties of TTF-TCNQ thin films, e.g. the Peierls transition, agree well with what has been known from TTF-TCNQ single crystals. Conversely, the Peierls transition in TTF-TCNQ domains is significantly altered.

A number of different substrate materials was considered in this thesis, and the influence of the substrate material on the Peierls transition in TTF-TCNQ thin films was analyzed. All used substrate materials did not cause a systematically quantifiable impact on the temperature of the Peierls transition, except for the NaCl(100) substrate. In this particular case, the dependence of the Peierls transition temperature on the film thickness could be identified. The influence of the substrate in this case could be explained by the epitaxial growth of TTF-TCNQ, which does not take place in other considered examples.

Due to their finite size, new physical aspects start to play a role for TTF-TCNQ microcrystals compared to thin films and single crystals. The Peierls transition in individual TTF-TCNQ grown domains is identified by a change of the transport regime and is about 50 K. Two competing factors, which influence the Peierls tran-

sition, were studied in the thesis: (i) electron beam irradiation-induced defects, and (ii) substrate-induced biaxial tensile strain. In spite of a thorough analysis of both factors performed in the thesis, the presently available experimental methods do not allow a single conclusion to be drawn concerning which factor plays the dominating role in influencing the Peierls transition. Therefore, two possible scenarios were suggested, aimed to inspire further experimental and theoretical studies in the field.

The (BEDT-TTF)TCNQ derivative of TTF-TCNQ was studied in the second part of the thesis. Contrary to TTF-TCNQ, (BEDT-TTF)TCNQ charge transfer thin films formed by the physical vapor deposition methods were not studied before. The monoclinic phase of (BEDT-TTF)TCNQ was successfully fabricated and discussed in the thesis. The study of differences and similarities in (BEDT-TTF)TCNQ and TTF-TCNQ allows to obtain an in-depth understanding of the underlying physical processes, which govern the transport properties in organic conducting materials. Advanced fabrication techniques, which were developed for analyzing the charge transfer phase formation in the gas phase, employed in this thesis, were successfully introduced in other scientific laboratories for studying similar organic charge transfer compounds [21].

The thesis provides a comprehensive study of TTF-TCNQ and (BEDT-TTF)-TCNQ charge transfer compounds with an overview of the existing experimental techniques and possible applications of the organic charge transfer compounds in industry. The physical vapor deposition method proved to be a promising tool for fabricating CT compounds in thin film form. The method significantly expands the possibilities of studying phase transition phenomena in various charge transfer complexes and allows for a flexible construction of organic electronic devices. The employment of the scanning electron microscope associated techniques, as focused ion and electron-induced deposition, in the study of the transport properties of organic charge transfer complexes was shown to be successful and can be applied in further experiments.

## PHOTOLITHOGRAPHY AND LIFT-OFF PROCESSES

The photolithography, lift-off and sputtering processes were employed to fabricate Au/Cr contacts. FIBID and FEBID contact deposition was performed between the pre-patterned Au/Cr contacts and TTF-TCNQ domains as described in chapter 3 and chapter 6.

### Photolithography

Si(100)/SiO<sub>2</sub>(285nm) substrates were covered by Au(100 nm)/Cr(20 nm) layers in a Pfeiffer Classic 500 coating system by means of electron beam evaporation. The photolithography process applied to the layers consisted of the following steps:

- Cleaning of the substrate covered with Au/Cr by acetone, isopropanol, ethanol, and distilled water two times.
- Spin coating of the positive resist AR-U-4040 on the substrate surface for 15 s with a frequency of 2000 rotations per minute and for 45 s with 8000 rotations per minute.
- Heating of the sample covered with the resist for 9 min at 90 °C on a hot plate.
- Photolithography of the substrate with the resist: illumination of the sample under the mask with UV light (mercury short arc lamp, HBO 350 W/S,  $\lambda = 365 \dots 400$  nm) having an energy flow of 70 mJoul/cm<sup>2</sup> and power about 6.3 mJoul/cm<sup>2</sup>s for 11 s.

- Developing of the exposed resist in the developer AR300-35 mixed with water 1:1 for 1.5 min. After the developing the substrate was rinsed with distilled water. For the positive resist the part exposed to the light is removed.
- Etching of the now exposed gold parts with Au etchant KI, I<sub>2</sub> mixed with water 2:18 for 3 min.
- The rest of the resist was removed by remover the AR 300-70 in the ultrasonic bath for 40..60 s and after that the substrate was left for 10 min lying unagitated in the solution.
- Removal of the exposed chrome by etching in chrome etchant for about 40 s. The etchant contained 500 ml of distilled water, 100 g of Cl(NH<sub>4</sub>)<sub>2</sub>(NO<sub>3</sub>)<sub>6</sub> and 18 ml of acetic acid (CH<sub>3</sub>COOH) that is diluted 1:3 with distilled water.

## Lift-off process

As an alternative to the photolithography step described above a lift-off process together with Au/Cr sputtering was employed for the fabrication of the Au/Cr contacts. The lift-off process included the following steps:

- Cleaning of the bare substrate by acetone, isopropanol, ethanol, and distilled water two times.
- Spin coating of the positive resist AR-U-4040 on the substrate surface for 3 s with frequency 2000 rotations per minute and for 57 s with 6000 rotations per minute.
- Heating of the substrate with resist on the hot plate for 2 min at 85 °C.
- Creation of the inverse photoresist pattern of the desired contact structure on the substrate. Exposure of the sample to UV light (70 mJ·cm<sup>-2</sup>) through a mask.
- Heating the substrate at 115 °C for 5 min on a hot plate (post exposure bake).
- Exposure of uncovered sample with UV light (180 mJ·cm<sup>-2</sup>).
- Developing of the resist for about 30 s in the developer AR 300-35 mixed 2:1 with distilled water, to selectively remove the photoresist in the areas where the contact material will be located after the final lift-off process by sputtering.

## Fabrication of the Au/Cr contacts in the sputtering chamber

The fabrication of the Au/Cr layers in the sputtering chamber was performed on substrates previously furnished with the lift-off structure, as described above. The sputtering process included the following steps:

- The sample is placed in three cathode UHV sputtering system with argon gas as sputter gas. A background pressure was in the range of  $5.7 \times 10^{-7} \dots 1.3 \times 10^{-6}$  mbar, a gas pressure was  $7.3 \times 10^{-3}$  mbar.
- To deposit chrome a *dc* potential of  $\sim 280 \dots 290$  V at a current of 10 mA are applied to the chromium target. A deposition time of 25 s corresponded to a thickness of the chrome film of about 10 nm. The deposition rate was 4 Å/s.
- To deposit gold a *dc* potential of 450...460 V at a current of 10 mA were applied to the gold target (gas pressure was  $7.2 \times 10^{-3}$  mbar). The deposition time for the gold layers of 250 s resulted in a film of 100 nm thickness. The deposition rate was 4 Å/s.
- To remove the rest of the resist the pure remover AR 300-70 was used and the sample was treated in ultrasound for about 2 hours at 60°C

The advantage of the lift-off process over the photolithography process is that open parts of substrate further used for TTF-TCNQ deposition are only covered with photoresist and do not react with chromium. Another benefit is that no aggressive etchant is applied to this part. Both aspects could have undesirable effects.



## EDX MEASUREMENTS OF TTF-TCNQ THIN FILMS

Energy-dispersive X-ray spectrometry (EDX) on TTF-TCNQ thin films grown by physical vapor deposition was performed in order to check the chemical composition of the TTF-TCNQ thin films grown from pre-reacted source material. A typical EDX spectrum for a TTF-TCNQ thin film grown on NaCl(100) is shown in Fig. B.1. The sulphur to nitrogen ratio for the measured TTF-TCNQ thin film was  $1.22 \pm 0.1$ . This is close the stoichiometric ratio of S:N for TTF-TCNQ being 1:1.

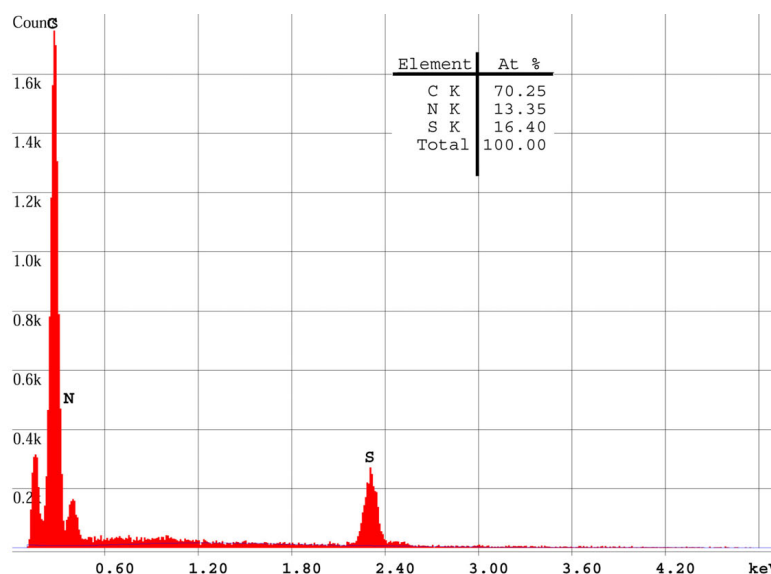


**Figure B.1:** EDX of a typical TTF-TCNQ thin film grown on NaCl(100).

The inspection of TTF-TCNQ thin films grown on NaCl(100) substrate was carefully performed. The EDX measurements of TTF-TCNQ thin film with a thickness of 175 nm showed the existence of two different areas. These areas were also observed in AFM measurements (see Fig. 5.7). The chemical composition of these areas was determined by EDX, too (see Fig. B.2). The first area corresponds to the top layer of the thin film where TTF-TCNQ crystallites with their  $b$ -axis oriented parallel to the  $\langle 110 \rangle$  and  $\langle \bar{1}10 \rangle$  axes of the NaCl(100) substrate could be identified (see Fig. 5.3 and Fig. 5.7d). The ratio of sulphur to nitrogen (corresponding to TTF:TCNQ) was  $0.92 \pm 0.1$ , as was verified by selected area EDX (see Fig. B.2a). The second area observed in AFM corresponds to a layer below the TTF-TCNQ crystallites of the grown thin film. The orientation of the crystallites in this region is parallel to the  $\langle 010 \rangle$  and  $\langle 001 \rangle$  directions of the NaCl(100) substrate (see Fig. 5.7b-c). The chemical composition of the crystallites of the lower layer of the thin film was measured by EDX and showed only the presence of nitrogen, demonstrating that this layer consists to a large extent of TCNQ molecules (see Fig. B.2b).

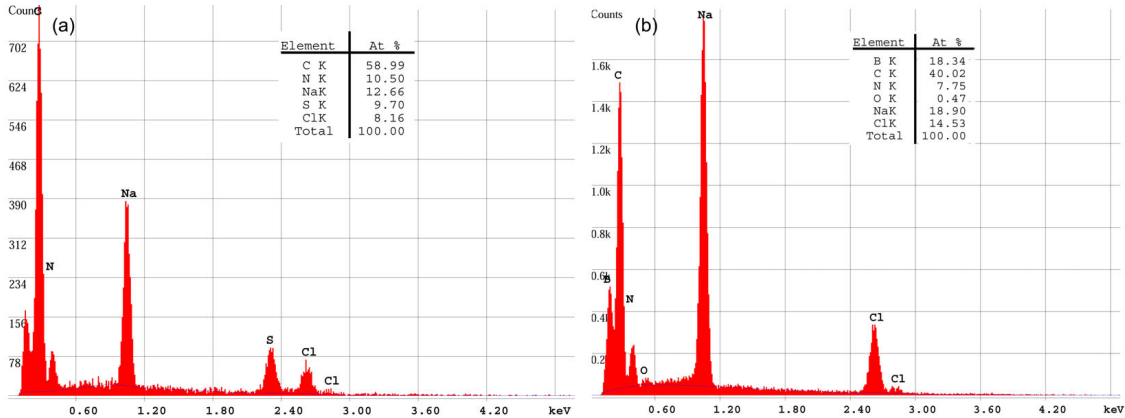


**Figure B.2:** (a) EDX of the top layer for a TTF-TCNQ thin film grown on NaCl(100). (b) EDX of the bottom layer for a TTF-TCNQ thin film grown on NaCl(100).



## FEBID AND FIBID PARAMETERS

The parameters for focused ion and electron beam induced deposition processes used in the experiments on the microcontact fabrication of individual TTF-TCNQ growth domains are compiled below.

**Table C.1:** *Parameters of electron and ion beam for tungsten-composite deposition, FIB etching and TMS deposition. In the case of FIB the thickness is the depth of etching.*

Parameters	W(CO) <sub>6</sub> deposition	FIB etching	TMS passivation
beam type	ion	ion	electron
thickness (nm)	200	100...150	~100...150
pitch (nm)	18	8	20
$t_D$ (ns)	200	200	500
passes	64748	(7110 ... 10665)	323977
$I$ (A)	10 pA	10 pA	0.4 nA
$U$ (V)	30 kV	30 kV	5 kV

**Table C.2:** *Parameters of the electron beam for platinum-composite and silicon (oxide) deposition, and snapshots.*

Parameters	Pt deposition	Pt irradiation	Si passivation	Snapshot
beam type	electron	electron	electron	electron

thickness (nm)	80	50	10	-
pitch (nm)	20	20	20	5.8
$t_D$ ( $\mu\text{s}$ )	1	1	10	3
passes	3676	$200 \times 10^3$	3163	1
$I$ (A)	1.6 nA	1.6 nA	1.6 nA	1.6 nA
$U$ (V)	5 kV	5 kV	5 kV	5 kV

---

## FITTING OF TEMPERATURE-DEPENDENT ELECTRICAL CONDUCTIVITY OF TTF-TCNQ THIN FILMS AND DOMAINS

A non-linear fit was applied to the temperature-dependent electrical conductivity measurements of TTF-TCNQ thin films and TTF-TCNQ domains. The used function is given by Eq. (6.3). The parameter  $\chi^2$  reflecting the quality of the fits is given in the Tab. D.1 for the investigated samples.

**Table D.1:** Values of  $\chi^2$  parameter used to test quality of fit of electrical conductivity data for temperatures (1)  $T \geq 50$  K and (2)  $T < 50$  K. The best fit results are given by bold letters.

Sample	non-irradiated thin film	irradiated thin film	microcrystal sample 7	microcrystal sample 6
<i>T &lt; 50 K</i>				
$\gamma = 1$	0.052	0.002286	0.0045	0.02584
$\gamma = 1/3$	0.00336	$5.02 \times 10^{-4}$	$5 \times 10^{-4}$	$7.44 \times 10^{-4}$
$\gamma = 1/2$	0.00201	0.0016	<b><math>4.47 \times 10^{-7}</math></b>	0.00333
$\gamma = 1/4$	<b>0.00164</b>	$8.6 \times 10^{-4}$	0.00114	<b><math>3.85 \times 10^{-4}</math></b>
$\gamma = 2/5$	0.00545	<b><math>3.64 \times 10^{-4}</math></b>	$1.83 \times 10^{-4}$	0.00148
<i>T ≥ 50 K</i>				
$\gamma = 1$	<b><math>5.02 \times 10^{-5}</math></b>	<b><math>3.4 \times 10^{-5}</math></b>	0.0107	0.0101

$\gamma = 1/3$	0.00125	0.00393	$4.25 \times 10^{-4}$	$4.19 \times 10^{-4}$
$\gamma = 1/2$	$7.94 \times 10^{-4}$	0.00198	0.00143	$1.44 \times 10^{-4}$
$\gamma = 1/4$	0.00151	0.00481	$1.4 \times 10^{-4}$	0.00125
$\gamma = 2/5$	0.00106	0.00297	$1.6 \times 10^{-4}$	<b><math>8.73 \times 10^{-5}</math></b>

---

## ACKNOWLEDGMENTS

Although only my name appears on the cover of this dissertation, a great many people have contributed to it. I owe my gratitude to all those people who have made this dissertation possible and because of whom my graduate experience has been one that I will cherish forever. The reported research work was performed in the framework of the Sonderforschungsbereich/ Transregio 49 (B9-*Thin films of charge-transfer salts*) research collaboration during the years 2008 to 2011 while employed at the Goethe University, Frankfurt am Main.

First and foremost I thank my supervisor Prof. Dr. Michael Huth for the possibility to perform the study, for his help and inspiration. His valuable comments and constructive criticism, expressed in a straight-forward but friendly manner, not only helped me gain new insights, but also motivated me time and time again. I am glad to have worked with Michael and grateful for having been his student.

I want to thank the entire “Dünneschichten” group for help and support. My special gratitude goes to Roland Sachser, Anna Cmyrev, Olexander Foyevtsov, Milan Rudloff, Dr. Fabritio Porrati, Eugenia Begun, Dr. Christian Schwalb, Christina Grimm and Jörg Franke. Additionally I would like to thank Olexander for his help in performing X-ray measurements and analysis, and Roland for his numerous assistance and support in the SEM measurements and cryostat experiments. I also would like to acknowledge Dr. Kerstin Keller, whose detailed explanations and assistance at the initial stage of my study in Frankfurt allowed me to gain an in-depth understanding of the experimental setups. I thank Milan Rudloff and Elena Solovyeva for helping me with the German “Zusammenfassung” and Carolyne Agnew and Dr. Mark Thomson for their help in the proofreading of this manuscript.

I want to thank Prof. Dr. Martin Aeschlimann and his group from TU Kaiserslautern, especially Dr. Indranil Sarkar, for the enjoyable collaborative work. I also thank Prof. Dr. Gerd Schönhense and his PhD student Katerina Medjanik and Dr. Andrei Hloskovskyy from Johannes Gutenberg University of Mainz for very fruitful discussions and cooperative work.

I want to thank my husband Dr. Ilia Solov'yov for the moral support, patience and understanding during the whole period of my PhD study and writing this thesis.

I doubt that I would have been able to overcome all difficulties without him. I am very thankful to Ilia for the careful reading of the thesis, his critical remarks and help in improving the contents of the dissertation.

I would like to express my heart-felt gratitude to my mother Elena and grandmother Slava for their patient and understanding. Most importantly, none of this would have been possible without the love and patience of them. My family has been a constant source of love, concern, support and strength all these years. I also would like to acknowledge my parent-in-law and my sister-in-law for their hospitality during the writing of the final part of the thesis. Finally I want to thank my friends, especially Marina and Mariya, for frequent discussions and patience in listening to me!

## BIBLIOGRAPHY

- [1] Amakatu, H., H. Inokuchi, and Y. Matsunaga. 1954. Electrical conductivity of the perylene-bromine complex. *Nature*. 173:168.
- [2] Mulliken, R. S. and W. B. Person. 1962. Donor-acceptor complexes. *Annu. Rev. Phys. Chem.* 13:107.
- [3] Ferraris, J., D. Cowan, V. Wlatka, and J. H. Perlstein. 1973. Electron transfer in a new highly conducting donor-acceptor complex. *J. Am. Chem. Soc.* 95:948.
- [4] Coleman, L. B., M. J. Cohen, D. J. Sandman, F. G. Yamagishi, A. F. Garito, and A. J. Heeger. 1973. Superconducting fluctuations and the Peierls instability in an organic solid. *Solid State Comm.* 12:1125.
- [5] Ishiguro, T., S. Kagoshima, and H. Anzai. 1976. dc conductivity anomalies at the transition points in TTF-TCNQ. *J. Phys. Soc. Jpn.* 41:351.
- [6] Friend, R. H., M. Miljak, and D. Jérôme. 1978. Pressure dependence of the phase transitions in tetrathiafulvalene-tetracyanoquinodimethane (TTF-TCNQ): Evidence for longitudinal lockin at 20 kbar. *Phys. Rev. Lett.* 40:1048.
- [7] Khanna, S. K., J. P. Pouget, R. Comes, A. F. Garito, and A. J. Heeger. 1977. X-ray studies of  $2k_F$  and  $4k_F$  anomalies in tetrathiafulvalene-tetracyanoquinodimethane (TTF-TCNQ). *Phys. Rev. B.* 16:1468.
- [8] Kagoshima, S., T. Ishiguro, and H. Anzai. 1976. X-ray scattering study of phonon anomalies and superstructures in TTF-TCNQ. *J. Phys. Soc. Jpn.* 41:2061.
- [9] Jérôme, D. and H. J. Schulz. 1982. Organic conductors and semiconductors. *Adv. Phys.* 31:299.

- [10] Humphrey, W., A. Dalke, and K. Schulten. 1996. VMD – Visual Molecular Dynamics. *Journal of Molecular Graphics*. 14:33.
- [11] Mori, T. 1998. Structural genealogy of BEDT-TTF-based organic conductors I. parallel molecules:  $\beta$  and  $\beta''$  phases. *Bull. Chem. Soc. Jpn.* 71:2509.
- [12] Mori, T. 1999. Structural genealogy of BEDT-TTF-based organic conductors II. inclined molecules:  $\theta$ ,  $\alpha$  and  $\kappa$  phases. *Bull. Chem. Soc. Jpn.* 72:179.
- [13] Laukhina, E., V. Tkacheva, A. Chekhlov, E. Yagubskii, R. Wojciechowski, J. Ulanski, J. Vidal-Gancedo, J. Veciana, V. Laukhin, and C. Rovira. 2004. Polymorphism of new bis(ethylenedithio)tetrathiafulvalene (BEDT-TTF) based molecular conductor; novel transformations in metallic BEDT-TTF layers. *Chem. Mater.* 16:2471.
- [14] Mori, T. and H. Inokuchi. 1987. Crystal structure of the mixed-stacked salt of bis(ethylenedithio)tetrathiafulvalene (BEDT-TTF) and tetracyanoquinodimethane (TCNQ). *Bull. Chem. Soc. Jpn.* 60:402.
- [15] Mori, T. and H. Inokuchi. 1986. Structural and electrical properties of (BEDT-TTF)(TCNQ). *Solid State Comm.* 59:355.
- [16] Yamamoto, H. M., M. Hagiwara, and R. Kato. 2003. New phase of (BEDT-TTF)(TCNQ). *Synth. Met.* 133:449.
- [17] Solovyeva, V. and M. Huth. 2011. Defect-induced shift of the Peierls transition in TTF-TCNQ thin films. *Synth. Met.* doi:10.1016/j.synthmet.2011.03.003. In press.
- [18] Solovyeva, V., A. Cmyrev, R. Sachser, H. Reith, and M. Huth. 2011. Influence of the substrate-induced strain and irradiation disorder on the peierls transition in TTF-TCNQ microdomains. Submitted to *J. of Phys. D: Appl. Phys.*, arXiv:1101.2333v1.
- [19] Solovyeva, V., K. Keller, and M. Huth. 2009. Organic charge-transfer phase formation in thin films of the BEDT-TTF/TCNQ donor-acceptor system. *Thin Solid Films*. 517:6671.
- [20] Sarkar, I., M. Laux, J. Demokritova, A. Ruffing, S. Mathias, J. Wei, V. Solovyeva, M. Rudloff, S. S. Naghavi, C. Felser, M. Huth, and M. Aeschliemann. 2010. Evaporation temperature-tuned physical vapor deposition growth



- engineering of one dimensional non-Fermi liquid tetrathiofulvalene tetracyanoquinodimethane thin films. *Appl. Phys. Lett.* 97:111906.
- [21] Medjanik, K., D. Kutnyakhov, S. Nepijko, G. Schönhense, S. Naghavi, V. Al-ijani, C. Felser, N. Koch, R. Rieger, M. Baumgarten, and K. Müllen. 2010. Electronic structure of large disc-type donors and acceptors. *Phys. Chem. Chem. Phys.* 12:7184.
- [22] Toyota, N., M. Lang, and J. Müller. 2007. *Low-Dimensional Molecular Metals*. Springer.
- [23] Fraxedas, J. 2006. *Molecular Organic Materials*. Cambridge University Press.
- [24] Brooks, J. S. 2010. Organic crystals: properties, devices, functionalization and bridges to bio-molecules. *Chem. Soc. Rev.* 39:2667.
- [25] Fraxedas, J. 2002. Perspectives on thin molecular organic films. *Adv. Mater.* 14:1603.
- [26] Inokuchi, H. 2006. The discovery of organic semiconductors. Its light and shadow. *Organic Electronics.* 7:62.
- [27] Saito, G. and Y. Yoshida. 2007. Development of conductive organic molecular assemblies: Organic metals, superconductors, and exotic functional materials. *Bull. Chem. Soc. Jpn.* 80:1.
- [28] Mori, T. and T. Kawamoto. 2007. Organic conductors-from fundamental to nonlinear conductivity. *Annu. Rep. Prog. Chem. Sec. C.* 103:134.
- [29] Koch, N. 2007. Organic electronic devices and their functional interfaces. *Chem. Phys. Chem.* 8:1438.
- [30] Medjanik, K., S. Perkert, S. Naghavi, M. Rudloff, V. Solovyeva, D. Chercka, M. Huth, S. A. Nepijko, T. Methfessel, C. Felser, M. Baumgarten, K. Müllen, H. Elmers, and G. Schönhense. 2010. A new charge-transfer complex in UHV co-deposited tetramethoxypyrene and tetracyanoquinodimethane. *Phys. Rev. B.* 82:245419.
- [31] Schwoerer, M. and H. C. Wolf. 2007. *Organic Molecular Solids*. Wiley-VCH.
- [32] Herbstein, F. H. 2005. *Crystalline Molecular Complexes and Compounds Structures and Principles*, volume 2. Oxford University Press.

- [33] Ashcroft, N. W. and N. D. Mermin. 1988. *Solid state physics*. CBS Publishing Asia LTD.
- [34] Giamarchi, T. 2006. *Quantum physics in one dimension*, volume 121 of *The international series of monographs on Physics*. Oxford University press.
- [35] Lee, C., W. Yang, and R. G. Parr. 1988. Development of the Colle-Salvetti correlation-energy formula into a functional of the electron density. *Phys. Rev. B.* 37:785.
- [36] Becke, A. D. 1988. Density-functional exchange-energy approximation with correct asymptotic behavior. *Phys. Rev. A.* 38:3098.
- [37] Becke, A. D. 1993. Density-functional thermochemistry. III. The role of exact exchange. *J. Chem. Phys.* 98:5648.
- [38] Kistenmacher, T. J., T. E. Phillips, and D. O. Cowan. 1974. The crystal structure of the 1:1 radical cation-radical anion salt of 2,2'-bis-1,3-dithiole (TTF) and 7,7,8,8-tetracyanoquinodimethane (TCNQ). *Acta Cryst. B.* 30:763.
- [39] Engler, E. M. and V. V. Patel. 1974. Structure control in organic metals. Synthesis of tetraselenofulvalene and its charge transfer salt with tetracyano-p-quinodimethane. *J. Am. Chem. Soc.* 96:7376.
- [40] Jérôme, D., A. Mazand, M. Ribault, and K. Bechgaard. 1980. Superconductivity in a synthetic organic conductor (TMTSF)<sub>2</sub>PF<sub>6</sub>. *J. Phys. Lett.* 41:95.
- [41] Bechgaard, K., D. O. Cowan, and A. N. Bloch. 1974. Synthesis of the organic conductor tetramethyltetraselenofulvalenium 7,7,8,8-tetracyano-p-quinodimethanide (TMTSF-TCNQ)[4,4',5,5'-tetramethyl- $\Delta^{2,2'}$ -bis-1,3-diselenolium 3,6-bis-(dicyanomethylene)cyclohexadienide]. *J. Chem. Soc., Chem. Commun.*:937.
- [42] Bechgaard, K., K. Carneiro, F. B. Rasmussen, M. Olsen, G. Rindorf, C. S. Jacobsen, H. J. Pedersen, and J. C. Scott. 1981. Superconductivity in an organic solid. Synthesis, structure, and conductivity of bis(tetramethyltetraselenafulvalenium) perchlorate, (TMTSF)<sub>2</sub>ClO<sub>4</sub>. *J. Am. Chem. Soc.* 103:2440.
- [43] Peierls, R. E. 1955. *Quantum Theory of Solids*. Oxford University press.

- 
- [44] Mizuno, M., A. F. Garito, and M. P. Cava. 1978. Organic metals: alkylthio substitution effects in tetrathiafulvalene-tetracyanoquinodimethane charge-transfer complexes. *J. Chem. Soc., Chem. Commun.*:18.
- [45] Kim, A. M., U. Geiser, H. H. Wang, K. D. Carlson, J. M. Williams, W. K. Kwok, K. G. Vandervoort, J. E. Thompson, D. L. Stupka, D. Jung, and M.-H. Whangbo. 1990. A new ambient-pressure organic superconductor,  $\kappa$ -(ET)<sub>2</sub>Cu[N(CN)<sub>2</sub>]Br, with the highest transition temperature yet observed (inductive onset  $T_C = 11.6$  K, resistive onset = 12.5 K). *Inorg. Chem.* 29:2555.
- [46] Williams, J. M., A. M. Kim, H. H. Wang, K. D. Carlson, U. Geiser, L. K. Montgomery, G. J. Pyrka, D. M. Watkins, J. K. Kommers, S. J. Boryschuk, A. V. Crouch, W. K. Kwok, J. E. Schirber, D. L. Overmyer, D. Jung, and M.-H. Whangbo. 1990. From semiconductor-semiconductor transition (42 K) to the highest- $T_C$  organic superconductor,  $\kappa$ -(ET)<sub>2</sub>Cu[N(CN)<sub>2</sub>]Cl ( $T_C = 12.5$  K). *Inorg. Chem.* 29:3272.
- [47] Kanoda, K. 1997. Electron correlation, metal-insulator transition and superconductivity in quasi-2D organic systems, (ET)<sub>2</sub>X. *Physica C.* 282:299.
- [48] Mori, T. 2008. Molecular materials for organic field-effect transistors. *J. Phys.: Condens. Matter.* 20:1.
- [49] Takahashi, Y., T. Hasegawa, Y. Abe, Y. Tokura, K. Nishimura, and G. Saito. 2005. Tuning of electron injections for n-type organic transistor based on charge-transfer compounds. *Appl. Phys. Lett.* 86:063504.
- [50] Electrical properties of Si. <http://www.ioffe.ru/SVA/NSM/Semicond/Si/electric.html>.
- [51] Ando, S., R. Murakami, J. Nishida, H. Tada, Y. Inoue, S. Tokito, and Y. Yamashita. 2005. n-type organic field-effect transistors with very high electron mobility based on thiazole oligomers with trifluoromethylphenyl groups. *J. Am. Chem. Soc.* 127:14996.
- [52] Chesterfield, R. J., J. C. McKeen, C. R. Newman, P. C. Ewbank, D. A. da Silva Filho, J. L. Bredas, L. Miller, K. R. Mann, and C. D. Frisbie. 2004. Organic thin film transistors based on N-alkyl perylene diimides: Charge transport kinetics as a function of gate voltage and temperature. *J. Phys. Chem. B.* 108:19281.

- [53] Sakai, M., M. Nakamura, and K. Kudo. 2007. Organic nanochannel field-effect transistor with organic conductive wires. *Appl. Phys. Lett.* 90:062101.
- [54] Sakai, M., H. Sakuma, Y. Ito, A. Saito, M. Nakamura, and K. Kudo. 2007. Ambipolar field-effect transistor characteristics of (BEDT-TTF)(TCNQ) crystals and metal-like conduction induced by a gate electric field. *Phys. Rev. B.* 76:045111.
- [55] Pope, M., H. Kallmann, and P. Magnante. 1963. Electroluminescence in organic crystals. *J. Chem. Phys.* 38:2042.
- [56] Tang, C. W. and S. A. van Slyke. 1987. Organic electroluminescent diodes. *Appl. Phys. Lett.* 51:913.
- [57] Burroughes, J. H., D. D. C. Bradley, A. R. Brown, R. N. Marks, K. Mackay, R. H. Friend, P. L. Burns, and A. B. Holmes. 1990. Light-emitting diodes based on conjugated polymers. *Nature.* 347:539.
- [58] Kallmann, H. and M. Pope. 1959. Photovoltaic effect in organic crystals. *J. Chem. Phys.* 30:585.
- [59] Tang, C. W. and A. C. Albrecht. 1975. Photovoltaic effects of metal-chlorophyll-a-metal sandwich cells. *J. Chem. Phys.* 62:2139.
- [60] Tang, C. W. 1986. Two-layer organic photovoltaic cell. *Appl. Phys. Lett.* 48:183.
- [61] Sakuma, H., M. Sakai, M. Iizuka, M. Nakanura, and K. Kudo. 2004. Fabrication of organic transistors using BEDT-TTF and (BEDT-TTF)-(TCNQ) CT-Complex films. *IEICE Trans. Electron.* 87:2049.
- [62] Gomar-Nadal, E., J. Puigmartí-Luis, and D. B. Amabilino. 2008. Assembly of functional molecular nanostructures on surfaces. *Chem. Soc. Rev.* 37:490.
- [63] Petty, M. C. 1996. *Langmuir-Blodgett Films*. Cambridge University Press.
- [64] Figueras, A., J. Caro, J. Fraxedas, and V. Laukhin. 1999. TTF-TCNQ thin films grown by organic CVD: Texture and transport properties. *Synth. Met.* 102:1611.
- [65] Mahan, J. E. 2000. *Physical vapor deposition of thin films*. John Wiley and Sons, INC, New York.

- 
- [66] Forrest, S. R. 1997. Ultrathin organic films grown by organic molecular beam deposition and related techniques. *Chem. Rev.* 97:1793.
- [67] Freund, L. B. and S. Suresh. 2009. *Thin Films Materials*. Cambridge University Press.
- [68] Nalwa, H. S. 2002. *Handbook of Thin film materials: Deposition and processing of thin films*. Academic Press.
- [69] Venables, J. A., G. D. T. Spiller, and M. Hanbucken. 1984. Nucleation and growth of thin films. *Rep. Progr. Phys.* 47:399.
- [70] Keller, K. 2009. *Organic donor-acceptor thin film systems: towards optimized growth conditions*. Ph.D. thesis, Goethe-Universität, Frankfurt am Main.
- [71] Macrae, C. F., I. J. Bruno, J. A. Chisholm, P. R. Edgington, P. McCabe, E. Pidcock, L. Rodriguez-Monge, R. Taylor, J. van de Streek, and P. A. Wood. 2008. Mercury CSD 2.0 – new features for the visualization and investigation of crystal structures. *J. Appl. Cryst.* 41:466.
- [72] Kobayashi, H., A. Kobayashi, Y. Sasaki, G. Saito, and H. Inokuchi. 1986. The crystal and molecular structures of bis(ethylenedithio)tetrathiafulvalene. *Bull. Chem. Soc. Jpn.* 59:301.
- [73] Long, R. E., R. A. Sparks, and K. N. Trueblood. 1965. The crystal and molecular structure of 7,7,8,8-tetracyanoquinodimethane. *Acta Cryst.* 18:932.
- [74] Marra, W. C., P. Eisenberger, and A. Y. Cho. 1979. X-ray total-external-reflection-Bragg diffraction: A structural study of the GaAs-Al interface. *Appl. Phys. Lett.* 50:6927.
- [75] Birkholz, M. 2006. *Thin Film Analysis by X-Ray Scattering*. Wiley-VCH.
- [76] Fei company. 2006. *The xT Nova NovaLab User' Manual*.
- [77] Goldstein, V. J., D. E. Newbury, D. C. Joy, P. Echlin, C. E. Lyman, and E. Lifshin. 2003. *Scanning Electron Microscopy and X-ray Microanalysis*. Springer, Netherlands.
- [78] Drouin, D., A. R. Couture, R. Gauvin, P. Hovington, P. Horny, and H. Demers. 2002. *Computer program CASINO V2.42*. University of Sherbrooke Quebec Canada.

- [79] Acker, D. S., R. J. Harder, W. R. Hertler, W. Mahler, L. R. Melby, R. E. Benson, and W. E. Mochel. 1960. 7,7,8,8- tetracyanoquinodimethane and its electrically conducting anion-radical derivatives. *J. Am. Chem. Soc.* 82:2471.
- [80] Chen, E. C. M. and W. E. Wentworth. 1975. A comparison of experimental determinations of electron affinities of pi charge transfer complex acceptors. *J. Chem. Phys.* 63:3183.
- [81] Conwell, E., editor. 1988. *Highly Conducting Quasi-One-Dimensional Organic crystals*, volume 27 of *Semiconductors and Semimetals*. Academic Press.
- [82] Wudl, F., G. M. Smith, and E. J. Hufnagel. 1970. Bis-1,3-dithiolium chloride: an unusually stable organic radical cation. *J. Chem. Soc. D*:1453.
- [83] Gleiter, R., E. Schmidt, D. O. Cowan, and J. P. Ferraris. 1973. The electronic structure of tetrathiofulvalene. *J. Electron. Spectrosc. Relat. Phenom.* 2:207.
- [84] Grüner, G. 1994. *Density waves in Solids*. Addison-Wesley Publishing company. The advanced book program.
- [85] Kohn, W. 1959. Image of the Fermi surface in the vibration spectrum of a metal. *Phys. Rev. Lett.* 2:393.
- [86] Fukuyama, H. and P. A. Lee. 1978. Dynamics of the charge-density wave. I. Impurity pinning in a single chain. *Phys. Rev. B.* 17:535.
- [87] Bak, P. and V. J. Emery. 1976. Theory of the structural phase transformations in tetrathiafulvalene-tetracyanoquinodimethane (TTF-TCNQ). *Phys. Rev. Lett.* 36:978.
- [88] Kagoshima, S., H. Anzai, K. Kajimura, and T. Ishiguro. 1975. Observation of the Kohn anomaly and the peierls transition in TTF-TCNQ by X-Ray scattering. *J. Phys. Soc. Jpn.* 39:1143.
- [89] Denoyer, F., F. Comes, A. F. Garito, and A. J. Heeger. 1975. X-ray-diffuse-scattering evidence for a phase transition in tetrathiafulvalene tetracyanoquinodimethane (TTF-TCNQ). *Phys. Rev. Lett.* 35:445.
- [90] Comes, R., S. M. Shapiro, G. Shirane, A. F. Garito, and A. Heeger. 1975. Neutron-scattering study of the 38- and 54-K phase transitions in deuterated tetrathiafulvalene- tetracyanoquinodimethane (TTF-TCNQ). *Phys. Rev. Lett.* 35:1518.

- 
- [91] Ellenson, W. D., R. Comes, S. M. Shapiro, G. Shirane, F. Garito, and A. J. Heeger. 1976. Neutron scattering study of 49 K phase transition in TTF-TCNQ. *Solid State Comm.* 20:53.
- [92] Wang, Z. Z., J. C. Girard, C. Pasquier, D. Jérôme, and K. Bechgaard. 2003. Scanning tunneling microscopy in TTF-TCNQ: Phase and amplitude modulated charge density waves. *Phys. Rev. B.* 67:121401.
- [93] Ishiguro, T., K. Yamaji, and G. Saito. 2001. *Organic Superconductors*. Springer.
- [94] Dumoulin, B., J. P. Pouget, and C. Bourbonnais. 1999. Theory of  $2k_F$  and  $4k_F$  fluctuations effects in strongly correlated peierls systems. *Synth. Met.* 103:1797.
- [95] Jérôme, D. 2004. Organic conductors: From charge density wave TTF-TCNQ to superconducting  $(\text{TMTSF})_2\text{PF}_2$ . *Chem. Rev.* 104:5565.
- [96] Chen, T. H. and B. H. Schechtman. 1975. Preparation and properties of polycrystalline films of TTF-TCNQ. *Thin Solid Films.* 30:173.
- [97] Vollmann, W., W. Berger, C. Hamann, and L. Libera. 1984. Relations between the morphology and conductivity on thin films of tetrathiofulvalinium-tetracyanoquinodimethane. *Thin Solid Films.* 111:7.
- [98] Sato, N., G. Saito, and H. Inokuchi. 1983. Ionization potentials and polarization energies of tetraselenafulvalene (TSF) derivatives determined from ultraviolet photoelectron spectroscopy. *Chem. Phys.* 76:79.
- [99] Kawamoto, A., K. Miyagawa, A. Shimizu, and K. Kanoda. 1997. NMR study of  $(\text{BEDT-TTF})(\text{TCNQ})$  at selective nuclear sites. *Synth. Met.* 85:1601.
- [100] Ishida, K., Y. Niino, Y. Kitaoka, K. Asayama, Y. Iwasa, and Y. Tokura. 1995.  $^1\text{H}$  NMR study in two dimensional Mott-Hubbard system,  $(\text{BEDT-TTF})-(\text{TCNQ})$ . *Synth. Met.* 70:881.
- [101] Iwasa, Y., K. Mizuhashi, T. Koda, Y. Tokura, and G. Saito. 1994. Metal-insulator transition and antiferromagnetic order in bis(ethylenedithio)tetrathiafulvalene-tetracyanoquinodimethane  $(\text{BEDT-TTF})(\text{TCNQ})$ . *Phys. Rev. B.* 49:3580.

- [102] Miyashita, M., K. Uchiyama, H. Taniguchi, K. Satoh, Y. Uwatoko, N. Tajima, M. Tamura, and R. Kato. 2004. High-pressure study of a Mott insulator (BEDT-TTF)(TCNQ). *J. Phys. IV France*. 114:333.
- [103] Eto, Y., A. Kawamoto, N. Matsunaga, K. Nomura, K. Yamamoto, and K. Yakushi. 2009. Evidence for exchange interaction between donor and acceptor layers in  $\beta'$ -(BEDT-TTF)(TCNQ). *Phys. Rev. B*. 80:174506.
- [104] Yamamoto, H. M., N. Tajima, M. Hagiwara, R. Kato, and J. I. Yamaura. 2003. Strange electric/magnetic behaviour of new (BEDT-TTF)(TCNQ). *Synth. Met.* 135:623.
- [105] Sakai, M. 2010. private communications.
- [106] Kimata, M., Y. Oshima, H. Ohta, K. Koyama, M. Motokawa, H. M. Yamamoto, and R. Kato. 2004. Magneto-optical measurements of  $\beta''$ -(BEDT-TTF)(TCNQ). *Physica B*. 346:382.
- [107] Kimata, M., Y. Oshima, H. Ohta, K. Koyama, M. Motokawa, H. M. Yamamoto, and R. Kato. 2007. Low-temperature Fermi surface of the organic conductor  $\beta''$ -(BEDT-TTF)(TCNQ)<sub>(1-x)</sub> (F1-TCNQ)<sub>x</sub>, (x=0..0.05) from magneto-optical measurements. *Phys. Rev. B*. 75:045126.
- [108] Uruichi, M., K. Yakushi, H. M. Yamamoto, and R. Kato. 2006. Infrared and Raman studies of the charge-ordering phase transition at 170 K in the quarter-filled organic conductor,  $\beta''$ -(ET)(TCNQ). *J. Phys. Soc. Jpn.* 75:074720.
- [109] Kilitziraki, M., A. J. Moore, M. C. Petty, and M. R. Bryce. 1998. Evaporated thin films of tetrathiafulvalene derivatives and their charge-transfer complexes. *Thin Solid Films*. 335:209.
- [110] Molas, S., J. Caro, J. Santiso, A. Figueras, J. Fraxedas, C. Meziere, M. Fourmigue, and P. Batail. 2000. Thin molecular films of neutral tetrathiafulvalene-derivatives. *J. Cryst. Growth*. 218:399.
- [111] Saito, G., T. Enoki, T. Toriumi, and H. Inokuchi. 1982. Two-dimensionality and suppression of metal-semiconductor transition in a new organic metal with alkylthio substituted TTF and perchlorate. *Solid State Comm.* 42:557.
- [112] Fernández Torrente, I. 2008. *Local spectroscopy of bi-molecular self-assemblies, screening, charge transfer, and magnetism at the molecular scale*. Ph.D. thesis, Freie Universität Berlin.



- 
- [113] Caro, J., J. Santino, A. Figueras, P. Gorostiza, and F. Sanz. 1999. Surface characterization of TTF-TCNQ thin films evaporated on alkali halide substrates. *Synth. Met.* 102:1607.
- [114] Fraxedas, J., S. Molas, A. Figueras, I. Jimenes, R. Gago, P. Auban-Senzier,, and M. Goffman. 2002. Thin films of molecular metals: TTF-TCNQ. *J. Solid State Chem.* 168:384.
- [115] Britten, J. F. 1995. Czochralski-grown SrLaGaO<sub>4</sub>. *Acta Cryst. C.* 51:1975.
- [116] Gloubokov, A., R. Jablonski, W. Ryba-Romanowski, J. Sass, A. Pajaczkowska, R. Uecker, and P. Reiche. 1995. On the preparation and crystal growth of SrLaAlO<sub>4</sub>. *J. Cryst. Growth.* 147:123.
- [117] Sasaki, S., K. Fujino, and Y. Takeuchi. 1979. X-ray determination of electron-density distributions in oxides, MgO, MnO, CoO, and NiO, and atomic scattering factors of their constituent atoms. *Proceedings of the Japan Academ.* 55:43.
- [118] Baur, W. H. 1956. Über die Verfeinerung der Kristallstrukturbestimmung einiger Vertreter des Rutiltyps: TiO<sub>2</sub>, SnO<sub>2</sub>, GeO<sub>2</sub> und MgF<sub>2</sub>. *Acta Cryst.* 9:538.
- [119] Tsirelson, V. G., M. Y. Antipin, R. G. Gerr, R. P. Ozerov, and Y. T. Struchkov. 1985. Ruby structure peculiarities derived from X-ray diffraction data localization of chromium atoms and electron deformation density. *Phys. Status Solidi A.* 87:425.
- [120] Walker, D., P. K. Verma, L. M. D. Cranswick, R. L. Jones, S. M. Clark, and S. Buhre. 2004. Halite-sylvite thermoelasticity. *Am. Mineral.* 89:204.
- [121] Bond, W. L. and W. Kaiser. 1985. Interstitial versus substitutional oxygen in silicon. *J. Phys.. Chem. Sol.* 16:44.
- [122] Yasuzuka, S., K. Murata, T. Arimoto, and R. Kato. 2007. Temperature-pressure phase diagram in TTF-TCNQ: Strong suppression of charge-density-wave state under extremely high pressure. *J. Phys. Soc. Jpn.* 76:033701.
- [123] Murata, K., Y. Weng, Y. Seno, N. R. Tamilselvan, K. Kobayashi, S. Arumugam, Y. Takashima, H. Yoshino, and R. Kato. 2009. Fluctuation of the charge density wave in TTF-TCNQ under high pressure. *Physica B.* 404:373.

- [124] Gunning, W. J., C. K. Chiang, A. J. Heeger, and A. J. Epstein. 1979. *Quasi One-Dimensional Conductors I, Proceeding of the International Conference Dubrovnik, SR Croatia, SFR Yugoslavia, 1978*, volume 95 of *Lecture Notes in Physics*.
- [125] Chiang, C. K., M. J. Cohen, P. R. Newman, and A. J. Heeger. 1977. Effect of controlled disorder on the electrical properties of TTF-TCNQ (tetrathiafulvalene-tetracyanoquinodimethane): High-temperature regime. *Phys. Rev. B.* 16:5163.
- [126] Zuppiroli, L., S. Bouffard, K. Bechgaard, B. Hilti, and C. W. Mayer. 1980. Irradiation effects in quasi-one-dimensional organic conductors: The evidence of a transverse fixed-range phonon-assisted hopping. *Phys. Rev. B.* 22:6035.
- [127] Chu, C. W., J. M. E. Harper, T. H. Geballe, and R. L. Greene. 1973. Pressure dependence of the metal-insulator transition in tetrathiofulvalinium tetracyanoquinodimethane (TTF-TCNQ). *Phys. Rev. Lett.* 31:1491.
- [128] Ishibashi, S., T. Hashimoto, M. Kohyama, and K. Terakura. 2004. *Ab initio* electronic structure study for TTF-TCNQ under uniaxial compression. *Phys. Rev. B.* 69:155111.
- [129] Murata, K., S. Kakoshima, S. Yasuzuka, H. Yoshino, and R. Kondo. 2006. High-pressure research in organic conductors. *J. Phys. Soc. Jpn.* 75:051015.
- [130] Bouffard, S. and L. Zuppiroli. 1978. Elastoresistivity of TTF-TCNQ and related compounds. *Solid State Comm.* 28:113.
- [131] Maesato, M., Y. Kaga, R. Kondo, and S. Kagoshimaa. 2000. Uniaxial strain method for soft crystals: Application to the control of the electronic properties of organic conductors. *Rev. Sci. Instrum.* 71:176.
- [132] Ceperley, D. M. and B. J. Alder. 1980. Ground state of the electron gas by a stochastic method. *Phys. Rev. Lett.* 45:566.
- [133] Perdew, J. P. and A. Zunger. 1981. Self-interaction correction to density-functional approximations for many-electron systems. *Phys. Rev. B.* 23:5048.
- [134] Perdew, J. P., K. Burke, and M. Ernzerhof. 1996. Generalized gradient approximation made simple. *Phys. Rev. Lett.* 77:3865.
- [135] Ishibashi, S. and M. Kohyama. 2000. *Ab initio* pseudopotential calculation for TTF-TCNQ and TSeF-TCNQ. *Phys. Rev. B.* 62:7839.

- 
- [136] Kawasugi, Y., o. Hiroshi M. Yamamot, M. Hosoda, N. Tajima, T. Fukunaga, K. Tsukagoshi, and R. Kato. 2008. Strain-induced superconductor/insulator transition and field effect in a thin single crystal of molecular conductor. *Appl. Phys. Lett.* 92:243508.
- [137] Figueras, A., S. Garelik, J. Caro, J. Cifre, J. Veciana, E. R. C. Rovira, E. Canadell, A. Seffar, and J. Fontcuberta. 1996. Preparation and characterization of conducting thin films of molecular organic conductors (TTF-TCNQ). *J. Cryst. Growth.* 166:798.
- [138] Reinhardt, C., W. Vollmann, C. Hamann, L. Libera, and S. Trompler. 1980. Properties of oriented TTF-TCNQ thin films. *Krist. Techn.* 15:243.
- [139] Chaudhari, P., B. A. Scott, R. B. Laibowitz, Y. Tomkiewicz, and J. B. Torrance. 1974. Characterization of epitaxially grown thin films of (TTF)(TCNQ). *Appl. Phys. Lett.* 24:439.
- [140] Nakajama, K., M. Kageshima, N. Are, and M. Yoshimura. 1993. Observation of thin film of one-dimensional organic conductor tetrathiofulvalene tetracyanoquinodimethane by means of atomic force microscopy. *Appl. Phys. Lett.* 62:1892.
- [141] Wada, H., D. de Caro, L. Valade, T. Ozawa, Y. Bando, and T. Mori. 2009. Thin-film phases of organic charge transfer complexes formed by chemical vapor deposition. *Thin Solid Films.* 518:299.
- [142] Gonzalez-Lakunza, N., I. Fernández-Torrente, K. J. Franke, N. Lorente, A. Arnau, and J. I. Pascual. 2008. Formation of dispersive hybrid bands at an organic-metal interface. *Phys. Rev. Lett.* 100:156805.
- [143] Dardel, B., D. Malterre, M. Grioni, P. Weibel, Y. Baer, and F. Lévy. 1991. Unusual photoemission spectral function of quasi-one-dimensional metals. *Phys. Rev. Lett.* 67:3144.
- [144] Zwick, F., D. Jérôme, G. Margaritondo, M. Onellion, J. Voit, and M. Grioni. 1998. Band mapping and quasiparticle suppression in the one-dimensional organic conductor TTF-TCNQ. *Phys. Rev. Lett.* 81:2974.
- [145] Claessen, R., M. Sing, U. Schwingenschlögl, P. Blaha, M. Dressel, and C. S. Jacobsen. 2002. Spectroscopic signatures of spin-charge separation in the quasi-one-dimensional organic conductor TTF-TCNQ. *Phys. Rev. Lett.* 88:096402.

- [146] Sing, M., U. Schwingenschlögl, R. Claessen, M. Dressel, and C. S. Jacobsen. 2003. Surface characterization and surface electronic structure of organic quasi-one-dimensional charge transfer salts. *Phys. Rev. B.* 67:125402.
- [147] Gupta, S. P. S. and P. Chatterjee, editors. 2002. *Powder Diffraction: Proceedings of the second international school on Powder Diffraction*. Allied Publisher Ltd.
- [148] Huang, K. 1947. X-ray reflexions from dilute solid solutions. *Proc. R. Soc. Lond. A. (Math. Phys. Sci.)*. 190:102.
- [149] Williamson, G. K. and W. H. Hall. 1953. X-ray line broadening from fided aluminium and wolfram. *Acta Metallurgica.* 1:22.
- [150] Hubbell, J. H. and S. M. Seltzer. 2004. Tables of X-ray mass attenuation coefficients and mass energy-absorption coefficients (version 1.4). National Institute of Standards and Technology, Gaithersburg, MD, <http://physics.nist.gov/xaamdi>.
- [151] Langford, J. I. and D. Louër. 1996. Powder diffraction. *Rep. Progr. Phys.* 59:131.
- [152] Foyevtsov, O. 2010. Program Project1 X-ray analysis. Goethe-Universität, Frankfurt am Main.
- [153] Al-Shamery, K., H.-G. Rubahn, and H. Sitter, editors. 2008. *Organic Nanostructures for Next Generation Devices*. Springer Series in Materials Science.
- [154] Huth, M. and C. P. Flynn. 1997. Titanium thin film growth on small and large misfit substrates. *Appl. Phys. Lett.* 71:2466.
- [155] Mihály, G. and L. Zuppiroli. 1982. Radiation effects in organic metals: the mechanisms of the damage production. *Phil. Mag. A.* 45:549.
- [156] Mantel, O. C., C. A. Bal, C. Langezaal, C. Dekker, and H. S. J. van der Zant. 1999. Sliding charge-density-wave transport in micron-sized wires of  $\text{Rb}_{0.30}\text{MoO}_3$ . *Phys. Rev. B.* 60:5287.
- [157] Abrikosov, A. A. and L. P. Gor'kov. 1961. Contribution to the theory of superconducting alloys with paramagnetic impurities. *J. Exp. Theor. Phys.* 12:1243.

- 
- [158] Patton, B. R. and L. J. Sham. 1974. Fluctuation conductivity in the incommensurate Peierls system. *Phys. Rev. Lett.* 33:638.
- [159] Pouget, J.-P. 2004. X-ray diffuse scattering as precursor of incommensurate Peierls transitions in one-dimensional organic charge transfer conductors. *Z. Kristallogr.* 219:771.
- [160] Kato, N. A., M. Fujimura, S. Kuniyoshi, K. Kudo, M. Hara, and K. Tanaka. 1998. Control of molecular orientation in TTF-TCNQ co-evaporated films by applying an electric field. *Appl. Surf. Sci.* 130-132:658.
- [161] Sakai, M., M. Iizuka, M. Nakamura, and K. Kudo. 2003. Fabrication and electrical characterization of tetrathiafulvalene-tetracyanoquinodimethane molecular wires. *Jpn. J. Appl. Phys.* 42:2488.
- [162] Sakai, M., H. Miyata, K. Itami, M. Nakamura, and K. Kudo. 2008. Spontaneous activation process for self-aligned organic nanochannel transistors. *Appl. Phys. Express.* 1:081802.
- [163] Sakai, M., M. Iizuka, M. Nakamura, and K. Kudo. 2005. Organic nanotransistor fabricated by co-evaporation method under alternating electric field. *Synthetic Metals.* 153:293.
- [164] Sai, T. P. and A. K. Raychaudhuri. 2008. Electric field directed growth of molecular wires of charge transfer molecules on prefabricated metal electrodes. *Mater. Res. Soc. Symp. Proc.* 1058:JJ05-03.
- [165] Sai, T. P. and A. K. Raychaudhuri. 2010. Observation of Peierls transition in nanowires (diameter  $\sim 130$  nm) of the charge transfer molecule TTF-TCNQ synthesized by electric-field-directed growth. *Nanotechnology.* 21:045703.
- [166] Lacoé, R. C., H. J. Schulz, D. Jérôme, K. Bechgaard, and I. Johannsen. 1985. Observation of nonlinear electrical transport at the onset of a Peierls transition in an organic conductor. *Phys. Rev. Lett.* 55:2351.
- [167] Forro, L., R. Lacoé, S. Bouffard, and D. Jérôme. 1987. Defect-concentration dependence of the charge-density-wave transport in tetrathiafulvalene tetracyanoquinodimethane. *Phys. Rev. B.* 35:5884.
- [168] Liu, H., J. Li, C. Lao, C. Huang, Y. Li, Z. L. Wang, and D. Zhu. 2007. Morphological tuning and conductivity of organic conductor nanowires. *Nanotechnology.* 318:495704.

- [169] Huth, M., D. Klingenberger, C. Grimm, F. Porrati, and R. Sachser. 2009. Conductance regimes of W-based granular metals prepared by electron beam induced deposition. *New J. Phys.* 11:033032.
- [170] Porrati, F., R. Sachser, and M. Huth. 2009. The transient electrical conductivity of W-based electron-beam-induced deposits during growth, irradiation and exposure to air. *Nanotechnology.* 20:195301.
- [171] Porrati, F., R. Sachser, C. H. Schwalb, A. S. Frangakis, and M. Huth. 2011. Tuning the electrical conductivity of Pt-containing granular metals by post-growth electron irradiation. *J. Appl. Phys.* 109:063715.
- [172] Ziegler, J. F. 2010. The stopping and range of ions in matter. <http://www.srim.org/#SRIM>.
- [173] Valentin, J. 2003. Relative biological effectiveness (RBE), quality factor ( $Q$ ), and radiation weighting factor ( $w_R$ ): ICRP Publication 92. *Annals of the ICRP.* 33:1.
- [174] Shklovskii, B. I. and A. L. Efros. 1984. *Electronic properties of doped semiconductors*. Number 45 in Springer series in solid-state sciences. Springer-Verlag Berlin, Heidelberg, New York, Tokyo.
- [175] Fogler, M. M., S. Teber, and B. I. Shklovskii. 2004. Variable-range hopping in quasi-one-dimensional electron crystals. *Phys. Rev. B.* 69:035413.
- [176] Zaitsev-Zotov, S. V. 2004. Finite-size effects in quasi-one-dimensional conductors with a charge-density wave. *Phys.-Usp.* 47:533.
- [177] van Smaalen, S., J. L. de Boer, C. Haas, and J. Kommandeur. 1985. Anisotropic thermal expansion in crystals with stacks of planar molecules, such as tetracyanoquinodimethanide (TCNQ) salts. *Phys. Rev. B.* 31:3496.
- [178] Ibach, H. 1969. Thermal expansion of silicon and zinc oxide (I). *Phys. Status Solidi B.* 31:625.
- [179] Finhol, A., G. Bravic, J. Gaultier, and D. Chasseau. 1981. Room- and high-pressure neutron structure determination of tetrathiafulvalene-7,7,8,8-tetracyano-p-quinodimethane (TTF-TCNQ). Thermal expansion and isothermal compressibility. *Acta Cryst. B.* 37:1225.

- 
- [180] Ishiguro, T., S. Kagoshima, and H. Anzai. 1977. Elastic property of tetrathiafulvalene-tetracyanoquinodimethane (TTF-TCNQ). *J. Phys. Soc. Jpn.* 42:365.
- [181] Tiedje, T., R. R. Haering, and W. N. Hardy. 1979. The application of capacitive transducers to sound velocity measurements in TTF-TCNQ. *J. Acoust. Soc. Am.* 65:1171.
- [182] Debray, D., R. Millet, D. Jérôme, S. Barisic, L. Giral, and J. M. Fabre. 1977. Neutron diffraction study of the compressibility of TTF-TCNQ under hydrostatic pressure. *J. Phys. Lett.* 38:227.
- [183] Puget, J. P., S. M. Shapiro, G. Shirane, A. F. Garito, and A. J. Heeger. 1979. Elastic- and inelastic-neutron-scattering study of tetrathiafulvalenium-tetracyanoquinodimethanide TTF-TCNQ: new results. *Phys. Rev. B.* 19:1792.
- [184] Caro, J., P. Gorostiza, S. Sanz, and J. Fraxedas. 2001. Nanomechanical properties of surface of molecular organic thin films. *Synth. Met.* 121:1417.
- [185] Solov'yov, I. A., M. Mathew, A. V. Solov'yov, and W. Greiner. 2008. Liquid surface model for carbon nanotube energetics. *Phys. Rev. E.* 78:051601.
- [186] Conwell, E. M. and N. C. Banik. 1982. High electric field transport in  $(\text{TMTSF})_2\text{PF}_6$  (bistetramethyltetraselenafulvalene hexafluorophosphate) at low temperature. *Mol. Cryst. Liq. Cryst.* 79:95.
- [187] Coppens, P., Y. W. Yang, R. H. Blessing, W. F. Cooper, and F. K. Larsen. 1977. The experimental charge distribution in sulphur containing molecules. Analysis of cyclic octasulphur at 300 and 100 K. *J. Am. Chem. Soc.* 99:760.
- [188] Miura, Y. F., S. Ohnishi, M. Hara, H. Sasabe, and W. Knoll. 1996. Conductive thin films of bis(ethylenedithio)tetrathiafulvalene salt fabricated by a successive dry-wet process. *Appl. Phys. Lett.* 68:2447.
- [189] Hüfner, S., editor. 2007. *Very High Resolution Photoelectron Spectroscopy*, volume 715 of *Lecture Notes in Physics*. Springer.
- [190] Hiroma, S., H. Kuroda, and H. Akamatu. 1971. Semiconductivity and photoconductivity of TCNQ crystals. *Bull. Chem. Soc. Jpn.* 44:974.
- [191] Kulshreshtha, A. P. and T. Mookherhji. 1970. Electrical conductivity and photoresponse in Tetracyanoquinodimethan. *Mol. Cryst. Liq. Cryst.* 10:75.

- [192] Hurditch, R. J., Vera M. Vincent, and J. D. Wright. 1972. Electrical conductivity of tetracyanoquinodimethane crystals. *J. Chem. Soc. – Faraday Trans. 1.* 68:46575.



## LIST OF FIGURES

1	Schema des Überlapps der $\pi$ -Orbitale der Donor (TTF) und Akzeptor (TCNQ) Stapeln entlang der Stapel Achse. Die $a$ -Achse ist senkrecht zur $b$ -Achse. Für diese Darstellung wurde das Programm VMD benutzt [10]. . . . .	iii
1.1	The schematic representation of (a) the donor molecule TTF and (b) the acceptor molecule TCNQ. The VMD program was used for molecules representation [10]. . . . .	2
1.2	Donor molecule bis(ethylenedithio)tetrathiafulvalene (BEDT-TTF) favoring the formation of two dimensional CT complexes. . . . .	3
2.1	Energy diagram for the donor and the acceptor energy levels. The process of charge transfer is schematically illustrated with the curved arrow. . . . .	7
2.2	Crystalline structure of TTF-TCNQ in the monoclinic crystal system with the space group $P2_1/c$ [38]. (a) Orthogonal view along the stacking $b$ -axis. (b) Orthogonal view along the direction perpendicular to the $(bc)$ -plane of TTF-TCNQ. The VMD program was used for molecules representation [10]. . . . .	9
2.3	Crystallographic modifications of the BEDT-TTF salts. The arrangement of the BEDT-TTF molecules is shown by red blocks. The unit cells are schematically shown by black lines. . . . .	10
2.4	Phase diagram of the $(BEDT-TTF)_2X$ salts proposed by Kanoda [47]. AF- is the abbreviation for antiferromagnetic. $U$ is the on-site Coulomb repulsion, $W$ is the bandwidth. The figure was adopted from [22]. . . . .	11

---

2.5	Possible stack structures of donor and acceptor molecules in the organic CT compounds. On the left side: the mixed stack structure; On the right: segregated stacking arrangement variant is presented.	12
2.6	Schematic illustration of the working principle of organic field effect transistor with top contacts. $V_G$ is the gate voltage, $V_D$ is the drain-source voltage, $I_D$ is the drain-source current. . . . .	14
2.7	Working principle of: (a) OLED and (b) OPVC. The cathode, anode and organic layers are shown. The light direction is depicted by an arrow. . . . .	16
3.1	Various processes taking place during thin film formation. The grey spheres depict the substrate surface while violet spheres represent the deposited organic molecules. . . . .	22
3.2	Schematic illustration of the Knudsen effusion cell and the deposition process of molecules on the substrate surface. The different quantities introduced in the figures are discussed in the text. $T_{effcell}$ , measured by, e.g., a thermocouple, is the effusion cell temperature. $z_{sub}$ is the re-evaporation flux corresponding to the desorption of the previously absorbed molecules. . . . .	24
3.3	Thin film growth modes on top of the substrate: (a) Frank-van der Merwe (layer by layer) growth mode, (b) Stranski-Krastanov (layer-island) growth mode, and (c) Volmer-Weber (island) growth mode.	26
3.4	Schematic illustration of an UHV deposition chamber with load-lock chamber and deposition chamber. The transfer arm is used to transport the substrate holder with the substrate from the load-lock chamber to the deposition chamber. . . . .	27
3.5	(a) X-ray diffractometer Bruker D8 Discover. (b) Illustration of Bragg's law. . . . .	30
3.6	The degradation of a TTF-TCNQ thin film grown on SrLaGaO <sub>4</sub> (100) substrate in the course of a current measurement at fixed bias voltage of 0.1 V. . . . .	34
3.7	Transport measurement chips and contact schemes: (a) Cryostat chip with the sample containing 5 stripes, (b) the drawing of the contacts on the cryostat chip and on the plate with the Cu-contacts. The measurement sectors and pin numbers are indicated. (c) Photolithography mask with four opening areas for four-probe measurements of the electrical conductivity of TTF-TCNQ microcrystals, (d) the cryostat chip. . . . .	35

3.8	The mask for the bilayer. . . . .	36
3.9	Scheme illustrating the working principle of the Oxford $^4\text{He}$ cryostat with liquid nitrogen shielding (2), liquid helium (3) and variable temperature insert (8). . . . .	37
4.1	Bandstructure for a half-filled band at different temperatures (a) above $T_P$ , (b) at $T < T_P$ . The electron density and lattice distortion are schematically shown. . . . .	41
4.2	Temperature dependence of the intra-chain ( $\xi_{\parallel}$ ) and inter-chain ( $\xi_{\perp}$ ) correlation lengths. $\xi_{1D}$ is the correlation length of the ideal one dimensional chain. $d_{\perp}$ is the distance between the neighboring chains. $T_P$ is the transition temperature, $T^*$ is a crossover temperature where the correlations among the neighboring chains develop and $T_{MF}$ is the mean field temperature, where the correlations start to form along the chain direction. . . . .	42
4.3	Conductivity of TTF-TCNQ single crystals along the $a$ , $b$ and $c^*$ -axes. $c^*$ -axis is the axis perpendicular to the $(ab)$ plane of TTF-TCNQ. The arrows show the position of the first order phase transition $T_L$ . The figure is adopted from [93]. . . . .	44
4.4	Crystallographic phases of the (BEDT-TTF)TCNQ CT complex: (a) monoclinic phase, (b) triclinic semiconductor $\beta'$ -phase, and (c) triclinic metallic $\beta''$ -phase. The VMD visualization program was used to represent the molecules [10]. . . . .	46
4.5	Transport characteristics of (BEDT-TTF)TCNQ CT complexes. (a) Temperature dependence of the resistivity along the $c$ -axis of a crystal of the $\beta'$ -phase for different pressures, taken from [101]. (b) Resistivity of a $\beta''$ -phase single crystal of (BEDT-TTF)TCNQ at ambient pressure, taken from [104]. . . . .	48
4.6	Crystals of the $\beta'$ -phase of (BEDT-TTF)TCNQ grown in DCE solution. . . . .	51
4.7	XRD patterns of (BEDT-TTF)TCNQ solution grown crystals from different solvents: (a) tetrahydrofuran, (b) fast evaporation from tetrahydrofuran solvents, (c) dichlorethane and dichlormethane, and (d) the references for (BEDT-TTF)TCNQ monoclinic and $\beta'$ -phases [14, 15]. . . . .	52

- 
- 4.8 Example of a microscope slide with (BEDT-TTF)TCNQ thin films, grown in the test chamber from the pre-reacted material. The different evaporation temperature areas were separated by a shadow mask during the deposition. . . . . 53
- 5.1 Pressure-temperature phase diagram for TTF-TCNQ single crystals: circles show the results from [6], while squares and triangles are taken from [122]. . . . . 56
- 5.2 X-ray diffraction pattern of TTF-TCNQ thin film. The black line shows the diffractogram for the TTF-TCNQ thin film grown on a glass substrate. The evaporation temperature was 110 °. The red line is the reference XRD pattern for TTF-TCNQ [38]. . . . . 60
- 5.3 Two domain growth of microcrystals of TTF-TCNQ on NaCl(100). The  $\langle 110 \rangle$  and  $\langle \bar{1}10 \rangle$  axes of the NaCl(100) substrate are indicated in white. The  $a$ - and  $b$ - axes of the TTF-TCNQ microcrystal are also shown in red. . . . . 61
- 5.4 SEM images of TTF-TCNQ thin films grown with an effusion cell temperature 90 °C on (a) NaCl(100) for 5 min, (b) NaCl(110) for 6 min and (c) NaCl(210) for 6 min. The scale bar applies to all panels. 62
- 5.5 (a) GID- $\varphi$  scans for TTF-TCNQ film (red line) grown on SrLaGaO<sub>4</sub>(100) (black line) with an effusion cell temperature of 120 °C. The peaks corresponding to the (100) crystallographic plane of the TTF-TCNQ film and the (002) plane of the SrLaGaO<sub>4</sub>(100) substrate are indicated with arrows.  $\varphi$  is the rotation angle around the normal to the substrate surface used in the GID measurement. (b) XRD pattern in symmetric Bragg condition of TTF-TCNQ thin film grown on SrLaGaO<sub>4</sub> (black line), compared with the reference pattern for TTF-TCNQ (red line) [38]. (c)-(d) SEM images of the TTF-TCNQ thin film, normal view and tilted view with 52 ° tilt angle. The scale bar in (c) applies to both panels. . . . . 63
- 5.6 SEM images of TTF-TCNQ thin films grown on NaCl(100) after (a) 1h deposition (corresponding to 175 nm thickness), (b) 2h deposition (corresponding to 350 nm), (c) 3h deposition (corresponding to 525 nm), (d) 4h deposition (corresponding to 700 nm) and (e) 5h deposition (corresponding to 825 nm). (f) XRD pattern of the sample. The scale bar in (a) applies to all panels. . . . . 65

---

5.7	AFM images of TTF-TCNQ thin film grown on the NaCl(100) after 1 hour of deposition at 110 °C effusion cell temperature. Plot (a) illustrates the mixed area of the TTF-TCNQ thin film, where both, TCNQ and TTF-TCNQ crystallites are observed. Plots (b) and (c) illustrate regions of the lower layer of the thin film, which to a large extent consists of TCNQ crystals. Plot (d) illustrates selected regions showing the upper layer of the thin film, consisting of TTF-TCNQ crystallites. . . . .	66
5.8	SEM images of TTF-TCNQ thin films grown on NaCl(210) after (a) 1h deposition, (b) 2h deposition, (c) 3h deposition, (d) 4h deposition and (e) 5h deposition. (f) XRD pattern of the sample. The scale bar in (a) applies to all panels. . . . .	67
5.9	TTF-TCNQ thin films grown on MgF <sub>2</sub> (001) after (a) 1h deposition (corresponding to 0.375 μm film thickness), (b) 2h deposition (corresponding to 0.7 μm), (c) 3h deposition (corresponding to 1.125 μm), (d) 4h deposition (corresponding to 1.5 μm) and (e) 5h deposition (corresponding to 1.875 μm). (f) XRD pattern of the sample. The scale bar in (a) applies to all panels. . . . .	69
5.10	SEM images of TTF-TCNQ thin films grown on MgO(100) after (a) 1h deposition, (b) 2h deposition, (c) 3h deposition, (d) 4h deposition and (e) 5h deposition. (f) XRD pattern of the whole sample. The scale bar in (a) applies to all panels. . . . .	70
5.11	SEM images of TTF-TCNQ thin films grown on α-Al <sub>2</sub> O <sub>3</sub> (11 $\bar{2}$ 0) after (a) 1h deposition, (b) 2h deposition, (c) 3h deposition, (d) 4h deposition and (e) 5h deposition. (f) XRD pattern of the sample. The scale bar in (a) applies to all panels. . . . .	71
5.12	SEM images of TTF-TCNQ thin films grown on MgF <sub>2</sub> (100) after (a) 1h deposition, (b) 2h deposition, (c) 3h deposition, (d) 4h deposition and (e) 5h deposition. (f) XRD pattern of the sample. The scale bar in (a) applies to all panels. . . . .	72
5.13	SEM images of TTF-TCNQ thin films grown on SrLaAlO <sub>4</sub> (100) after (a) 1h deposition, (b) 2h deposition, (c) 3h deposition, (d) 4h deposition and (e) 5h deposition. (f) XRD pattern of the sample. The scale bar in (a) applies to all panels. . . . .	73

5.14	SEM images of TTF-TCNQ thin films grown on SrLaGaO <sub>4</sub> (100) after (a) 1h deposition, (b) 2h deposition, (c) 3h deposition, (d) 4h deposition and (e) 5h deposition. (f) XRD pattern of the sample. The scale bar in (a) applies to all panels. . . . .	74
5.15	SEM images of TTF-TCNQ thin films grown on Si(100)/SiO <sub>2</sub> with an effusion cell temperature (a), (d) 90 °C; (b), (e) 110 °C; (c), (f) 130 °C. (a)-(c) normal view and (d)-(f) tilted view with 52 ° tilt angle. The scale bar applies to all panels. . . . .	75
5.16	X-ray pattern for TTF-TCNQ thin film grown on MgO(100). . . . .	77
5.17	Integrated energy dispersive curves for TTF-TCNQ thin films measured at room temperature and at 77 K. The insets show the fit of the low energy part by a power law for the curves measured at 77 K and at room temperature. $\alpha(300\text{ K}) = 1.2$ . $\alpha(77\text{ K}) = 0.85$ . . . . .	78
5.18	Bragg reflection for the (002) crystallographic plane of the striped TTF-TCNQ thin film grown on NaCl(100) (see Fig. 5.6) fitted by the Pearson function (see Tab. 5.3) for each stripe separately. The width of the stripe corresponding to 5h deposition time equals to a half width of other stripes. The inset illustrates the principle of the integrated breadth calculation. . . . .	83
5.19	Electrical conductivity (circles) and the Peierls transition temperature (squares) measured for TTF-TCNQ thin films with different thicknesses grown on the NaCl(100). The inset shows the dependence of the logarithmic derivative of the resistivity on temperature, Eq. (5.4), for the films grown for 4 hours. . . . .	85
5.20	(a) Current-voltage characteristics for a TTF-TCNQ thin film grown on NaCl(100) after 1 hour growth. (b) Threshold electric field for TTF-TCNQ thin films grown on NaCl(100) and on Si(100)/SiO <sub>2</sub> after 1 and 2 hours growth. . . . .	87
5.21	Dependence of the Peierls transition temperature on the root mean square microstrain in TTF-TCNQ thin films, extracted from a line profile analysis (see sections 5.4). The film thicknesses are indicated. . . . .	89
5.22	Normalized distribution of the Peierls transition temperature of different TTF-TCNQ thin films grown at different conditions. $N_{max}$ is the number of samples for which the distribution has a maximum. The total number of investigated TTF-TCNQ samples is 40. . . . .	90

5.23	(a) The change of the electrical current measured at fixed bias voltage in a TTF-TCNQ thin film as function of time of irradiation. (b) The Peierls transition for the non-irradiated and irradiated TTF-TCNQ thin film. The irradiation dose was 1.4 GGy. . . . .	91
6.1	Schematic illustration of the deposition process of the TTF-TCNQ microdomains on the substrate through a shadow mask. The substrate with bonded Au/Cr contacts is shown on the chip used for <i>in situ</i> conductivity measurements in the electron microscope during the irradiation experiment, as well as for the low-temperature measurements. . . . .	97
6.2	Contacted TTF-TCNQ microcrystal grown on NaCl(100) (sample 1): (a) domain with attached contacts, (b) broken TTF-TCNQ domain after transportation to the cryostat. The arrow indicates the site of crystal breakage. The scale bar applies to both panels. . . . .	99
6.3	Schematic illustration of the contact fabrication process on a TTF-TCNQ microcrystal. SEM images of (a) the TTF-TCNQ microcrystals formed on the substrate (see Fig. 6.1), (b) a TTF-TCNQ microcrystal is chosen for contacting, (c) TTF-TCNQ microcrystal with Pt contacts attached, (d) contacts extension by FEBID, (e)-(f) contacts extension by FIBID, (g) a zoomed-out SEM image of the TTF-TCNQ microcrystal with FEBID/FIBID contacts together with the pre-patterned Au/Cr contacts. (h) AFM image of the TTF-TCNQ microcrystal and (j) AFM cross section view of the TTF-TCNQ domain. The position of the cross section is shown by arrow in (h). AFM images were taken after the transport measurements. . . . .	101
6.4	Cross-section view of absorbed energy by TTF-TCNQ microcrystal grown on a Si(100)/SiO <sub>2</sub> (285 nm) substrate for (a) sample 6 and (b) sample 7. The grey shade ranges from light to dark as the density increases; the 10% line, for example, is the frontier between the area containing 90% of the absorbed energy and the rest of the sample. . . . .	104
6.5	Temperature dependence of the resistivity (squares) measured for two TTF-TCNQ domains irradiated by the electron beam with (a) 1.3 GGy radiation dose (sample 7) and (b) 2.36 GGy radiation dose (sample 6). The exponents $\gamma$ used in Eq. (6.3) are given for each graph. The applied voltage is 0.2 V. The insets show the temperature dependence of the logarithmic derivative $d(\ln R)/d(1/T)^\gamma$ with $\gamma$ as indicated. Detailed results of the fits are given in Appendix D. . . . .	106

6.6	Transport regimes in quasi-one-dimensional Wigner crystal with defects depending on the average segment length. The figure is adopted from [175]. . . . .	108
6.7	Current voltage characteristics for a TTF-TCNQ microcrystal (sample 6) measured in the temperature range of 10...290 K. . . . .	109
6.8	Differential resistance of a TTF-TCNQ domain (sample 6) measured in the temperature range of 4.2... 265 K. The irradiation dose of the microcrystal was 2.36 GGy. The inset shows the temperature dependence of the threshold electric field for sample 3 (shown by triangles), sample 6 (shown by squares) and sample 7 (shown by circles). . . . .	110
6.9	Schematic illustration of the clamping principle. (a) organic microcrystal at room temperature and (b) at the Peierls transition temperature. . . . .	112
7.1	BEDT-TTF thin films, grown in the “test” chamber: (top) X-ray diffraction patterns for BEDT-TTF thin films grown at evaporation temperature (a) 130 °C, (b) 140 °C, (c) 150 °C, (d) 160 °C, (e) 170 °C and (f) 180 °C. The reference XRD pattern for BEDT-TTF [72] is shown by the red line in (d). The reference XRD pattern for sulphur [187] is shown by the blue line in (f). (bottom) Optical images of BEDT-TTF thin films. Each indicated temperature corresponds to 1 hour deposition time. . . . .	119
7.2	TCNQ thin films, grown in the “test” chamber: (top) X-ray diffraction patterns for TCNQ thin films grown at evaporation temperature (a) 90 °C, (b) 100 °C, (c) 110 °C, (d) 120 °C, (e) 130 °C and (f) 140 °C. The XRD reference pattern for TCNQ [73] is shown by the red line in (a). (bottom) Optical images of TCNQ thin films. Each indicated temperature corresponds to 1 hour deposition time. . . . .	120
7.3	BEDT-TTF/TCNQ bilayers grown on glass substrates with prefabricated Au/Cr contacts (a) before and (b) after annealing. The color change of the film indicates the formation of a CT phase. . . . .	122



- 7.4 Optical microscopy images of (BEDT-TTF)TCNQ bilayer samples. Top row: bilayer grown on a glass substrate. Bottom row: bilayer grown on a Si/SiO<sub>2</sub> substrate one half of which is covered with a gold layer. Images (a) and (c) show the bilayer after the deposition of the BEDT-TTF layer on top of the TCNQ layer. Image (c) shows the bilayer grown on the bare Si/SiO<sub>2</sub>. Images (b) and (d) show the bilayer after the post-growth annealing. The dashed line in (d) indicates the border between the bare Si/SiO<sub>2</sub> and Au-covered Si/SiO<sub>2</sub> surface. . . . . 123
- 7.5 (a) SEM image of individual (BEDT-TTF)TCNQ crystal formed in the course of the post-growth annealing procedure of a bilayer grown on a glass substrate. The characteristic size of the crystal is  $\sim 10 \mu\text{m}$ , as indicated in the figure. (b) A group of (BEDT-TTF)TCNQ crystals which had been formed during the post-growth annealing of a bilayer grown on a Si(100)/SiO<sub>2</sub> substrate. The characteristic size of one crystal in this case is  $< 5 \mu\text{m}$ , as indicated in the figure. . . . . 124
- 7.6 Casino simulation [78]: cross-section view of absorbed electron energy caused by the BEDT-TTF thin film. The operating voltage is 5 kV. The electron penetration depth is below 500 nm. . . . . 125
- 7.7 EDX element maps. (a) Overlay of the nitrogen element map (*K*-line) with a SEM image of a crystallite group protruding from the annealed bilayer grown on Si/SiO<sub>2</sub>. Nitrogen indicates the presence of TCNQ molecules. (b) Overlay of the sulphur element map (*K*-line) with the SEM image of the same crystallite group. Sulphur indicates the presence of BEDT-TTF molecules. . . . . 126
- 7.8 Results of the HAXPES measurements: core levels spectra for (a) carbon (C), (b) sulphur (S), (c) nitrogen (N) of the annealed (red line) and not annealed (black line) BEDT-TTF/TCNQ bilayers grown on a Si/SiO<sub>2</sub> substrate covered with Au/Cr layer. . . . . 128
- 7.9 SEM images of FIB cross-section through the bilayers grown on a Si(100)/SiO<sub>2</sub> substrate, (a) before and (b) after the post-growth annealing. The images were recorded for the sample being inclined to the electron beam by 52°. BEDT-TTF/TCNQ layers and (BEDT-TTF)TCNQ crystals are indicated. The scale bar applies to both panels. . . . . 129

7.10	X-ray diffraction patterns for the as-grown and annealed BEDT-TTF/TCNQ bilayer grown on Si(100)/SiO <sub>2</sub> substrate shown by dashed and solid lines, respectively. Inset: Angular range in which a small new Bragg peak (indicated by the arrow) appears at 12.66° after annealing. See text for details. . . . .	130
7.11	Temperature dependence of the current through the TCNQ/BEDT-TTF bilayer in $\ln \sigma$ vs. $1/T$ representation at a fixed bias of 0.1 V. The squares represent data before bilayer annealing and the dots show data after 12 hrs annealing of the bilayer. The solid lines show the results of a linear fit. Room-temperature currents are shown in the inset for the sample before and after annealing by dashed and solid lines, respectively. . . . .	131
7.12	Optical microscopy image of “single-CT” thin films grown on glass slides kept at room temperature. The effusion cell temperature was within the range of 120...180 °C. . . . .	134
7.13	(a) The XRD pattern recorded for the “single-CT” thin film sample grown on glass substrate held at room temperature. The effusion cell temperature is 150 °C. (b) X-ray diffraction pattern of the “co-A/CT” sample grown on $\alpha$ -Al <sub>2</sub> O <sub>3</sub> (a-plane) substrate kept at 100 °C. (0 $\ell\ell$ ) reflections of BEDT-TTF can be identified up to fourth order. The intensity of the peaks is shown in arbitrary units. . . . .	135
7.14	Optical microscopy images of the “co-A/CT” samples grown on $\alpha$ -Al <sub>2</sub> O <sub>3</sub> (11 $\bar{2}$ 0) (a) and on Si(100)/SiO <sub>2</sub> (b) substrates taken in differential interference contrast. Average crystal size is about 4 $\mu$ m and 6.5 $\mu$ m for $\alpha$ -Al <sub>2</sub> O <sub>3</sub> (11 $\bar{2}$ 0) and for Si(100)/SiO <sub>2</sub> substrates, respectively. Images were taken at 500 $\times$ magnification. . . . .	136
7.15	X-ray diffraction pattern of “co-A/CT” (BEDT-TTF)TCNQ samples grown on Si/SiO <sub>2</sub> (dotted line) and on $\alpha$ -Al <sub>2</sub> O <sub>3</sub> (a-plane) (solid line). The intensity of the peaks is given in arbitrary units. Dashed line: Reference diffraction pattern simulated using Mercury 2.3 [71] for the monoclinic phase of (BEDT-TTF)TCNQ. . . . .	136
B.1	EDX of a typical TTF-TCNQ thin film grown on NaCl(100). . . . .	145
B.2	(a) EDX of the top layer for a TTF-TCNQ thin film grown on NaCl(100). (b) EDX of the bottom layer for a TTF-TCNQ thin film grown on NaCl(100). . . . .	146

## LIST OF TABLES

4.1	Different phases of (BEDT-TTF)TCNQ charge transfer complex obtained using the solution growth method depending on the choice of the solvent and on the growth conditions. The boiling point for each used solvent is given. . . . .	50
4.2	Substrate materials used in growth experiments of TTF-TCNQ thin films. TTF-TCNQ lattice parameters are included for illustration purpose. . . . .	54
5.1	Different growth modes of TTF-TCNQ thin films observed for the investigated substrates. . . . .	76
5.2	Mass attenuation coefficients $\mu/\rho$ ( $\text{cm}^2/\text{g}$ ) for atoms contained in TTF-TCNQ [150]. . . . .	81
5.3	Integral breadth for the model functions in line profile analysis. $2w$ is the full width at half maximum of the peak, $\Gamma(m)$ is the gamma function, $A=0.9039645$ , $B=0.7699548$ , $C=1.364216$ , $D=1.136195$ and $E=2(\ln 2\pi)^{\frac{1}{2}}=0.9394372$ are constants, $m$ is the adjustment parameter in the Pearson function. The parameter $\eta$ is the amount of the Cauchy contribution in the Pseudo Voigt function, which represents a mixture of Gauss and Cauchy profiles. $k = \frac{\beta_C}{\sqrt{\pi}\beta_G}$ is the scaling factor between the Cauchy and Gauss profiles. . . . .	82
5.4	The minimal ( $\sigma_{min}$ ) and the maximal ( $\sigma_{max}$ ) values of the room temperature electrical conductivity $\sigma$ recorded for TTF-TCNQ thin films grown on different substrates. 5 different samples were measured for each substrate. The reference conductivity of TTF-TCNQ for single crystals is $\sigma_b \approx 500 (\Omega \text{ cm})^{-1}$ , $\sigma_a \approx 3 (\Omega \text{ cm})^{-1}$ [5]. . . . .	84

6.1	Summary of the geometrical parameters, electrical conductivity $\sigma_b$ and employed processes for the individual TTF-TCNQ microdomains. The process description is given in the text. TMS is the abbreviation for tetramethylsilane. NPS is the abbreviation for neopentasilane. . . . .	98
6.2	Radiation doses of TTF-TCNQ domains caused by the electron beam when the snapshot images of the sample were taken. . . . .	103
6.3	Exponent $\gamma$ and $T_0$ (K) characterizing the electrical transport behavior of TTF-TCNQ thin films and microcrystals at temperatures (1) $T \geq 50$ K and (2) $T < 50$ K. . . . .	107
6.4	Thermal expansion coefficients of TTF-TCNQ and calculated values for tensile strain and stress in TTF-TCNQ microcrystals at 50 K along $a$ - and $b$ -crystallographic axes. . . . .	113
C.1	Parameters of electron and ion beam for tungsten-composite deposition, FIB etching and TMS deposition. In the case of FIB the thickness is the depth of etching. . . . .	147
C.2	Parameters of the electron beam for platinum-composite and silicon (oxide) deposition, and snapshots. . . . .	147
D.1	Values of $\chi^2$ parameter used to test quality of fit of electrical conductivity data for temperatures (1) $T \geq 50$ K and (2) $T < 50$ K. The best fit results are given by bold letters. . . . .	149

## BIOGRAPHY (LEBENS LAUF)

**Name** Vita Solovyeva  
**Address** Physikalisches Institut,  
Goethe – University  
Max – von – Laue Str. 1  
60438 Frankfurt am Main, Germany  
**Tel. Nr.** +49 (069) 79847263  
**E-mail** levitan@physik.uni-frankfurt.de  
**Date of Birth** 21 March 1983  
**Place of Birth** Leningrad/St.-Petersburg, USSR/Russia



### Education and Academic Degrees

2008–2011 Ph.D. at the Goethe University, Frankfurt am Main, Germany  
Advisor: Prof. Dr. Michael Huth

2007–2008 Doctoral study at the Denmark Technical University, Kgs. Lyngby,  
Denmark  
Advisor: Prof. Dr. Peter Uhd Jepsen

2004–2006 M.Sc. in Physics, Physical-Technical Department of  
St. Petersburg State Polytechnical University, Russia  
Advisor: Prof. Dr. Sergey A. Gurevich

2000–2004 B.Sc. in Physics, Physical-Technical Department of  
St. Petersburg State Polytechnical University, Russia.  
Advisor: Prof. Dr. Alexander Ya. Vul’

1998–2000 Physical-mathematical Lyceum No 239, Saint-Petersburg, Russia  
High School Diploma

1990–1998 French Lyceum No 172, St. Petersburg, Russia.

## **Awards**

- 2000      Third place in mathematical olympiad in Polytechnical University,  
St. Petersburg, Russia
- 2006      Medal for the best Master work 2006 from The Ministry of Educa-  
tion and Science of the Russian Federation,  
St. Petersburg, Russia

## LIST OF PUBLICATIONS

### Manuscripts

1. V. Solovyeva, "Investigation of influence of structural properties of platinum nanoparticles on their electrocatalytical activity in the methanol oxidation reaction", Master of Science thesis, St. Petersburg State Polytechnical University, Saint Petersburg, Russia, pp. 1-70 (2006) (in Russian).
2. V. Solovyeva, "Surface functional groups of ultradispersed diamonds", Bachelor of Science thesis, St. Petersburg State Polytechnical University, Saint Petersburg, Russia, pp. 1-30 (2004) (in Russian).

### Journal Publications

1. R.K. Olsson, T.V. Andersen, L. Leick, V. Levitan (Solovyeva), P. Uhd Jepsen, D. Turchinovich. Femtosecond all-polarization-maintaining fiber laser operating at 1028nm, *Proceedings of SPIE* **7022**, 70221E (2007).
2. V. Solovyeva, K. Keller and M. Huth. Organic charge transfer phase formation in thin films of the BEDT-TTF/TCNQ donor-acceptor system, *Thin Solid Films* **517**, 6671 (2009).
3. I. Sarkar, M. Laux, J. Demokritova, A. Ruffing, S. Mathias, J. Wei, V. Solovyeva, M. Rudloff, S.S. Naghavi, C. Felser, M. Huth and M. Aeschlimann. Evaporation temperature-tuned physical vapor deposition growth engineering of one dimensional non-Fermi liquid TTF-TCNQ thin films, *Applied Physics Letters* **97**, 111906 (2010).
4. K. Medjanik, S. Perkert, S. Naghavi, M. Rudloff, V. Solovyeva, M. Huth, S. Nepijko, T. Methfessel, C. Felser, M. Baumgarten, K. Müllen, H.J. Elmers

- and G. Schönhense. A new charge-transfer complex in UHV co-deposited tetramethoxypyrene (TMP) and tetracyanoquinodimethane (TCNQ), *Physical Review B*, **82**, 245419 (2010).
5. V. Solovyeva and M. Huth. Defect-induced shift of the Peierls transition in TTF-TCNQ thin films, *Synthetic Metals*, doi:10.1016/j.synthmet.2011.03.003 (2011).
  6. V. Solovyeva, A. Cmyrev, R. Sachser, H. Reith and M. Huth. Influence of the substrate-induced strain and irradiation disorder on the Peierls transition in TTF-TCNQ microdomains, submitted to *Journal of Physics D: Applied Physics*, arXiv:1101.2333v1 (2011).